Constraints on the Equation of State of Nuclear Matter from Heavy-Ion Collisions

Dissertation
zur Erlangung des Doktorgrades
der Naturwissenschaften

vorgelegt beim Fachbereich Physik der
Johann Wolfgang Goethe-Universität
in Frankfurt am Main

von
Justin Mohs
aus Frankfurt am Main

Frankfurt 2024
(D 30)

Vom Fachbereich Physik (13) der
Johann Wolfgang Goethe-Universität als Dissertation angenommen.

Dekan: Prof. Dr. Roger Erb
Gutachter: Prof. Dr. Hannah Elfner und Priv. Doz. Dr. Hendrik van Hees
Datum der Disputation: 31. März 2025

Zusammenfassung

Diese Dissertation basiert auf den folgenden Publikationen:

1. Collective flow at SIS energies within a hadronic transport approach: Influence of light nuclei formation and equation of state. Justin Mohs, Martha Ege, Hannah Elfner, Markus Mayer, Phys.Rev.C 105 (2022) 3, 034906 [1].

2. Constraints on the Equation of State of Nuclear Matter from Systematically Comparing SMASH Calculations to HADES Data. Justin Mohs, Simon Spies, Hannah Elfner, arXiv:2409.16927 [nucl-th] (2024) [2].

3. Flow and Equation of State of nuclear matter at $E_{\mathrm{kin}}/A = 0.25 - 1.5\,\mathrm{GeV}$ with the SMASH transport approach. Lucia Anna Tarasovičová, Justin Mohs, Anton Andronic, Hannah Elfner, Karl-Heinz Kampert, Eur.Phys.J.A 60 (2024) 11, 232 [3].

4. Deuteron, triton, helium-3 and hypertriton production in relativistic heavy-ion collisions via stochastic multi-particle reactions. Martha Ege, Justin Mohs, Jan Staudenmaier, Hannah Elfner, arXiv:2409.04209 [nucl-th] (2024) [4].

Materie, wie sie uns im täglichen Leben umgibt, is aus Atomen zusammengesetzt. Atome bestehen wiederum aus einer Hülle von Elektronen und einem Atomkern im Zentrum. Der Atomkern ist im Vergleich zur Hülle extrem klein, macht jedoch fast das gesamte Gewicht des Atoms aus.

Der Atomkern beinhaltet Protonen und Neutronen, welche durch die starke Wechselwirkung, auch Kernkraft genannt, zusammengehalten werden. Die zugrundeliegende Theorie der starken Wechselwirkung ist die Quantenchromodynamik. Hier wird die Kernkraft durch die Interaktion von Quarks und Gluonen beschrieben, die sogenannte Farbladungen tragen. Berechnungen im Rahmen der Quantenchromodynamik sind extrem kompliziert und die Theorie kann in nur wenigen physikalischen Situationen gelöst werden.

Kernmaterie gehört nicht dazu. Daher können die Eigenschaften der Kernmaterie nur über effektive Theorien oder basierend auf experimentellen Befunden bestimmt werden. Neben Messungen an Atomkernen können auch astrophysikalische

Beobachtungen aufschlussreich sein, denn Kernmaterie ist auch in Neutronensternen vorhanden. Messungen der Masse und des Radius von Neutronensternen erlauben es, Rückschlüsse auf die Zustandsgleichung von Kernmaterie zu ziehen. Die Zustandsgleichung stellt thermodynamische Zustandsvariablen, wie zum Beispiel Druck, Dichte, und Temperatur in ein Verhältnis und charakterisiert dadurch die betrachtete Materie. Der Zusammenhang zwischen möglichen Abmessungen eines Neutronensterns und der Zustandsgleichung kann über die Tolman-Oppenheimer-Volkoff-Gleichungen hergestellt werden. Die Messung von Gravitationswellen, die bei der Kollision zweier Neutronensterne emittiert wurden, stellt einen Durchbruch dar und ermöglicht weitere Rückschlüsse über die Zustandsgleichung von Kernmaterie. Astrophysikalische Beobachtungen sind besonders wertvoll für die Bestimmung der Zustandsgleichung, da Kernmaterie hier in deutlich höheren Dichten vorliegt als in Atomkernen. Dadurch kann die Zustandsgleichung in einem anderen Bereich eingegrenzt werden.

Eine weitere Möglichkeit Kernmaterie in hohen Dichten zu untersuchen ist in Kollisionen schwerer Atomkerne. Bei der Kollision trifft Kernmaterie aufeinander und wird dabei komprimiert. Das führt, abhängig von der Kollisionsenergie, zu hohen Dichten. Schwerionenkollisionen können unter kontrollierten Bedingungen in großen Experimenten herbeigeführt werden und in hoher Anzahl wiederholt werden. Dementsprechend ist es von experimenteller Seite möglich, sehr präzise Messdaten bereitzustellen.

Für die Bestimmung der Zustandsgleichung ist jedoch eine theoretische Beschreibung der Schwerionenkollision unverzichtbar, denn im Experiment können lediglich Teilchen im Endzustand, nach der Kollision, detektiert werden. Rückschlüsse auf die heiße und dichte Phase der Kollision sind also nur im Rahmen von Modellrechnungen möglich. Die Schwierigkeit bei solchen Modellrechnungen ergibt sich dabei daraus, dass es sich bei Schwerionenkollisionen um extrem dynamische Prozesse handelt, bei denen nicht davon ausgegangen werden kann, dass ein thermisches Gleichgewicht vorliegt. Dementsprechend erfolgt die theoretische Beschreibung zumeist im Rahmen von Transportmodellen, die für die Berechnung der Nichtgleichgewichtsdynamik anwendbar sind.

Für die Bestimmung der Zustandsgleichung werden hadronische Freiheitsgrade verwendet. Hadronen, wie zum Beispiel Protonen und Neutronen, interagieren durch Stöße oder über Potenziale. Die Potenziale beschreiben die Änderung der Bewegungsgleichungen aufgrund der Anziehung und Abstoßung umliegender Teilchen. Die Potenziale können über thermodynamische Betrachtungen mit der Zustandsgleichung in Relation gesetzt werden. Der Weg zur Bestimmung der Zustandsgleichung führt also über ein Verständnis der Potenziale.

Das Hauptziel dieser Dissertation ist es, mithilfe von Transportrechnungen für Schwerionenkollisionen Rückschlüsse auf die Potenziale und damit auf die Zustands-

gleichung, zu ziehen. Dafür wird das Transportmodell SMASH verwendet. Der Kollisionsterm im SMASH Transportmodell beinhaltet diverse Reaktionsmöglichkeiten. Neben elastischen Kollisionen ist es möglich, eine Reihe von Resonanzen anzuregen. In diesem Punkt unterscheidet sich das Modell von einigen anderen Modellen, die in der Literatur zur Bestimmung der Zustandsgleichung herangezogen werden.

Die Potenziale in SMASH setzen sich aus verschiedenen Komponenten zusammen. Die Abhängigkeit von der Baryonendichte wird durch das Skyrme-Potenzial beschrieben. Protonen und Neutronen zählen zu den Baryonen und das Skyrme-Potenzial ist maßgeblich dafür verantwortlich, Atomkerne zu stabilisieren. Bei geringerer Dichte ist es anziehend, bei hoher Baryonendichte ist es abstoßend. In Streuexperimenten von Protonen an Kernen hat man festgestellt, dass das Potenzial ebenfalls von dem Impuls des Protons abhängt. Diese Impulsabhängigkeit wurde im Rahmen dieser Arbeit zu dem Skyrme-Potenzial in SMASH hinzugefügt. Neben dem Skyrme-Potenzial gibt es ein Symmetriepotenzial. Vereinfacht gesagt versucht dieses, eine Asymmetrie zwischen Protonen und Neutronen auszugleichen. Dabei ist es zum Beispiel attraktiv für Protonen sofern lokal mehr Neutronen als Protonen vorhanden sind. Die Asymmetrie in Neutronensternen ist enorm, da diese fast ausschließlich aus Neutronen bestehen. Daher ist das Symmetriepotenzial für astrophysikalische Anwendungen von besonderem Interesse. Weiterhin wurde im Rahmen dieser Arbeit das Coulomb-Potenzial implementiert. Die langreichweitige elektromagnetische Wechselwirkung ist numerisch aufwendig zu berechnen, trägt jedoch zu einer genaueren Bestimmung der Zustandsgleichung bei.

Aufgrund der starken Kompression der Kernmaterie in Schwerionenkollisionen eignen sie sich hervorragend zur Bestimmung der Baryonendichteabhängigkeit der Zustandsgleichung. Diese kann am besten durch die Betrachtung von eben solchen Baryonen quantifiziert werden. Protonen wie Neutronen treten jedoch häufig gebunden in leichten Kernen auf. Um einen angemessenen Vergleich zu experimentellen Messungen zu ermöglichen, muss daher auch die Bildung leichter Kerne in der theoretischen Beschreibung realisiert werden.

Es gibt verschiedene Herangehensweisen, die Entstehung leichter Kerne zu modellieren. Eine Möglichkeit beschränkt sich auf die Betrachtung von Protonen und Neutronen im Endzustand der Kollision. Nukleonen, die sowohl im Ortsraum, als auch im Impulsraum nah beieinander liegen, können als leichte Kerne interpretiert werden. Dieses Modell heißt Koaleszenz.

Ein grundlegend anderer Ansatz ist die dynamische Formation und Desintegration leichter Kerne durch Stöße von Nukleonen. Die Formation leichter Kerne tritt zumeist katalysiert durch ein Pion oder ein weiteres Nukleon auf. Solche Mehrteilchenreaktionen können direkt über stochastische Kollisionsraten oder aufgeteilt über einen Zwischenschritt realisiert werden. Die dynamische Beschreibung erlaubt es die Entstehung leichter Kerne zeitlich aufzulösen. Gleichzeitig ist dieser Ansatz limitiert

in der Größe der produzierten Kerne, da alle notwendigen Reaktionen individuell implementiert werden müssen.

Die erste Studie, die im Rahmen dieser Arbeit durchgeführt wurde, hat das Ziel, Observablen zu bestimmen, welche robuste Rückschlüsse auf die Zustandsgleichung ermöglichen. In Schwerionenkollisionen bildet sich basierend auf eine Asymmetrie im Anfangszustand eine anisotrope Teilchenverteilung in der transversalen Ebene, senkrecht zur Kollisionsachse. Diese Übersetzung vom Anfangszustand zum Endzustand ist besonders sensitiv auf die Zustandsgleichung. Die Anisotropie in der Verteilung der Teilchen wird durch sogenannte Flusskoeffizienten quantifiziert. Besonders die Koeffizienten der Verteilung von Protonen sind in der Literatur als exzellente Observablen für die Studie der Zustandsgleichung bekannt. Moderne Experimente liefern Daten mit exzellenter Statistik. Diese erlauben eine differenzielle Betrachtung der Flusskoeffizienten, fein aufgeteilt in Bereiche des Phasenraums.

Flusskoeffizienten, wie sie am HADES-Experiment in Kollisionen von Goldatomkernen gemessen werden, werden mit verschiedenen Zustandsgleichungen berechnet. Die Sensitivität der Koeffizienten auf die Zustandsgleichung wird dabei bestätigt. Weiterhin kann ein Vergleich der zwei Modelle für die Entstehung leichter Kerne Aufschluss darüber geben, in welchem Phasenraumbereich die Koeffizienten wenig von der Produktion der Kerne beeinflusst werden. Basierend auf diesem Bereich können besonders robuste Rückschlüsse auf die Zustandsgleichung gezogen werden.

Für diese Sensitivitätsstudie war die Impulsabhängigkeit der Potenziale noch nicht im SMASH Modell implementiert. Dementsprechend wurde noch keine zufriedenstellende Übereinstimmung zwischen Modell und Experiment erreicht. Im Anschluss wurde die Impulsabhängigkeit hinzugefügt und zusätzlich das Coulomb-Potenzial implementiert. Basierend auf den zuvor identifizierten Observablen wird eine Folgestudie, mit dem Ziel, die Zustandsgleichung quantitativ zu bestimmen, durchgeführt. Für einen systematischen Datenvergleich wird eine bayessche Analyse durchgeführt. Diese liefert auf kontrollierte Weise eine A-posteriori-Wahrscheinlichkeitsverteilung für die Parameter der Potenziale, also indirekt der Zustandsgleichung. Die Wahrscheinlichkeitsverteilung gibt nicht nur Aufschluss über die von der Messung bevorzugten Parameter, sondern quantifiziert auch die statistische Unsicherheit. Die Durchführung der bayesschen Analyse über das Markow-Chain-Monte-Carlo-Verfahren erfordert die häufige Evaluation des Modells. Da die Berechnung von Schwerionenkollisionen mit genügender Statistik einen enormen numerischen Aufwand erfordert, wird das SMASH Transportmodell hierfür mit einem Gaußschen Prozess emuliert.

Die so gewonnene Wahrscheinlichkeitsverteilung für die Potenziale offenbart eine relativ feste Zustandsgleichung verglichen mit vorhergegangenen Abschätzungen der Zustandsgleichung in der Literatur. Außerdem ist die statistische Unsicherheit sehr klein, was die Aussagekraft der experimentellen Daten bestätigt. Bei der Interpretation der A-posteriori-Wahrscheinlichkeitsverteilung sollte jedoch bedacht werden,

dass diese keine Unsicherheiten der theoretischen Beschreibung beinhaltet. In der Zukunft führt der Weg zur Zustandsgleichung also darüber, ein Verständnis der Unterschiede zwischen den Modelle aufzubauen, und Unsicherheiten zu reduzieren.

Die oben genannten Studien sind fokussiert auf experimentelle Daten der HADES Kollaboration für eine feste Kollisionsenergie. Am FOPI-Experiment wurden Gold–Gold-Kollisionen bei einer Reihe von Kollisionsenergien vermessen. Da sich mit der Kollisionsenergie auch die Dichte des Systems ändert, bieten diese Messungen die Möglichkeit, mehr über die Dichteabhängigkeit der Zustandsgleichung zu erfahren. Betrachtet wird weiterhin die Anisotropie der Teilchenverteilung in der transversalen Ebene. Die Übereinstimmung von Rechnungen mit verschieden festen Zustandsgleichungen wird hier durch die Berechnung eines χ^2 quantifiziert. Beim Vergleich zwischen weichen und festen Zustandsgleichungen scheint eine weichere Zustandsgleichung insgesamt die Messungen besser zu beschreiben. Diese Beobachtung ist konsistent mit vorhergegangenen Analysen der Daten vom FOPI Experiment. Betrachtet man jedoch den zweiten Flusskoeffizienten, welcher die Elliptizität der Verteilung beschreibt, bemerkt man, dass dieser mit steigender Kollisionsenergie nur durch eine härtere Zustandsgleichung beschrieben werden kann. Das ist wiederum konsistent mit den oben genannten Studien von Daten des HADES Experiments. Eine kompliziertere Dichteabhängigkeit der Zustandsgleichung ließe sich daher vermuten. Die Bestimmung der Zustandsgleichung ist aber modellabhängig.

In den bisher vorgestellten Studien ist die Formation leichter Kerne eine Notwendigkeit für einen realistischen Datenvergleich. Die Modellierung leichter Kerne ist jedoch nicht nur eine potenzielle Fehlerquelle, sondern kann auch maßgeblich zum Verständnis starkwechselwirkender Materie beitragen. Aufgrund verschiedener Beobachtungen wird davon ausgegangen, dass man in Schwerionenkollisionen am Brookhaven National Laboratory und am CERN Materie erzeugt, in der die Quarks und Gluonen, die Bestandteile von Protonen und Neutronen, nicht mehr gebunden in Hadronen auftreten. Man spricht bei Materie in diesem Zustand von einem Quark-Gluon-Plasma. Die Existenz einer weiteren Phase legt die Frage nach dem Charakter des Phasenübergangs nah. Verbunden mit dieser Frage ist die Suche nach einem kritischen Punkt im Phasendiagramm. Die Erforschung des Phasendiagramms starkwechselwirkender Materie ist eine der Kernfragen der Schwerionenphysik.

In der Nähe eines kritischen Punktes erwartet man, dass Fluktuationen verstärkt auftreten. Insbesondere die Fluktuation der Anzahl von Baryonen ist im Fokus aktueller Forschung. Leichte Atomkerne sind zusammengesetzte Objekte aus Baryonen. Die Produktion leichter Kerne ist daher stark abhängig von der Baryonenzahl. Somit stellt die Produktion leichter Kerne ein exzellentes Werkzeug für die Suche nach dem kritischen Punkt dar.

Dynamische Modelle zur Beschreibung der Kernproduktion sind unverzichtbar um ein tieferes Verständnis zu erlangen und um Signale eines kritischen Punktes zu

erkennen. Das Modell darf dabei nicht auf die Beschreibung hadronischer Materie limitiert sein, daher werden oft sogenannte Hybridmodelle verwendet. Diese setzen sich unter anderem aus einer Entwicklung der besonders heißen Phase des Systems durch relativistische Hydrodynamik, verbunden mit einer hadronischen Transportbeschreibung für die späte „afterburner“-Phase, zusammen. Für die Beschreibung der letzten Phase ist SMASH geeignet. Durch die dynamische Produktion leichter Kerne im Modell kann ein Beitrag zur Suche nach dem kritischen Punkt geleistet werden, auch wenn der kritische Punkt nicht modelliert wird. Durch den Vergleich mit experimentellen Messdaten zur Häufigkeit leichter Kerne und der Analyse der Reaktionsraten zu Produktion und Desintegration leichter Kerne im Modell, wird die Notwendigkeit der „afterburner“-Phase offensichtlich. Des Weiteren werden Verhältnisse der Anzahl verschiedener Kerne gebildet und mit dem Experiment verglichen. Diese Verhältnisse sind so konstruiert, dass sie sensitiv zum kritischen Punkt sind. Dementsprechend ist es nicht überraschend, dass keine Übereinstimmung mit dem Experiment erreicht wird.

Inhaltsverzeichnis

Kapitel 1

Introduction

1.1 Standard Model and Strong Interaction

To our best understanding, there are four fundamental types of interaction: the strong interaction, the weak interaction, the electromagnetic interaction, and gravitation. Gravity, on a basic level, describes the attractive force between massive objects. On a closer look, it can be understood in terms of general relativity [5], where mass and energy deform space-time as formulated in Einstein's field equations.

The strong, weak, and electromagnetic interactions can be described in a unified theory called the Standard Model of particle physics. A grand unification of the standard model with gravity has not been achieved so far, and it remains a big open question for modern theoretical physics. The Standard Model is not presented in much detail in this thesis, but a brief overview can be given by introducing the elementary particles included in this theory. Each elementary particle corresponds to a quantum field. An introduction to the theory of quantum fields can be found in [6].

All particles are compiled in Figure 1.1. The figure is split into fermions on the left and bosons on the right. Fermions and bosons differ in their spin – a quantity often compared to intrinsic angular momentum. Interactions are modeled via the exchange of bosons, and each boson can be attributed to one of the fundamental forces.

The photon is a famous example of an exchange boson. It is the mediator of the electromagnetic interaction and is associated with electromagnetic waves. Electromagnetic waves in various ranges of frequency are essential in daily life. Most importantly, visible light, but also X-rays and radio waves are electromagnetic waves and understood as photons on a quantum field level. All particles with an electric charge can interact via photons. The electric charge of the elementary particles is

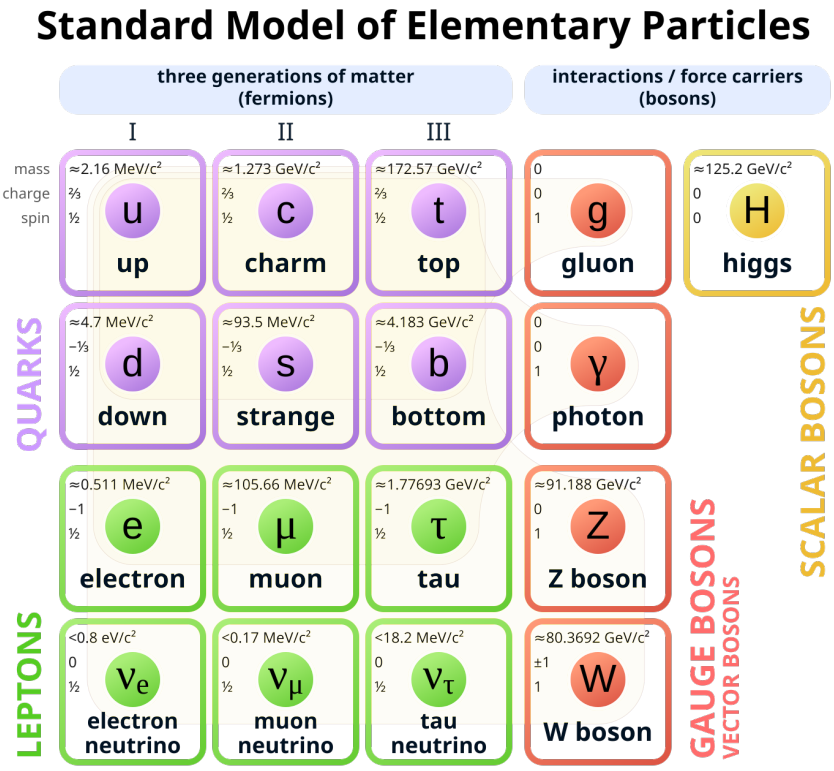

Abbildung 1.1: Particles of the Standard Model of particle physics. The particles are grouped into quarks, leptons, and bosons. Taken from [7].

depicted in Figure 1.1 in units of the elementary charge. Most prominently, the electron couples to the photon, but also the quarks, which are constituents of the proton.

The Z^0 and the W^+ and W^- are the exchange bosons of the weak interaction. As the name suggests, the weak interaction exhibits a relatively small force, which can be explained by the large mass of the exchange particle. Due to the large mass, much energy is required to emit an exchange boson, which makes processes of the weak interaction unlikely. All fermions in Figure 1.1 take part in the weak interaction, but especially the neutrinos only interact weakly. The weak interaction is unique in the sense that it is the only interaction that can change the flavor of the quark. A prominent example is beta minus decay (or β^--decay) where a neutron decays into a proton, emitting an electron and an electron anti-neutrino – the anti-particle of the electron neutrino. On the level of elementary particles, the proton is a composite particle consisting of two up and one down quark bound by the strong interaction, whereas the neutron contains two down quarks and an up quark. Therefore, beta minus decay is a down quark changing flavor to an up quark by radiating a W^-, which then decays into leptons. This process and the inverse process are highly relevant in astrophysics, for example, within neutron stars or for the synthesis of atomic nuclei in supernovae or collisions of neutron stars.

The main focus of this work is on the strong interaction. It is the most important interaction at small scales and is responsible for the stability of atomic nuclei. The theory of the strong interaction is quantum chromodynamics (QCD). As the name suggests, it describes the dynamics of the elementary particles that carry a color charge. This includes the quarks and the gluon, which is the exchange boson of the strong interaction. Each quark carries one of three color charges, often referred to as red, blue, and green. Their anti-particles carry anti-color charges: anti-red, anti-blue or anti-green. A unique feature of QCD is that the exchange bosons themselves carry color charge. More precisely, each gluon carries a color charge and an anti-color charge. Due to this property, gluons themselves can interact via further gluons, which is essential for the characteristic behavior of the strong interaction that we discuss in the following.

One consequence of the strong interaction is confinement. Confinement refers to the finding that only color-neutral objects can be observed freely. Color-neutral objects can be created by combining a quark and an anti-quark with matching (anti-)colors. A state of a quark and anti-quark is called a meson. One can further create a color-neutral objects from three quarks of different colors. This is referred to as a baryon. Following their aforementioned quark content, the proton and the neutron are baryons. Both mesons and baryons are subsets of hadrons, which is an umbrella term for composite particles bound by the strong interaction.

There is no proof of confinement starting from quantum chromodynamics. Ho-

wever, the potential of a quark and an anti-quark has been evaluated in numerical lattice QCD [8] calculations (see [9], for example). It shows a linear rise of the potential as a function of the distance, together with a $\propto r^{-1}$ term which is important only for small radii. An interpretation of the linear form of the potential is that a string of gluons is spanned between the quarks. The energy contained in this string is proportional to its length. If one were to put energy into the quark-anti-quark pair trying to separate them, the string breaks into two as a new quark and an anti-quark are produced once sufficient energy is available. This is the underlying picture of the Lund string model [10], which is also described in Section 2.2.4.

Confinement and the formation of such color strings are consequences of the non-perturbative nature of QCD in soft processes. For a comprehensive description of perturbation theory in quantum field theory, the reader is referred to [6]. On a basic level, for each physical process, there are many microscopic possibilities to reach the same final state. They are usually visualized in terms of Feynman diagrams, and their contribution to the probability of a process can be derived from the diagrams. Depending on the complexity of a diagram, the contribution is proportional to coupling constants raised to a higher power for complex diagrams or a lower power for more basic diagrams. The coupling constant of the electromagnetic interaction is small, meaning that the simple diagrams are the most important. Neglecting complex diagrams, therefore, causes only a minor error, and is referred to as perturbation theory in this context. In general, there is also a dependence of the coupling constant on the transfer of momentum. For the electromagnetic interaction, this dependence is very weak but it is defining for the strong interaction, and it is known as the running coupling. Estimates of the coupling constant α_s of the strong interaction are compiled in Figure 1.2. One can clearly see that the coupling constant is small if the transfer of momentum is large. Processes with large momentum transfer are considered hard. In such a setting, perturbation theory is applicable. The coupling constant increases for low momentum transfer, and more complex diagrams are no longer negligible. QCD calculations in this soft, non-perturbative regime are very challenging.

To explore the nature of the strong interaction at low momentum transfer, methods are developed and applied that do not rely on a small coupling, such as the Dyson-Schwinger equations [12], [13] or the functional renormalization group [14], [15]. The aforementioned lattice QCD is a very prominent approach to this problem. In lattice QCD, spacetime is discretized and the theory can be solved in some scenarios under immense numerical effort. It is restricted to a small density of net baryons, and calculations of time-dependent quantities are extremely challenging. For thermalized QCD matter at vanishing baryon density however, a calculation from first principles can be obtained using lattice QCD. From such calculations we have learned that there is a crossover transition from hadronic matter to quarks and

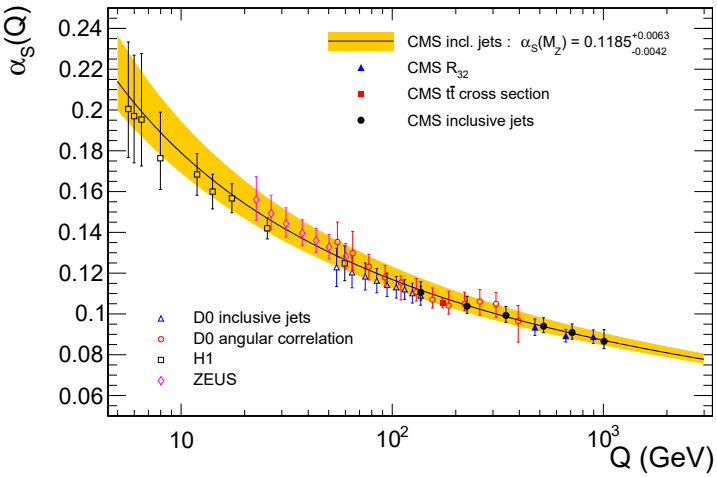

Abbildung 1.2: Running coupling of the strong interaction as a function of the momentum transfer. A compilation of experimental estimates of the coupling is given and one can observe that the coupling decreases significantly with increasing momentum transfer Q. Taken from [11]

.

gluons at $T_c \approx 155\,\text{MeV}$ [16]–[18]. This new state of matter, where strongly interacting matter is deconfined, is called quark-gluon plasma (QGP). Understanding the QGP is one of the main goals of current research.

Large experimental facilities performing heavy-ion collisions (see Section 1.2) claim to have observed the quark-gluon plasma. In the year 2000, CERN [19] stated that this new form of matter was created [20]. Later, in the year 2005, scientists at the Relativistic Heavy Ion Collider (RHIC)[21] concluded that they had probed the QGP as well and that it behaves like a nearly perfect fluid [22] (see [23] for a comprehensive explanation of how this statement is based on experimental data and theoretical calculations).

Different phases of matter are well known in daily life from water, which we frequently experience as ice, liquid water, or vapor. QCD matter has a complex phase structure too and a first phase diagram was proposed by Cabibbo and Parisi already in the seventies [24]. This version of the phase diagram had a second-order phase transition at vanishing baryon density. From lattice QCD calculations we now know that the transition is a smooth crossover in that region [25] which one can imagine like the melting of butter.

A sketch of the current understanding of the phase transition is shown in Figure 1.3. The sketch includes many structures, most prominently the transition between hadrons and the QGP. It is displayed here in terms of the baryon chemical potential μ_B, which is closely related to the baryon density. A smooth transition is illustrated

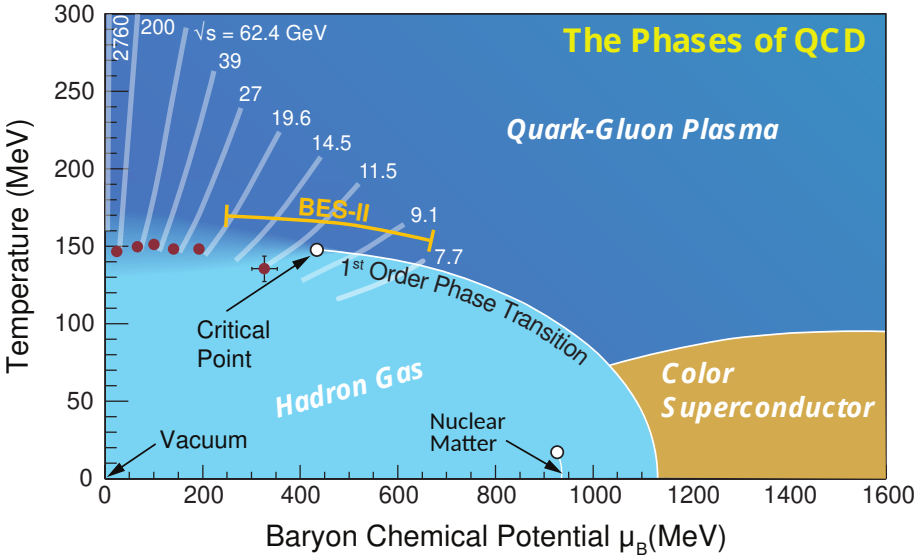

Abbildung 1.3: Sketch of the phase diagram of QCD matter. The different phases are represented by differently colored regions. A first-order phase transition and a critical point are present in the sketch. Trajectories in the phase diagram, traversed in heavy-ion collisions at a range of collision energies, are also depicted. Taken from [26].

at small μ_B to resemble the crossover. At larger baryon densities, there might be a first-order phase transition that ends with a critical point. The critical point is further studied in Section 6. A color-superconducting phase is further expected at very large μ_B. At low temperatures, there is a transition between the hadron gas and nuclear matter. This transition and the QGP transition at $\mu_B \approx 0$ are relatively well known, but especially the central region of the phase diagram is not fully settled.

Exploring the phase diagram of QCD matter is one of the main goals in the research field. The possible phase transition and critical point are presumably located in the phase diagram in a region where the temperature and density are extreme. This region of the phase diagram can, in terrestrial experiments, only be probed in heavy-ion collisions, which are introduced in the following.

1.2 Heavy-Ion Collisions

An excellent way to investigate the properties of matter on microscopic scales is to perform scattering experiments. Prominently, the Rutherford scattering experiment [27] was an important contribution to our current understanding of the structure of atoms. One can further gain insight into the structure off atomic nuclei by scattering electrons of individual nucleons within the nucleus. With increasing energy, a

scattering between a lepton and a quark within a nucleon becomes possible. This process is called deep inelastic scattering, and it is used to study the inner structure of nucleons (see e.g. [28]).

Scattering experiments are performed to study the properties of QCD matter and to explore the QCD phase diagram. At the bear mountain workshop in 1974, collisions of atomic nuclei were suggested to create a large volume in which strongly interacting matter could be probed under extreme conditions [29]. After this workshop, heavy-ion collisions were performed in various experiments. This led to the aforementioned announcements about probing the quark-gluon plasma at CERN and BNL, and the research on QCD matter in heavy-ion collisions is still ongoing. See [30] for a short review of the history of heavy-ion physics.

1.2.1 Scanning the Phase Diagram

A sketch of the QCD phase diagram is shown in the previous section, and, as mentioned before, one of the main goals of heavy-ion physics is to explore this phase diagram. To scan the phase diagram, one needs to change the temperature and the baryon density in the system. There are various handles to experimentally influence which region in the phase diagram is probed. Higher temperatures can be accessed by increasing the collision energy. Large experimental facilities are built to provide enough collision energy to probe the quark-gluon plasma. The highest energy is currently reached at the Large Hadron Collider (LHC) [31] at CERN, where the center-of-mass energy per nucleon pair in a collision of two lead nuclei was initially $\sqrt{s_{NN}} = 2.76\,\text{TeV}$ and is currently 5.02 TeV due to upgrades. At BNL, the Relativistic Heavy Ion Collider reaches the second-highest energies, with $\sqrt{s_{NN}} = 200\,\text{GeV}$ in collisions of gold nuclei. To cover a larger region of the phase diagram, the energy is varied in the Beam Energy Scan (BES) and Beam Energy Scan II (BES II) programs. The sketch of the phase diagram in Figure 1.3 also includes trajectories that roughly indicate the temperature and baryon chemical potential probed within a heavy-ion collision at various collision energies from RHIC to LHC. With increasing energy, the temperature naturally increases, but at the same time, the baryon chemical potential decreases.

This is, at first, counterintuitive because one would think that the nuclei are compressed more when the collision energy is large. That would lead to a large baryon density and ultimately a large μ_B, which is indeed the case at sufficiently low collision energies. The collision dynamics change, however, with increasing energy, and the baryons from the colliding nuclei are only stopped at low collision energies, while the nuclei become more and more transparent at higher collision energies and deposit an enormous amount of energy, but few net-baryons. Baryon stopping is investigated with the SMASH transport model (see Chapter 2) used in this work in [32].

Large baryon densities can therefore be probed at smaller collision energies. Indeed, the HADES collaboration has shown that nuclear matter is probed under similar conditions in collisions of neutron stars and in heavy-ion collisions at $E_{\mathrm{kin}} = 1.23A\,\mathrm{GeV}$ ($\sqrt{s_{NN}} \approx 2.4\,\mathrm{GeV}$) [33]. In consequence, collisions at relatively low energies are very interesting, as they allow for interdisciplinary studies between astrophysics and heavy-ion physics (see Section 1.3.1).

Experimentally, there are more handles to control the baryon density. One possibility is by changing the collision system. Colliding smaller nuclei reduces the density probed in the experiment. Following this line of thought, experiments are performed with various nuclei, from large nuclei like $^{207}\mathrm{Pb}+^{207}\mathrm{Pb}$ and $^{197}\mathrm{Au}+^{197}\mathrm{Au}$ to smaller nuclei like $^{108}\mathrm{Ag}+^{108}\mathrm{Ag}$, $^{96}\mathrm{Ru}+^{96}\mathrm{Ru}$, and $^{96}\mathrm{Zr}+^{96}\mathrm{Zr}$, $^{40}\mathrm{Ar}+^{45}\mathrm{Sc}$ down to small collision systems like $^{12}\mathrm{C}+^{12}\mathrm{C}$, $^{9}\mathrm{Be}+^{9}\mathrm{Be}$, $d+^{197}\mathrm{Au}$, $p+^{207}\mathrm{Pb}$, $p+^{197}\mathrm{Au}$, and $p+p$.

An overview of the various experimental facilities for heavy-ion collisions is given in [34]. For this thesis, the most important experimental measurements are performed with the HADES [35] experiment and at the FOPI [36] experiment located at GSI. These experiments operate at relatively low collision energies below $2A\,\mathrm{GeV}$ to study hadronic matter at large densities.

In Chapter 6, experimental data from the STAR [37] experiment within the Beam Energy Scan program is considered at $7.7\,\mathrm{GeV} < \sqrt{s_{NN}} < 19.6\,\mathrm{GeV}$. This energy region is particularly interesting for the search for a critical point in the phase diagram of QCD matter.

Besides varying the collision system, the system size, and with it the density can be varied by performing a centrality selection. If the colliding nuclei hit head-on, the most energy is deposited, and higher temperatures and densities are to be expected. However, head-on collisions are rare, and it is more likely that nuclei hit each other with a sizable impact parameter. By selecting the events based on the activity, one can vary the probed region in the phase diagram. Grouping collisions into centrality classes gives a chance to focus on a restricted region of the phase diagram. Still, a heavy-ion collision is a dynamic process in which the system evolves from a very hot and compact system to a cooler state as it expands until the hadronic end products eventually reach the detector. Clearly, a heavy-ion collision traverses a trajectory in the phase diagram, as illustrated in Figure 1.3 but additionally, a heavy-ion collision is not homogeneous. The density and temperature are not the same throughout the created system but it is typically hotter and denser in the center. From this fact, it becomes clear that each collision really encodes information on an entire region in the phase diagram, and it is an extremely complex task to disentangle this information given only the final state.

1.2.2 Important Observables

Before iterating through the most relevant theoretical models, it is instructive to quickly introduce the most important observables that can be compared to experimental measurements. A very basic observable is the multiplicity. It refers to the number of particles of some category. Usually, the multiplicities of specific identified hadron species are considered but the number of charged particles can already be insightful.

Further, the multiplicity can be subdivided into different kinematic regions. The kinematic regions are most commonly defined in terms of rapidity or transverse momentum. The rapidity is a measure of the velocity in the beam direction and can be calculated from the longitudinal component of the velocity β_z as

$$y = \frac{1}{2} \ln \left(\frac{1 + \beta_z}{1 - \beta_z} \right) = \frac{1}{2} \ln \left(\frac{E + p_z}{E - p_z} \right) . \tag{1.1}$$

The transverse momentum of a particle is obtained as

$$p_T = \sqrt{p_x^2 + p_y^2} \tag{1.2}$$

when the coordinate system is chosen such that the x and y directions span the transverse plane, which is perpendicular to the beam axis. Compared to the absolute value of the momentum $p = \sqrt{p_x^2 + p_y^2 + p_z^2}$, the transverse momentum disregards the contribution from the longitudinal part. In the sense that the rapidity carries only information about the longitudinal direction, and the transverse momentum incorporates only information in transverse direction, the two kinematic variables are complementary.

Binning the number of identified particles (here denoted by N) into rapidity and transverse momentum, so-called particle spectra are obtained. Assuming sufficiently fine binning, the rapidity spectrum is referred to as dN/dy and the transverse momentum spectrum is dN/dp_T. The double-differential spectrum $d^2N/dydp_T$ is related to the rapidity spectrum and the momentum spectrum via an integral, as the notation suggests.

Particle spectra already contain a wealth of information about the dynamics of a heavy-ion collision. However, the distribution of particles within the transverse plane is not captured by just the rapidity and the transverse momentum. For this purpose, the azimuthal angle ϕ is introduced to describe the anisotropy in the transverse plane. To define the angle, a reference plane is required. In the simplest case, the reaction plane is used as the reference. This plane is spanned by the beam direction and the offset of the colliding nuclei in the transverse plane. In model calculations, the coordinate system is often chosen such that the beam direction is in the z-direction and the offset of the nuclei is in x-direction. In such a setup, the angle with respect to the reaction plane is simply $\phi = \arctan(p_y/p_x)$.

The distribution in ϕ is always periodic, and it is possible to express the distribution in terms of a Fourier expansion

$$\frac{dN}{d\phi} \propto 1 + 2\sum_{n=1}^{\infty} v_n \cos(n\phi)\,. \tag{1.3}$$

In this expansion, the information is contained in the flow coefficients v_n which are referred to as directed flow (v_1), elliptic flow (v_2), triangular flow (v_3), etc. The flow coefficients can be evaluated as

$$v_n = \langle \cos(n\phi) \rangle\,, \tag{1.4}$$

where the average runs over particles. In this way, the coefficients can be determined for each bin in transverse momentum and rapidity separately if sufficient statistics are available.

1.2.3 Theoretical Description

It is evident that theoretical models are required to extract information about QCD matter from the experimental observations in the detector. There are various models for heavy-ion collisions that make conclusions about the underlying physics possible.

Statistical Hadronisation Model

The statistical hadronization model [38]–[40] can be used to predict particle yields by assuming that they are produced in a thermal medium. A comprehensive introduction with the necessary equations can be found in [34]. The statistical hadronisation model is also known as thermal model. Particle multiplicities are evaluated using thermodynamics in a grandcanonical ensemble. The centerpiece of such a calculation is the partition function, which includes the Hamiltonian of the system. The Hamiltonian encodes the microscopic information of the system that is to be described. In this case, the Hamiltonian resembles a hadron resonance gas without explicit interactions. To be specific, the Hamiltonian includes only the kinetic terms for all hadron species and for hadronic resonances as well with no interaction term. Resonances are usually related to interactions, as they are excitations of hadrons. In the thermal model, there is just a statistical production of resonances.

An expectation value for the particle yield can be obtained for a given temperature, chemical potential, and volume. For a given hadron species, there is an additional contribution to the yield from each resonance that can decay into the considered hadron. The particle yield must scale linearly with the volume. By considering the ratio of particles, the volume always cancels out and no information on the form or size of the fireball is required. Since there are no net strange quarks

present in the colliding nuclei and because the number of net strange quarks is conserved in the strong interaction, one can enforce the net strangeness to vanish. The thermal model then has only the temperature and baryochemical potential as parameters. The two parameters can be fitted to the multiplicities of the various hadronic species, and a good description is obtained.

The success of the model suggests that particles are produced thermally at the fitted temperature and that the particle yields are, despite resonance decays, fixed from that point on. Figure 1.3 includes this estimate of where the freeze-out takes place in the phase diagram. Considering that the system freezes out at such a large temperature in the model, it is surprising that even light nuclei production can be described very well [41], [42]. Light nuclei have a small binding energy, and their existence at extremely high temperatures is compared to ßnowballs in hell"[43]. This interesting finding led to further studies of dynamical light nuclei production that we discuss in Chapter 6.

The statistical hadronization model gives a good description of particle yields, especially considering its simplicity. However, the model is based on the assumption that a thermalized medium is the origin of all particles and resonances. This makes it hard to access information about the early stage of a heavy-ion collision, where the system is under even more extreme conditions.

Hybrid Models

A motivation for performing heavy-ion collisions is to study the very hot matter that was present in the early stages of the universe. To understand the hottest stage of a heavy-ion collision, dynamical models must be applied to make a connection between that stage and the measurement in the final state.

Heavy-ion collisions at sufficiently large energies to create a QGP are frequently modeled in hybrid approaches. A hybrid approach is really a combination of models, of which each one describes a certain stage of a heavy-ion collision best, as well as the transition between them. In the early stage, just after the nuclei collide, the system is far from thermal equilibrium. So-called initial state models are applied for this stage until the system is sufficiently close to thermal equilibrium so that a hydrodynamic evolution is possible.

There are various models for the description of this stage. The Glauber model (see [44] for a review) is commonly employed for this purpose. Based on the initial distribution of nucleons in the colliding nuclei, the deposition of energy is calculated considering their overlap along the collision axis. This can be done analytically, but is more commonly performed numerically in Monte Carlo Glauber calculations. The results presented in Chapter 6 are obtained using a hybrid model incorporating an extension of the Monte Carlo Glauber model.

In the color glass condensate framework the nuclei are treated as sources for the

color fields, which are described as a real scalar field that captures important features of QCD [45]. The IP-Glasma model [46] is based on the color glass condensate and takes into account the impact parameter of the colliding nuclei. A good agreement with the experimentally quantified anisotropy in the azimuthal particle distribution was found in a hybrid approach that incorporates the IP-Glasma model in the initial state [47].

A very flexible initial state can be obtained with the TRENTo model [48]. It provides a parametric initial state that can give a similar initial state to other models, depending on the parameter choices. This is particularly useful for data-driven analyses (for example [49]) where the flexibility allows to find the initial state that leads to the best description of the experimental data and enables inferences about properties of the initial state.

To describe the non-equilibrium dynamics in the initial state, one can apply a transport model. The transport model SMASH is introduced in much detail in Chapter 2. Transport calculations for the initial state start with atomic nuclei propagating towards each other until they collide and eventually the switch to a hydrodynamic evolution is performed. Most conveniently for the description of the nuclei in the initial state, hadronic degrees of freedom are chosen for this purpose. At first the transport calculation for the initial state may seem very similar to the Glauber model as in both cases nucleons are sampled within two colliding nuclei and collisions between them are found in the following. The main difference is that a transport model allows for secondary interactions. Thereby the system dynamically approaches equilibrium. The applicability of a hadronic description for this early stage, where the energy density is very large, is not obvious as the system should eventually be described in terms of quarks and gluons. One can argue that the first, highly energetic, interactions are usually performed within a string model that create and fragment color strings on a quark level, see Section 2.2.4. The fragmentation of the strings in this situation is probably not wanted if one understands the formation of the QGP as overlapping of the color fields. In the fragmentation process the energy is however conserved and the energy density profile required for the hydrodynamic evolution should be reasonable.

Realizations of hadronic transport for the initial state in a hybrid approach have been developed using UrQMD [50] and SMASH [51]. A partonic transport initial state is part of the AMPT hybrid model [52].

In the following stage of a heavy-ion collision, the system is closer to thermal equilibrium and hadronic degrees of freedom are no longer suitable to describe the possibly deconfined matter. A hydrodynamic evolution considers only macroscopic degrees of freedom, such as energy density and conserved currents. Hydrodynamics is based on the conservation laws (see e.g. [53])

$$\partial_\mu T^{\mu\nu} = 0 \tag{1.5}$$

$$\partial_\mu j^\mu = 0 \tag{1.6}$$

where $T^{\mu\nu}$ are the components of the energy-momentum tensor and j^μ are the components of a conserved current density.

For an ideal fluid the energy-momentum-tensor can be expressed in terms of the Landau velocity u^μ, the energy density ϵ, and the pressure P as

$$T^{\mu\nu} = (\epsilon + P)u^\mu u^\nu - P g^{\mu\nu} \tag{1.7}$$

where the metric tensor $g^{\mu\nu}$ is given by $\mathrm{diag}(1, -1, -1, -1)$ in the Minkowski metric. In the Landau rest-frame, where the energy-momentum tensor is diagonal, the components are $T^{\mu\nu} = \mathrm{diag}(\epsilon, P, P, P)$ with the energy density ϵ and the pressure P. The current density can then be related to the charge density as $j^\mu = \rho u^\mu$. Due to the constraint $u_\mu u^\mu = 1$ for the velocity, only three independent variables in the velocity remain. Together with the energy density, the pressure and the charge density, there are six variables to solve for. Counting the number of equations, there are four due to the open index in Equation 1.5 plus one from Equation 1.6. One additional equation is required to solve this system of equations. The final one is the equation of state (EoS), which relates the pressure to the energy density and charge density. Thereby the EoS incorporates the information about how the specific fluid behaves under different circumstances. Microscopic information about matter enters the calculation via the EoS. In the specific case of a heavy-ion collision, the equation of state can include the change in degrees of freedom implicitly. The EoS is an important subject in this thesis and it is introduced in more detail in Section 1.3.

The above example is only for ideal hydrodynamics. There are however various extensions to this simple description. Dissipative hydrodynamics means hydrodynamics that is not ideal, meaning the entropy is not conserved but it can increase due to friction and similar effects.

Each dissipative term contains a transport coefficient that incorporates information about how the specific medium approaches equilibrium. The transport coefficients, thereby, include further information about the microscopic properties of the considered fluid. Information on the transport coefficients can, therefore, be obtained through microscopic calculations. The SMASH transport model is, for example, applied to extract various transport coefficients [54]–[56].

One of the dissipative effects is shear. The intuitive picture for it is that there is friction between two surfaces of the fluid that have a different velocities. The shear viscosity is an important ingredient for a realistic description of a heavy-ion collision, even though the shear-viscosity-to-entropy ratio of the QGP was estimated to be close to the minimal possible value of $1/4\pi$ [57]. Due to this finding, the QGP is often referred to as the most ideal fluid.

Bulk viscosity is also needed to describe the evolution of the fireball. It actually describes the resistance of a medium against rapid expansion or compression. The bulk viscosity is more complicated to estimate in a transport model, but, as it is an input to hydrodynamic calculations, inference about it can be made from experimental data of heavy-ion collisions. This is usually done in combination with other model parameters, including the shear viscosity (see [49], [58], for example).

The diffusion of charges is another dissipative effect. A diffusion current is induced by a gradient in the density of a given charge. For example, the stopping of baryons has been studied in relation to the diffusion caused by the gradient in the baryon density [59]. Considering the diffusion on a microscopic level, the different charges cannot diffuse independently. In hadronic matter, for example, many baryons are also electrically charged, meaning that a gradient in one density may cause a diffusion current of another charge. A full diffusion matrix to couple the different charges was introduced in [60], [61] to take this effect into account.

As the system expands, it eventually becomes dilute. Once this point is reached, a hydrodynamic evolution is not suitable for this problem anymore. Instead, a change from macroscopic degrees of freedom to individual hadrons is performed. As the system is not homogeneous, the criterion to switch models is not satisfied everywhere simultaneously. The criterion is usually defined by the temperature or the energy density dropping below a certain threshold. This defines a hypersurface in the (3+1)D evolution of the system that needs to be determined (see [62]). On a given hypersurface, Cooper-Frye sampling [63] is performed to finalize the switch in degrees of freedom.

Once a particle list is sampled, the evolution can continue with the hadronic rescattering (or afterburner) using a microscopic model. Usually Boltzmann-type transport models or QMD-type (see Section 2.1.6) models are applied for the final stage of the evolution. SMASH is a transport model that is frequently used for afterburner studies. One example is the study presented in Chapter 6. Details of the model are given in Chapter 2.

At the end of the afterburner stage, the full information about all hadrons is determined and accessible. This allows for a comparison to experimental observations for numerous measurable quantities, which is not possible with the statistical hadronisation model.

Hadronic Transport

Transport models are applicable in the early stage of a heavy-ion collision and also in the final stage. The necessity for a hydrodynamical evolution arises from the change in degrees of freedom when the system is sufficiently hot and dense to form a QGP. In heavy-ion collisions at relatively low collision energies, no QGP is expected, and the whole evolution can be described within one continuous transport calculation.

This approach is used for the calculations presented in Chapters 3, 4, and 5, and a detailed description of the SMASH transport model is given in Chapter 2. As further details on transport calculations are given in Chapter 2, this section aims to only highlight transport simulations as an excellent tool to model heavy-ion collisions at low collision energies.

1.3 Equation of State

One of the main goals pursued in this thesis is to understand the behavior of nuclear matter under extreme conditions. The equation of state encodes information about the behavior of matter by making a connection between the thermodynamic state variables. The most prominent equation of state is the ideal gas law, which is a relation of the pressure P to the volume V, temperature T and particle number N

$$PV = Nk_BT\,. \tag{1.8}$$

With the units used in this thesis (see Appendix A), the Boltzmann constant k_B is set to one, so it is usually omitted in equations within this thesis.

From the ideal gas equation of state one can directly see that the pressure increases linearly with the temperature and the number density. Relations like this can be observed in daily life. When studying different forms of matter, the EoS is clearly key to gaining an understanding of the properties of matter. Additionally, the equation of state is related to the microscopic composition and interactions on a microscopic level via thermodynamics. Due to this connection, knowledge of the EoS can help in the task of understanding even microscopic aspects of matter.

As mentioned earlier, the equation of state is not only interesting in itself but it is required for hydrodynamic calculations. Such calculations are performed to model the dynamics of many interesting physical situations. Heavy-ion collisions, as mentioned in the previous section, are modeled using hydrodynamics, but also astrophysical events, such as neutron star collisions and supernovae, can be studied using hydrodynamics. Constraints on the equation of state are therefore highly demanded in both heavy-ion physics and astrophysics.

The equation of state of nuclear matter depends both on the baryon density ρ_B and on the asymmetry $\delta = (\rho_n - \rho_p)/\rho_B$ between proton density ρ_p and the neutron density ρ_n. The energy per nucleon is often expanded (see [64], for example) in the asymmetry

$$E(\rho_B, \delta) = E_0(\rho_B) + E_{\text{sym}}(\rho_B)\delta^2 + \mathcal{O}(\delta^4) \tag{1.9}$$

and the individual contributions are, again, expanded around the saturation density ρ_0

$$E_0 = m_N - B_0 + \frac{1}{2}\kappa x^2 + \frac{1}{6}Qx^3 + \ldots \tag{1.10}$$

$$E_{\mathrm{sym}} = J + Lx + K_{\mathrm{sym}}x^3 + \dots \,, \tag{1.11}$$

where $x = (\rho_B - \rho_0)/3\rho_0$. The ground state where the baryon density is the saturation density ($x = 0$) is energetically most stable. Therefore no linear terms in x are present in the expansion. At the same time, there is a symmetry between protons and neutrons, meaning the binding energy has to be symmetric around $\delta = 0$, which precludes odd terms in the expansion. E_{sym} denotes the symmetry energy. Quantifying the symmetry energy is one of the main goals when studying the EoS. m_N denotes the mass of a nucleon and the binding energy at saturation density is called B_0 here. The incompressibility of symmetric nuclear matter κ can be estimated in heavy-ion collisions. Q is referred to as the skewness. The symmetry energy at the saturation density is called J in this expansion and the slope of the symmetry energy is referred to as L. Finally, the incompressibility of the symmetry energy is denoted by K_{sym}.

There are various constraints on the parameters appearing in the above expansion (see [64] for a review). First of all, the mass of the nucleon is known to be $m_N \approx 938\,\mathrm{MeV}$ and the binding energy at saturation density is $B_0 \approx 16\,\mathrm{MeV}$. The saturation density is set to a relatively high value of $\rho_0 = 0.168\,\mathrm{fm}^{-3}$ in the transport model SMASH (Chapter 2) but values down to $\rho_0 = 0.15\,\mathrm{fm}^{-3}$ are used in other models.

The binding energy and saturation density can be obtained from the measurement of masses [65] and electric charge distributions [66]–[68], extrapolating to infinite matter.

Further insight into the EoS of nuclear matter lies in the excitations of nuclei. The giant monopole resonance, often called the breathing mode, is a compression mode of a nucleus [69]. As the density varies while the nucleus expands and deflates, this mode allows one to learn about the incompressibility of nuclear matter.

To extract the incompressibility of infinite nuclear matter, a theoretical model is required to describe the experimental findings. Depending on the model, the findings for the incompressibility vary significantly. Relativistic mean-field models suggest a larger incompressibility than non-relativistic models (see [70] and references therein). Additional uncertainties in the extraction of κ due to a variation of Q in the models are pointed out in [71].

The giant dipole resonance can be understood as an oscillation within the nucleus, where the entirety of protons oscillates relative to the neutrons [28]. Analyses of the giant dipole resonance constrain the symmetry energy, mainly the coefficients J and L [72]–[74].

In scattering experiments with protons and atomic nuclei, the polarizability of a nucleus can be measured [75]. It is estimated to be sensitive to the symmetry energy and to the neutron skin of nuclei [76]. Based on the measurement of the polarizability [75], analyses were performed to constrain J and L [77]–[79].

There are various experimental approaches to determine the neutron skin thickness, which is the difference in the (root mean square) radius of the neutrons and the radius of the protons in a nucleus. The neutron skin is, again, sensitive to the symmetry energy so there is a possibility to learn about the latter. For a summary of the experimental methods and constraints based on the neutron skin effect, see [64].

Studies of atomic nuclei constrain the equation of state near the saturation density. Further reliable constraints can be obtained at extremely large densities, where perturbative QCD is applicable [80], [81]. On the other side of the spectrum, effective field theories are applicable at low densities, where they provide another theoretical constraint on the equation of state [82], [83].

From the equation of state, one can calculate the speed of sound. The speed at which a sound wave propagates in a given medium is moderate in the atmosphere of the Earth, with roughly $c_s \approx 300\,\mathrm{m/s}$ but is comparable to the speed of light in nuclear matter. The speed of sound can be calculated as the derivative of the pressure with respect to the energy density ϵ

$$c_s^2 = \left(\frac{\partial P}{\partial \epsilon}\right)_s . \tag{1.12}$$

The fact that the speed of sound can never exceed the speed of light can even help to constrain the EoS. The constraints at low density from effective field theory and at high densities from pQCD can be combined with the limit on the speed of sound and further constraints from astrophysical observations (see Section 1.3.1) to restrict the allowed region for the equation of state in the intermediate density regime [84], [85]. The same ansatz is also applied without actively taking the astrophysical constraints into account [86]. In the following, the most important astrophysical observations, leading to constraints on the EoS, are elaborated.

1.3.1 Equation of State in Astrophysics

Aiming to understand nuclear matter, the most obvious starting point is to study atomic nuclei. As nuclear matter at large densities is present in astrophysical objects, they offer an opportunity to study the EoS in a region of the phase diagram that cannot easily be probed. It is remarkable that one of the best ways to study nuclear matter, which is described on length scales on the order of a femtometre, is by observing objects and events at astronomical distances.

The astrophysical constraints covered in this thesis involve neutron stars. An important difference between nuclear matter in neutrons stars and atomic nuclei is the composition. Matter in neutron stars mostly consists of neutrons, as it is present in β-equilibrium. In β-equilibrium, the reaction $p + e \leftrightarrow n + \nu_e$ takes place and the

baryon number and the electric charge are conserved. However, the neutrinos can escape the neutron star freely, so that the lepton number is not conserved [87]. Due to the Pauli principle, the electrons need to occupy states of higher energy when the density is large. At a critical density, it is energetically favored to convert protons and electrons to neutrons even though neutrons have a larger mass than the sum of the proton and the electron.

Sufficient densities are reached due to gravitation. The gravitation in neutron stars is so strong that Newtonian gravity is not applicable, and a description in terms of general relativity is necessary. Considering a static spherically symmetric system, where the pressure of an ideal fluid compensates the gravitation, the Einstein equations reduce to the Tolman–Oppenheimer–Volkoff (TOV) equations [88]

$$\frac{\mathrm{d}P(r)}{\mathrm{d}r} = -\frac{Gm_r(r)\epsilon(r)}{r^2}\left(1+\frac{P(r)}{\epsilon(r)}\right)\left(1+\frac{4\pi r^3 P(r)}{m_r(r)}\right)\left(1-\frac{2Gm_r(r)}{r}\right)^{-1}, \quad (1.13)$$

where $m(r)$ is given by [87]

$$m_r(r) = 4\pi\int_0^r \mathrm{d}r' r'^2 \epsilon(r') \quad (1.14)$$

and the gravitational constant is denoted by G. To solve the TOV equation, the EoS is required to relate the pressure P and the energy density ϵ. Given an equation of state, this ordinary differential equation (ODE) can be solved for a given pressure in the center of the neutron star. Integrating the ODE from the center ($r = 0$) to the outside, the radius R of the star is determined by vanishing pressure $P(r = R) = 0$. This way, one obtains a combination of a mass $M = m_r(R)$ and the corresponding radius for each given central pressure. The different possible stars can be compiled in a mass-radius plot, covering all combinations of possible mass and radius for a given EoS.

The mass-radius curves can be used to rule out equations of state that cannot reproduce astrophysical observations. Firstly, there are observations of neutron stars with a mass above twice the mass of the Sun [89]–[91]. Some equations of state are not sufficiently stiff to stabilize such a heavy neutron star against the gravitational pressure. Consequently, equations of state that do not reach two solar masses are ruled out due to this constraint.

The next constraint comes from the NICER (Neutron Star Interior Composition Explorer Mission) x-ray observatory, which has measured the radius of the neutron stars PSR J0740+6620 [92], [93] and PSR J0437–4715 [94]. The combination of the mass and a radius leads to very valuable information on the EoS. The mass-radius curve for a given EoS needs to pass through a confidence region of the measurement. Otherwise, the EoS is ruled out.

To conclude, a constraint based on the observation of two merging neutron stars is covered here. As the two neutron stars approach each other in a spiraling motion,

spacetime is heavily deformed. Resulting from the Einstein equations, the deformation of spacetime propagates in the form of gravitational waves. The LIGO and VIRGO detectors detected the gravitational waves from such a merger event in 2017 [95] and the electromagnetic counterpart [96]. From the gravitational wave signal, conclusions about the tidal deformability of the neutron stars were drawn [97]. The tidal deformability, in turn, depends on the compactness of the neutron star $C = GM/R$, which is again linked to the equation of state via the TOV equations.

1.3.2 Nuclear Equation of State in Heavy-Ion Physics

The astrophysical observations alone contribute strongly to the knowledge about the EoS of nuclear matter. Nuclear matter can additionally be probed at high density in terrestrial experiments. The HADES collaboration has demonstrated in [33] that heavy-ion collisions at the energies accessible at the SIS 18 accelerator probe nuclear matter under conditions comparable to those present in neutron star mergers. One main difference between neutron star matter and colliding atomic nuclei is the composition. As neutron stars are mainly consisting of neutrons, the atomic nuclei are close to symmetric nuclear matter, meaning the number of protons and neutrons is not far from equal. Therefore, heavy-ion collisions give valuable complementary information on the equation of state (see [98] for a review). The difficulty in extracting the EoS from heavy-ion collisions is that only the final state of the collision can be accessed experimentally. To obtain information about the early stage of the collision, where the density is large, one relies on theoretical models. As a realistic description of the system is very challenging to achieve, some uncertainty lies in the theoretical modeling, which is usually done with transport or QMD approaches. Since model and implementation choices affect the information extracted from heavy-ion collisions, one of the main goals of the field is to understand the differences in various models and to converge towards more consistent theory predictions. For this purpose the transport model evaluation project (TMEP) [99] started. As the majority of models relevant for the extraction of the EoS (including SMASH) participate in the TMEP, further progress in the estimation of the EoS can be expected in the near future.

Important for the extraction of the EoS is a set of observables that are sensitive to it. To give an understanding of how the EoS influences the dynamics of a heavy-ion collision, Figure 1.4 illustrates the baryon density in a semi-central heavy-ion collision at $E_{\mathrm{kin}} = 1.23A\,\mathrm{GeV}$. Compared are the densities when employing a soft EoS (left) and a hard EoS (right). Clearly a larger density is reached when the EoS is soft. In this case, the kinetic energy of the accelerated nuclei is sufficient to achieve a large compression. With a stiffer EoS, more energy is needed for the compression so that the probed density is significantly smaller.

The difference in the density translates to various observables. An important

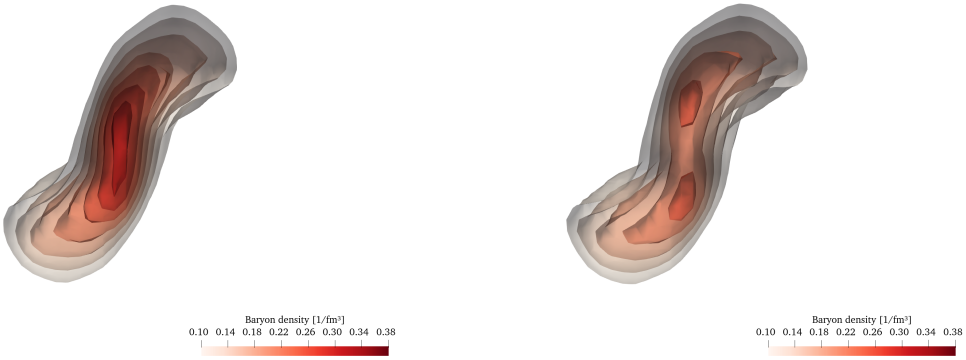

Abbildung 1.4: Baryon density in a semi-central gold-gold collision at $E_{\mathrm{kin}} = 1.23A\,\mathrm{GeV}$. On the left, a simulation with a soft equation is shown in comparison to a stiffer equation of state on the right. The density reached with a soft EoS is higher as it is more difficult to compress more stiffer nuclear matter.

example is the production of particles below the threshold. In this context, "below threshold"means that the production of the particle species would not be possible in a proton-proton reaction at the same energy. With a chain of reactions or due to the modification of particle properties in the medium the process can be realized in a heavy-ion collision, however. The production rate below the threshold is, of course, much larger when a more dense medium is created. This way, the particle production below threshold is very sensitive to the EoS. Kaons are produced below threshold, and are therefore a useful observable to consider for constraining the EoS as suggested in [100]. A review of the findings from studying the production of kaons can be found in [101]. The description of kaons is not trivial, however. First of all, the cross sections for the production of kaons need to be known and all the necessary channels need to be implemented. Further, there is some uncertainty about the potentials that kaons and other strange particles should experience. Aiming to cancel some uncertainties, the ratio of the kaon yield in gold-gold collisions to the yield in carbon-carbon collisions is used to constrain the EoS [102], [103]. A relatively small incompressibility of nuclear matter is extracted from kaon analyses.

Another approach to constraining the EoS is by studying the anisotropic flow of protons and light nuclei. A stiffer EoS leads to a stronger repulsive force when matter is contracted. As baryons are pushed to the outside, an anisotropic distribution in the transverse plane builds up, which can be quantified with flow coefficients, as introduced in Section 1.2.2. A study on the origin of the anisotropy is given in [104]. The anisotropy, and with it the flow coefficients, are enhanced by a stiffer EoS. Measurements of the flow coefficients can therefore be related to the EoS using

transport calculations (see [105] for a review of the early works).

First conclusions on the EoS from the momentum distribution concluded that the incompressibility of nuclear matter is large ($\kappa \approx 380\,\mathrm{MeV}$) [106]. This conclusion was drawn witohut a momentum-dependent part in the potential (see Section 2.1.2). However, in the beginning, a stiff EoS was also favored, including the momentum-dependent part in [107]. Including various collision systems and more observables, a soft momentum-dependent EoS turned out to best describe the observables, and an ambiguity between soft momentum-dependent and hard constant EoS was disentangled [108], [109].

In BUU calculations, the influence of various model parameters was observed [110]. Here, it was found that the conclusions drawn about the EoS strongly depend on the resonance content of the applied model. The aforementioned works do not include heavy resonances.

In the work by Danielewicz, Lacey, and Lynch [111], a systematic constraint is given, including an estimated uncertainty. The allowed region for the EoS provided in this work is often used as the input from heavy-ion collisions in interdisciplinary works on the EoS and is sometimes referred to as "Danielewicz constraint".

The FOPI experiment has provided very detailed data on the anisotropic flow [112]. Based on this data, the relatively soft EoS was confirmed in QMD calculations [113], which do not include heavy resonances. Recently, more flow measurements from the HADES collaboration became available [114], including even higher flow coefficients. The UrQMD model [115], [116] was applied to extract the EoS from the flow of protons [117] and deuterons [118], concluding that a hard EoS best describes the data. No momentum-dependence is included, but a large set of resonances can be excited in these works. Similar findings are presented by comparing to HADES data in Chapters 3 and 4, without and with momentum-dependent potentials respectively. The PHQMD model [119] was also confronted with the aforementioned flow data from the FOPI and HADES experiments in [120]. PHQMD includes heavier resonances and momentum-dependent potentials. A soft momentum-dependent EoS is reported to work best, but a stiffer momentum-dependent EoS is not compared to data in [120]. These results suggest that a significant part of the model uncertainty in extracting the EoS is related to the resonance content, as pointed out in [110].

As the search for the EoS is an interdisciplinary topic, combined analyses of different constraints push our current knowledge of the EoS [121]–[124]. When information from various sources is compiled, it is extremely beneficial to have an understanding of the uncertainty of each individual contribution. To provide a systematic estimate of the constraint, including statistical uncertainties, Bayesian analyses are performed [125], [126]. Chapter 4 presents work where Bayesian inference is applied to determine the EoS using the SMASH transport model.

1.4 Structure of the Thesis

Meaningful conclusions can only be drawn from calculations and experimental input when the capabilities, assumptions, and limitations of the model are kept in mind. To achieve this, a detailed description of the transport model SMASH, that is used for all calculations presented here, is given in Chapter 2. Firstly the applied mean-field potentials are described in detail with some emphasis on the newly implemented momentum-dependent term. Afterwards the collision term is described, giving a comprehensive description of each possible interaction. The model description concludes with an explanation of the light nuclei formation, which can be modeled via scatterings or final state coalescence.

Results of different studies are presented in the following chapters, beginning with a sensitivity study in Chapter 3. Calculations of flow coefficients are compared for different methods of modeling the formation of light nuclei and varying nuclear potentials. The influence of light nuclei treatment and the EoS on flow observables is explored to understand which observables are best suited to constrain the EoS using HADES data. This chapter is based on [1].

In the subsequent study presented in Chapter 4, the understanding of the observables is applied to provide a systematic constraint on the EoS using Bayesian inference. For this analysis, the nuclear potentials are upgraded to include a momentum-dependent term and the Coulomb potential is included. This chapter is based on [2].

To continue, Chapter 5 compares the agreement of different equations of state with data from the FOPI experiment which covers a range of collision energies. Scanning the energy range, it appears that a stiffer EoS is required for the higher energies than for lower energies. This chapter is based on [3].

The final study included in this thesis is presented in Chapter 6. Here, the focus lies on the production of light nuclei, which can give insights into the phase diagram of QCD matter. The formation of light nuclei, specifically deuteron triton, helium-3 and hypertriton, is modeled in multiparticle reactions and compared with measurements from the STAR collaboration. This chapter is based on [4].

The thesis concludes with a summary of the findings in Chapter 7.

Kapitel 2

Model Description

Many facets of heavy-ion collisions are discussed in this thesis with the aim to obtain information on the equation of state and the structure of the phase diagram of QCD. Heavy-ion collisions provide one of the few possibilities to investigate strongly interacting matter at large temperatures and densities. At the same time, it is difficult to obtain information directly from a heavy-ion collision. Experimentally, only particles in the final state can be observed, meaning that the time evolution of a heavy-ion collision can only be accessed in theoretical calculations.

Such calculations must be applicable in a non-equilibrium system, as the early stage of a collision, just after the impact of the nuclei, is far from thermal equilibrium. Additionally, at a later stage, after rapid expansion, the system is not equilibrated. The problem can be described within transport theory, which revolves around the relativistic Boltzmann equation

$$p^\mu \frac{\partial f_i}{\partial x^\mu} + m_i \frac{\partial (K^\mu f_i)}{\partial p^\mu} = C_i \,. \tag{2.1}$$

It is an equation for the phase-space distributions $f_i(\mathbf{r}, \mathbf{p}, t)$ for different species i, that are related to the number of particles by

$$dN_i = \frac{g_i}{(2\pi)^3} d^3r d^3p f_i(\mathbf{r}, \mathbf{p}, t) \tag{2.2}$$

with the spin degeneracy factor g_i. The force acting on particles is denoted by $K^\mu = \frac{dp^\mu}{d\tau}$, and the collision term on the right hand side is abbreviated by C_i. It describes the interactions via scattering between particles. The interactions implemented in the model are described in Section 2.2.

The first term of the relativistic Boltzmann equation is related to the propagation of particles, and the second term on the left-hand side takes into account the influence of the force. Forces in the model originate from mean-field potentials,

which are described in detail in Section 2.1. The equation of state enters a transport calculation via nuclear potentials, meaning that transport calculations are well suited to obtain information on the equation of state. This is the main goal of this thesis.

Before going into details on the interactions via potentials and scatterings, some key information about the transport model SMASH, which is applied throughout this work, is given. Further, a calculation of a heavy-ion collision within SMASH is illustrated to give the reader a basic picture of the model.

The degrees of freedom of a model define a range of applicability. In the SMASH model, the degrees of freedom are mainly hadrons. This means that SMASH can only be applied in a system where the active degrees of freedom are hadronic. A system in which quarks and gluons are not confined in hadrons can therefore not be described. SMASH is therefore restricted to the region in the phase diagram below the transition to a quark-gluon-plasma. Hadrons and resonances, included as active degrees of freedom, are taken from the Particle Data Group [127]. More details on the treatment of resonances in the model are given in 2.2.2. A list of all hadrons and resonances present in the calculation is provided in [128], but the resonance properties are always subject to small changes within the uncertainties provided by the Particle Data Group. An up-to-date version of the particle list can always be obtained together with the code base, that is publicly available [129]. The full list is not quoted here because many resonance properties will be modified in the near future, as they are tuned to experimental cross sections using a genetic algorithm [130]. To give a rough idea about the degrees of freedom, there are over 200 hadrons and resonances, plus their different isospin states included in SMASH. Additionally, photons and some leptons can be propagated, and light nuclei can be treated as active degrees of freedom or as a set of nucleons interacting via potentials, as described in Section 2.3.

Screenshots of a heavy-ion collision, as it is described in the model, are given in Figure 2.1. The distribution function is represented by a large number of test particles (see Section 2.1). The momenta and positions of the test particles are known at all times, which makes such a visualization possible and is essential for studying the time evolution of the system. In the beginning, the initial state needs to be created. The system, in this case, is a gold-gold collision for which the nuclei are sampled according to a Woods-Saxon distribution [131]. The nuclei are then boosted according to the collision energy and are thereby Lorentz-contracted.

Test particles then propagate according to the equations of motion in the presence of nuclear potentials, for which details can be found in Section 2.1. They propagate until they partake in an interaction, which is found using the collision criterion, as described in Section 2.2.6. In these interactions, new particles are produced. At this stage, the medium is compressed to high densities. This is where the

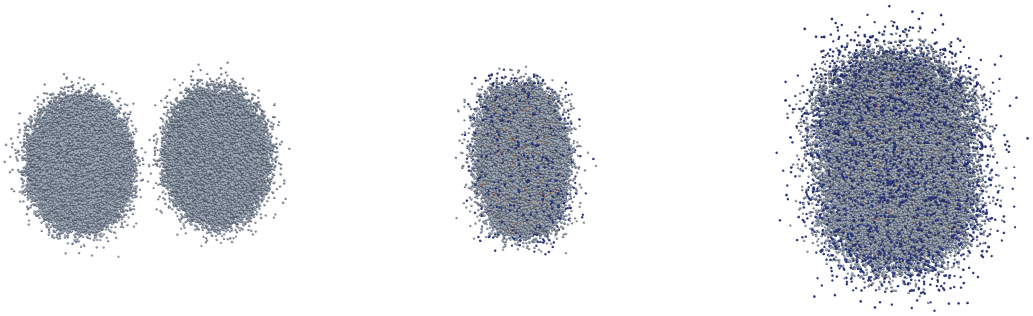

Abbildung 2.1: Illustration of a heavy-ion collision. The test particles are represented by small spheres and three different points in time are presented. The first screenshot is taken 2.5 fm before the nuclei touch. The second one is taken 12.5 fm after the nuclei touch, and the last one at $t = 20$ fm. Blue particles are light and heavier particles are colored in red.

nuclear potentials are most important, and information about the equation of state at high densities can be extracted.

Later, the number of interactions decreases as the system becomes more dilute due to its expansion. One can see the beginning of the expansion in the final picture of Figure 2.1. During this time, unstable particles decay, and stable particles eventually propagate freely. At this point one can extrapolate from the momenta of the particles to determine where they hit the detector, and predictions for an experimental outcome can be made. We note that this description is fully based on hadrons and resonances. Clearly, it can only be applied if no QGP is created. For a description of a system at higher energies, a switch can be made to a hydrodynamic evolution for the very hot and dense phase where a QGP is expected. Since the hydrodynamic evolution requires the system to be close to equilibrium, it cannot be applied to all phases of a heavy-ion collision. A switch to the hadronic transport model is required for the final stage. The final stage is referred to as the afterburner. A framework for such a hybrid approach is created with a hydrodynamic evolution, implemented in the vHLLE code [132], and SMASH used in both the initial stage and the afterburner [51]. SMASH is further available as a module for the afterburner stage in X-SCAPE and JETSCAPE [133], that are frameworks combining several models for the description of heavy-ion collisions in a hybrid approach.

Screenshots of a heavy-ion collision are shown in Figure 2.2. Here, we observe that the colliding nuclei are much more contracted. This is because the collision energy, and therefore the velocity of the nuclei, is higher. In the next step, the description of the hot and dense matter switches to a hydrodynamic evolution. As

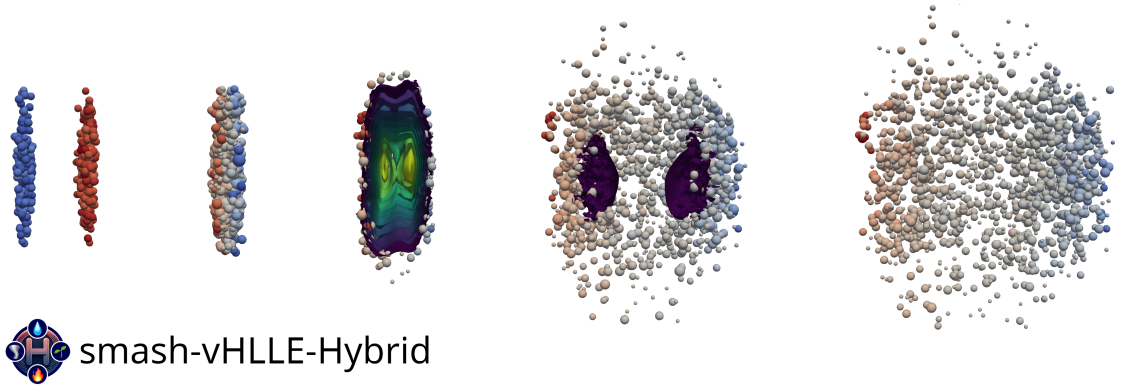

Abbildung 2.2: Screenshots of a central gold-gold collision at $\sqrt{s_{NN}} = 17.3\,\mathrm{GeV}$ [134]. The first image shows the initially sampled and Lorentz-contracted nuclei, followed by a pre-equilibrium stage modeled using the hadronic transport model. The next screenshot illustrates the hydrodynamic evolution of the system, and in the subsequent frame, the system is partially described by hadronic transport as it cools down. In the final image, the system has cooled to a point where it can be fully modeled using hadronic transport.

the system expands, the medium cools down, and the description changes back tp transport in the afterburner stage, based on the temperature or energy density.

In Chapter 6, results are presented for an afterburner calculation coupled to a hydrodynamic evolution within the MUSIC code [53], [59], [135], [136]

This quick illustration of the model in two different scenarios should give a basic picture of the model. Let us proceed with detailed information on the most important ingredients of a transport calculation. We start with a description of the potentials, followed by the collision term. Since light nuclei formation in SMASH is essential for some of the results in the later chapters, it is introduced in Section 2.3.

2.1 Potentials

Potentials are the handle to modify the equation of state in a transport calculation. This makes them the most interesting feature of the model for this project. In this Section we iterate through the potentials available in SMASH We start with the Skyrme potential, and continue in Section 2.1.2 with the momentum-dependent term, that was implemented in this work. The equations of motion are needed for the implementation, and they are provided before the connection to the equation of state is made. Further, the constraints used to fix the parameters are given, and a comparison to the optical model is presented. The section about the momentum-dependent part of the potential concludes with the cold nuclear matter assumption,

which is made to reduce numerical cost, being put to test. The symmetry potential is introduced in Section 2.1.3. Finally, the Coulomb potential is described, followed by details on the density.

2.1.1 Skyrme Potential

The Skyrme [137] potential is widely used in many transport models, but also for various applications in astrophysics. It is based on an expansion of the effective nucleon-nucleon interaction in terms of relative momentum for a phenomenological description of nuclear matter properties. Parameters of the expansion are fitted to various observables and many parametrizations, including different expansion terms, are available. In [123] 240 different Skyrme parametrizations are tested against constraints from different fields.

In SMASH, a simple expression for the single-particle energy is used. The potential is given in terms of the baryon density ρ_B

$$U_{\text{Skyrme}} = A\left(\frac{\rho_B}{\rho_0}\right) + B\left(\frac{\rho_B}{\rho_0}\right)^{\tau} . \tag{2.3}$$

A, B, and τ are parameters. Equation 2.3 is expressed in terms of the nuclear ground state density ρ_0, but the parameters of the potential need to be chosen such that the binding energy is largest for that density. We will discuss the parameter estimation in Section 2.1.2.

For the dynamical description within a transport model, we consider the Skyrme potential to be the zeroth component of a vector potential in the local rest-frame $V^\mu = (U_{\text{Skyrme}}, 0, 0, 0)^T$. The rest-frame is defined to be the frame where the spatial components of the baryon current vanish. For details on the calculation of the current, see Section 2.1.5. We note that this prescription is inconsistent as the expression for the Skyrme potential transforms like a Lorentz scalar and not like the zeroth component of a vector, since ρ_B refers to the baryon density in the local rest-frame. Even though a fully relativistic description is not obtained this way, we proceed in a similarly to the Walecka model. The Walecka model includes a scalar and a vector potential in the Lagrangian density [138]. The Euler-Lagrange equations yield a Dirac equation, from which one obtains the dispersion relation $(p^\mu - V^\mu)(p_\mu - V_\mu) - (m+S)^2 = 0$. This can be expressed as $\Pi^\mu\Pi_\mu - (m^*)^2 = 0$ by introducing the kinetic momentum $\Pi^\mu = p^\mu - V^\mu$ and the effective mass $m^* = m + S$.

Using $E = p^0 = \sqrt{\mathbf{\Pi}^2 + (m^*)^2} + V^0$, one can rewrite the transport equation

$$\left[\partial_t + \nabla_p E \cdot \nabla_r - \nabla_r E \cdot \nabla_p\right] f(\mathbf{r}, \mathbf{p}) = C(\mathbf{r}, \mathbf{p}) \tag{2.4}$$

in terms of the kinetic momentum which leads to [139]–[141]

$$\frac{1}{\Pi^0}\left[\Pi^\mu\partial_\mu - (\Pi_\mu F^{\mu a} - m^*\partial^a m^*)\frac{\partial}{\partial\Pi^a}\right]\tilde{f}(\mathbf{r}, \mathbf{\Pi}) = C(\mathbf{r}, \mathbf{p}) , \tag{2.5}$$

where $F^{\mu\nu} = \partial^\mu V^\nu - \partial^\nu V^\mu$. The sum over a includes only the spatial components.

Let us now derive the equations of motion for test particles using the transport equation, specifically for the case of the Skyrme potential. For this purpose, we disregard the collision term, as we are interested in the propagation in the presence of the potential. The collision integral, expressed in terms of the kinetic momenta, can be found in [140].

For this purpose, we first examine the term $\Pi_\mu F^{\mu a}$ in our special case. Treating the Skyrme potential such that it is taken as a zero component of a vector field in the local rest frame, we can obtain the vector potential in an arbitrary frame by performing a Lorentz-boost

$$V^\mu = (\Lambda^{-1})^\mu{}_\nu V'^\nu = (\Lambda^{-1})^\mu{}_0 V'^0\,, \tag{2.6}$$

where $V'^\mu = (U_{\text{Skyrme}}(\rho_B), 0, 0, 0)$ is the vector potential in the local rest frame, and $(\Lambda^{-1})^\mu{}_\nu$ denotes the Lorentz-transformation from the local rest frame to the arbitrary calculation frame. The components of the boost can be expressed in terms of the velocity of the rest-frame in the calculation frame considering that the inverse boost is a boost with negative velocity

$$(\Lambda^{-1})^0{}_0 = u^0 = \gamma \tag{2.7}$$

$$(\Lambda^{-1})^i{}_0 = -u^i = -\gamma\beta^i\,, \tag{2.8}$$

where β is the velocity of the rest frame in the calculation frame and $\gamma = 1/\sqrt{1-\beta^2}$. Expanding the sum, one obtains

$$\Pi_\mu F^{\mu a} = \Pi_0\partial^0 V^a - \Pi_0\partial^a V^0 + \Pi_i\partial^i V^a - \Pi_i\partial^a V^i\,. \tag{2.9}$$

Using the expressions from Equations 2.7 and 2.8, we obtain $V^0 = \gamma U_{\text{Skyrme}}$ and $V^i = -\gamma\beta^i U_{\text{Skyrme}}$. Applying the chain rule for the derivatives $\partial^\mu U_{\text{Skyrme}}(\rho_B) = U'_{\text{Skyrme}}(\rho_B)\partial^\mu\rho_B$ we obtain

$$\Pi_\mu F^{\mu a} = \Pi^0\frac{\partial U_{\text{Skyrme}}}{\partial\rho_B}\left[-\beta^a\gamma\partial_t\rho_B - \gamma\partial^a\rho_B - \gamma\beta^a\frac{\Pi_i}{\Pi^0}\partial^i\rho_B + \gamma\beta^a\frac{\Pi_a}{\Pi^0}\partial^a\rho_B\right], \tag{2.10}$$

where we can identify the baryon current $j^\mu_B = \rho_B u^\mu$ so that the above expression becomes

$$\Pi^0\frac{\partial U_{\text{Skyrme}}}{\partial\rho_B}\left[-\partial_t j^a_B - \partial^a j^0_B - \frac{\Pi_i}{\Pi^0}\partial^i j^a_B + \frac{\Pi_a}{\Pi^0}\partial^a j^a_B\right]. \tag{2.11}$$

Using the Grassmann identity, we can identify the cross product in the two rightmost terms and switch to a vectorial formulation

$$\Pi^0\frac{\partial U_{\text{Skyrme}}}{\partial\rho_B}\left[-(\nabla_r j^0_B + \partial_t\mathbf{j}_B) + \frac{\mathbf{\Pi}}{\Pi^0}\times(\nabla_r\times\mathbf{j}_B)\right] \equiv \Pi^0\mathbf{F}\,. \tag{2.12}$$

Here, we have defined a vector $\mathbf{F}$, which reminds of the Lorentz-force and, indeed, we will show in the following using the test particle ansatz, that it is the time derivative of the kinetic momentum of a test particle, and that $\mathbf{\Pi}/\Pi^0$ is the velocity.

With the previous result, considering that the effective mass is just the rest mass in the absence of a scalar potential and disregarding the collision term, Equation 2.5 becomes,

$$\left[\partial_t + \frac{\mathbf{\Pi}}{\Pi^0}\cdot\nabla_r - \mathbf{F}\cdot\nabla_\Pi\right]\tilde{f}(\mathbf{r},\mathbf{\Pi}) = 0 \tag{2.13}$$

The test particle ansatz, first used in a similar context in [142], is applied directly for the distribution function in terms of the kinetic momentum. The ansatz reads

$$\tilde{f}(\mathbf{r},\mathbf{\Pi}) = \frac{(2\pi)^3}{gN_{\text{test}}}\sum_{i=1}^{NN_{\text{test}}}\delta^3(\mathbf{\Pi}-\mathbf{\Pi}_i)\delta^3(\mathbf{r}-\mathbf{r}_i)\,, \tag{2.14}$$

where N_{test} is the number of test particles per real particle and N is the number of particles. We note that the ansatz can only describe the distribution function in the limit of N_{test} going to infinity. The steps to derive the equations of motion are outlined for a similar problem in [143]. Inserting the ansatz into equation 2.13, one requires the derivatives of the delta functions. Using the chain rule, one can formulate the time derivative as

$$\begin{aligned}\partial_t\tilde{f}(\mathbf{r},\mathbf{\Pi}) = \frac{(2\pi)^3}{gN_{\text{test}}}\sum_{i=1}^{NN_{\text{test}}}\Bigg[&\delta^3(\mathbf{\Pi}-\mathbf{\Pi}_i)\nabla_{r-r_i}\delta^3(\mathbf{r}-\mathbf{r}_i)\cdot\frac{\partial(\mathbf{r}-\mathbf{r}_i)}{\partial t}\\ &+\delta^3(\mathbf{r}-\mathbf{r}_i)\nabla_{\Pi-\Pi_i}\delta^3(\mathbf{\Pi}-\mathbf{\Pi}_i)\cdot\frac{\partial(\mathbf{\Pi}-\mathbf{\Pi}_i)}{\partial t}\Bigg]\,.\end{aligned} \tag{2.15}$$

With $\partial_t(\mathbf{r}-\mathbf{r}_i) = -\partial_t\mathbf{r}_i$ and $\partial_t(\mathbf{\Pi}-\mathbf{\Pi}_i) = \partial_t\mathbf{\Pi}_i$ we can substitute the ansatz into Equation 2.13. Ordering the terms in a convenient way, one obtains

$$\begin{aligned}0 =&\frac{(2\pi)^3}{gN_{\text{test}}}\sum_{i=1}^{NN_{\text{test}}}\left[\frac{\mathbf{\Pi}}{\Pi^0}-\frac{\partial\mathbf{r}_i}{\partial t}\right]\delta^3(\mathbf{\Pi}-\mathbf{\Pi}_i)\nabla_\Pi\delta^3(\mathbf{r}-\mathbf{r}_i)\\ &+\frac{(2\pi)^3}{gN_{\text{test}}}\sum_{i=1}^{NN_{\text{test}}}\left[\mathbf{F}-\frac{\partial\mathbf{\Pi}_i}{\partial t}\right]\delta^3(\mathbf{r}-\mathbf{r}_i)\nabla_r\delta^3(\mathbf{\Pi}-\mathbf{\Pi}_i)\,.\end{aligned} \tag{2.16}$$

A solution of this equation is obtained only if both square brackets vanish. Taking the δ-distributions into account, we obtain the equations of motion

$$\dot{\mathbf{r}}_i = \frac{\mathbf{\Pi_i}}{\Pi_i^0} \tag{2.17}$$

$$\dot{\mathbf{\Pi}}_i = \frac{\partial U_{\text{Skyrme}}}{\partial\rho_B}\left[-(\nabla_r j_B^0 + \partial_t\mathbf{j}_B) + \frac{\mathbf{\Pi}_i}{\Pi_i^0}\times(\nabla_r\times\mathbf{j}_B)\right]\,. \tag{2.18}$$

For clarity, Equation 2.18 omits explicit mention of the dependencies of the potential and current, and where they are evaluated. $\partial U_{\text{Skyrme}}/\partial \rho_B$ depends on the rest-frame density ρ_B, which, like the current, depends on the position. Both are evaluated at the position $\mathbf{r}_i$ of the test particle under consideration.

The equations of motion are solved in SMASH using the Euler method. It is based on short time steps of size Δt and at each time step, the momenta and positions are updated according to

$$\mathbf{r}_i(t + \Delta t) = \mathbf{r}_i(t) + \dot{\mathbf{r}}_i(t)\Delta t \tag{2.19}$$

$$\mathbf{\Pi}_i(t + \Delta t) = \mathbf{\Pi}_i(t) + \dot{\mathbf{\Pi}}_i(t)\Delta t\,. \tag{2.20}$$

2.1.2 Momentum-Dependence

We have so far discussed the Skyrme potential which is widely used in many transport models. By itself it depends, in the local rest-frame, only on the baryon density. Scattering experiments between protons and nuclei have been performed and using the optical model, the potential was extracted for different collision energies in [144], [145]. The potential extracted from this experimental measurement depends on the kinetic energy, and hence on the momentum, of the particle. To incorporate this finding in the transport models, a momentum-dependent term is added to the Skyrme potential such that the optical potential is reproduced at saturation density. Adding a momentum-dependent term does not fully follow the idea of the Skyrme potential which originates from an expansion of the interaction in terms of momenta. But this prescription is widely used in the field and yields a decent phenomenological description of the potential. Calculations including a momentum-dependent term have already been performed in the 1980s in a Boltzmann-type calculation [146] and in quantum molecular dynamics [107].

In the Walecka model the momentum-dependence arises from the inclusion of a scalar potential. A momentum-independent scalar potential cannot describe the optical potential however (see further below in this section). An extension to momentum-dependent scalar and vector potential is presented in [147].

For this work, the momentum-dependent term as suggested by Welke et al. [148] is implemented. The momentum-dependent term of the single-particle potential is written as

$$U_{\text{MD}} = \frac{2C}{\rho_0} g \int \frac{d^3p'}{(2\pi)^3} \frac{f(\mathbf{r}, \mathbf{p}')}{1 + \left(\frac{\mathbf{p}-\mathbf{p}'}{\Lambda}\right)^2}\,. \tag{2.21}$$

Here, C and Λ are parameters that are tuned to the optical potential at saturation density, as described later in this section. The integral can be evaluated using the test particle ansatz, but this approach is computationally expensive when dealing with many test particles. Therefore, we follow the implementation in GiBUU [141]

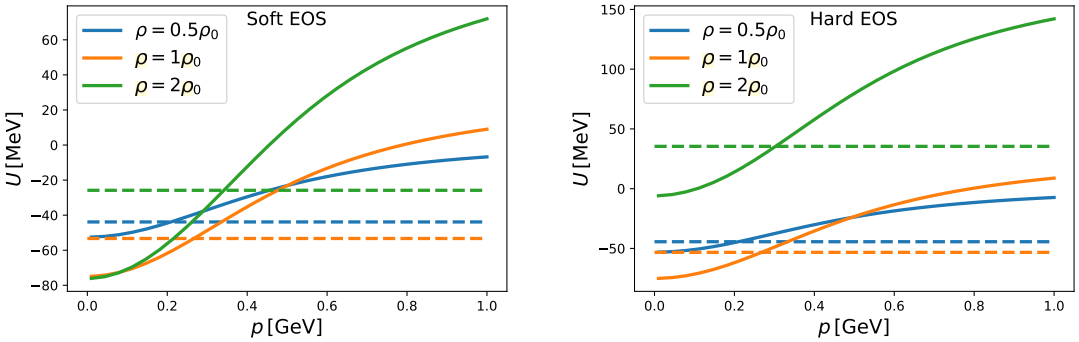

Abbildung 2.3: Single-particle potential as a function of the momentum of the particle under consideration for different baryon densities for a soft (left) and a hard (right) equation of state. The dashed lines represent the single particle potential for a Skyrme potential without the momentum-dependent part but with the same incompressibility as for the full lines. The incompressibility is $\kappa = 215\,\mathrm{MeV}$ for the soft EoS and $\kappa = 380\,\mathrm{MeV}$ for the hard EoS.

by assuming cold nuclear matter for the distribution function

$$f(\mathbf{r}, \mathbf{p}) = \Theta(p - p_F(\rho_B(\mathbf{r})))\,, \tag{2.22}$$

where $p_F = (6\pi^2\rho_B/g)^{1/3}$ denotes the Fermi momentum. Consistent with the cold nuclear assumption the degeneracy factor g is four due to the spin and isospin degeneracy of nucleons. Using this assumption, the integral in the potential can be solved analytically such that the single-particle potential can be obtained with minimal numerical effort. The difference in potential between a realistic distribution function and this assumption is investigated towards the end of this section. The solution to the integral is given in [148] and the expression is quoted here for completeness

$$\begin{aligned}\frac{2C}{\rho_0} g \int \frac{d^3p'}{(2\pi)^3} \frac{\Theta(p_F - p')}{1 + \left(\frac{\mathbf{p}-\mathbf{p}'}{\Lambda}\right)^2} = \frac{2C}{\rho_0} \frac{g\pi\Lambda^3}{(2\pi)^3} \Bigg[\frac{p_F^2 + \Lambda^2 - p^2}{2p\Lambda} \ln \frac{(p+p_F)^2 + \Lambda^2}{(p-p_F)^2 + \Lambda^2} \\ + \frac{2p_F}{\Lambda} - 2\left(\arctan\frac{p+p_F}{\Lambda} - \arctan\frac{p-p_F}{\Lambda}\right)\Bigg]\,.\end{aligned} \tag{2.23}$$

The single-particle energy determines the dynamics of test particles in a calculation and some valuable insights can be obtained from a visualisation and a comparison to the pure Skyrme potential. A simple plot of the single particle potential as a function of momentum is shown for different densities in Figure 2.3 for a soft and a more stiff equation of state. In comparison to the potential with momentum-dependence, the dashed curves show the potential when including only

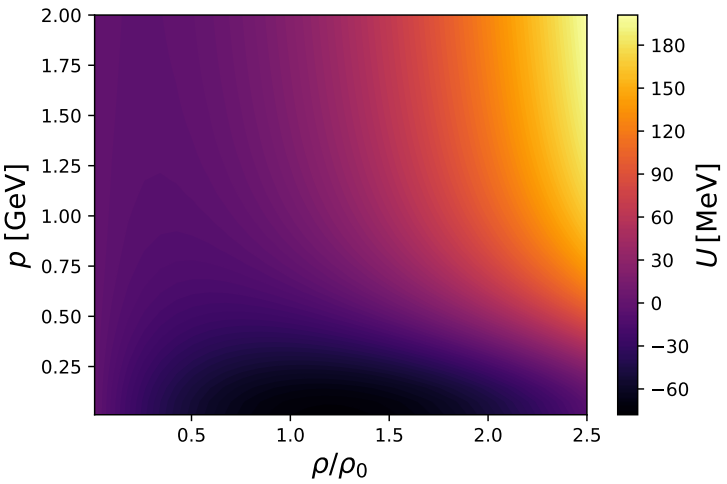

Abbildung 2.4: Single-particle potential as a function of the baryon density and the momentum of the particle of interest. It is shown exemplarily for a medium-stiff equation of state with an incompressibility of $\kappa = 290\,\mathrm{MeV}$.

the Skyrme part, but with the same stiffness of the equation of state at saturation density (the quantification of the stiffness is described further below). In general, one can observe that the momentum-dependent potential is reduced at lower momenta and enhanced at higher momenta as compared to the pure Skyrme potential. The large values of the potential at high momenta indicate that high-momentum particles experience a stronger influence from the potential as compared to from the Skyrme part.

A clearer picture of the influence of the momentum-dependence can be obtained by examining the potential as a function of both density and momentum, as shown, for a medium-stiff EoS, in Figure 2.4. As in Figure 2.3, one observes that the potential becomes very large for high densities and momenta and in the low momentum region the potential grows only very slowly, even for large densities. Considering a test particle propagating through matter at rest with a given momentum, it experiences an attractive force if the single-particle energy decreases with increasing density. In Figure 2.4, it is evident that the potential above saturation density is more repulsive for test particles with higher momenta than for those with low momenta.

To make it more evident, the derivative of the potential with respect to density is shown in Figure 2.5. In this picture, a particle with momentum p experiences an attractive force in the blue region and a repulsive force in the red region. It ca be seen that test particles with low momenta experience an attractive force even above saturation density whereas test particles with a higher momentum are deflected even if the density is below saturation density. This behaviour is important for

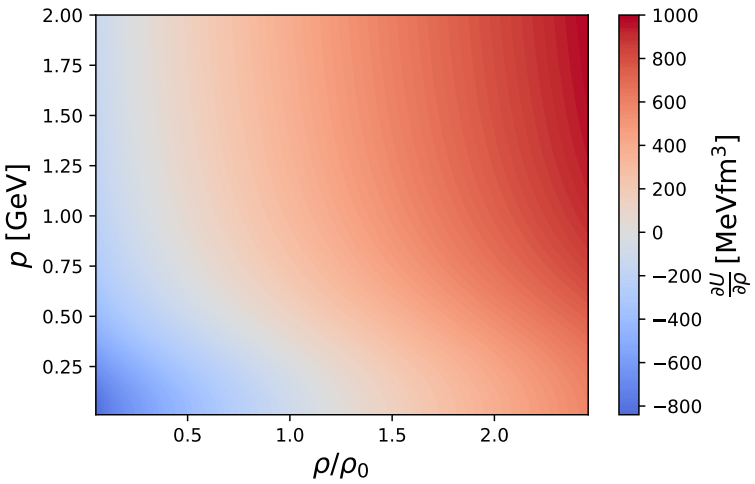

Abbildung 2.5: Derivative of the single-particle potential with respect to the baryon density as a function of the baryon density and the momentum of a particle of interest. Consistent with Figure 2.4, the stiffness is set to be $\kappa = 290\,\mathrm{MeV}$.

understanding how the particle production is influenced in heavy-ion collisions when including this potential.

Equations of Motion

To obtain the equations of motion, we start from the Boltzmann equation in the same form as for the Skyrme potential (Eq. 2.4)

$$[\partial_t + \nabla_p E \cdot \nabla_r - \nabla_r E \cdot \nabla_p]\, f(\mathbf{r}, \mathbf{p}) = C(\mathbf{r}, \mathbf{p})\,. \tag{2.24}$$

Here, the single-particle energy is written as $E = \sqrt{p^2 + m^2} + U(\rho_B, \mathbf{p})$, where U is the sum of the Skyrme part and the momentum-dependent term. The potential is incorporated as a zero component of a vector potential within the relativistic kinematics of the model. A full relativistic description is not obtained this way, as the potential does not behave this way under Lorentz-transformation.

In this case, the propagation is not performed, like in the case for the pure Skyrme potential, in terms of the kinetic momentum. Instead, the test particle ansatz is applied directly in terms of the momenta

$$f(\mathbf{r}, \mathbf{p}) = \frac{(2\pi)^3}{g N_{\mathrm{test}}} \sum_{i=1}^{N N_{\mathrm{test}}} \delta^3(\mathbf{r} - \mathbf{r}_i)\delta^3(\mathbf{p} - \mathbf{p}_i)\,. \tag{2.25}$$

The equations of motion follow in the same way as for the Skyrme potential by inserting this expression into the Boltzmann equation. One obtains

$$\dot{\mathbf{p}}_i = -\nabla_r E_i \tag{2.26}$$

$$\dot{\mathbf{r}}_i = \frac{\mathbf{p}_i}{\sqrt{p_i^2 + m^2}} + \nabla_p U \,. \tag{2.27}$$

Since the potential is not written in a covariant form, it is evaluated in the local rest frame and boosted to the calculation frame for the evaluation of the gradient in Equation 2.26. The boost of the single-particle energy is not trivial. With the assumed transformation behaviour, the energy and momentum in the calculation frame and the local rest frame (LRF) are related as

$$E^2 - p^2 = E_{\mathrm{LRF}}^2 - p_{\mathrm{LRF}}^2 \,. \tag{2.28}$$

The momentum in the local rest frame is obtained by boosting and thus depends on $\mathbf{p}$ and E. The energy E_{LRF} is then obtained from $\mathbf{p}_{\mathrm{LRF}}$ using the expressions for the Skyrme potential and the simplified form (Eq. 2.23) of the momentum-dependent term. Hence, the energy in the local rest frame implicitly depends on the energy in the calculation frame, and thus a numerical root-finding algorithm needs to be applied to find the calculation frame energy, such that Equation 2.28 is satisfied. A bisection method is applied to find the root of $E^2 - p^2 - (E_{\mathrm{LRF}}^2 - p_{\mathrm{LRF}}^2)$, because this method always finds the root, if there is exactly one in a given interval. Technically, we start with a small interval around the kinetic energy of the test particle and increase the width in case no root exists in that interval.

This way, the energy is evaluated for six points around the position of the test particle, so that the energy gradient for Equation 2.26 can be obtained using finite difference. The second term in equation 2.27 is neglected. The difficulty in including this term is not in its evaluation, which could be done using finite difference like for the spatial gradient, as it is done in the GiBUU transport model. However, the relation $\beta = \mathbf{p}/E$ between velocity and momentum is widely explicitly and implicitly used in the code base, making a modification rather involved.

To quickly recap the implemented features, the momentum-dependence, in the form as suggested in [148], is implemented. The potential is not written in a covariant form and the treatment is not fully relativistic. We evaluate the potential in the local rest frame, in which the cold nuclear matter assumption for the distribution function is made. Finally, the term $\nabla_p U$ for the propagation is neglected but it can be added in future work.

Binding Energy and Equation of State

The main goal of this thesis is to acquire knowledge about the equation of state of nuclear matter. In a transport calculation, the equation of state enters via potentials,

and we discuss how the connection is made in the following. Further, the binding energy is introduced, which is an important quantity for fixing the parameters to nuclear matter constraints.

For both the equation of state and the binding energy, the energy density of a system is required. An important ingredient for the energy density is the potential energy density v. It is related to the single particle potential by $U = \delta v/\delta\rho_B$, and the existence of such a potential is important for the conservation of energy. For the Skyrme potential with the momentum-dependent term, the potential energy density is given by

$$v(\mathbf{r}) = \frac{A}{2}\frac{\rho_B^2}{\rho_0} + \frac{B}{\rho^{\tau+1}}\frac{\rho_B^{\tau+1}}{\rho_0^{\tau}} + \frac{C}{\rho_0}\int \frac{gd^3p}{(2\pi)^3}\int \frac{gd^3p'}{(2\pi)^3}\frac{f(\mathbf{r},\mathbf{p})f(\mathbf{r},\mathbf{p}')}{1+\left(\frac{\mathbf{p}-\mathbf{p}'}{\Lambda}\right)^2}\,. \tag{2.29}$$

The first two terms generate the Skyrme potential whereas the final term is related to the momentum-dependent part. Considering cold nuclear matter, the form of the distribution function is $f(\mathbf{r},\mathbf{p}) = \Theta(p_F - p)$. For this case, the integral can be solved analytically, and we quote the solution that is given in [148]

$$\begin{aligned}\int d^3p \int d^3p' \frac{\Theta(p_F-p)\Theta(p_F-p')}{1+\left(\frac{\mathbf{p}-\mathbf{p}'}{\Lambda}\right)^2} = \\ \frac{32\pi^2}{3}p_F^4\Lambda^2\left[\frac{3}{8} - \frac{\Lambda}{2p_F}\arctan\left(\frac{2p_F}{\Lambda}\right) - \frac{\Lambda^2}{16p_F^2}\right. \\ \left. + \left(\frac{3}{16}\frac{\Lambda^2}{p_F^2} + \frac{1}{64}\frac{\Lambda^4}{p_F^4}\right)\ln\left(1+\frac{4p_F^2}{\Lambda^2}\right)\right]\,.\end{aligned} \tag{2.30}$$

An additional contribution to the energy density is the kinetic part that contains essentially a sum of the kinetic energies of free test particles

$$\epsilon_{\text{free}} = \int \frac{gd^3p}{(2\pi)^3}\sqrt{m^2+p^2}f(\mathbf{r},\mathbf{p})\,. \tag{2.31}$$

This expression can also be solved analytically for cold nuclear matter and one finds

$$\epsilon_{\text{free}} = \frac{g}{16\pi^2}\left[\sqrt{p_F^2+m^2}(2p_F^3+m^2p_F) - m^4\arcsin\left(\frac{p_F}{m}\right)\right] \tag{2.32}$$

when substituting the Heavyside function for the distribution function. In total, the energy density is the sum $\epsilon = \epsilon_{\text{free}} + v$ of the two contributions. The binding energy per nucleon is then obtained by dividing the energy density by the baryon density and subtracting the mass

$$\frac{E_B}{A} = \frac{\epsilon}{\rho_B} - m\,. \tag{2.33}$$

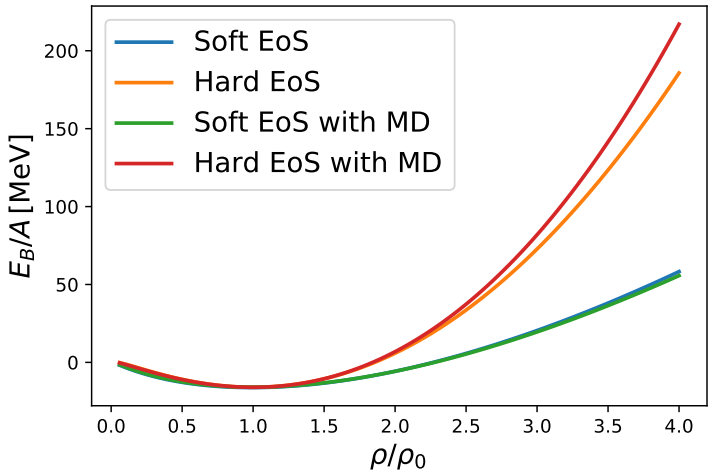

Abbildung 2.6: Binding energy per nucleon as a function of the baryon density at zero temperature. The binding energies are shown for the Skyrme potential, with and without the momentum-dependent (MD) part, for an incompressibility of $\kappa = 215\,\mathrm{MeV}$ (soft) and $\kappa = 380\,\mathrm{MeV}$ (hard).

The binding energy per nucleon is obtained this way for symmetric nuclear matter at zero temperature. It is visualized for a soft and a hard equation of state with and without momentum-dependence in Figure 2.6. At saturation density, all curves show a minimum at $E_B/A = -16\,\mathrm{MeV}$. This is enforced by nuclear matter constraints and the parameters are tuned to fulfil the constraint as described later in this section. One can observe in Figure 2.6 that more energy is required to deviate the density from saturation density for the hard EoS. Finally a comparison between the potentials with and without the momentum-dependent part can be made. In general, the difference between the binding energies is subtle compared to the influence of varying the stiffness. One finds a slightly larger energy per nucleon at higher densities when including the momentum-dependent term. A statement that the momentum-dependence effectively only makes a soft equation of state hard is not supported by this plot as the soft momentum-dependent equation of state is far below the hard EoS at $\rho_B = 4\rho_0$ in terms of energy. Figure 2.6 does, however, only give information on the binding energy at vanishing temperature and such a statement may be more realistic for a hot medium such as a heavy-ion collision.

The equation of state itself is most commonly given as the pressure as a function of the baryon density. The pressure can be calculated from the energy density by taking the derivative with respect to the baryon density

$$P(\rho_B) = \rho_B^2 \frac{\partial(\epsilon/\rho_B)}{\partial \rho_B}\,. \tag{2.34}$$

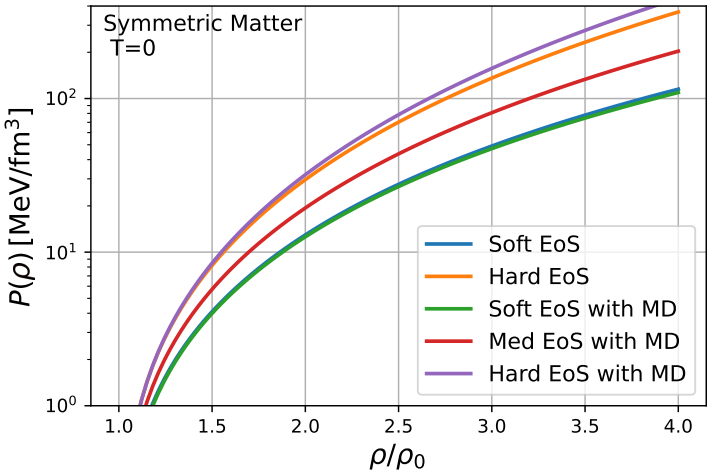

Abbildung 2.7: Pressure for symmetric nuclear matter at zero temperature as a function of the baryon density. The pressure is shown for varying stiffness, and with and without the inclusion of the momentum-dependent term.

The pressure is given for varying stiffness with and without the momentum-dependent term in Figure 2.7 as a function of the baryon density. Including the momentum dependent term, a very similar equation of state is obtained, but one observes, same as for the binding energy, a difference at higher densities. This is due to the fact that the momentum-dependent potentials are setup such that they have the same stiffness as the pure Skyrme potential at saturation density, but the behaviour at higher densities can differ. At all densities, the difference between soft and hard is far more prominent than the inclusion of the momentum-dependence. The fact that the equation of state at vanishing temperature is almost unchanged by the inclusion of the momentum-dependent part is interesting, especially since it will become evident in the results section that the impact on the dynamics in a heavy-ion collision is strong. One should note, that the potentials with the momentum-dependent part differ from the ones without the momentum-dependent part not just by adding the additional term, but additionally, the parameters need to be readjusted to physical constraints as described in the following.

Parameter Estimation

The potentials described in this chapter have the five parameters A, B, C, τ, and Λ including the Skyrme part. The nuclear ground state density ρ_0 also appears in the potential, but is fixed in the present work to a value of $0.168\,\mathrm{fm}^{-3}$. Other transport models use slightly different nuclear ground state densities, and it would be very

interesting to test the sensitivity to that number.

The five parameters are not free in the sense that the nuclear matter constraints are formulated in four equations, such that only a single parameter is free after taking them into account. The nuclear binding energy is introduced above, and already in Figure 2.6, the observation was made that each curve has a minimum at the nuclear ground state density, with a value of $E_B/A = -16\,\mathrm{MeV}$. This is enforced, as the parameters are chosen to match exactly the two conditions

$$\left(\frac{E_B}{A}\right)_{\rho_B=\rho_0} = -16\,\mathrm{MeV} \tag{2.35}$$

$$\left(\frac{\partial(E_B/A)}{\partial\rho_B}\right)_{\rho_B=\rho_0} = 0 \tag{2.36}$$

The constraint on the value of the binding energy at saturation density (Eq. 2.35) can be related to the volume term in the Bethe-Weizsäcker mass formula [149], [150], that is also known as the liquid drop model. An estimation of the parameters of the liquid drop model is performed in [151], and the coefficient of the volume term is estimated to be roughly 16 MeV.

The second constraint (Eq. 2.36) is more of the definition of the nuclear ground state energy than an experimental constraint (even though the value of the ground state density needs to be determined experimentally). Equation 2.36 expresses that the nuclear ground state density is energetically the most favorable density.

To find a value for the five parameters of the potential, three more equations are required in addition to Equations 2.35 and 2.36. Two of them are used to fix the momentum-dependent part of the potential so that the aforementioned optical potential is reproduced. The optical model is used to extract the momentum-dependence from scattering experiments in [144], [145]. The so-called Schrödinger equivalent potential U_{SEP} is provided by the optical model and can be compared to the potential that is applied in this work. The Schrödinger equivalent potential can be calculated as [139]

$$U_{\mathrm{SEP}} = U_S + U_0 + \frac{1}{2m}(U_s^2 - U_0^2) + \frac{U_0}{m}E_{\mathrm{kin}}\,, \tag{2.37}$$

where the kinetic energy is $E_{\mathrm{kin}} = \sqrt{p^2+m^2} - m$. The Schrödinger equivalent potential is plotted as a function of the kinetic energy in Figure 2.8. The figure contains values from [145] that were extracted from proton-lead scattering. Further, various Skyrme potentials with and without momentum-dependence are presented. The Skyrme potentials are treated like the zero component of the vector potential U_0 with no scalar potential. Naturally, the Schrödinger equivalent potential is linear without explicit momentum-dependence, as only the last term in Equation 2.37

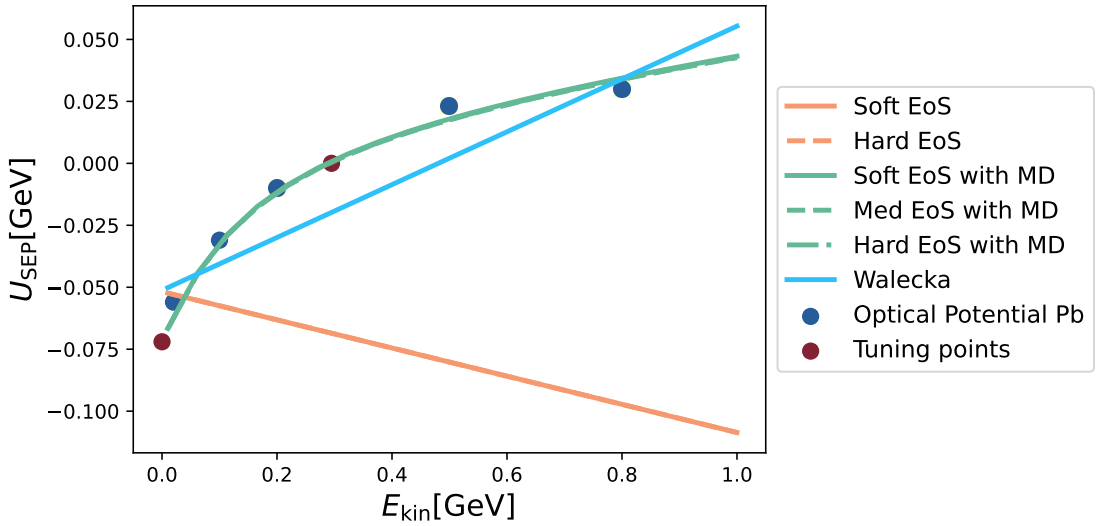

Abbildung 2.8: Schrödinger equivalent potential as a function of kinetic energy. The soft and hard Skyrme potentials without the momentum-dependent term are shown. These two curves overlap but exhibit an incorrect trend. A parameter set for the Walecka model is also displayed. It follows the trend but does not match the measurements. Finally, the Skyrme potentials with momentum dependence also overlap and correctly describe the experimental data from [145].

yields a dependence on the kinetic energy. For the pure Skyrme potential, the energy dependence is completely different from the optical model estimation. The Walecka model includes a scalar and a vector potential, but they are not dependent on the momentum. Hence, only a linear energy dependence is obtained, which can be tuned to roughly reproduce the optical potential. The form that we use in this work with the momentum-dependence does describe the optical model estimate very well. The parameters are, for this potential, only tuned to the two orange points in Figure 2.8, which were suggested already in [148], and are given in terms of the single-particle potential at a given momentum as

$$U(\rho_0, p = 0) = -75\,\mathrm{MeV} \tag{2.38}$$

$$U(\rho_0, p = 800\,\mathrm{MeV}) = 0\,\mathrm{MeV}\,. \tag{2.39}$$

Since, for the soft, the medium-stiff and the hard equation of state, all points of the optical model estimate are reproduced when they are tuned to only Equations 2.38 and 2.39, the two points are sufficient for the parameter estimation.

The Equations 2.35, 2.36, 2.38, and 2.39 are the constraints from nuclear matter that are taken into account for the parameter estimation. As there are five parameters and so far only four equations to constrain them, there is still one free parameter

remaining. In order to give a physical meaning to the final parameter, the incompressibility at saturation density is widely used to quantify the stiffness of the equation of state. The incompressibility κ will serve in our case as the last free parameter. It can be obtained as the second derivative of the binding energy with respect to the density as

$$\kappa = 9\rho^2 \frac{\partial^2}{\partial \rho_B^2} \left(\frac{E_b}{A} \right)_{\rho_B = \rho_0} . \tag{2.40}$$

As it is essentially the second derivative of the binding energy, it controls the curvature in Figure 2.6 such that a larger change in the energy with increasing density is generated with a stiffer equation of state (or a larger incompressibility).

For a given value of κ, the five equations can be solved numerically to obtain the five parameters of the Skyrme potential, including the momentum-dependent term. When the momentum-dependent term is neglected, the three remaining parameters A, B, and τ can be obtained without the constraints from the optical model, so that the parameters are fixed using Equations 2.35, 2.36, and 2.40.

Cold Nuclear Matter Assumption

The momentum-dependent term of the potential contains an integral over the distribution function. In a transport model, the distribution function can be accessed at all times. It is represented by test particles in the aforementioned test particle ansatz (see Eq. 2.25). As the integral over the distribution function is simplified in dynamic calculations within SMASH, it is instructive to write down the form of the potential without this assumption and compare.

We begin by recalling the momentum-dependent term of the potential, to which we will in this case apply the test particle ansatz

$$U_{\mathrm{MD}} = \frac{2C}{\rho_0} g \int \frac{d^3p'}{(2\pi)^3} \frac{f(\mathbf{r}, \mathbf{p}')}{1 + \left(\frac{\mathbf{p} - \mathbf{p}'}{\Lambda} \right)^2} . \tag{2.41}$$

In a consistent description, the distribution function would not take the form $f(\mathbf{r}, \mathbf{p}) = \Theta(p_F - p)$, but would instead be expressed as a sum of δ-functions

$$f(\mathbf{r}, \mathbf{p}) = \frac{(2\pi)^3}{g} \frac{1}{N_{\mathrm{test}}} \sum_{i=1}^{NN_{\mathrm{test}}} \delta(\mathbf{p} - \mathbf{p}_i) \delta(\mathbf{r} - \mathbf{r}_i) . \tag{2.42}$$

This form of the distribution function is at first glance convenient as the integral over the momentum can be analytically solved with little effort

$$U_{\mathrm{MD}} = \frac{2C}{\rho_0} \frac{1}{N_{\mathrm{test}}} \sum_{i=1}^{NN_{\mathrm{test}}} \frac{\delta(\mathbf{r} - \mathbf{r}_i)}{1 + \left(\frac{\mathbf{p} - \mathbf{p}_i}{\Lambda} \right)^2} . \tag{2.43}$$

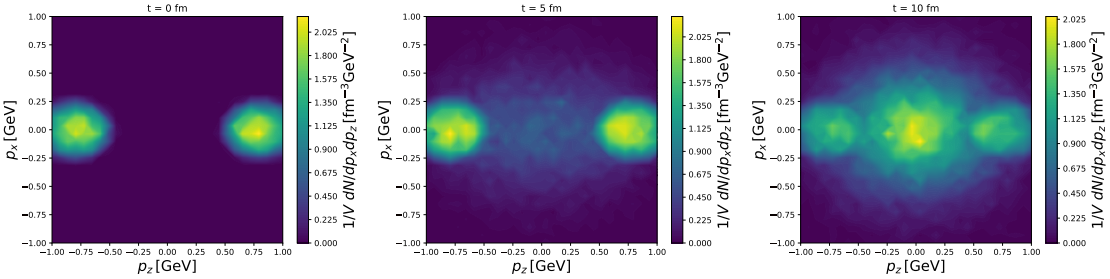

Abbildung 2.9: Distribution of test particles in momentum space at different times during a head-on gold-gold collision at $E_{\mathrm{kin}} = 1.23A\,\mathrm{GeV}$. The distribution is calculated for a central cell in configuration space, and is integrated over p_y.

However, the integral is in this case replaced by a sum that is numerically expensive to evaluate when many test particles are involved. It is important to note that the single-particle potential needs to be evaluated for each test particle at each time step and each time the sum over all surrounding particles needs to be calculated.

In this section, we will examine the differences in the single-particle potential between the cold nuclear matter assumption and the evaluation of the full sum. The comparison is done in a scenario similar to the early stage of a heavy-ion collision. It was suggested by Welke et al. (see Figure 6 in [148]) to consider a situation where two nuclei overlap in configuration space, but the nucleons from the two nuclei are distributed in distinct spheres in momentum space. This is the case in a very early stage of the heavy-ion collision, before the interactions take place, with the system far from equilibrium. The spheres in momentum-space are due to Fermi momentum, and they are shifted because of the velocity of the entire nuclei.

Before investigating the consequences of this form for the distribution function, this picture is verified by looking at the momentum distribution at different times during a central gold–gold collision at SIS-18 energy, as shown in Figure 2.9. The time is defined such that the surfaces of the nuclei touch at $t = 0\,\mathrm{fm}$. At this time, two distinct regions in momentum space can be clearly identified. Figure 2.9 further illustrates the situation at $t = 5\,\mathrm{fm}$. At $t = 5\,\mathrm{fm}$, the nuclei overlap in configuration space. Until this stage of the evolution, the situation in momentum-space has not changed much. Equilibrium is certainly not reached, and distinct spheres in momentum space are still clearly visible. By $t = 10\,\mathrm{fm}$ most of the test particles have undergone a sufficient number of interactions and the momentum distribution is more concentrated on the central region.

Since the scenario proposed by Welke et al. is realistic in the early stages of a heavy-ion collision, we compare the cold nuclear matter ansatz with the full sum, given in Equation 2.43. To reduce numerical costs, only a single point in time is considered, and no full transport calculation is performed. For this purpose, test

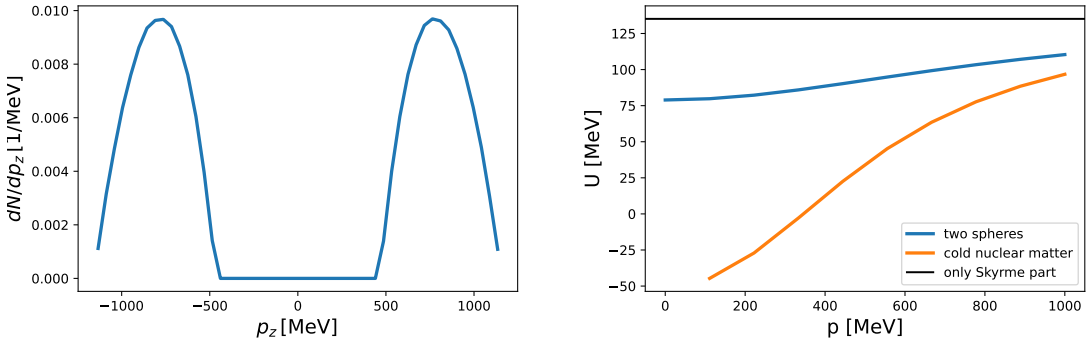

Abbildung 2.10: Longitudinal momentum distribution of nucleons in a gold-gold collision at $E_{\text{kin}} = 1.23A\,\text{GeV}$ on the left side. The distribution is created by sampling two Fermi spheres and boosting them according to the collision energy. The single particle potential in the same situation is calculated by evaluating the full sum in the line depicted by "two spheres", and in comparison with the cold nuclear matter assumption. The contribution to these curves from the momentum-independent terms of the Skyrme potential is given in black.

particles are sampled according to the distribution function, and the sum is evaluated. In practice, Fermi spheres are sampled for each nucleus and boosted according to the collision energy. The momentum distribution obtained this way is presented along with the corresponding single-particle potential in Figure 2.10. On the left-hand side, a typical distribution of the initial state of a heavy-ion collision is displayed, which can serve as a sanity check. Using the sampled test particles, the single-particle energy is evaluated by calculating the full sum and by applying the cold nuclear matter assumption. For comparison, the contribution from only the momentum-independent terms of the Skyrme potential to the single-particle potential is given by the black curve. With this curve as a baseline, one can clearly see that the contribution from the momentum-dependent part is changed significantly due to the cold nuclear matter assumption in this scenario. This difference calls for further investigation of the influence of the assumption, and the assumption should be dropped if possible.

2.1.3 Symmetry Potential

For a System of protons and neutrons, it is energetically favorable to have an equal number of protons and neutrons, when the electromagnetic interaction is disregarded. This is reflected in the binding energy of nuclei and is encapsulated in the symmetry term of the phenomenological Bethe-Weizsäcker formula [149], [150]. A large excess of neutrons is often present in astronomical objects, especially neutron

stars. The symmetry energy describes on how the energy depends on the asymmetry of protons and neutrons. Give the large asymmetry in many astrophysical applications, the symmetry energy is a research topic of great interest.

This thesis focuses on heavy-ion collisions, where the probed matter is more symmetric. However, due to the electromagnetic contribution to the binding energy, large stable nuclei exhibit an excess of neutrons compared to protons. Gold nuclei, for example, consist of 79 protons and 118 neutrons, which is nearly 50% more neutrons than protons. The asymmetry from the nuclei is also present in heavy-ion collisions. On one hand, this necessitates the inclusion of the symmetry potential in the calculation, but on the other hand, it provides and opportunity to study the symmetry energy in heavy-ion collisions.

Considering only protons and neutrons for the symmetry potential is not sufficient for dynamic calculations within the SMASH model, as many resonances and other hadrons are produced, which carry the asymmetry, at least temporarily.

To apply the symmetry potential to the extensive list of particles in SMASH, it is expressed in terms of the density corresponding to the third component of the isospin More precisely the density corresponding to the relative isospin I_3/I is used, which we define here as ρ_{I_3}. The third component of the isospin is $+1/2$ for up-quarks and $-1/2$ for down quarks. Other quarks do not carry any isospin charge. For hadrons, the third component of the isospin is the sum of the isospin of the valence quarks. Therefore, it can be calculated easily from the number of up and down quarks n_u and n_d

$$I_3 = \frac{1}{2}(n_u - n_d)\,. \tag{2.44}$$

The total isospin is $I = 1/2$ for both protons and neutrons. Compared to other formulations of the symmetry potential that express it in terms of the density of the I_3 charge instead of the relative isospin I_3/I, this introduces a factor of two in some cases, which must be taken into account when comparing with other models and results.

The symmetry potential is implemented in SMASH following the description given in [99], where it is expressed in terms of $\delta = (\rho_n - \rho_p)/\rho_B$ as

$$U_{\text{sym}} = \pm 2 S_{\text{pot}} \left(\frac{\rho_B}{\rho_0}\right) \delta\,. \tag{2.45}$$

In this expression, the positive sign is for neutrons and the negative sign is for protons. In SMASH the δ is generalized in terms of the density of the relative isospin $\rho_{I_3} = -\delta\rho_B$, so that the symmetry potential is written as

$$U_{\text{sym}} = \pm S_{\text{pot}} \left(\frac{\rho_{I_3}}{\rho_0}\right)\,. \tag{2.46}$$

Note that now the positive sign applies to protons and the negative sign to neutrons. To avoid the confusion about the sign, a more accurate description of the potential would omit the sign, as it enters from the charge of the particle of interest

$$U_{\text{sym}} = S_{\text{pot}} \left(\frac{\rho_{I_3}}{\rho_0} \right) . \tag{2.47}$$

The contribution from the symmetry potential to the single-particle energy of a particle with given relative isospin is then UI_3/I which is consistent with the description of the Skyrme potential, where anti-baryons experience the force with opposite sign compared to baryons. In the current version of SMASH, the potential acts only on baryons. For the symmetry potential, this is not consistent because mesons such as π^+ and π^- contribute to the isospin density and should consistently experience the symmetry potential as well.

The propagation of test particles in the presence of the symmetry potential follows the same equations of motion as for the Skyrme potential Following the same prescription, the time derivative of the kinetic momentum of a test particle is given by

$$\dot{\mathbf{\Pi}}_i = \frac{I_3}{I} \frac{\partial U_{\text{sym}}}{\partial \rho_{I_3}} \left[-(\nabla_r j^0_{I_3} + \partial_t \mathbf{j}_{I_3}) + \frac{\mathbf{\Pi}_i}{\Pi^0_i} \times (\nabla_r \times \mathbf{j}_{I_3}) \right] . \tag{2.48}$$

This equation assumes that the symmetry potential is the zeroth component of a vector potential in the local rest-frame. However, this is not fully consistent with the expression for Usym, which transforms as a scalar, since ρI_3 refers to the density in the local rest-frame. Another caveat is that both the Skyrme and the symmetry potential are evaluated in the local rest-frame and then boosted to the calculation frame for the equations of motion. However, these rest frames are different, as they correspond to different charges. For a consistent description, the potentials must be evaluated in the same frame.

There is room to extend the symmetry potential. In a study aimed at extracting the symmetry energy from pion yields and ratios from the SπRIT experiment [152], an additional term was introduced to account for a non-trivial dependence on the baryon density

$$S(\rho_B) \left(\frac{\rho_{I_3}}{\rho_B} \right)^2 , \tag{2.49}$$

where the function $S(\rho_B)$ is given by

$$S(\rho_B) = 12.3\,\text{MeV} \times \left(\frac{\rho_B}{\rho_0} \right)^{2/3} + 20\,\text{MeV} \times \left(\frac{\rho_B}{\rho_0} \right)^{\gamma} . \tag{2.50}$$

Here, γ is a free parameter that controls the strength of the baryon density dependence of the symmetry potential. The additional term is not applied in the results

presented in this thesis, but the influence of this term can be studied in further work.

In this work, the symmetry potential is considered to be independent of the momentum. However, introducing a momentum dependence to the symmetry potential is an interesting extension of the model. It can be included in a BUU calculation in the form that is suggested in [153].

2.1.4 Electromagnetic Potentials

Heavy-ion collisions are performed with the intent to study the strong interaction under extreme conditions. The electromagnetic interaction is, in this endeavor, not the main interest and plays a weaker role in the dynamics of a heavy-ion collision than the strong interaction. However, at relatively low collision energies, Coulomb repulsion has a significant impact on various observables. In Section 4.1, a calculation of the elliptic flow coefficient including the Coulomb potential is compared to one in which it is neglected.

The electromagnetic interaction has a longer range compared to the strong interaction. This long range makes it more challenging to treat numerically in transport calculations, as the equations of motion cannot be formulated solely in terms of the local density, current, and their derivatives, as is done for the other potentials described above.

The electromagnetic potentials implemented in SMASH do not fully account for electrodynamics, but rather incorporate only its basic features. A rigorous description of electrodynamics would certainly be beneficial, but a simplified version is justified, because the strong interaction remains the most important driver for the dynamics of the system.

The force experienced by test particles due to electrodynamics is given by the Lorentz force. To evaluate this force, the electric and magnetic fields must be computed. The calculation of the fields is simplified in the model by assuming all currents to be stationary. Under this assumption, the electric field is obtained from the Poisson law in integral form and the magnetic field is computed using the Biot-Savart law

$$\begin{aligned} \mathbf{E}(\mathbf{r}) &= -\nabla\phi(\mathbf{r}) = -\nabla \int dV' \frac{\rho(\mathbf{r}')}{|\mathbf{r}-\mathbf{r}'|} = \int dV' \frac{\rho(\mathbf{r}')(\mathbf{r}-\mathbf{r}')}{|\mathbf{r}-\mathbf{r}'|^3} \\ \mathbf{B}(\mathbf{r}) &= \nabla \times \mathbf{A}(\mathbf{r}) = \nabla \times \int dV' \frac{\mathbf{j}(\mathbf{r}')}{|\mathbf{r}-\mathbf{r}'|} = \int dV' \mathbf{j}(\mathbf{r}') \times \frac{\mathbf{r}-\mathbf{r}'}{|\mathbf{r}-\mathbf{r}'|^3} \,. \end{aligned} \tag{2.51}$$

The current and density is given on a rectangular lattice with cell centers $\mathbf{r}_i$. See Section 2.1.5 for details on the density calculation. The strategy is to evaluate the electric and magnetic fields on the lattice points, and to interpolate the fields to the

position of each test particle of interest. Currently, only a zeroth order interpolation is performed, but an extension to higher orders is possible. The electric and magnetic fields are computed by expressing the integrals as sums over the discretized volume, where the current and density are assumed to be uniform within each small lattice cell. The integrals then simplify to

$$\begin{aligned} \mathbf{E}(\mathbf{r}_j) &= \sum_{i \neq j} \frac{\rho(\mathbf{r}_i)(\mathbf{r}_j - \mathbf{r}_i)}{|\mathbf{r}_j - \mathbf{r}_i|^3} \Delta V \\ \mathbf{B}(\mathbf{r}_j) &= \sum_{i \neq j} \mathbf{j}(\mathbf{r}_i) \times \frac{\mathbf{r}_j - \mathbf{r}_i}{|\mathbf{r}_j - \mathbf{r}_i|^3} \Delta V \,, \end{aligned} \tag{2.52}$$

where the sum excludes the contribution from the lattice cell where the field is to be calculated. The contribution from this cell vanishes due to symmetry, as we assume uniform current and density within the cell.

Evaluating the sum for electric and magnetic field for each lattice point is numerically expensive because it requires iterating all lattice points for each cell in which the fields are calculated. To reduce computational cost, the sum can be restricted to a subset of the lattice points that are within a defined proximity to the point of interest. A user-defined size determines a rectangular sublattice, limiting the iteration to nearby points. One needs to verify the stability of results when cutting the integral however, because, even though the integrands decrease with distance, the contribution from larger distances can still be significant due to the large number of contributing cells. In practice, the contribution from distant points is typically small, as the density in a heavy-ion collision vanishes at large distances in the finite system.

Finally, the Lorentz force can be evaluated and taken into account for the propagation

$$\mathbf{F} = q(\mathbf{E} + \mathbf{v} \times \mathbf{B}) \,. \tag{2.53}$$

Figure 2.11 illustrates the electric and magnetic fields in the initial state of a heavy-ion collision, before the nuclei touch. The electric field is represented by blue arrows, while the magnetic field is shown by red arrows. The basic features of the fields are correctly captured: the electric field points away from the positively charged nuclei, and the magnetic field forms closed circular loops around the nuclei, as expected for a stationary current. However, there are noticeable shortcomings in this simplified version of the Coulomb potential. Specifically, the transformation behavior with respect to the boost is incorrect. The field should be stronger in the transverse direction, but in this case, it is enhanced in the longitudinal direction due to the contraction of the nuclei.

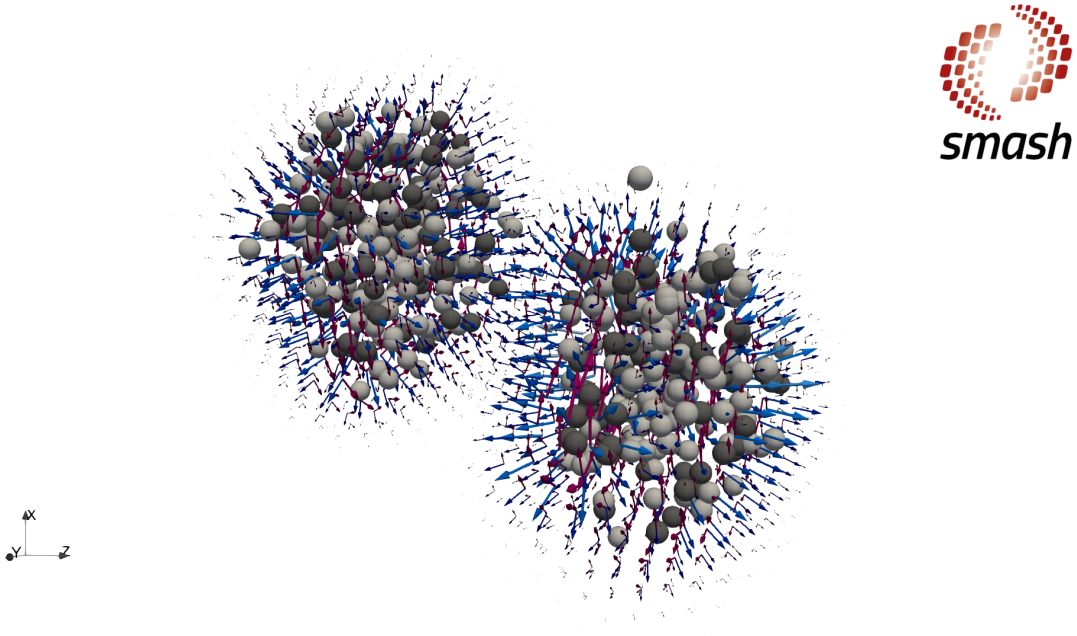

Abbildung 2.11: Illustration of the electric and magnetic fields in the initial state of a heavy-ion collision. The electric field is represented by blue arrows, and the magnetic field by red arrows. The fields are scaled differently for better visibility, and the calculation uses only a single test particle per real particle, as high precision is not required for this visualization [134]..

2.1.5 Density Calculation

All potentials discussed in the previous sections are expressed in terms of particle densities. Consequently, it is crucial for the model to have a stable calculation of these densities. Let us recall the test particle ansatz (see Eq. 2.25), that is used to connect the Boltzmann equation with the equations of motion of test particles

$$f_j(\mathbf{r},\mathbf{p},t) = \frac{1}{N_{\text{test}}}\sum_i \delta(\mathbf{r}-\mathbf{r}_i(t))\frac{(2\pi)^3}{g}\delta(\mathbf{p}-\mathbf{p}_i(t))\,. \tag{2.54}$$

Here, g is the degenracy factor for a given particle species j. This ansatz leads to a solution of the Boltzmann equation in the limit of infinitely many test particles. Since the number of test particles can, in practice, never be infinite, the density given by $\int \frac{d^3pg}{(2\pi)^3} f(\mathbf{r},\mathbf{p}) = \frac{1}{N_{\text{test}}}\sum_i \delta(\mathbf{r}-\mathbf{r}_i)$ is zero everywhere except at the finite set of positions where test particles are located. At these positions the density becomes singular. To obtain smooth, well-defined densities suitable for numerical simulations, a modification is necessary. In the SMASH model, this is achieved by applying a smearing kernel $K(\mathbf{r})$ to replace the Dirac delta function $\delta(\mathbf{r}-\mathbf{r}_i)$

$$f(\mathbf{r},\mathbf{p},t)_j = \frac{1}{N_{\text{test}}}\sum_i K(\mathbf{r}-\mathbf{r}_i(t))\frac{(2\pi)^3}{g}\delta(\mathbf{p}-\mathbf{p}_i(t))\,. \tag{2.55}$$

Different forms for the smearing kernel are possible provided it is normalized such that $\int d^3r K(\mathbf{r}) = 1$. The smearing kernel used throughout this work is a Lorentz-contracted Gaussian, as described in [154]

$$K(\mathbf{r}) = \frac{\gamma}{\sqrt{2\pi\sigma^2}^3}\exp\left(-\frac{\mathbf{r}^2+(\mathbf{r}\cdot\mathbf{u})^2}{2\sigma^2}\right)\,, \tag{2.56}$$

where $\mathbf{u}$ denotes the spatial components of the four-velocity. The width σ of the Gaussian is a technical parameter, and determining its optimal value is not straightforward. For smaller values of σ, the smearing kernel approaches a δ-distribution, meaning that a smaller width brings the kernel closer to the original ansatz. However, a larger width results in more test particles contributing to the density at a given position, yielding a smoother distribution. Another important consideration when choosing σ is that large gradients may not be accurately represented with too wide a Gaussian. Two examples are shown in Figure 2.12, where slices of a gold nucleus at rest are depicted for the cases of 100 and 1000 test particles. We compare a Gaussian smearing width of $\sigma = 1\,\text{fm}$ to $\sigma = 0.5\,\text{fm}$. In the case with 100 test particles, the orange curve for $\sigma = 1\,\text{fm}$ is more stable whereas the blue curve, representing the calculation with $\sigma = 0.5\,\text{fm}$, fluctuates more. Compared to the Woods-Saxon distribution from which the test particles are sampled, the density

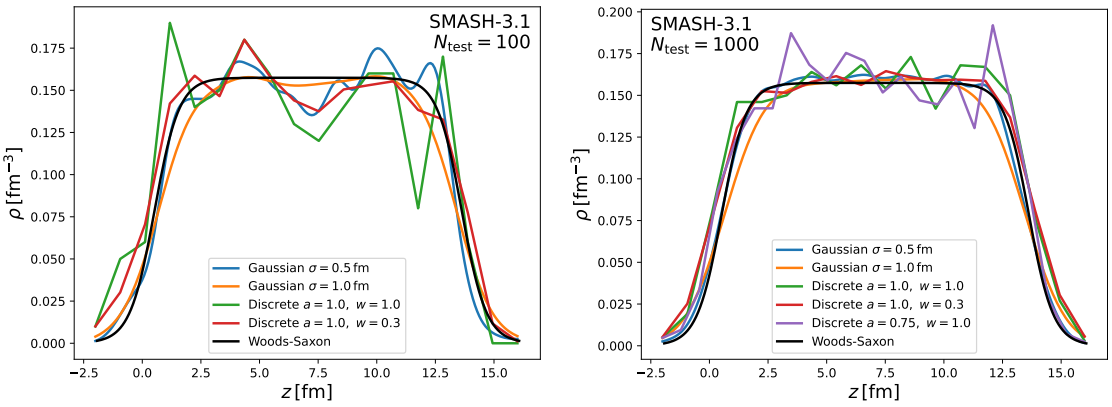

Abbildung 2.12: Baryon density in a slice through a gold nucleus at rest. The density is calculated using covariant Gaussian smearing with different widths and discrete smearing with varying cell sizes and weightings. On the left, a calculation using 100 test particles is shown, while on the right, 1000 test particles are used. The Woods-Saxon distribution is the distribution originally used to sample the nucleons.

close to the center of the nucleus is well reproduced for the larger width. Towards the edges of the nucleus, we observe that the $\sigma = 1\,\text{fm}$ curve falls off slower, as the gradient at the edge of the nucleus cannot be reproduced by a sum of wider Gaussian distributions. For $\sigma = 0.5\,\text{fm}$, the gradient is better reproduced, but the curve still exhibits fluctuations in this region..

For 1000 test particles, the $\sigma = 1\,\text{fm}$ curve barely changes compared to the case with 100 test particles. While the $\sigma = 0.5\,\text{fm}$ curve improves with more test particles, visible fluctuations remain. It is important to note that 1000 test particles per real particle is a large number, making it computationally very expensive for dynamic simulations.

Figure 2.12 also includes curves calculated using discrete smearing. In this approach, test particles are binned into a spatial grid with cell length a. A more general version of this method is also available for density calculations in SMASH. Typically, the contribution to the density is assigned entirely to the cell containing the test particle. However, an alternative approach allows a fraction of the charge to be distributed to neighboring cells. This distribution is controlled by a weight factor, w, which defines how much charge is allocated to the cell of the test particle. The remaining charge is then evenly distributed among the 6 adjacent cells. With $w = 1$, conventional binning is recovered. Figure 2.12 shows curves for both $w = 1$ and $w = 0.3$. For the conventional curve with $w = 1$ we observe that the curves fluctuate tremendously for 100 test particles. Reducing the weight, and, in the process, distributing the charge over multiple cells, we observe smaller fluctuations in the density

as expected.

For the calculations with 1000 test particles, we observe a similar behavior to the case with the Gaussian smearing kernel at larger widths. The density profile is relatively smooth when using $w = 0.3$, but the gradient at the nucleus edge is insufficient to accurately reproduce the Woods-Saxon distribution. In the right hand plot of Figure 2.12, a calculation with a smaller cell size of $a = 0.75\,\mathrm{fm}$ is additionally presented. This curve illustrates that even with 1000 test particles, a reasonable density profile cannot be obtained with smaller cell sizes, while the Gaussian smearing with a smaller width provides a better description of the Woods-Saxon distribution. The default form for $K(\mathbf{r})$ in SMASH is the Gaussian smearing with width of $\sigma = 1\,\mathrm{fm}$, and this value will be used for all calculations in this work unless otherwise specified.

The Eckart current density for a given charge can be obtained by summing the distribution function across all contributing particle species

$$j^\mu = \sum_j g_j \int \frac{d^3p}{(2\pi)^3} \frac{p^\mu}{p^0} q_j f_j(\mathbf{r}, \mathbf{p}, t)\,, \tag{2.57}$$

where q_j is the charge carried by a particle of species j. By applying the test particle ansatz, the integral over momentum space can be evaluated, simplifying the expression to

$$j^\mu = \frac{1}{N_{\mathrm{test}}} \sum_i q_i \frac{p^\mu}{p^0} K(\mathbf{r} - \mathbf{r}_i) \tag{2.58}$$

where we have implicitly changed the numbering of the test particles such that the sum runs over all test particles from all particle species, and q_i is the charge of the species to which test particle i belongs.

Gradients and time derivatives of the density can then be obtained using finite difference, or, in the case of Gaussian smearing directly by summing over the gradient of the smearing kernel. In many situations, the density in the local rest-frame, defined by vanishing currents $j^i = 0$, is required. As j^μ are components of a Lorentz-vector, it can be calculated in any frame using $\rho^2 = j_\mu j^\mu$. A complication arises, however, when positive and negative charges predominantly flow in opposite direction. In such case, the spacial components add up whereas the zero-component of the current cancels. This can lead to j^μ becoming a spacelike vector, making it impossible to evaluate the density using the relation $\rho = \sqrt{(j^0)^2 - \mathbf{j}^2}$. The issue arises because the Eckart rest-frame is not well-defined in this scenario. In the model, the density is instead split in positive and negative contributions of which the rest-frame densities ρ_{pos} and ρ_{neg} can individually be evaluated, and the density is finally calculated via $\rho = \rho_{\mathrm{pos}} - \rho_{\mathrm{neg}}$. This approach allows for a real-valued density, but the rest frames for positive and negative charges may differ significantly, meaning that simply adding the rest-frame densities is not a complete solution. Fortunately, this issue typically

does not arise in practice, as test particles usually move collectively, ensuring that the current remains timelike.

2.1.6 Brief Comparison to Quantum Molecular Dynamics

SMASH is a BUU-type model, and the implementation of nuclear potentials along with the resulting equations of motion from the test particle ansatz have been discussed in detail above. An alternative approach for modeling off-equilibrium dynamics in heavy-ion collisions is Quantum Molecular Dynamics (QMD) [155]. While QMD is not used in this thesis, it is widely employed in studies of the equation of state (EoS), and thus, a brief description of the model is provided here.

An overview of various implementations of Quantum Molecular Dynamics can be found in [156]. Unlike the test particle approach used in BUU, QMD assumes that the Wigner density — a quantum generalization of the distribution function — of each individual particle is represented by a Gaussian wave packet

$$f_i(\mathbf{r},\mathbf{p},t) = \frac{1}{\pi^3}\exp\left[-\frac{2}{L}(\mathbf{r}-\mathbf{r}_i)^2\right]\exp\left[-\frac{L}{2}(\mathbf{p}-\mathbf{p}_i)^2\right]. \tag{2.59}$$

Here, L defines the width of the wave packet, with its center in configuration space given by $\mathbf{r}_i$ and in momentum space by $\mathbf{p}_i$. This form is constructed to satisfy the uncertainty principle. A generalized version of the Ritz variational principle is then used to derive the equations of motion for the centroids $\mathbf{r}_i$ and $\mathbf{p}_i$ [155]. Based on the assumption for the Wigner density, the centroids propagate according to the classical equations of motion

$$\dot{r}_i = \frac{\partial\langle H\rangle}{\partial p_i} \tag{2.60}$$

$$\dot{p}_i = -\frac{\partial\langle H\rangle}{\partial r_i}. \tag{2.61}$$

The expectation value of the Hamiltonian $\langle H\rangle$ is written in terms of the two-particle potential $V(\mathbf{r}_i,\mathbf{r}_j,\mathbf{p}_i,\mathbf{p}_j)$ as

$$\langle H\rangle = \sum_i \frac{\mathbf{p}_i^2}{2m_i} + \sum_i\sum_{j>i}\int d^3p\, d^3p'\, d^3r\, d^3r'\, f_i(\mathbf{r},\mathbf{p},t) f_j(\mathbf{r}',\mathbf{p}',t) V(\mathbf{r},\mathbf{r}',\mathbf{p},\mathbf{p}'). \tag{2.62}$$

Here, m_i is the mass of particle i. Without providing further details in this thesis, the integral is usually written by introducing an interaction density. By expressing the Hamiltonian in terms of the two-particle potential, information on correlations between individual particles can be studied within QMD calculations. This can be of interest, especially for studying light nuclei formation.

Since the equations of motion in a BUU model also follow classical equations of motions (disregarding relativistic terms), the question arises, what the main differences in the technical realization of the models are. The most important difference is between test particles in BUU and wave packets in QMD. The wave packet in a QMD calculation corresponds to a real particle, while the test particle in BUU technically represents the continuous distribution function that is evolved. BUU calculations require a large number of test particles, and the interactions are expressed in terms of densities, as discussed earlier. In contrast, QMD calculations consider the interaction between individual particles, which can be seen in the sum for the potential part of the Hamiltonian.

2.2 Collision Term

Up to this point, we have primarily focused on nuclear potentials, which play a key role in transport calculations. We emphasize their importance in this work, as they provide essential information about the equation of state, which is incorporated into the model through these potentials. However, the collision term also plays a crucial role in the Boltzmann equation, as it accounts for all scatterings between particles. In many applications, transport models are employed in cascade mode, where the potential interactions are neglected, and particles propagate freely between scatterings. In this regime, the dynamics are governed solely by collisions.

We will present some calculations performed in cascade mode in Chapter 6, but also the investigations aiming to learn about the nuclear potentials heavily rely on the collision term. Before iterating through the different interaction types and discussing how they are realized in the model, let us have a look at how frequently they occur in central heavy-ion collisions.

Figure 2.13 illustrates the contribution of different reaction types to the total number of interactions at two distinct collision energies. At lower collision energies, we observe that elastic binary scatterings are by far the most frequent reactions, and, therefore, play an important role for the dynamics of the system. Resonance formation in inelastic $2 \rightarrow 1$ and $2 \rightarrow 2$ processes with subsequent resonance decays are most important for the particle production in this case, but are slightly less frequent. The heavy-ion collisions at the higher energy, shown on the right side of Figure 2.13, correspond to those studied in the Beam Energy Scan program at RHIC

As expected, at higher collision energies, we observe a larger number of inelastic interactions compared to elastic scatterings. An key difference to lower energies is the onset of string excitations, that are discussed in detail in Section 2.2.4. Although the reaction rate for string excitations is relatively low, they make a significant contribution to particle production.

Having discussed the relevance of various interaction types in different collision

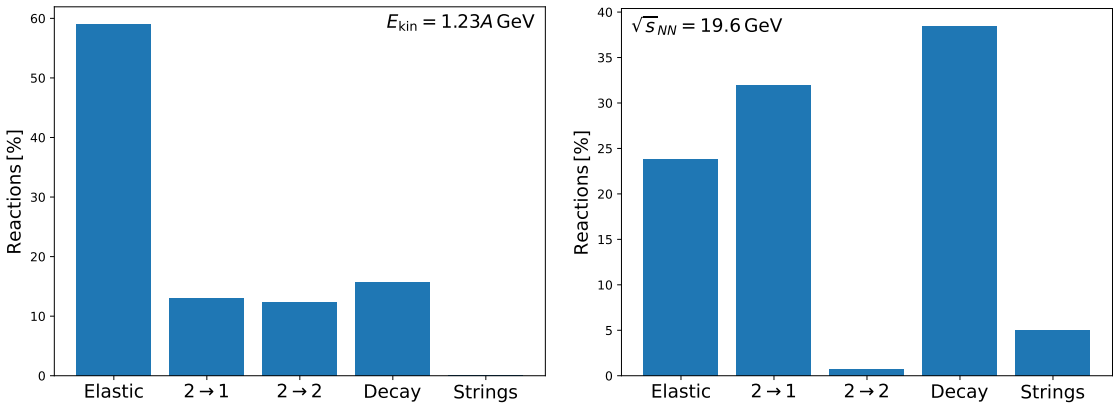

Abbildung 2.13: Contribution of different reaction types to the total number of interactions in head-on gold-gold collisions at $E_{\mathrm{kin}} = 1.23A\,\mathrm{GeV}$ (left) and at $\sqrt{s_{NN}} = 19.6\,\mathrm{GeV}$ (right) in percent. Shown are (from left to right) elastic binary scatterings, two-to-one resonance formations, inelastic two-to-two scatterings, resonance decays, and string excitations. The calculation was performed using SMASH version 3.1.

systems, we now turn to a more detailed examination of the individual mechanisms, beginning with elastic scatterings."

2.2.1 Elastic Scattering

Binary elastic scattering involves two incoming particles that collide and exchange momentum. In this process, the species and masses of the particles remain unchanged. To begin, we will discuss the kinematics of elastic scattering before addressing the cross section. Let us consider two particle, A and B. The kinematics are most easily described in the two-particle center-of-mass frame, where the spatial components of the incoming momentum four-vectors are $\mathbf{p}_A = \mathbf{p}$ and $\mathbf{p}_B = -\mathbf{p}$. Considering momentum conservation, we find that the total momentum also vanishes in the final state $\mathbf{p}'_A = \mathbf{p}' = -\mathbf{p}'_B$. The center of mass energy is also conserved, which yields another equation

$$\sqrt{m_A^2 + p^2} + \sqrt{m_B^2 + p^2} = \sqrt{m_A^2 + p'^2} + \sqrt{m_B^2 + p'^2}\,, \tag{2.63}$$

which can only be satisfied if $p^2 = p'^2$. Hence, the absolute value of the momentum in the center of mass frame before and after the scattering is equal, but the orientation may differ. The direction of the outgoing momenta can, in principle, be determined using angular momentum conservation. But since the contribution from

spin to the angular momentum is not kept track of throughout the calculation, angular momentum conservation cannot be achieved in individual interactions in the model. Nevertheless, global angular momentum is conserved on average, provided the number of test particles is sufficiently large [157].

Since the remaining degrees of freedom cannot be determined through angular momentum conservation, we use a phenomenological parametrization of the angular distribution [158]. This parametrization is applied to determine the polar angle, while the azimuthal angle is sampled from a uniform distribution, reflecting the rotational invariance of the system around the **p**-axis.

Angular distributions are provided only for nucleon-nucleon interactions and for low momenta in [158]. For momenta exceeding 2, GeV, we switch to a parametrization based on STAR data [159]. Since elastic collisions can occur between all particle species, this parametrization is applied to all elastic interactions.

After evaluating the final momenta in the center of mass frame, a Lorentz-transformation to the frame in which the rest of the calculation is carried out is necessary. The velocity of the center of mass frame is obtained from the four-momenta p_A^μ and p_B^μ of the incoming particles as

$$v_{\mathrm{cm}}^i = \frac{p_{\mathrm{cm}}^i}{p_{\mathrm{cm}}^0} \quad \text{with} \quad p_{\mathrm{cm}}^\mu = p_A^\mu + p_B^\mu \,, \tag{2.64}$$

where the above quantities are expressed in the calculation frame, and $\mathbf{v}_{\mathrm{cm}}$ is the velocity of the two-particle center-of-mass frame. A boost from the two-particle center-of-mass frame to the calculation frame is carried out with the velocity $-\mathbf{v}_{\mathrm{cm}}$.

The final ingredient for elastic interactions is the cross section. It is important to note that not all processes in which the ingoing and outgoing particle species are identical are treated using this mechanism. As will be discussed in more detail in Section 2.2.2, a resonance X can be formed from the incoming particles A and B, which then decays back into exactly A and B

$$A + B \to X \to A + B \,. \tag{2.65}$$

Such a process would be considered elastic in the experiment, as only the final state particles can be observed. Therefore, elastic cross sections from experimental measurements are therefore not directly implemented in the model. Instead, the resonance contribution to the elastic cross section is subtracted first. In this way parametrized cross sections are implemented for $p + p$, $n + p$, $p + \bar{p}$, with the parametrization for the latter taken from [115]. Additional parametrizations are available for $p + \pi^+$ and $p + \pi^-$. These are also applied to the π^0, for which the cross section is assumed to be the average of π^+ and π^-. Cross sections are also available for $p + K^+$ and $p + K^-$, where the parametrizations are adopted from [141]. Assuming isospin symmetry, the cross sections for K^+ are also applied for the K^0, and the K^- cross sections applied

for the $\bar{K}^0$. Additionally, parametrizations based on experimental data are used for deuteron-nucleon scattering and deuteron-pion scattering.

Elastic cross sections for all other processes are calculated using the additive quark model (AQM) as described in [115]. For processes where experimental data is unavailable, the cross sections are mapped to known processes. Specifically, all baryon-baryon scatterings are mapped to proton-proton scatterings, and meson-baryon interactions are mapped to $\pi^+ + p$ scatterings. Meson-meson interactions are similarly mapped to $p + \pi^+$ scatterings, with an additional factor of $2/3$ introduced to account for the smaller number of quarks in a meson compared to a proton. The cross section for more exotic processes is then given by the base cross section, multiplied by a factor of $(1 - 0.4x_1^s)(1 - 0.4x_2^s)$, where x_1^s and x_2^s represent the fractions of strange quarks in the two colliding hadrons, respectively.

At low center-of-mass energies, most hadronic cross sections exhibit non-trivial resonance structures. These structures are specific to the interacting hadron pairs and are not desirable in the AQM cross sections for other species. Therefore, a parametrization is used that captures the general trend of the base cross section while excluding the fine resonant structures.

2.2.2 Resonance Formation and Decay

Resonance formation and subsequent decay is the main source for particle production at low collision energies, as we have already seen in Figure 2.2.2. In this section, we will focus on the details of $2 \to 1$ resonance formation, the properties of resonances, and their decay processes. For baryon-dominated systems, resonance formation in $2 \to 2$ scatterings plays a crucial role and will be discussed in Section 2.2.3.

We begin with the spectral function, where we assume a vacuum Breit-Wigner distribution with a mass-dependent width for all resonances

$$\mathcal{A}(m) = \frac{2\mathcal{N}}{\pi} \frac{m^2 \Gamma(m)}{\left(m^2 - M_0^2\right)^2 + m^2 \Gamma(m)^2} \,. \tag{2.66}$$

Here, $\mathcal{N}$ is a normalization factor, m is the mass of the resonance, and M_0 is the mass at the resonance pole. The total decay width, $\Gamma(m)$, is mass-dependent. Together with M_0, the width at the pole, $\Gamma(M_0)$, is taken from the Particle Data Group [127]. The total decay width of a resonance R is given by the sum of the partial widths for the different reaction channels

$$\Gamma(m) = \sum_{a,b} \Gamma_{R \to ab}(m) \,. \tag{2.67}$$

As indicated by the mass dependence in the function argument, the partial widths $\Gamma_{R \to ab}(m)$ are functions of the resonance mass, following the prescription provided

in [160]. The calculation of the mass-dependent width requires the partial width of the resonance at the pole $\Gamma^0_{R\to ab}$, which is the total width multiplied by the partial width at the pole. Given this value as an input parameter, the mass-dependent partial width for the decay channel $R \to ab$ is

$$\Gamma_{R\to ab} = \Gamma^0_{R\to ab} \frac{\rho_{ab}(m)}{\rho_{ab}(M_0)}\,, \tag{2.68}$$

where

$$\rho_{ab}(m) = \int dm_a dm_b \mathcal{A}_a(m_a)\mathcal{A}_b(m_b)\frac{p_f}{m} B_L^2(p_f R)\mathcal{F}_{ab}^2(m) \tag{2.69}$$

incorporates more detailed information on the specific decay process. The integration is performed over the spectral functions $\mathcal{A}_a$ and $\mathcal{A}_b$ of the decay products, as the mass of the decay products determines the amount of kinetic energy that the decay products obtain as momentum in the final state $p_f = p_f(m, m_a, m_b)$ (see Eq. 2.72). The factor p_f increases the decay width when a larger phase space is available for decay products. $B_L(p_f R)$ are the Blatt-Weisskopf functions [161] that incorporate information on the angular momentum L of the decay and $\mathcal{F}_{ab}$ is a form factor that is applied for unstable decay products. More detailed information on the spectral function in the SMASH model can be found in the main SMASH publication [128].

For a resonance with a given decay width, one can compute the lifetime as the inverse

$$\tau = \frac{1}{\Gamma}\,. \tag{2.70}$$

The time evolution in SMASH is based on time steps. In the beginning of each time step, every resonance is assigned a decay time, which is sampled from the exponential decay law $P(\tau_{\text{decay}}) \propto \exp(-\Gamma\tau_{\text{decay}})$ in the resonance rest frame, and boosted back to the frame in which the propagation is performed. Once the decay time is found, the specific channel is chosen based on the partial widths such that each decay channel has the probability $\Gamma_{R\to ab}/\Gamma$.

Decays are performed in the rest-frame of the resonance. With masses m_a and m_b of the decay products sampled from their spectral functions, one can obtain the momentum p_f of the daughter particles, as mentioned above, from energy conservation. Starting from

$$m = \sqrt{s} = \sqrt{m_a^2 + p_f^2} + \sqrt{m_b^2 + p_f^2}\,, \tag{2.71}$$

which can be solved for p_f, leading to

$$p_f^2 = \frac{[m^2 - (m_a + m_b)^2][m^2 - (m_a - m_b)^2]}{4m^2}\,. \tag{2.72}$$

In the rest frame of the resonance, the direction of $\mathbf{p}_f$ must be determined but, since there is no preferred axis in the system (as spin degrees of freedom are not kept track

of in the model), an angle has to be chosen isotropically. Note that the angle is not isotropic in the calculation frame since angles are modified by a Lorentz boost. In the calculation frame, daughter particles from the decay of a faster resonance tend to become more collimated.

Resonance formation in $2 \to 1$ processes plays an important role for the dynamics in collisions at all collision energies as we have observed in Figure 2.13.

Like other processes, resonance formation is most conveniently described in the two-particle center-of-mass frame, which is the rest frame of the resonance in the final state, due to momentum conservation. In this frame, the incoming particles each have a given absolute momentum p_i with opposite directions (it can be calculated easily using Equation 2.72 replacing m with $\sqrt{s}$). The partial cross section for a process is then, based on [141], written as

$$\sigma_{ab\to R}(s) = \frac{2J_R+1}{(2J_a+1)(2J_b+1)} \mathcal{S}_{ab} \frac{2\pi^2}{p_i^2(s)} \Gamma_{ab\to R}(\sqrt{s}) \mathcal{A}_R(\sqrt{s}) \,, \tag{2.73}$$

where J_R, J_a and J_b are the spins of the resonance and the incoming particles, respectively. $\mathcal{S}_{ab}$ is a symmetry factor, which takes the value 2 if a and b are of the same particle species and 1 otherwise. $\mathcal{A}_R$ is the spectral function of the resonance to be formed and $\Gamma_{ab\to R}$ is the in-width. The in-width is similar to the resonance decay width (Eq. 2.68), but it differs in that, for unstable incoming particles a or b, their mass is fixed, and no integration over their spectral functions is necessary.

$$\Gamma_{ab\to R}(\sqrt{s}) = \Gamma^0_{R\to ab} \frac{p_i B_L^2(p_i R) \mathcal{F}_{ab}(\sqrt{s})}{\sqrt{s}\rho_{ab}(M_0)} \,. \tag{2.74}$$

The partial cross sections of all possible resonance formations are calculated and contribute to the total cross section (see Section 2.2.5).

Performing a resonance formation, the mass of the created resonance is directly given by the center of mass energy of the incoming particles and, as mentioned above, the resonance is at rest in the center of mass frame. The same boost as for elastic collisions is applied to determine the momentum of the resonance in the calculation frame.

2.2.3 Inelastic Binary Scattering

Inelastic binary scattering plays a crucial role in particle production in heavy-ion collisions, where only baryons are present in the initial state, as $2 \to 1$ processes are forbidden by baryon number conservation. We consider here the two cases $ab \to Rc$ and $ac \to R_1R_2$, so either a single or two resonances in the final state. The particles a and b in the initial state may also be unstable in both cases. Starting with the

case containing a single resonance in the final state, the cross section is given by

$$\sigma_{ab\to Rc}(s) = \frac{(2J_R+1)(2J_c+1)}{sp_i} \sum_I \left(C^I_{ab} C^I_{Rc}\right)^2 \frac{|\mathcal{M}|^2_{ab\to Rc}(s,I)}{16\pi} \int_{m_R^{\min}}^{\sqrt{s}-m_c} dm \mathcal{A}_R(m) p_f \tag{2.75}$$

where p_i and p_f are the momenta of the incoming and outgoing particles in the center of mass frame respectively. J_R and J_c are the spins of the outgoing particles and C^I_{ab} and C^I_{Rc} are Clebsch-Gordan coefficients, which encode how the states couple to the total isospin I. Since the mass of the resonance is not fully determined by the energy in the initial state, we integrate over all kinematically allowed masses. The minimum is the lowest mass, where the spectral function is non-zero, defined by the masses of the lightest decay products (see Section 2.2.2). The maximum is given by total available energy in the collision minus the mass of particle c, which is the minimum energy particle c can have. An important ingredient to the cross section is the matrix element $M_{ab\leftrightarrow Rc}$, for which we apply simple parametrizations. For the, at low energies very important, process $NN \to N\Delta$, the parametrization is reproducing a one-boson-exchange model [162]. A simpler, energy independent matrix element is used for all other implemented processes, which are $NN \to NN^*$, $NN \to N\Delta^*$, $NN \to \Delta\Delta$, $NN \to \Delta N^*$, and $NN \to \Delta\Delta^*$. The values for the matrix element of each process can be found in [128].

For performing a the process, one first requires the mass of the outgoing resonance. Consistently with the contribution of different resonance masses to the cross section (see last factor in Eq. 2.75), the mass of the resonance is sampled in the range $(m_R^{\min}, \sqrt{s} - m_c)$ weighted by $\mathcal{A}_R(m)p_f$. Once the mass of the resonance is determined, the momentum of the outgoing particles, p_f, is fixed. The remaining degrees of freedom are in the direction of the outgoing momenta, which must be sampled. As in the elastic case, the azimuthal angle is sampled from a uniform distribution due to symmetry. The polar angle, however, is sampled from an anisotropic angular distribution. Following [158] for the process $NN \to N\Delta$, the same angular distribution as for elastic nucleon-nucleon scattering is applied. For the processes $NN \to NN^*$ and $NN \to N\Delta^*$, a different parametrization is used. The parameters are in this case tuned to data from the HADES experiment [163]. All other inelastic $2 \to 2$ processes are performed isotropically.

Extending the cross section to account for two unstable particles in the final state, an integral over the spectral function of both final-state resonances needs to be evaluated

$$\begin{aligned}\sigma_{ab\to R_1R_2}(s) = \frac{(2J_{R_1}+1)(2J_{R_2}+1)}{sp_i} \sum_I \left(C^I_{ab} C^I_{R_1R_2}\right)^2 \frac{|\mathcal{M}|^2_{ab\leftrightarrow R_1R_2}(s,I)}{16\pi} \\ \times \int_{m_1^{\min}}^{\sqrt{s}-m_2^{\min}} dm_1 \mathcal{A}_1(m_1) \int_{m_2^{\min}}^{\sqrt{s}-m_1^{\min}} dm_2 \mathcal{A}_2(m_2) p_f(\sqrt{s}, m_1, m_2)\,.\end{aligned} \tag{2.76}$$

The resonance masses are, also in this case, weighted with the spectral functions times the corresponding outgoing momentum. Consistently, the masses m_1 and m_2 of the resonances R_1 and R_2 are sampled together, using rejection sampling, from the distribution

$$P(m_1, m_2) \propto \mathcal{A}_1(m_1)\mathcal{A}_2(m_2)p_f(\sqrt{s}, m_1, m_2)\,. \tag{2.77}$$

With fixed masses, the rest of the calculation is exactly the same as in the case with a single resonance in the final state.

In addition to the previously discussed inelastic binary interactions, the model also includes cross sections for strange particles. These processes describe interactions between nucleons and kaons, Δ-resonances and kaons, as well as hyperons and pions. In these cases, the angular distributions are isotropic, and the matrix elements can be found in [164], [165].

2.2.4 String Excitation and Fragmentation

Since there are no resonances with masses greater than $m \approx 2\,\text{GeV}$ in the model, the cross section for resonance formation diminishes as the center-of-mass energy of the interacting hadrons increases. This behavior is illustrated in the proton-pion cross section shown in Figure 2.14, which already includes contributions from a string model. The string model was introduced in SMASH to study baryon stopping in reference [32], on which this section is based.

In this context, 'strings' refer to color strings that form when a color-neutral object becomes highly excited. Due to confinement, the constituents of a color-neutral object cannot be separated. Instead, a color string is formed, connecting the quarks. As more energy is added to the system, the color string can store enough energy to create new quark-antiquark pairs. These pairs can then combine to form new color-neutral objects. This process, known as string fragmentation, is responsible for the creation of new hadrons from the color fields. Models of string fragmentation have been developed and are known to be highly successful in describing elementary processes, such as e^+e^- collisions, as well as small collision systems like $p + p$.

The calculation for the string excitation is split into hard and soft processes. The hard string processes are relevant for very high energetic binary interactions, as can be seen in figure 2.14, where perturbative QCD is applicable. For the description of the pQCD scatterings, the string excitation, and the string fragmentation, Pythia [10], [166] is used. The hard string process, where pQCD interactions are involved, is based on the p_T-ordered multiparton interaction (MPI) framework with initial and final state radiations [167]. Given that pQCD is not applicable at low momentum scale, the lower p_T threshold of those partonic interactions is chosen to be 1.5 GeV, and the pQCD cross section is computed accordingly. The hard string routine is described in more detail further below.

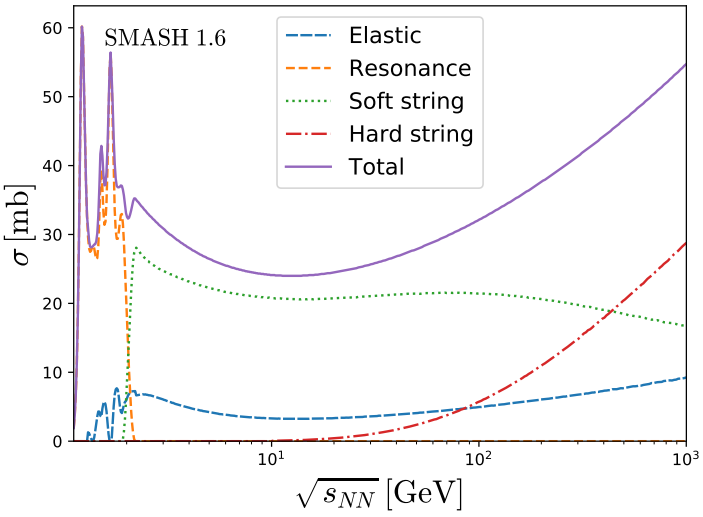

Abbildung 2.14: Cross section for a proton interacting with a negatively charged pion as a function of the center-of-mass energy of the colliding hadrons within SMASH. The total cross section is broken down into contributions from elastic collisions, resonance formations, soft string excitations, and hard string excitations via PYTHIA. Taken from [32].

In the transition region where the energy is too large to have cross sections via resonances, but too low to apply pQCD, a phenomenological model for the excitation of strings is implemented. In single diffractive, double diffractive, and non-diffractive processes, strings are excited in hadronic interactions. Using the calculated mass and momentum of the string as well as the flavor of the leading quarks, PYTHIA is employed only for the fragmentation of the string. Details of the string excitation at intermediate energies are given after a discussion of the cross section.

Cross Sections for String Processes

The total σ_{tot} and the elastic σ_{el} cross sections, which are shown for the example of p-π^- collisions in Figure 2.14, are parameterized to fit experimental data and are taken from [127] and [141], [168] respectively. The inelastic cross section σ_{inel} is the difference between the two

$$\sigma_{\text{inel}} = \sigma_{\text{tot}} - \sigma_{\text{el}} \,. \tag{2.78}$$

No other inelastic processes are implemented for high energies, so σ_{inel} is the sum of the string cross sections. For the process selection, cross sections for both the single σ_{SD} and double diffractive σ_{DD} processes are necessary. They are estimated in [169] and implemented in PYTHIA. From σ_{SD} and σ_{DD}, the non-diffractive cross section

σ_{ND} is derived

$$\sigma_{\mathrm{ND}} = \sigma_{\mathrm{inel}} - \sigma_{\mathrm{SD}} - \sigma_{\mathrm{DD}} \,. \tag{2.79}$$

The non-diffractive cross section includes the hard and soft non-diffractive processes. The cross section for hard non-diffractive processes is based on the pQCD cross section σ_{hard} from partonic interactions. It is given by

$$\sigma_{\mathrm{hard}} = \sum_{i,j,k} \int dx_1 \int dx_2 f_i(x_1) f_j(x_2)\, \sigma^k_{i,j}|_{\hat{p}_{T,\mathrm{min}}} \,, \tag{2.80}$$

where $\sigma^k_{i,j}|_{\hat{p}_{T,\mathrm{min}}}$ is the cross section for a subprocess k between two partonic flavors i and j with minimum transverse momentum transfer $\hat{p}_{T,\mathrm{min}}$, which is chosen to be 1.5 GeV. The parton distribution function $f_i(x)$ provides the average number of flavor i carrying the momentum fraction x of the incoming hadron. The NNPDF 2.3 parton distribution function with QED correction [170] is used for this purpose. The sum takes each possible combination of partons from each ingoing hadron into account.

This pQCD cross section can be larger than σ_{ND}, incorporating the information of multi-parton scattering. We take the multi-partion interaction (MPI) picture [171] and interpret the ratio $\sigma_{\mathrm{hard}}/\sigma_{\mathrm{ND}}$ to be the average number of partonic interactions involved in a hadronic interaction, rather than the probability to have a single hard non-diffractive interaction. In addition, the number of parton interactions is assumed to follow a Poisson distribution. The probability of having no hard interaction is calculated according to the Poissonian distribution as

$$P(0) = \exp\left(-\frac{\sigma_{\mathrm{hard}}}{\sigma_{\mathrm{ND}}}\right) \,. \tag{2.81}$$

In this case of no hard partonic scattering, the process is assumed to be soft non-diffractive, leading to a soft non-diffractive cross section of

$$\sigma_{\mathrm{ND,soft}} = \sigma_{\mathrm{ND}} \exp\left(-\frac{\sigma_{\mathrm{hard}}}{\sigma_{\mathrm{ND}}}\right) \,. \tag{2.82}$$

Finally, the cross section $\sigma_{\mathrm{ND,hard}}$ for the hard string process follows as

$$\sigma_{\mathrm{ND,hard}} = \sigma_{\mathrm{ND}} - \sigma_{\mathrm{ND,soft}} \,. \tag{2.83}$$

Since the pQCD cross sections can only be applied at sufficiently large energies, there is no contribution from hard non-diffractive processes below collision energies of 10 GeV. If the energy is smaller, all non-diffractive processes will be soft.

Due to the fact that Pythia 8 accepts only (anti-)nucleons and pions as incoming hadrons, it is necessary to extrapolate these processes to handle arbitrary

pairs of incoming hadrons. This is done by mapping hadronic species onto pions and nucleons and then rescaling cross sections based on the AQM. The cross section is then obtained in the same way as for elastic collisions but, of course, based on parametrizations of inelastic cross sections in this case.

Hard String Routine

Hard non-diffractive string excitations dominate the hadronic cross section at large center of mass energies. As mentioned in section 2.2.4, Pythia 8 accepts only a limited number of species as incoming hadrons, and it is necessary to extrapolate hard non-diffractive scattering handled by Pythia 8 to all other hadronic species. This is particularly crucial in high-energy heavy-ion collisions, where plenty of hadrons other than (anti-)nucleons and pions are produced in primary nucleon-nucleon collisions. To do this extrapolation, we rely on the assumption that the structure functions (or parton distribution functions) of all mesons and (anti-)baryons look similar to respectively those of pions and (anti-)nucleons once we swap the valence quark flavors.

Technically, this is achieved by mapping different hadron species to (anti-)nucleons and pions, where the quantum numbers of the original and mapped particle are as similar as possible. Before the produced strings are fragmented within the Pythia calculation, light (anti-)quarks are exchanged with quarks of the original flavor. The momenta of all particles are rescaled in order to conserve the energy of the system, since the constituent masses are affected by the flavor exchange. Due to annihilation processes, it is not always possible to find a quark with the flavor of the mapped quark. In this case, a gluon is split into a quark-antiquark pair with the flavor of the mapped quark or anti-quark.

Soft String Routine

Soft string excitations are the most abundant processes in the intermediate energy range, as can be seen in figure 2.14. As in UrQMD [115], [116], the excitation of a soft string can be performed according to one of three subprocesses, the single diffractive, the double diffractive, and the non-diffractive case, which is the most common case. All soft string processes rely on Pythia for the fragmentation of the strings into final-state hadrons.

Single Diffractive

Let us start with the single diffractive process, which describes the interaction between two hadrons, where exactly one of the two colliding hadrons A and B is excited

to form a string X

$$A + B \to A + X \quad \text{or} \quad A + B \to X + B \,. \tag{2.84}$$

The differential cross section as a function of the string mass M_X is given by [172]

$$\frac{d\sigma_{\mathrm{SD}}}{dM_X^2} \propto \frac{1}{M_X^2} \,. \tag{2.85}$$

Once the string mass is sampled, the three-momentum p_f of the string in the center-of-mass frame can be evaluated in the same way as for the previous reaction types, treating the string like a single particle. Following the UrQMD approach, the transverse momentum transfer $\mathbf{p}_\perp$ between the incoming hadrons is assumed to follow a Gaussian distribution

$$\frac{d\sigma_{\mathrm{SD}}}{d^2\mathbf{p}_\perp} \propto \exp\left(-\frac{p_\perp^2}{\sigma_T^2}\right) \,, \tag{2.86}$$

where σ_T is a free parameter that is tuned to exprimental data from proton-proton collisions. To completely determine the kinematics of the string-hadron system, we sample the transverse momentum transfer $\mathbf{p}_\perp$ with a maximum of $p_{\perp,\max} = p_f$. The string has a longitudinal momentum $p_\parallel = \left(p_f^2 - p_\perp^2\right)^{1/2}$. Knowing the mass and the momenta of the reaction products, one can calculate the velocity of the string in order to boost into its rest frame, where the fragmentation machinery from Pythia is employed to obtain the particles in the final state of the interaction.

Double Diffractive

The double diffractive subprocess is a collision in which the two incoming hadrons A and B are both excited to strings

$$A + B \to X + X \,. \tag{2.87}$$

The dynamics of the interaction are determined in the center-of-mass frame of the incoming hadrons. The collision axis is defined to be the longitudinal direction. Kinematics of the double-diffractive excitation ar modeled via pomeron exchange, which can be viewed as a double gluon exchange [173]. Each exchanged gluon carries light-cone momenta $p^\pm = (E \pm p_\parallel)/\sqrt{2}$, where the fraction this gluon carries is sampled from a parton distribution function of the form

$$\mathrm{PDF} \propto \frac{1}{x}\,(1-x)^{\beta+1} \,. \tag{2.88}$$

Here, β is set to be 0.5 and α is treated as a free parameter. The light cone momenta of the exchanged gluons are calculated as $q_A^+ = x p_A^+$ and $q_B^- = x p_B^-$ respectively. Note

that the collision axis is defined as the direction in which the hadron A is moving. The distribution for the transverse momentum transfer $\mathbf{p}_\perp$ between gluons is taken to be Gaussian, whose width is the same as in the single-diffractive case (see equation (2.86)). The light cone momenta q_A^- and q_B^+ are obtained, based on the requirement that the gluons are on-shell, remembering that $q^+q^- = (E^2 - p^2)/2$.

$$2\left(x_A^+ p_A^+\right) q_A^- - p_\perp^2 = 0\,, \tag{2.89}$$

$$2\left(x_B^- p_B^-\right) q_B^+ - p_\perp^2 = 0\,. \tag{2.90}$$

The light cone momentum $Q^\pm$ transferred from the hadron B to A is then obtained by solving the above equations for the gluon light cone momenta

$$Q^+ = -q_B^+ = -\frac{p_\perp^2}{2\,x_B^- p_B^-}\,, \tag{2.91}$$

$$Q^- = q_A^- = \frac{p_\perp^2}{2\,x_A^+ p_A^+}\,. \tag{2.92}$$

The transferred energy ΔE and longitudinal momentum $\Delta p_\parallel$ are then

$$\Delta E = \frac{Q^+ + Q^-}{\sqrt{2}}\,, \qquad \Delta p_\parallel = \frac{Q^+ - Q^-}{\sqrt{2}}\,. \tag{2.93}$$

The mass of both excited strings can be calculated individually using the energy-momentum relation. Each string is further fragmented in its rest frame, again, using the implementation of the fragmentation within Pythia.

Non-Diffractive

The non-diffractive string excitation is the most probable soft process, and therefore has the largest impact on the dynamics of the produced particles in the intermediate energy region. During the interaction, each hadron emits one valence quark, which is adopted by the other hadron. The exchanged valence quark carries a fraction of the longitudinal momentum of the hadron it is emitted from. The light cone momentum fraction carried by the exchanged quark is sampled according to the parton distribution function for quarks, which is assumed to have the functional form

$$\text{PDF} \propto x^{\alpha-1}(1-x)^{\beta-1}\,. \tag{2.94}$$

Here, α and β are free parameters. They are adjusted such that the measured dynamics in proton-proton collisions are reproduced as well as possible, while supporting the physical picture of a valence quark exchange.

The momentum transfer in the transverse direction is sampled according to the same Gaussian as in the single diffractive and double diffractive case, using equation

2.86. With the light cone momentum fraction each exchanged quark carries and the transferred transverse momentum, the light cone momentum transfer is written as

$$Q^+ = -x_A^+ p_A^+ + \frac{p_T^2}{2x_B^- p_B^-} \tag{2.95}$$

$$Q^- = x_B^- p_B^- - \frac{p_T^2}{2x_A^+ p_A^+} ., \tag{2.96}$$

where x_A and x_B are the light cone momentum fractions for the exchanged quarks, $p_A^\pm$ and $p_B^\pm$ are the light cone momenta of the colliding hadrons before the collision and p_T is the transferred transverse momentum. The exchanged energy and longitudinal momentum can, again, be calculated using equation 2.93. The masses of the strings are obtained using the relativistic energy-momentum relation and each string is fragmented individually in the rest frame of the string using Pythia.

String Fragmentation

Once the mass of the excited string and the flavor of the quarks spanning the string is determined, the string is fragmented into hadrons by employing Pythia. Within Pythia, the species of the fragmented hadron follows from the flavor of the quark-antiquark or diquark-antidiquark pair that is produced. While the light quarks have the same probability to be produced, there are empirical suppression factors for producing heavier quarks and diquarks.

The transverse momentum of each string fragment is sampled from a Gaussian distribution with a width of $\sigma_{T,\text{string}}$ which is a free parameter that is tuned to kaon production in proton-proton reactions measured at the NA61 experiment at the Super Proton Synchrotron (SPS) at CERN [174]. The longitudinal momentum of each string fragment is determined using the fragmentation function. Pythia is based on the symmetric Lund fragmentation function [10], which has the following shape

$$f(z) \propto \frac{1}{z}(1-z)^a \exp\left(-b\frac{m_T^2}{z}\right) . \tag{2.97}$$

m_T is the transverse mass of the string fragment while a and b are free model parameters. For the fragmentation of leading baryons produced in soft non-diffractive processes, the parameters a and b are chosen differently from Pythia. Note that both the different string excitation in the soft case and the mentioned modification to the string fragmentation necessitate retuning the parameters for the fragmentation and the available tunes for Pythia are not necessarily compatible. The process of finding a new tune is described detail in [32].

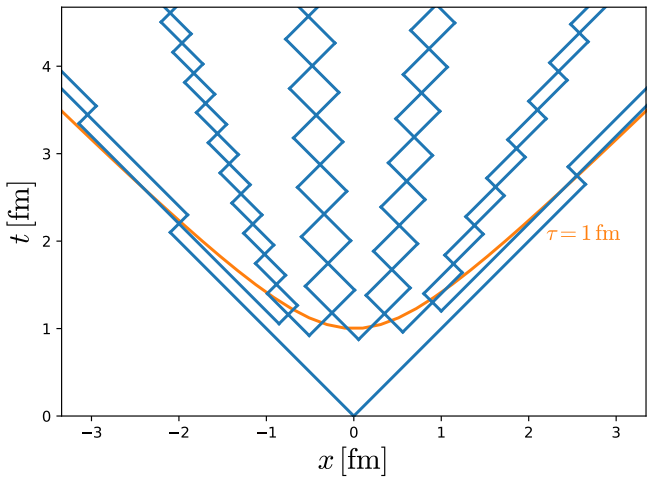

Abbildung 2.15: Sketch of a string fragmenting within the yoyo model. Taken from [32].

Particle Formation

A string fragments into hadrons by producing quark-antiquark pairs. In a dynamical picture, the pair production does not happen simultaneously but at different points in time. Figure 2.15 illustrates how a string fragments in coordinate space within the yoyo model. The straight lines indicate the trajectories of (anti)quarks or (anti)diquarks. While the pair production occurs at different points in time, the time when they recombine to hadrons fluctuates around a constant proper time. In principle, the formation time and position of all string fragments can be calculated using the yoyo model and the momenta of the fragments obtained from Pythia. For simplicity, the fluctuations in the formation time are neglected so that all string fragments form at a constant proper time in SMASH. The effect of changing the formation time on baryon stopping and hadron production in heavy-ion collisions is investigated in [32].

In practice, all particles in SMASH are immediately produced once the colliding hadrons reach their point of closest approach. Until the formation time has passed, the cross section of the string fragments are multiplied by a cross section scaling factor f_σ. For most string fragments, this factor is initially 0. However, since the leading string fragments contain quarks that do not originate from a pair production but from the initially colliding hadrons, the initial cross section scaling factor is not zero for leading string fragments. The initial cross section scaling factor for each string fragment is set to be the number of quarks from the initially colliding hadrons contained in the fragment divided by the total number of quarks of that fragment. For example, a leading baryon that contains a diquark from the initially colliding

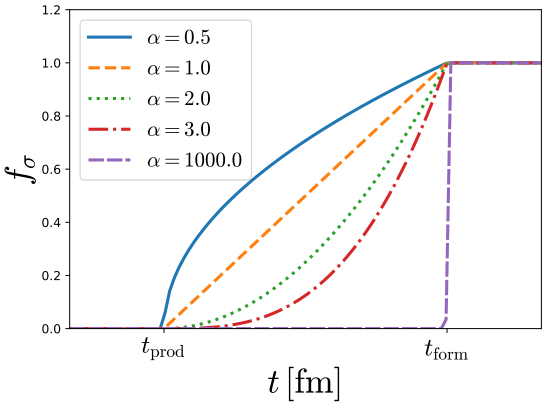

Abbildung 2.16: Cross-section scaling factor f_σ as a function of time for different powers α with which the cross section grows over time. In this example, the initial cross-section scaling factor is set to $f_\sigma(t_{\text{prod}}) = 0$. Taken from [32].

hadrons is assigned a scaling factor of $f_\sigma = 2/3$ and a meson at the other end of the string that contains another quark from the initially colliding hadrons is assigned a scaling factor of $f_\sigma = 1/2$.

Instead of having a constant cross section scaling factor until the time of formation, where the particle suddenly is allowed to interact, it is possible to mimic a continuous formation process by increasing the cross section scaling factor with time. Timely increasing cross sections have been studied in a similar fashion within the GiBUU model [175]. To realize a continuous formation, the cross section scaling factor becomes a function of time $f_\sigma = f_\sigma(t)$. This function needs to have the initially assigned scaling factor f_0 as described above at the time t_{prod} when the particle is produced and $f_\sigma(t_{\text{form}}) = 1$ at the formation time t_{form}. Between the two points, the cross section scaling factor grows with a given power α in order to have a simple but flexible functional shape. Using the three conditions, the function $f_\sigma(t)$ is written as follows

$$f_\sigma(t) = (1 - f_0) \left(\frac{t - t_{\text{prod}}}{t_{\text{form}} - t_{\text{prod}}} \right)^\alpha + f_0 \,. \tag{2.98}$$

This function is only used for $t_{\text{prod}} < t < t_{\text{form}}$, since it has no meaning before the particle is produced and the scaling factor is $f_\sigma(t) = 1$ for $t > t_{\text{form}}$, when the particle is fully formed. The cross section scaling factor as a function of time for different values of α is shown in figure 2.16. The initial cross section scaling factor is set to $f_0 = 0$ in this figure. In the limit of α going to infinity, one recovers a step function, while for small positive values of α, the particles form immediately. In [32], the effect of the details of the particle formation on particle spectra in heavy-ion collisions is investigated.

2.2.5 Total Cross Section and Workflow

In the previous sections, we have discussed the most important interactions and their corresponding cross sections. An essential component of the model is the total cross section, which is obtained by combining the partial cross sections from the earlier discussions. Here, we explain how the total cross section is evaluated, how it is applied in the model, and how the interaction channel is selected.

In the dynamic calculation of a system within the SMASH model, scatterings and decays are handled differently. Both processes evolve in discrete time steps. As described in Section 2.2.2, decay times are determined at the start of each time step. Similarly, potential scatterings are identified based on the collision criteria (see Section 2.2.6) at the beginning of each time step. However, the key difference is that the scattering cross section accounts for all possible scattering processes, and a specific interaction channel is selected based on the partial cross sections when the interaction occurs. Whether a decay or a scattering takes place is, in contrast, determined by the interaction time. All processes are executed chronologically, meaning that potential interactions at later times are invalidated if the involved particles have already participated in a previous interaction. Therefore, a decay can only happen if it occurs before other interactions. Importantly, this does not imply that only one interaction per particle is allowed per time step. This common limitation in transport models is overcome in SMASH by finding new interactions between outgoing particles and all surrounding particles after each interaction. This procedure leads to very stable collision rates, independent of the time step size as shown in [176].

When a scattering takes place, the channel is chosen based on the partial cross sections σ_i such that the probability for a channel P_i is given by

$$P_i = \frac{\sigma_i}{\sum_j \sigma_j} \,. \tag{2.99}$$

The sum of partial cross sections in the denominator is the total cross section, which is required for collision finding as described in Section 2.2.6.

Constructing the total cross section in a bottom-up manner from individual cross sections does not always guarantee that experimentally measured total cross sections will be reproduced. In some cases, a rescaling of the cross sections is applied. However, this approach is not without issues, as it can disrupt detailed balance, a key requirement for a transport model to ensure that the correct equilibrium distribution is reached. Detailed balance is also necessary for proving the H-theorem, which asserts that entropy never decreases.

A modification of the cross sections occurs in the center of mass energy region, where resonance contributions gradually fade out and a transition to string excitation takes place. Since backward reactions are not implemented for string excitation and fragmentation processes, detailed balance is already broken in this region. As

the resonance cross section decreases and the string cross section increases to match the measured total cross section, a discontinuity would arise. To avoid this, a transition region is introduced where the resonance cross section is smoothly scaled down while the string cross section increases with energy. A linear scaling function is used to modify the cross sections, ensuring that the sum of the scaling factors always equals 1.

This approach guarantees a smooth transition. However, a dip in the cross section may occur if the resonance cross section is already too small in the transition region. To address this, a method similar to the prescription used in UrQMD [115], [116] is applied to enhance the resonance cross section. The deficit in the cross section within the transition region is compensated by scaling up the resonance formation cross section. Specifically, the cross section of the resonance whose pole mass is closest to the center of mass energy is scaled to completely fill the missing inelastic cross section.

Another adjustment to the cross sections is made in the lower energy region, where the inelastic cross section is determined by resonance formation. In this region, the cross section depends on the masses, widths, and decay probabilities of the resonances. Finding resonance properties that reproduce the most important cross sections in a bottom-up approach is a complex task. Although a set of resonance properties has been found that describes most available data very well, and is distributed with the source code, it is often desirable to add or remove resonances. Since modifying resonance properties can lead to poor reproduction of measured total cross sections, an option (enabled by default) is available to rescale the total cross sections to match the measured values when experimental data is available. In this procedure, all partial cross sections are scaled by the same factor. However, it is important to note that this rescaling option breaks detailed balance and should not be used in studies that rely on an accurate equilibrium distribution, such as the evaluation of transport coefficients [55], [56], [177].

2.2.6 Collision Criteria

To conclude the discussion on the collision term, we now explain how the model determines whether a scattering event occurs and when it takes place. In the SMASH model, there are two geometric collision criteria and a stochastic collision criterion. In the geometric interpretation, the cross section is treated as an area orthogonal to the collision axis. This area is used to determine if an interaction occurs. The area is assumed to be circular, so that an interaction happens if the transverse distance between the incoming particles is smaller than the radius of a circle with an area equal to σ

$$d_{\text{trans}} \leq \sqrt{\frac{\sigma}{\pi}}\,. \tag{2.100}$$

The geometric collision criteria in the SMASH model primarily differ in how the transverse distance is calculated and how the collision time is determined. The first geometric criterion, adapted from [115], is not formulated in a covariant manner, and thus relies on evaluating the transverse distance in the two-particle center-of-mass frame. Before presenting the expression for the transverse distance, we first discuss the determination of the collision time, which is evaluated in the calculation frame. For two particles with positions $\mathbf{r}_a$ and $\mathbf{r}_b$, and velocities $\mathbf{v}_a$ and $\mathbf{v}_b$, respectively, the time of closest approach can be derived by assuming that the particles propagate along straight lines within a given time step. For this purpose, we try to find a minimum of the squared distance $(\mathbf{r}_a(t+\Delta t) - \mathbf{r}_b(t+\Delta t))^2$, where $\mathbf{r}_{a/b}(t+\Delta t) = \mathbf{r}_{a/b}(t) + \mathbf{v}_{a/b}\Delta t$. We find the time until the collision Δt by requiring the derivative of the squared distance with respect to Δt to vanish

$$\frac{d}{d\Delta t}\left[\mathbf{r}_a(t+\Delta t) - \mathbf{r}_b(t+\Delta t)\right]^2 = 2[\mathbf{r}_a(t) + \mathbf{v}_a\Delta t - \mathbf{r}_b(t) - \mathbf{v}_b\Delta t]\cdot(\mathbf{v}_a - \mathbf{v}_b) = 0\,. \tag{2.101}$$

This equation is easily solved, provided the velocities are not parallel, yielding

$$\Delta t = -\frac{[\mathbf{r}_a(t) - \mathbf{r}_b(t)]\cdot(\mathbf{v}_a - \mathbf{v}_b)}{(\mathbf{v}_a - \mathbf{v}_b)^2}\,. \tag{2.102}$$

Lorentz invariance is not satisfied, as this equation is not written in a covariant form and is evaluated in a fixed frame. It is important to emphasize that a potential collision occurs at the point of closest approach in this case. An analogy with finite-sized balls, where a collision happens when the surfaces (as defined by the cross section) touch, is not accurate in this context.

The transverse distance can be calculated based on the collision time and the trajectories of the particles. It is given by

$$d^2_{\text{trans}} = (\mathbf{r}_a - \mathbf{r}_b)^2 - \frac{[(\mathbf{r}_a - \mathbf{r}_b)\cdot(\mathbf{v}_a - \mathbf{v}_b)]^2}{(\mathbf{v}_a - \mathbf{v}_b)^2}\,, \tag{2.103}$$

where the time argument was dropped for clarity, but the positions are required at time t in this equation. This equation is evaluated in the two-particle center-of-mass frame within the model, ensuring that the decision of whether a collision occurs is independent of the chosen calculation frame.

Since the interaction occurs instantaneously over a finite distance, a fully relativistic description cannot be achieved. However, a method to reduce frame dependence has been proposed by Kodama and collaborators [178]. In this approach, the transverse distance is generalized to a Lorentz-invariant expression, and collision times are evaluated in the rest frame of each incoming particle. The prescription from [178] ensures that interactions are forbidden if they directly violate causality. Specifically, an interaction between particles a and b is permitted only if it is their first interaction in their both respective rest frames.

The calculation of the collision time for each incoming particle in its rest frame is performed in a covariant manner as described in [179]. However, it is still not possible to achieve a fully covariant description of the problem. This becomes evident when the collision time in the calculation frame is needed. Boosting the two collision times back to the calculation frame results in two different times, introducing some ambiguity. In the SMASH model, the collision is performed at the average of these two times after applying the covariant expressions from [179].

The stochastic collision criterion offers a fundamentally different approach to the problem. Rather than modeling finite-distance interactions, space is divided into small cells, where the interaction probability can be calculated. A decision on whether an interaction occurs is then made based on this probability. A key advantage of this approach, compared to the geometric criteria, is that it is not limited to binary interactions. This makes it particularly useful for problems involving multi-particle reactions, such as light nuclei formation in catalysis reactions [180], baryon-antibaryon annihilation with corresponding backward reactions [181], and interactions between three gluons in a parton-based transport model [182]. The stochastic collision criterion was recently implemented in the SMASH transport model [183] and has been applied to deuteron production in catalysis reactions [184] as well as baryon-antibaryon interactions [185].

We will briefly discuss the equations required to apply the stochastic collision criterion and refer the reader to the thesis of Jan Staudenmaier for more details [183]. To illustrate the concept, we begin with the probability for a $2 \to n$ reaction, which is given by

$$P_{2\to m} = \frac{\Delta t}{\Delta^3 x} v_{\text{rel}} \sigma_{2\to n} \,. \tag{2.104}$$

This expression defines the probability for an interaction between two particles within a small cell of volume $\Delta^3 x$ during a time interval Δt. Here, v_{rel} represents the relative velocity of the incoming particles, and $\sigma_{2\to n}$ is the corresponding cross section. The basic idea is that the two particles are located somewhere within the volume Δx, with no further positional information. Naturally, the probability of interaction increases when considering a longer time interval, while a larger volume (indicating greater separation between the particles) decreases the likelihood of interaction. The combination of v_{rel} and the cross section can be interpreted as a volume swept by one particle per time interval, assuming the other particle is at rest. In this framework, an interaction occurs if the second particle is located within this volume. Therefore, the probability for an interaction to occur during a time step is given by the ratio of the covered volume to the total cell volume. This probability must be evaluated for all possible pairs of test particles. For more detailed expressions, including those for multiple incoming and outgoing particles, we refer the reader to [183].

For a stable calculation, both the cell size and time interval must be sufficiently small to ensure that the particles are evenly distributed within the cell and that

this distribution remains roughly constant during the time step. At the same time, each cell must contain a sufficiently large number of particles. Given these technical constraints, using a large number of test particles per real particle is ideal for a calculation employing the stochastic collision criterion. However, since the probability must be evaluated for all possible particle combinations within a cell, the combinatorics grow rapidly, especially for multi-particle reactions. Therefore, the calculation depends critically on a careful selection of technical parameters, considering all of the factors discussed above. To verify that the chosen parameters are reasonable, one can check if the results are, within a certain range, independent of these technical settings. In this work, we rely on the parameter setup that was tested in [183].

2.3 Light Nuclei Formation

Matter, as we know it, is composed of atoms. Atomic nuclei, which contain nearly all of the atom's mass, are themselves fascinating objects of study. In the context of heavy-ion collisions, light nuclei are of particular interest due to their nature as composite objects made up of protons, neutrons, and occasionally more exotic baryons, such as the hypertriton ($^3_\Lambda$H), which consists of a proton, a neutron, and a Λ-baryon. Since nuclei are formed by multiple nucleons, the production of light nuclei is highly sensitive to the number of baryons present in the system. As such, their production provides crucial insight into the baryon number and its fluctuations, which are expected to increase near the critical point of the system.

Another key aspect that makes the formation of light nuclei a significant area of current research is their relatively low binding energy, especially when compared to the average kinetic energy of particles in a hot fireball. This raises the question of how such loosely bound objects can form in a heavy-ion collision. The challenge of understanding these 'snowballs in hell' requires a dynamical modeling approach, as discussed in Section 1.2.

Even if the formation of light nuclei is not the primary focus of a study, it is unavoidable to consider their formation in heavy-ion collisions at lower energies. This is because a significant fraction of the protons in the final state are not free, but instead are bound in light nuclei, as shown in [186].

In this thesis, two models for the formation of light nuclei are employed. One of them is final-state coalescence and the other one is the creation of light nuclei in collisions. Both models are explained in detail in the following.

Binding light nuclei with potentials is not possible in a BUU-type approach, because only the single-particle distribution function is evolved. In a QMD-type model, potentials can bind light nuclei, but it is very challenging to create nuclei that are stable over a long time.

2.3.1 Coalescence

The coalescence picture considers the distribution of protons and neutrons in the final state of a heavy-ion collision and draws conclusions about the formation of light nuclei based on the overlap of the two.

As only the final state is taken into account, the model cannot be considered dynamic. However, by evolving the heavy-ion collision in a dynamical simulation, the production of light nuclei based on the final state can provide valuable insights into the mechanisms of light nucleus formation.

In this thesis, coalescence is performed based on a final state created with the SMASH transport model, either after a pure SMASH run in Chapters 3 and 4 or after using SMASH as an afterburner in Chapter 6.

Coalescence can be performed in various ways. One important aspect is whether the distribution in configuration space is considered or only the information in momentum space is taken into account. The information about the final state momenta is, of course, essential, because light nuclei, which have a small binding energy, can only form if the constituents have a relatively small relative momentum. However, even though they are extended objects in configuration space, light nuclei can only form if the constituents are sufficiently close.

Therefore, the positions of nucleons are explicitly included in our coalescence model. However, this introduces additional technical challenges that must be addressed. As discussed earlier, nuclei are not bound by the mean-field potentials used in the model. As a result, the distances between nucleons continue to increase over time until the calculation is stopped. The stopping time is a technical parameter and should not affect the physical outcomes. Clearly, with a naive approach based solely on final positions, stable results cannot be obtained

To address this issue, we adopt the approach from [187], where the coalescence criterion is applied at a time determined by the scatterings that have occurred. For each pair of particles, the relevant time is defined as the latest moment at which one of the particles participated in an interaction.

To express the criterion in a Lorentz-invariant manner, the frame is chosen as the two-particle center-of-mass frame of the candidates for coalescence. After boosting to this frame, coalescence occurs if both the spatial distance between the particles is below a threshold of 3 fm and the momentum difference is less than 300 MeV.

The coalescence approach applied in Chapter 3 was in an early stage and could only distinguish between nucleons that fulfill such a criterion and nucleons that do not. As a consequence, light nuclei are not really created but only filtered out to obtain free protons.

Results presented in the Chapters 4 and 6 are based on a more involved implementation that is capable of identifying various light nuclei. For this purpose, a bottom-up procedure is performed. In a first step, all pairs of protons and neutrons

are checked and the closest ones in phase space are combined to deuterons. Further iterations are performed, where all existing nucleons and nuclei are considered and combined to larger nuclei. Only nuclei with a lifetime of at least 100 fm are allowed in this stage. Combining two electrically charged nuclei is more difficult due to the repulsion. This can be seen by the reduced number of ^{3}He compared to ^{3}H (triton) in heavy-ion collisions. The repulsion is taken into account by introducing a penalty in the momentum-difference of 20 MeV. This value was tuned to the helium-3 and triton abundances as observed in gold-gold collisions at the HADES experiment. The thresholds in distance and momentum-difference are also estimated based on the abundances of nuclei in this collision system. The distance criterion is consistent with the width of the deuteron wave function, which is reassuring.

Nuclei are combined this way until no more stable nuclei can be created. At this point the coalescence is completed.

2.3.2 Deuteron Formation via Intermediate State

A fully dynamic evolution of light nuclei in a heavy-ion collision can be obtained by treating them as an active degrees of freedom in the calculation. The formation of light nuclei is then considered in the collision term of the model. This way, light nuclei are created and destroyed according to microscopic cross sections, and one can study the time evolution of their abundances and the production and destruction rates.

The formation of light nuclei is not trivial to include in the collision term, as the most important processes for this endeavor have multiple particles in the initial state. Deuterons are formed in the reactions

$$NN \leftrightarrow d\pi \tag{2.105}$$

$$pnX \leftrightarrow dX\,, \tag{2.106}$$

where the X stands for a catalyst that can be a pion or nucleon in the current implementation. N stands for either proton or neutron in this case and the isospin state of the pion in the final state is such that the electric charge is conserved in this interaction. The cross section for the catalysis reactions is much larger than the $2 \to 2$ process for the formation of the deuteron.

The geometric collision criterion only considers two incoming particles and can, therefore, not directly be applied to the catalysis reaction. Before the stochastic collision criterion was available in SMASH, a workaround for this challenge was introduced in [188]. The $3 \leftrightarrow 2$ process is, in the geometric implementation, split into a $2 \leftrightarrow 1$ and subsequent $2 \leftrightarrow 2$ process as follows

$$pn \leftrightarrow d' \tag{2.107}$$

$$d'X \leftrightarrow dX\,, \tag{2.108}$$

where the d' is a fictional dibaryon resonance with a lifetime of 1 fm to mimic the overlapping proton and neutron. This method is used to study the flow of deuterons as presented in Chapter 3.

2.3.3 Nuclei Formation via Stochastic Rates

The production of light nuclei with the geometric collision criterion is limited to deuterons as only the dibaryon resonance is implemented. An additional shortcoming of the splitting of the multiparticle reaction into two steps is that the equilibration process is expected to be faster when multiparticle reactions are taking place [182].

Multiparticle reactions can be performed in a transport calculation using the stochastic collision criterion, as introduced in Section 2.2.6. The formation of deuterons with the stochastic collision criterion was studied in SMASH in [184] and previously in [180].

The probability for the production of deuterons is given in Equation 6 in [184], and it is based on the cross section for the reverse process which is parametrized in [188].

The limitation to only deuteron production is not present anymore when switching to the stochastic collision criterion, because the interaction probability can be written for any $n \to 2$ process as long as the cross section for the inverse process is available. An extension to nuclei with mass number 3 is implemented in the SMASH model and is presented in [4] and in Chapter 6. The considered nuclei are triton, helium-3 and hypertriton. To produce these nuclei, the relevant processes are

$$nnpX \leftrightarrow tX \tag{2.109}$$

$$nppX \leftrightarrow {}^3\mathrm{He}X \tag{2.110}$$

$$np\Lambda X \leftrightarrow {}^3_\Lambda\mathrm{H}X\,, \tag{2.111}$$

where the X, again, stands for either a nucleon or a pion.

The cross section for the $2 \to 4$ process is obtained by an extrapolation of the proton-deuteron and pion-deuteron cross sections. For this purpose, the cross sections between the deuteron and the catalysts are expressed in terms of the kinetic energy

$$T = \frac{(s - m_A + m_{\mathrm{cat}})^2}{2m_A}\,. \tag{2.112}$$

The mass of the nucleus and the mass of the catalyst are denoted by m_A and m_{cat}. In a simple picture, we consider only the number of constituents of the nuclei, such that the cross section of an $A = 3$ nucleus is equal to 3/2 times the cross section of a deuteron at the same kinetic energy.

To summarize, the cross section for all $A = 3$ nuclei with a given catalyst X is

$$\sigma_{AX\to NNNX}(T) = \frac{A}{2}\sigma_{dX\to pnX}(T)\,. \tag{2.113}$$

The cross sections are given in terms of $\sqrt{s}$ in Figure 2.17 for both nucleon and pion catalysis reactions. The difference between the cross sections for different nuclei emerge from the different masses, as the kinetic energy at a given center of mass energy is smaller for heavier particles. Since the triton and ^{3}He nuclei have very similar masses, the curves overlap in Figure 2.17.

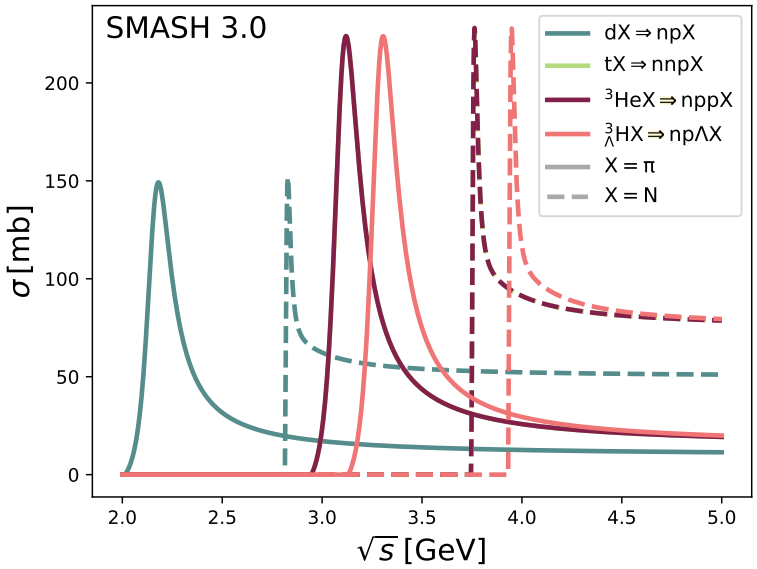

Abbildung 2.17: Interaction cross sections for $2 \to 3$ and $2 \to 4$ light-nuclei catalysis reactions as a function of center-of-mass energy in SMASH. Solid lines represent cross sections for interactions with pions, while dashed lines correspond to interactions with nucleons. Taken from [4].

The angular distributions are treated isotropically. One should emphasize that the large cross sections do not imply an interaction over a large distance in the transport description, since collision finding is based on small cells as described in Section 2.2.6. Even though light nuclei are large sized objects, they are represented as point-like particles in the test particle picture, just like all other particles in SMASH.

Kapitel 3

Anisotropic Flow Study without Momentum Dependence

This chapter presents a study of anisotropic flow, which is published in [1]. The aim of the study is to assess the sensitivity of the flow signal to both the formation of light nuclei and the equation of state. Anisotropic flow of protons has proven to be an well-suited probe for the stiffness of the equation of state, as discussed in Section 1.3.2. Experimental efforts have lead to excellent statistics that allow for very differential studies of flow coefficients with small uncertainties. The sensitivity study presented in the following explores which kinematic regions are most suitable for a clean extraction of the equation of state, while minimizing the impact of technical choices in the implementation of the transport model.

Modeling the formation of light nuclei in heavy-ion collisions becomes more complex at lower collision energies. As the abundances of light nuclei increase, their formation cannot be neglected, even when only protons are considered (see [186]). This study compares two methods for light nuclei formation, identifying regions where the models agree and where differences arise due to the inclusion of light nuclei formation. By focusing on the kinematic regions where the models are in agreement, we can reduce model dependence in future studies aimed at constraining the equation of state using improved potentials.

At this stage, the comparison to data is motivated purely by curiosity. The literature suggests that a momentum-dependent term must be included in the nuclear potentials to accurately describe the measurements (see Section 1.3.2). Additionally, scattering data from protons on nuclei can only be reproduced when the potentials explicitly depend on momentum, as discussed in Section 2.1.2. The momentum-dependence was now yet available for this study. Therefore, experimental data is not well described.

3.1 Technical Setup

In the following, we present results for the flow coefficients of protons and deuterons and compare them to experimental data [114], [189]. To ensure consistency with the measurements, the flow coefficients are evaluated with respect to the reaction plane, which is spanned by the beam axis and the impact parameter. In our calculation setup, the reaction plane is fixed to the x-z plane. For details on the estimation of flow coefficients, the reader is referred to Section 1.2.2. The centrality of the events is determined by constraining the impact parameter to a specific range. We focus on the 20% to 30% most central gold-gold collisions, which correspond to an impact parameter range of $6.6\,\mathrm{fm} < b < 8.1\,\mathrm{fm}$, as estimated using the Glauber model in [190].

The collision energy considered in this study is $E_{\mathrm{kin}}/A = 1.23\,\mathrm{GeV}$, and all calculations are performed in the center-of-mass frame. For the calculations presented in this chapter, only the basic Skyrme potential (described in Section 2.1.1) and the symmetry potential (described in Section 2.1.3) are applied. Since, at the time of this study, the momentum-dependent part of the potential and the Coulomb potential had not yet been implemented in the model. The study focuses on estimating the difference between a 'hard' and a 'default' equation of state. They are defined by the incompressibility κ at saturation density. The hard EoS has an incompressibility of $\kappa = 380\,\mathrm{MeV}$ and the default EoS has an incompressibility of 240 MeV. Calculation for the ßoftËoS ($\kappa = 215\,\mathrm{MeV}$) are not presented in this study as the flow signal would be very weak compared to the data because no momentum-dependence is implemented in this study.

The density calculation required for the propagation of the test particles in the mean-field is obtained using the covariant Gaussian smearing kernel as described in Section 2.1.5. The smearing kernel has the width σ as a technical parameter. Throughout this thesis the value of it is set to $\sigma = 1\,\mathrm{fm}$ except in Section 3.5.2, where the sensitivity of our results to a variation in σ is studied.

The density calculation relies on a significant number of test particles, as described in Section 2.1.5. In this chapter, the number of test particles per real particle is set to 20. Section 3.5.1 demonstrates that the results remain unchanged when the number of test particles is doubled. However, by using parallel ensembles, improved statistics can be achieved, so that a much larger number of parallel ensembles is employed in the following chapters. The propagation relies on small time steps. Calculations presented here are performed with a time step of $\Delta t = 0.1\,\mathrm{fm}$.

In this chapter, a relatively simple coalescence model (see Section 2.3) is applied, which only selects the nucleons that are considered bound. While an improved model, used in the following chapters, may lead to slight changes in the results, the coalescence model employed here is a reasonable choice and is well-suited for the sensitivity studies performed in this chapter.

We compare calculations using the coalescence model with a dynamic approach to light nuclei formation. In the dynamic model, deuterons are formed through catalysis reactions, which are divided into two steps involving the fictional dibaryon resonance d' (see Section 2.3 for details).

3.2 Directed flow of protons and deuterons

We begin by calculating the first-order flow coefficients of protons and deuterons in gold-gold collisions at $E_{\text{kin}} = 1.23A\,\text{GeV}$. Calculations are performed for different bins in rapidity and transverse momentum to explore the sensitivity of the equation of state (EoS) and light nuclei formation across a broad phase-space region.

Figure 3.1a shows the directed flow of protons as a function of rapidity for different bins in transverse momentum. While the shape of the flow is in good agreement with experimental measurements, only the calculation using the hard equation of state (EoS) captures the correct magnitude. Two calculations consider the formation of light nuclei by clustering in the final state, with varying stiffness of the EoS. Additionally, a third calculation is presented, where clustering is not performed. Instead, deuterons are explicitly treated as degrees of freedom and are created through catalysis reactions in two steps using the geometric collision criterion. For this calculation, the hard equation of state is used. A slight difference can be observed between the solid lines (representing clustering) and the dash-dotted lines (representing dynamic deuteron formation). This difference is more pronounced in the lower of the two transverse momentum intervals considered.

Figure 3.1b shows the directed flow as a function of transverse momentum for different rapidity bins. Of course also as a function of p_T, the hard equation of state best describes the experimental data. The difference between the two options to account for nuclei formation is clearly visible at low transverse momentum but vanishes at larger p_T. The significance of clustering in the low-momentum region can be attributed to the higher phase-space density, which makes the formation of nuclei more likely. Compared to the data, clustering gives the best description, but produces a small kink in the low p_T region, The dynamic deuteron formation gives a reasonable description of the data and the curve is more smooth, but does not follow the data as closely.

The dotted lines represent the same calculation as the solid lines with the hard equation of state and clustering, but with the exclusion of spectators, defined as particles that have not collided. We observe almost no difference, because the spectators are expected more forward in rapidity.

From the calculation where deuterons are explicitly propagated, the directed flow of deuterons themselves is extracted. The results shown in Figure 3.2 compare the deuteron flow with the hard and the default equations of state. Considering

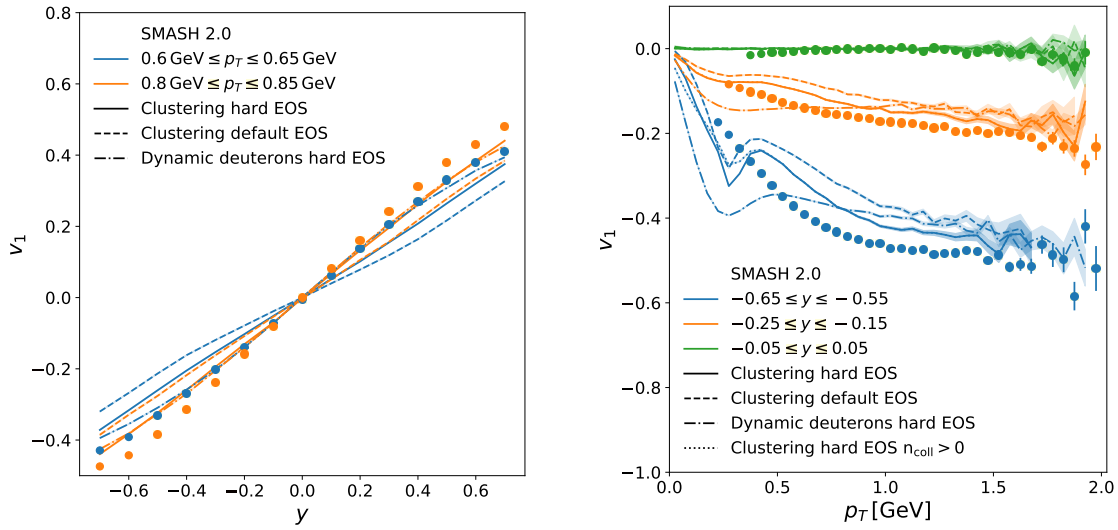

(a) Directed flow of protons as a function of rapidity.

(b) Directed flow of protons as a function of transverse momentum.

Abbildung 3.1: Directed flow of protons in 20%-30% central gold-gold collisions at $E_{\text{kin}} = 1.23A\,\text{GeV}$, compared to experimental data points from [189]. Solid lines are obtained with a hard equation of state, while dashed lines use the default equation of state. The curve labeled "Dynamic deuteronsäccounts for the formation of light nuclei by explicitly producing deuterons during the collision, as described in Section 2.3. Taken from [1].

that the model for the light nuclei formation was originally designed for high-energy collisions [188], where the composition of the system is very different and nuclear potentials are negligible, it is not obvious that the directed flow of deuterons can be described. A reasonable agreement with the experimental data is observed, except in the forward region, where the p_T-dependence does not follow the data. This may be related to the fact that only deuterons can be formed in this calculation. In the forward region, one would expect a significant yield of nuclei larger than deuterons. The model may incorrectly identify these nuclei as multiple deuterons, which could enhance the directed flow signal.

To conclude the findings from the comparison to the measured v_1, the hard equation of state is clearly favored in this setup without momentum-dependence. Overall a reasonable agreement with the data is observed, but the clustering setup follows a bit closer the transverse momentum dependent v_1 of nucleons. The deuteron flow is matched reasonably well in the calculation with explicit deuteron formation.

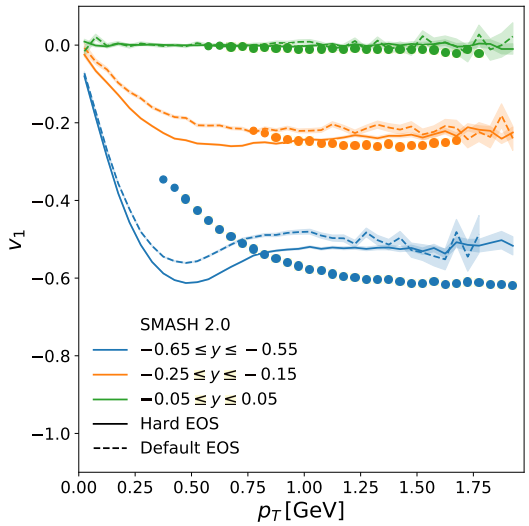

Abbildung 3.2: Directed flow of deuterons as a function of transverse momentum in 20%-30% central gold-gold collisions at $E_{\text{kin}} = 1.23A\,\text{GeV}$, for different rapidity bins, compared to experimental data points from [189]. Deuterons are dynamically treated as particles in this calculation. Taken from [1].

3.3 Elliptic flow of protons and deuterons

Continuing with the second order flow harmonic, Figure 3.3a shows the elliptic flow as a function of rapidity in semi central gold-gold collisions. Again, two calculations with different equations of state are compared. Here, coalescence is used to form light nuclei. Additionally a calculation with dynamic deuterons employing a hard equation of state is provided. Naturally, the second-order flow coefficient is more difficult to describe than the first-order one. In general, the magnitude of v_2 is too small at large transverse momenta. The missing momentum-dependence in the potentials is the reason for the insufficient elliptic flow signal at large momenta. The repulsion due to the mean-field for high-p_T particles will be enhanced by the momentum-dependent term as described in Section 2.1.2.

Same as for v_1, the hard equation of state produces a stronger flow signal and is thus preferred by the data in the presented setup. Additionally, the magnitude of v_2 is larger when deuterons are explicitly treated in the calculation This approach yields the best agreement with the data As with v_1, in the low p_T region (specifically, the $0.4\,\text{GeV} < p_T < 0.45\,\text{GeV}$ bin), the results are highly sensitive to how the formation of light nuclei is modeled.

The elliptic flow of nucleons as a function of the transverse momentum is shown in Figure 3.3b. Also here, it is clearly visible, that the elliptic flow is not well described,

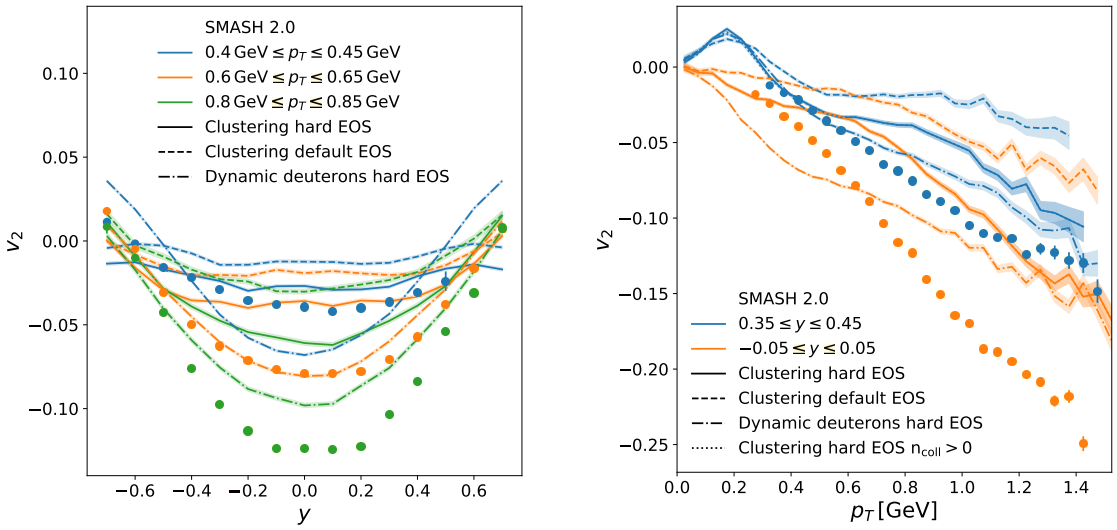

(a) Elliptic flow of protons as a function of rapidity for different p_T bins.

(b) Elliptic flow of protons as a function of p_T for different rapidity bins.

Abbildung 3.3: Elliptic flow of protons in 20%-30% central gold-gold collisions at $E_{\text{kin}} = 1.23A\,\text{GeV}$, compared to experimental data points from [189]. Solid lines are obtained with a hard equation of state, while dashed lines use the default equation of state. The curve labeled "Dynamic deuteronsäccounts for the formation of light nuclei by explicitly producing deuterons during the collision, as described in Section 2.3. Taken from [1].

especially in the high p_T region. In the low p_T region, the clustering performs better, while the calculation with explicit deuteron production works better at intermediate transverse momentum. The difficulties in describing the v_2 at high p_T arise from the lack of momentum-dependence in the potentials as mentioned above. The differences between the calculation with clustering and the one with explicit deuteron formation vanish at high transverse momentum. This finding suggests that information on the equation of state can be extracted more cleanly in the large p_T interval. Because of this observation, the equation of state is constrained based on flow observables in the $1\,\text{GeV} < p_T < 1.5\,\text{GeV}$ region in the following Chapter.

The elliptic flow of deuterons can additionally be calculated when the deuterons are treated as active degrees of freedom. The results are shown, as a function of rapidity, in Figure 3.4a. For the hard equation of state, the flow signal is overestimated, while the default equation of state is in agreement with the data. Examining the p_T-dependence of the elliptic flow of deuterons in Figure 3.4b, we observe that the agreement with experimental data is good only for the default equation of state. It is possible that all flow data could be consistently described with more sophisticated

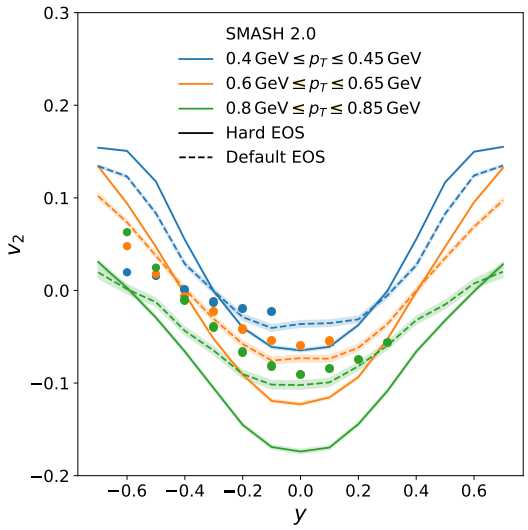

(a) Elliptic flow of deuterons as a function of rapidity for different bins in p_T.

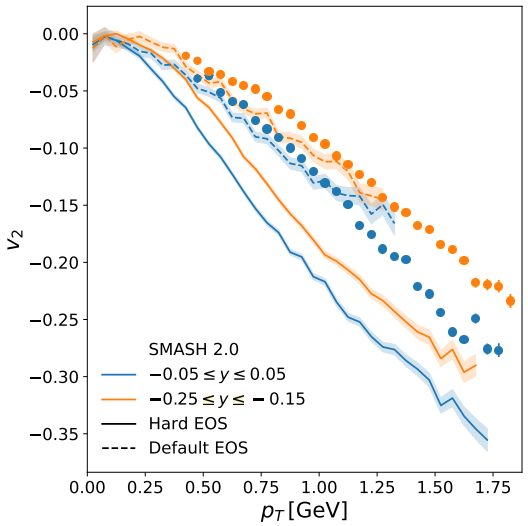

(b) Elliptic flow of deuterons as a function of p_T for different bin in rapidity.

Abbildung 3.4: Elliptic flow of deuterons in 20%-30% central gold-gold collisions at $E_{\text{kin}} = 1.23A\,\text{GeV}$, compared to experimental data points from [189]. A hard equation of state was used, and deuterons were dynamically treated as particles in this calculation. Taken from [1].

potentials. This is studied in Chapter 4. On one hand, achieving a consistent description of both proton and deuteron flow in a dynamic calculation is a challenging task. On the other hand, once a realistic prescription is developed, the deuteron flow could provide valuable insights into the equation of state.

To conclude this section, the elliptic flow is observed to be highly sensitive to how the light nuclei formation is taken into account, which leads to some uncertainty in the extraction of the EoS. The elliptic flow of nucleons at large transverse momenta is underestimated in the SMASH calculations without momentum-dependence, but the best agreement is found with a hard equation of state. The results of this section suggest that this kinematic region is best suited to study the equation of state.

3.4 Evolution of Flow Coefficients

In this section we focus on the temporal evolution of flow coefficients to identify when the anisotropy is developed and which stages are most important. The timing when the flow signal builds up encodes the information at which densities the EoS is probed when studying flow coefficients. We concentrate on the setting that worked best in

comparison to experimental data, namely, the calculation with explicit deuteron formation and a hard equation of state.

The first two panels of Figure 3.5 show the multiplicity of nucleons and deuterons as a function of time, respectively. The initially present nucleons from the two gold nuclei begin interacting, forming resonances and deuterons, which causes their number to decrease. Meanwhile, the number of deuterons steadily increases throughout the evolution of the heavy-ion collision.

The third panel illustrates the slope of the directed flow at mid-rapidity as a proxy for the magnitude of v_1 for both nucleons and deuterons. To evaluate this slope, the $v_1(y)$ is fit at each time step using the function $v_1(y) = ay + by^3$, where the cubic term accounts for the curvature observed in Figure 3.1a. The fitting is performed using Bayesian parameter estimation with Markov chain Monte Carlo sampling. The inner band represents the 68% credible interval, and the outer band corresponds to the 95% credible interval.

At early times, the uncertainty is large because not enough particles have interacted yet, and deuterons have not yet been produced. As time progresses, the flow signal starts building from zero, reaching a maximum around ≈ 15 fm, which corresponds to the time it takes for the nuclei to pass through each other. After this point, the flow signal for both nucleons and deuterons slightly weakens, before the deuteron flow increases again and eventually reaches a higher plateau.

The final panel of Figure 3.5 compares the elliptic flow at mid-rapidity between nucleons and deuterons. Once enough particles have been produced and are located in the relevant kinematic region, the elliptic flow of nucleons and deuterons becomes nearly identical, with the only difference being that the deuteron flow continues to increase at later times. This is not intuitively clear since no mass number scaling is applied here.

A closer look at the evolution of v_2 reveals that a positive elliptic flow signal initially builds up, but shortly afterward, v_2 drops below zero and remains negative throughout the rest of the evolution. Positive elliptic flow is typically linked to pressure gradients in the initial state. However, at low collision energies, a competing effect known as ßqueeze-out"leads to a negative v_2 signal, as the slow spectator nuclei block the path and push particles out of the reaction plane [191]. Both of these effects contribute to the observed elliptic flow.

It is interesting to note that, particularly for nucleons, the v_2 exhibits a significantly different time evolution compared to v_1. The challenges in describing both the elliptic and directed flow using the same set of parameters may stem from the fact that these flow coefficients are sensitive to different stages of the collision dynamics.

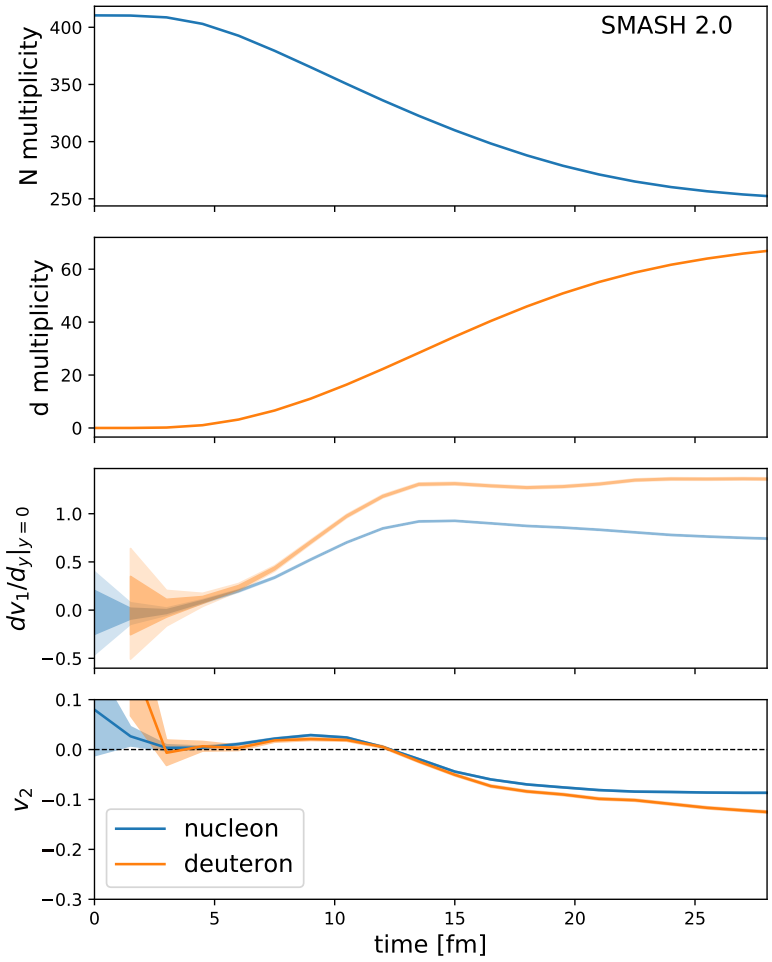

Abbildung 3.5: Nucleon and deuteron multiplicities, slope of the first order flow coefficient at mid-rapidity, and v_2 of nucleons and deuterons as a function of time in 20% - 30% central gold-gold collisions at $E_{\text{kin}} = 1.23A\,\text{GeV}$. The flow coefficients are evaluated for particles that satisfy $0.75\,\text{GeV} < p_T < 0.8\,\text{GeV}$, but the number of particles refers to the total multiplicity. Taken from [1].

3.5 Validation

Before summarizing the conclusions from this work in the following section, one should show that the results presented in the previous sections are not altered when technical parameters are varied in a reasonable range. This is not only aiming to verify the conclusions drawn so far but also to establish a set of technical parameters that can be used in future work. Relevant for calculations with nuclear potentials are the number of test particles and the smearing width. The sensitivity of the results on both of them are studied in the following.

3.5.1 Dependence on Test Particle Number

As mentioned in Section 2.1, the mean fields are expressed in terms of densities and their derivatives and hence rely on the density to be smooth and statistical fluctuations to be under control. A sufficient number of test particles is a tool to obtain the smooth density profile necessary for a reliable calculation. Test particle are, however, not only applied to obtain sufficient statistics for the density calculation. Taking the test particle ansatz seriously, the distribution function is expressed as a sum of delta distributions. This only works if the number of test particles is infinite or, in practice, large.

In the following we investigate the dependence on the number of test particles N_{test} used in the calculation to represent a physical particle by repeating the previous calculations for directed and elliptic flow. The result for the directed and elliptic flow of nucleons in the calculation, where deuterons are explicitly propagated is shown in Figure 3.6a and 3.6b respectively. The results for one and five test particles are basically identical. However, increasing the number of test particles to twenty, a significant difference can be observed for both v_1 and v_2. Compared to the calculation with twenty test particles, doubling the number of test particles does not lead to a difference in the flow coefficients. For completeness, the same consistency check has been performed for the directed and elliptic flow of deuterons, where the same dependence on the number of test particles was found so the plots are omitted here. We conclude that representing each particle by twenty test particles is sufficient for the setup presented here.

Since the introduction of parallel ensembles in the SMASH transport model, one can with feasible numerical effort obtain much better statistics. For the work presented in the following chapters, the twenty test particles are therefore replaced by a larger number of parallel ensembles (300 in Chapter 5 and 1000 in Chapter 4).

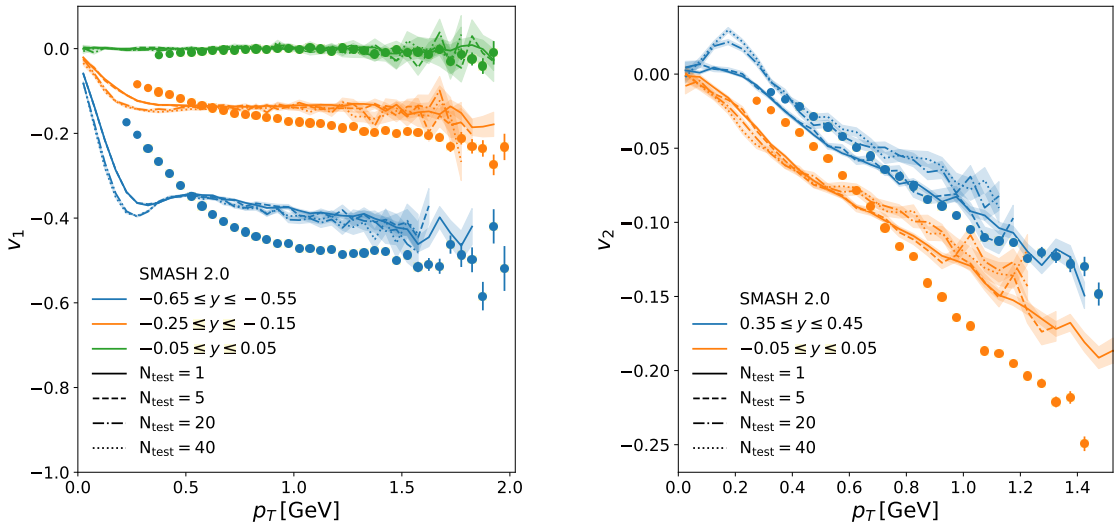

(a) Directed flow of nucleons.

(b) Elliptic flow of nucleons.

Abbildung 3.6: Flow of nucleons as a function of transverse momentum in 20%-30% central gold-gold collisions at $E_{\text{kin}} = 1.23A\,\text{GeV}$ for different rapidity bins, compared to experimental data points from [189]. The calculations compare cases where each particle is represented by a different number of test particles, N_{test}. Taken from [1].

3.5.2 Dependence on Smearing Width

For the results presented in this work a smearing kernel is applied to each test particle for calculating the densities required for the evaluation of the potentials. The specific form of the covariant Gaussian smearing that was used is introduced in [154]. Applying the Gaussian smearing one can efficiently calculate the density with a moderate number of test particles as described in the previous section. However, the smearing introduces a free parameter to the model that is the smearing width σ of the Gaussian. The smearing parameter is set to $\sigma = 1.0\,\text{fm}$ for all results presented in this thesis.

In Figures 3.7a and 3.7b the results for v_1 and v_2 for nucleons obtained with $\sigma = 1.0\,\text{fm}$ are compared to $\sigma = 0.75\,\text{fm}$ and $\sigma = 0.25\,\text{fm}$. One can see a significant dependence on the smearing width. However, the difference between $\sigma = 1.0\,\text{fm}$ and $\sigma = 0.75\,\text{fm}$ is small enough so that the conclusions from this work would still hold for $\sigma = 0.75\,\text{fm}$. For $\sigma = 0.25\,\text{fm}$ the difference is large. The reason for this difference is that the width is in this case too small and no smooth density profile can be obtained with only 20 test particles. For a more clear comparison the number of test particles is kept equal throughout this plot but a better agreement between the calculations is expected with a larger number of test particles.

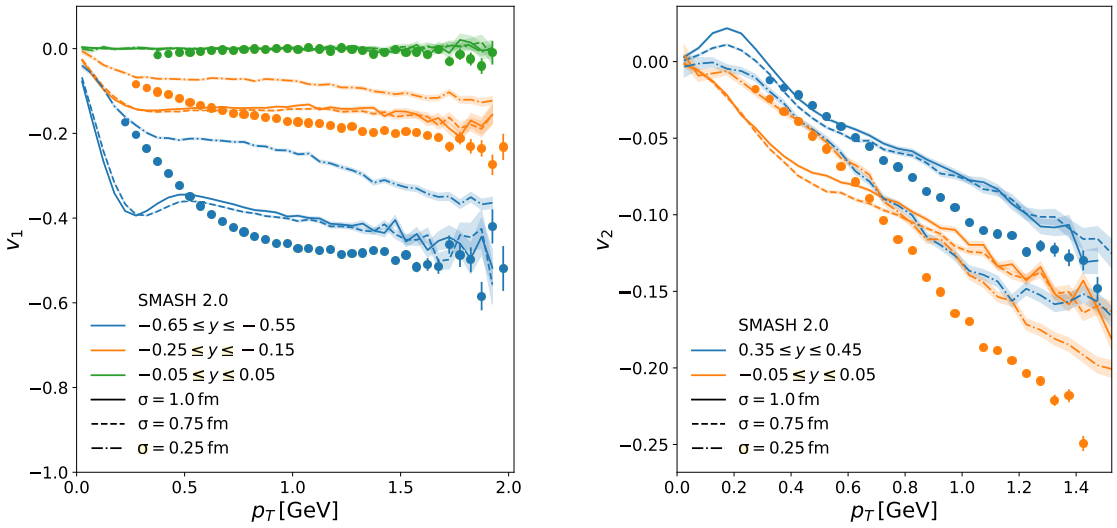

(a) Directed flow of nucleons.

(b) Elliptic flow of nucleons.

Abbildung 3.7: Flow of nucleons as a function of transverse momentum in 20%-30% central gold-gold collisions at $E_{\text{kin}} = 1.23A\,\text{GeV}$ for different rapidity bins, comparing three calculations with varying smearing widths. Taken from [1].

3.6 Conclusions

In this study, the double-differential directed and elliptic flow of protons and deuterons is compared to experimental flow measurements from Au+Au collisions at $E_{\text{kin}} = 1.23A, \text{GeV}$, as provided by the HADES collaboration. Different parameter sets for the Skyrme potential, each corresponding to a distinct equation of state, are employed.

With the currently implemented potentials, the elliptic flow of nucleons and deuterons cannot be accurately described. Therefore, more sophisticated potentials, including momentum dependence, are necessary to extract the equation of state from flow measurements. Such potentials will be applied in the following chapters.

The main focus of this work is the formation of light nuclei in low-energy heavy-ion collisions, which cannot be neglected even when considering only the flow of nucleons. Two different approaches for accounting for deuteron formation are implemented. By comparing these methods, we identify kinematic regions where the extraction of the equation of state is cleaner, as the observables are less sensitive to the light nuclei formation mechanism. Flow coefficients in the high-momentum region are found to be particularly well-suited for a systematic study of the EoS.

In the setup with dynamic deuteron formation, the evolution of the multiplicity and flow of nucleons and deuterons over time is studied. The flow of nucleons and

deuterons shows very similar time dependence, although the directed and elliptic flow coefficients are sensitive to different stages of the evolution. The directed flow develops from the outset due to the bounce-off effect, while the time-dependence of the elliptic flow is more complex. For elliptic flow, pressure gradients initially lead to a positive flow signal, which later becomes negative due to interactions with the remnants of the colliding nuclei.

Kapitel 4

Bayesian Constraints on the Equation of State based on HADES Data

The primary goal of this thesis is to constrain the equation of state of nuclear matter. In this chapter, we present work that builds on the sensitivity study from Chapter 3. This work focuses on comparing theoretical results to experimental flow data from the HADES collaboration and makes use of the previous finding that the EoS is most effectively studied by comparing flow data at relatively high transverse momentum.

Compared to the previous study, several key upgrades have been implemented in the model. The momentum-dependent component of the potential is now available, which is crucial for making meaningful statements about the equation of state, as discussed in Section 4.1. Additionally, electromagnetic potentials have been incorporated into SMASH (see Section 2.1.4), and their influence is considered in the calculations performed in this chapter (see Section 4.1). Moreover, the coalescence model has been improved to explicitly form light nuclei, enabling us to study their flow as well (for details on clustering, see Section 2.3).

With the improvements to various facets of the model, a good agreement to the experimental data is achieved, as presented in Section 6.3. This calls for a more sophisticated extraction of the EoS from the data. To achieve this, a Bayesian parameter estimation is performed and presented in this chapter. Using this method, the best parameter set can be identified in a controlled way and a statistical uncertainty can be determined. The results presented in this chapter are part of Reference [2].

4.1 Sensitivity Study

Before advancing to the results, a short study of the influence of newly implemented features in the model is presented. The aim is to make a well informed decision on technical options regarding the comparison to experimental data, and to study the importance of including physics features, namely the Coulomb potential and the momentum-dependent term in the potential.

All model curves shown in this section are obtained by training a Gaussian process on real SMASH calculations, and evaluating that Gaussian process. A verification of the Gaussian process is presented for the final model choice in Section 4.2. Of course, such a verification has been performed all the curves presented in this chapter.

Next, the differences in elliptic flow resulting from various methods of centrality selection are investigated, followed by an evaluation of the necessity of electromagnetic potentials and momentum dependence.

4.1.1 Centrality selection

The classification of events into centrality intervals is an important task, since the directed and elliptic flow signals are induced by the geometry of the system. In that sense, the impact parameter, to a large extend, determines the anisotropy in the final state. We compare, in this section, two methods of performing the centrality selection.

The first one is by using a fixed range of impact parameters for each centrality class, as it is extracted from the Glauber model. The impact parameter ranges used for the comparison to gold-gold collisions at the HADES experiment have been determined in [190]. The centrality selection in the experiment is, however, performed event by event, based on the number of hits in the detector. Naturally, small impact parameters correlate to more activity in the detector but not every single event with a small impact parameter yields a larger number of tracks in the detector than an event with a larger impact parameter. Clearly, it is worthwhile to investigate how large the difference is, if the activity in the detector is simulated for every individual event of the model calculation, and the events are grouped into centrality classes based on that. For this purpose, the number of detector hits is calculated in a large number of minimum-bias events in the model. The events are then grouped into centrality classes based on the number of hits, and a mapping from the number of hits to the corresponding centrality class is created. This way, the centrality selection can be performed based on detector hits, even if the model does not necessarily describe the produced number of particles perfectly.

Taking the acceptance and efficiency of the detector into account, such a centrality determination is performed here. A comparison between the centrality selection

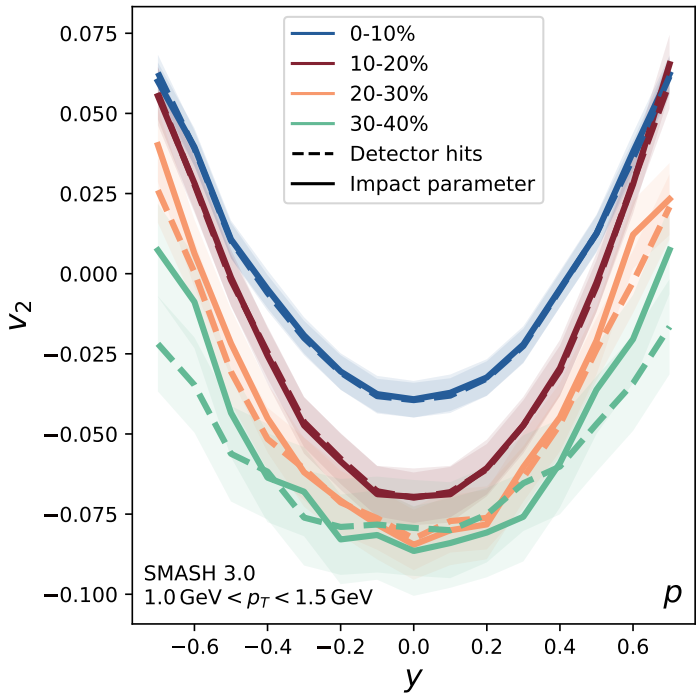

Abbildung 4.1: Directed flow of protons for different centrality intervals in gold-gold collisions at $E_{\text{kin}} = 1.23A\,\text{GeV}$, comparing different methods for classifying centrality intervals. Solid lines represent centrality selection based on the impact parameter, while dashed lines correspond to selection based on the simulated number of tracks in the detector. The curves are generated using a Gaussian emulator trained on SMASH calculations. The potential parameters chosen for this figure are set at the center of the prior range. Taken from [2].

via the impact parameter and via the number of detector hits is shown, in Figure 4.1, for the elliptic flow of protons in different centrality classes. For this observable, mostly no difference is found for the elliptic flow, except in the forward and backward region, but even there the difference is statistically not significant. Figure 4.1 does not include experimental data points, because both calculations were performed without the momentum-dependent term, which is essential for a reasonable description of the data, as we show in Section 4.1.3. This comparison is performed without momentum-dependence, because the mapping from detector hits to centrality classes has been generated for the potentials without momentum-dependence. The observation was made that the dynamics of the system change quite significantly when including the momentum-dependent part, such that the other mapping cannot be applied without modification.

As we do not observe a significant difference between the two methods in Figure 4.1, the centrality selection is performed based on the impact parameter in the following calculations. Still, the method is very interesting, as it is very close to the experiment, and it may be important for different observables or other kinematic ranges.

4.1.2 Coulomb Potential

Charged particles interact electromagnetically. Clearly, this should be taken into account for a realistic calculation, but one should study here how big the impact of electromagnetic potentials is. The thought behind this sensitivity study is, that the long range of the electromagnetic interaction makes is numerically expensive to include in a BUU-type calculation. The difference in the elliptic flow of protons between a calculation including the Coulomb potential and a one neglecting the Coulomb potential is presented in Figure 4.2. While the observed elliptic flow is almost unchanged in central events, a sizable effect is observed in other centrality classes. As the system is positively charged, the Coulomb potential asserts a repulsive force, so that the elliptic flow signal is enhanced due to the inclusion of the Coulomb potential.

We conclude that the inclusion of the Coulomb potential is worth the numerical costs. The results presented in Section 4.2 are obtained with the Coulomb potential included. This is, for this study, especially needed, because the symmetry potential is treated as a parameter of the Bayesian analysis, and only when the Coulomb potential is included in the calculation, one can cleanly extract the contribution of the symmetry energy.

4.1.3 Momentum-dependent Potentials

The optical model has been used to extract constraints on the momentum-dependence of the nuclear potential at saturation density from $p + A$ scattering experiments in [144], [192]. The potential extracted this way can, of course, only be described including a momentum-dependence in the potentials.

It is still instructive to investigate the influence of the momentum-dependent term on flow observables in the SMASH model to verify the necessity of the momentum-dependence based on heavy-ion collisions. In this section, we further aim to show how good of an agreement with experimental data can be achieved with and without momentum-dependence when the parameters are tuned to the experimental data.

For this purpose, we perform the Bayesian analysis, that is described in more detail for the full model in Section 6.3, once with and once without momentum-dependence. We find the maximum of the posterior distribution, which is the parameter set that has the most overlap with the experimental data. In Figure 4.3,

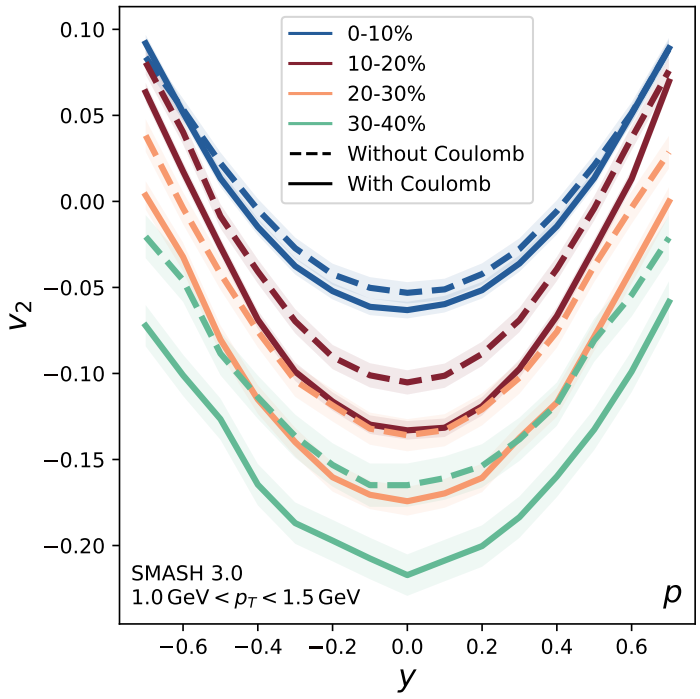

Abbildung 4.2: Elliptic flow of protons for different centrality intervals in gold-gold collisions at $E_{\text{kin}} = 1.23A\,\text{GeV}$, comparing calculations that include and disregard the Coulomb potential. The curves are generated using a Gaussian emulator trained on SMASH calculations. The potential parameters for this figure are set at the center of the prior range. Taken from [2].

we present the elliptic flow of protons for the best possible parameter set including momentum-dependence and for the best parameter set without momentum-dependence. Note that the parameters are not tuned to only this observable but to v_1 and v_2 of protons and deuterons (see Fig. 4.4). For the sensitivity test presented in Figure 4.3, the Coulomb potential is neglected, but one can clearly see that the data cannot be described without momentum-dependence in SMASH. When the momentum-dependent part is included, one observes a stronger elliptic flow signal. It is still weaker than the experimental measurement, but a further improvement is presented in Section 4.2, where the Coulomb potential is added.

All results presented in the following include the momentum-dependent part of the potential, as it is necessary to be consistent with the findings from the optical model and it strongly enhances the agreement with experimental data.

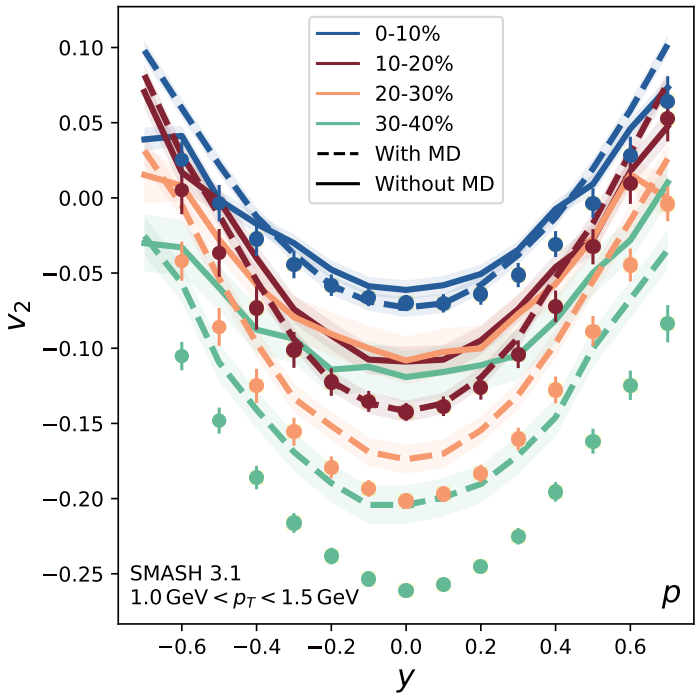

Abbildung 4.3: Elliptic flow of protons for different centrality bins in gold-gold collisions at $E_{\text{kin}} = 1.23A\,\text{GeV}$, comparing calculations with and without the momentum-dependent term. All curves are predicted using a Gaussian process trained on SMASH output. For both models, the parameters that provide the best overall description of the data shown in Figure 4.4 are selected. Taken from [2].

4.2 Results

Let us start this section with a plot of the experimental data [114], that we include in the Bayesian analysis. It is shown in the four panels of Figure 4.4, together with a prediction from the Gaussian process, that was trained on output from the SMASH transport model. The prediction from the Gaussian process was done for a parameter set located in the center of the covered parameter space to validate that the Gaussian process can provide realistic results, before finding the best parameter set.

To further test the Gaussian process prediction for different points in the parameter space, Figure 4.5 shows the elliptic flow of protons in a single centrality class. Let us start by comparing the curves for the small ($\kappa = 201\,\text{MeV}$) and large $\kappa = 400\,\text{MeV}$ incompressibilities. We observe that a larger incompressibility leads to a stronger elliptic flow signal, which is reassuring, because a stiffer equation of state amplifies the squeeze-out effect. As expected, the same behaviour for deuterons in

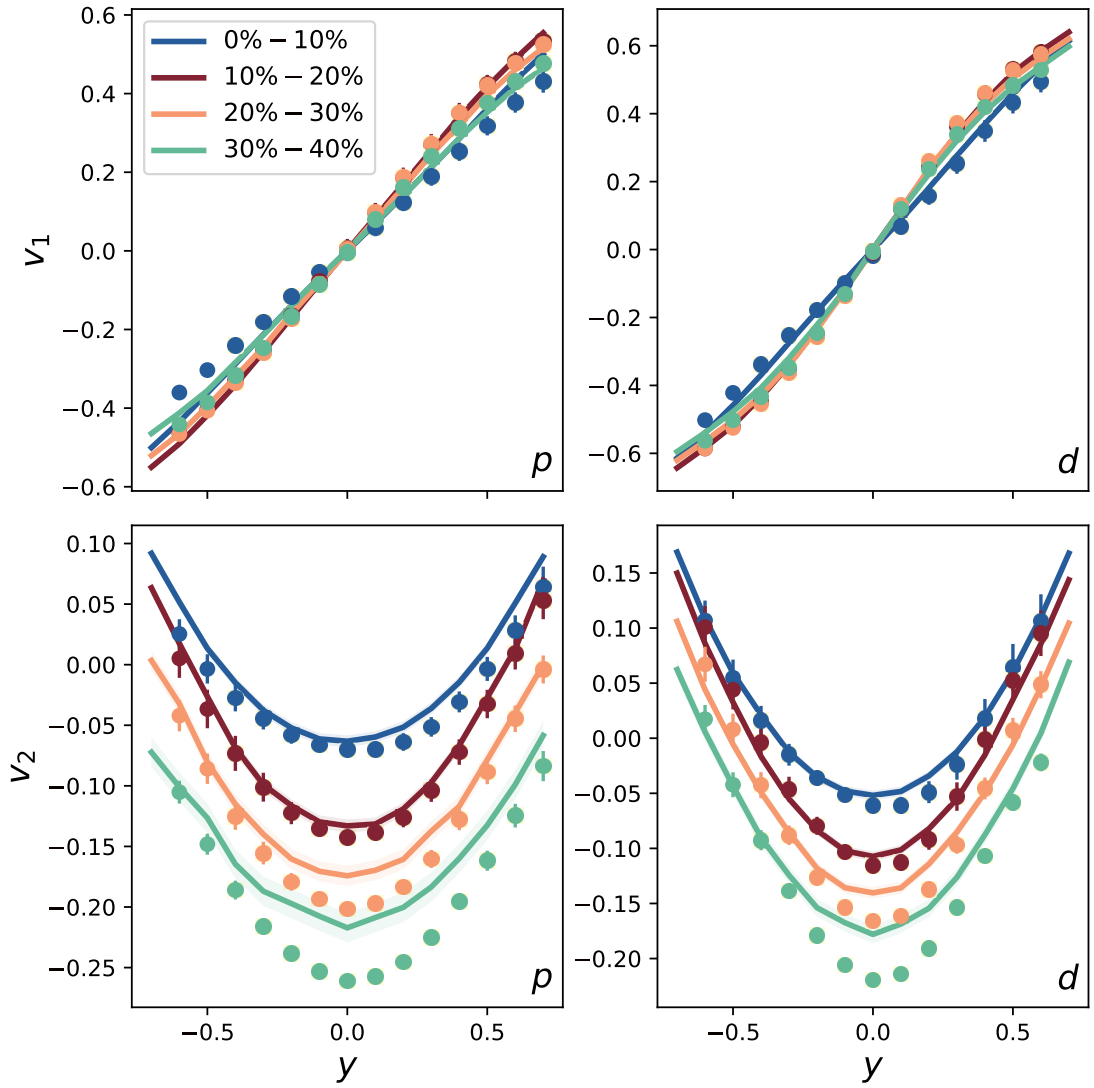

Abbildung 4.4: Directed flow v_1 and elliptic flow v_2 for protons and deuterons as a function of rapidity for $1.0\,\mathrm{GeV} < p_T < 1.5\,\mathrm{GeV}$ in gold-gold collisions at $E_{\mathrm{kin}} = 1.23A\,\mathrm{GeV}$. The circles represent experimental data [114] and the lines are predictions from the Gaussian process trained on SMASH calculations. The Gaussian process is, for validation, evaluated in the center of the parameter space $\kappa = 300.5\,\mathrm{MeV},\ S_{\mathrm{Pot}} = 15\,\mathrm{MeV}$. Taken from [2].

Figure 4.6 is observed. The impact of the symmetry potential is shown Figures 4.5 and 4.6 at a fixed value for the incompressibility. Comparing the curves for a small and a large symmetry potential, we observe no difference for the deuterons. This is

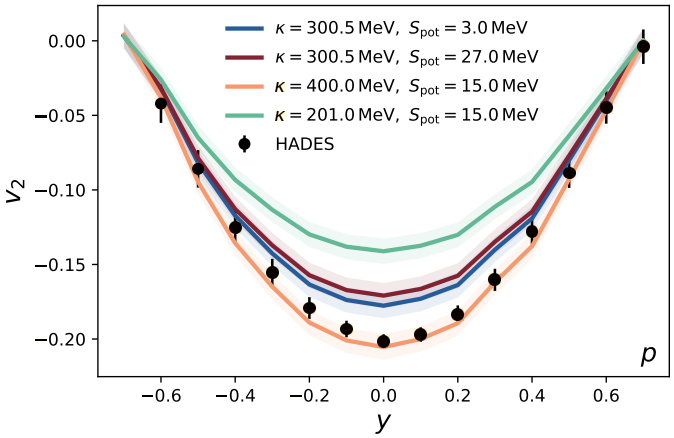

Abbildung 4.5: Elliptic flow v_2 of protons as a function of rapidity for $1.0\,\mathrm{GeV} < p_T < 1.5\,\mathrm{GeV}$ in the $20\% - 30\%$ most central gold-gold collisions at $E_{\mathrm{kin}} = 1.23A\,\mathrm{GeV}$. Experimental data [114] are shown as black circles and compared predictions from the Gaussian process trained on SMASH calculations for different points in the parameter space. Taken from [2].

expected, as it does not experience any force from that potential, since the deuteron does not carry isospin charge. For protons, we find that the elliptic flow signal is slightly more pronounced with a weaker symmetry potential. As the gold nuclei have more neutrons than protons, the I_3 density is negative in the system. That means, the symmetry potential is attractive for protons, which leads to the smaller elliptic flow that we observe in Fig. 4.5.

As the Gaussian process emulator reproduces the behavior that we would expect from the transport model, we can perform a Bayesian analysis based on it. The posterior distribution that we obtain as a result is shown in Figure 4.7. The 68.3% credibility interval of our parameters is $\kappa = 348.2^{+4.0}_{-3.9}\,\mathrm{MeV}$ and $S_{\mathrm{Pot}} = 15.8^{+4.7}_{-4.6}\,\mathrm{MeV}$. First thing to note is that this analysis leads to a relatively stiff equation of state compared to [111], for example. According to this analysis, there is only a small uncertainty on the value for the incompressibility, and the results are, therefore, not consistent with previous estimates. We would like to highlight here, that the parameter estimation is based on the assumption that the model is flawless, which is of course not the case. The problem that a different equation of state is required to describe the data, depending on the applied transport model, persists, but efforts within the Transport Model Evaluation Project (TMEP) aim to resolve this issue in the future.

The symmetry potential we find is consistent with the default value $S_{\mathrm{Pot}} = 18\,\mathrm{MeV}$ used in previous studies [1], [3], but the uncertainty on this parameter is

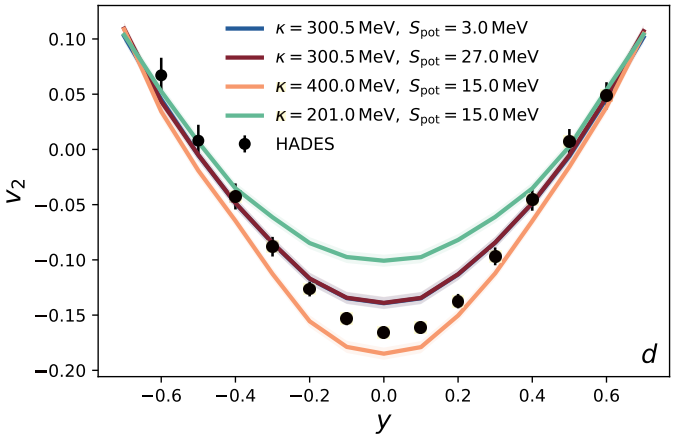

Abbildung 4.6: Elliptic flow v_2 of deuterons as a function of rapidity for $1.0\,\mathrm{GeV} < p_T < 1.5\,\mathrm{GeV}$ in the $20\% - 30\%$ most central gold-gold collisions at $E_{\mathrm{kin}} = 1.23A\,\mathrm{GeV}$. Experimental data [114] are shown as black circles and compared predictions from the Gaussian process trained on SMASH calculations for different points in the parameter space. Taken from [2].

quite large. One reason for the low sensitivity is that the system has only a small asymmetry, as there is no large excess of neutrons in the gold nuclei compared to protons as it is the case in neutron star mergers, for example. Another reason is that the choice of observables, proton and deuteron flow, is done to mainly obtain information on the stiffness, but not so much on the symmetry energy. The value for S_{Pot} can be related to the symmetry energy at saturation density S_0. For the 68.3% credibility interval we find $24.2\,\mathrm{MeV} < S_0 < 33.5\,\mathrm{MeV}$.

One can take the maximum of the posterior distribution and calculate the observables based on the Gaussian process, as shown in Figure 4.8. As the prior was chosen to be flat, the maximum of the posterior is the parameter set that has the best agreement with the experimental data. A good overall agreement with the experimental data found. This is, on one hand, expected, as we fit the potentials to match the flow data, but, on the other hand, reassuring that a fair description for so many data points was achieved by varying only two parameters.

The equation of state for symmetric nuclear matter at vanishing temperature can be calculated from the estimated parameters. It is given in terms of the pressure as a function of the baryon density in Figure 4.9 in comparison with the estimates from Danielewicz [111] and Huth [122]. Especially compared to the work by Danielewicz et al., a relatively stiff equation of state is obtained here. This may be related to the large amount of resonances present in the SMASH model. The influence of the resonance content in the calculation on the conclusions regarding the EoS has been

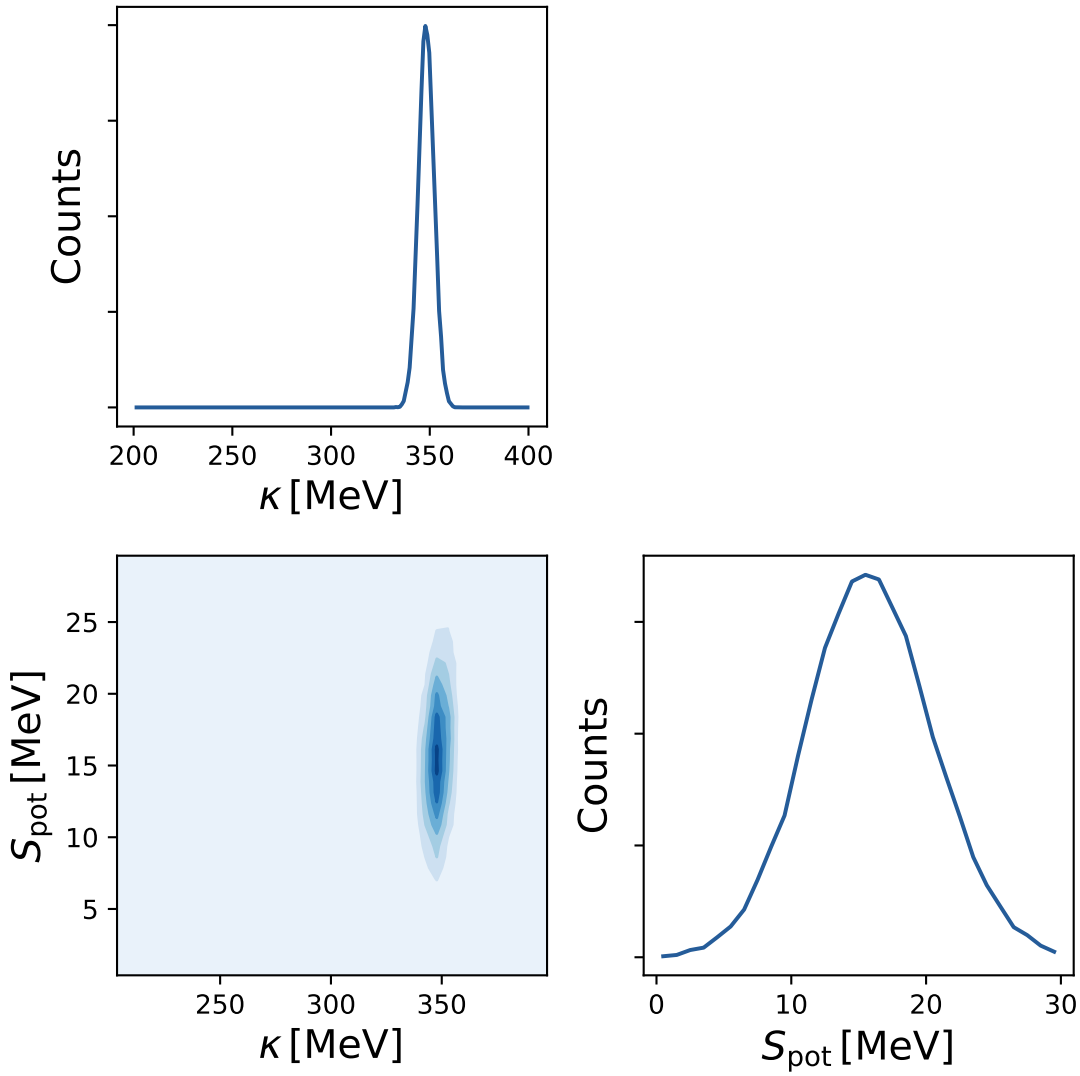

Abbildung 4.7: Posterior distribution for the parameters κ and S_{Pot}. The bottom-left panel shows the posterior distribution as a function of both parameters, while the upper and right panels show the posterior as a function of κ and S_{Pot}, respectively, with the other parameter integrated out. Taken from [2].

reported in [110]. Another difference of the models, that can alter the required EoS to describe data, is the assumed form of the potentials. Figure 4.9 contains only information at zero temperature. Since nuclear matter is probed in a hot system in heavy-ion collisions, a different form of the potential can lead to a different equation of state at vanishing temperature.

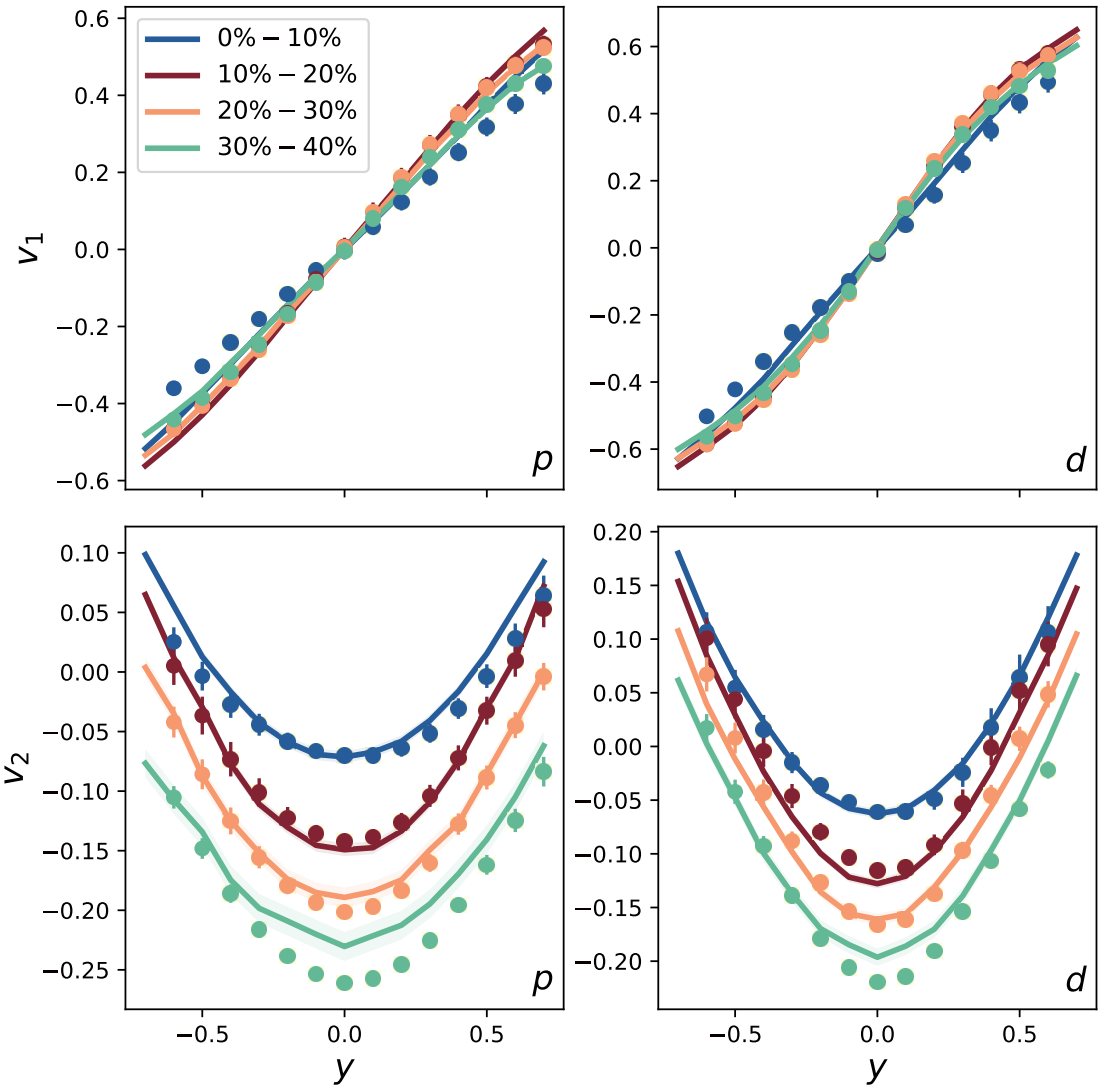

Abbildung 4.8: Directed flow v_1 and elliptic flow v_2 for protons and deuterons as a function of rapidity for $1.0\,\mathrm{GeV} < p_T < 1.5\,\mathrm{GeV}$ in gold-gold collisions at $E_{\mathrm{kin}} = 1.23A\,\mathrm{GeV}$. The circles represent experimental data [114], and the lines are predictions from the Gaussian process trained on SMASH calculations. The Gaussian process is evaluated at the maximum of the posterior distribution $\kappa = 348.2\,\mathrm{MeV}$, $S_{\mathrm{Pot}} = 15.8\,\mathrm{MeV}$. Taken from [2].

In addition to the difference in the pressure, one can observe that the uncertainty from this work, presented in Figure 4.9, is very small. This is due to the fact that only statistical uncertainties are included in the determination of the posterior dis-

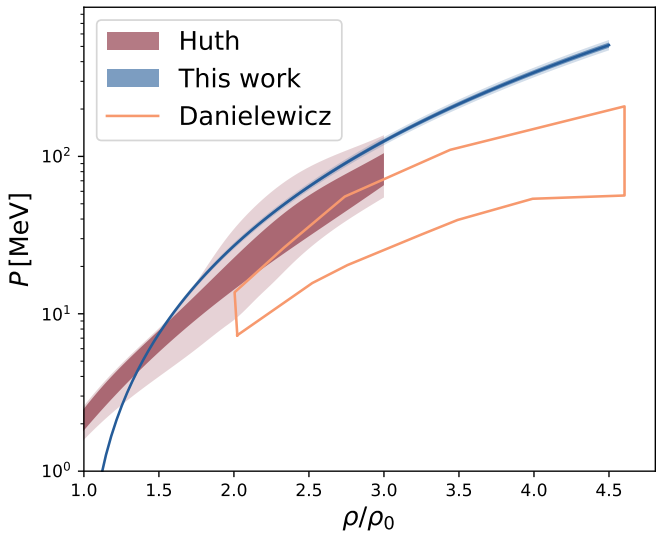

Abbildung 4.9: Equation of state of symmetric nuclear matter at zero temperature as a function of the baryon density. The estimate from this work is compared to the results from [122] and [111]. Taken from [2].

tribution, but systematic model uncertainties are not taken into account. The small width of the posterior distribution demonstrates how much information is contained in the experimental data, showing a great perspective for future studies, once models have converged in their predictions for flow observables.

4.3 Meson Spectra

In this section, calculations for the yield of pions and kaons within the improved settings of SMASH, including nuclear mean fields compatible with the flow measurements are presented. While the kaon production is known as an excellent probe for the equation of state, the pion yield is not often considered as a suitable observable. In the SMASH model, there is a strong sensitivity of the pion yield to the EoS, and, therefore, the number of pions that are obtained when including the momentum-dependent potentials, with the parameters that best describe the flow measurement, is presented. The incompressibility and symmetry potential are set to $\kappa = 349.5\,\text{MeV}$ and $S_{\text{pot}} = 18.16\,\text{MeV}$ respectively, which is close to the maximum of the posterior from Section 6.3[1]. In Figure 4.10, the rapidity spectra for positively

[1]The parameters of the potential slightly differ from the MAP values because they were obtained in a previous analysis

and negatively charged pions is compared to experimental data in different centrality classes. For the model, we present the direct calculation using SMASH and a Gaussian process that is trained on the model output and agrees with the direct model calculation. We choose not to include the pion spectra in the Bayesian analysis due to the observed overshoot in the pion yield compared to the measurement. The pions in the SMASH model do not experience nuclear potentials and, as there is some tension between the pion multiplicity measured at the HADES and at the FOPI experiment, the pions are not taken into account in the likelihood function.

In the current version of the SMASH model, kaons also do not experience potentials. Strangeness potentials are considered to be an important ingredient for describing the production of kaons. There is, however, a strong influence of the inclusion of the momentum-dependent term as well as variation of the stiffness of the equation of state on the kaon yield in SMASH calculations. A similar dependence was obtained in a QMD calculation in [194]. Without strangeness potentials, the kaons are not included in the Bayesian analysis but the yield is presented in Figure 4.11.

The positively charged kaons slightly overshoot the experimental measurement, but a realistic number of kaons is found. The rapidity distribution for the positively charged kaons is found to be more tight than observed in the experiment.

The multiplicity of negatively charged kaons is very small. One can see, that the kaon yield is quite well described, and the shape of the spectrum seems to be described better than for the positively charged kaons. The limited amount of statistics does not allow for more definite statements however. In future work, including the kaon yield is certainly interesting as it provides a different angle to study the equation of state in heavy-ion collisions. Even though the yield can be described consistently with the flow measurements, one should investigate the influence of strangeness potentials before including the kaon spectra in the analysis.

4.4 Conclusions

In this chapter, the SMASH transport model is applied to extract constraints on the equation of state from flow measurements at the HADES experiment. Compared to Chapter 3, several model improvements are introduced: the inclusion of a momentum-dependent term in the nuclear potential, the Coulomb potential, and an enhanced coalescence approach for light nuclei formation. The model is then compared to the directed and elliptic flow of protons and deuterons in gold-gold collisions across multiple centrality classes.

Constraints on the incompressibility of nuclear matter at saturation density and the symmetry potential are obtained. Through Bayesian analysis, a tight constraint on a relatively stiff equation of state was found, while a looser constraint was obtai-

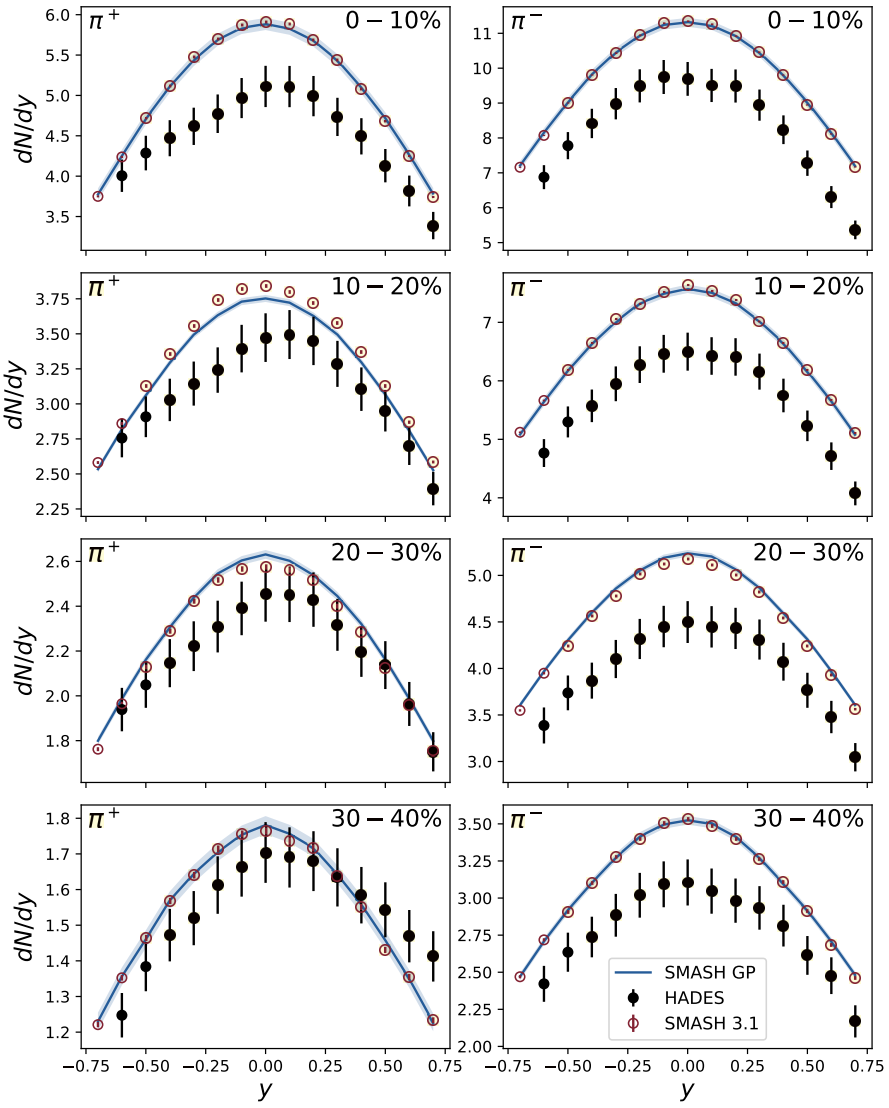

Abbildung 4.10: Rapidity spectra for positively and negatively charged pions for different centrality classes, compared to experimental data from the HADES experiment [193]. A direct calculation with the SMASH transport model is presented together with the prediction from the Gaussian process, that was trained on SMASH output. The incompressibility and symmetry potential are set to $\kappa = 349.5\,\mathrm{MeV}$ and $S_{\mathrm{pot}} = 18.16\,\mathrm{MeV}$, respectively. Taken from [2].

ned for the symmetry potential

The findings are based on a single model with all its limitations. Therefore, extending this Bayesian analysis to include multiple transport approaches would be

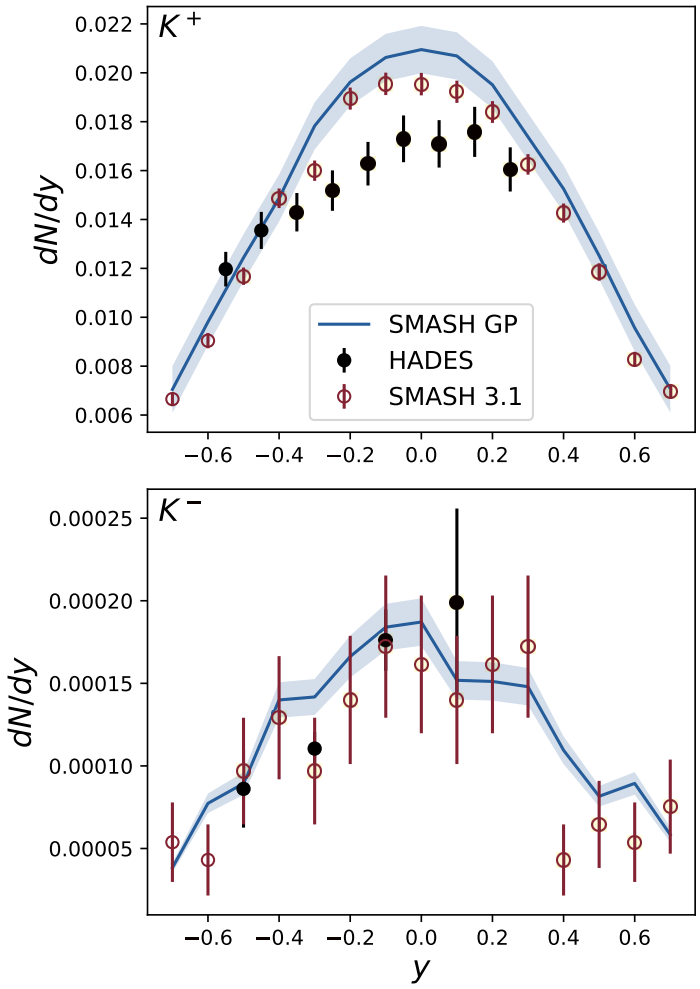

Abbildung 4.11: Rapidity spectra of positively and negatively charged kaons in the 0−40% centrality interval, compared to experimental data [195]. A direct calculation with the SMASH transport model is presented together with the prediction from the Gaussian process, that was trained on SMASH output. The incompressibility and symmetry potential are set to $\kappa = 349.5\,\mathrm{MeV}$ and $S_{\mathrm{pot}} = 18.16\,\mathrm{MeV}$, respectively. Taken from [2].

valuable, allowing for the estimation of a global systematic uncertainty in future studies.

Kapitel 5

Investigation of the Equation of State by Comparing to FOPI Data

To obtain information about the EoS, it is instructive to probe it at different densities. In the previous chapters, conclusions about the EoS are drawn by comparing SMASH calculations only to experimental data for gold-gold collisions at a single collision energy. The probed density is, of course, not constant throughout the evolution of a heavy-ion collision, but evolves over time and depends on the centrality. Still, one can actively vary the probed region in the phase diagram by changing the collision system (see Section 1.2). Useful handles to do so are by changing the collision energy and the size of the colliding nuclei.

Flow observables have been measured at various collision energies at the FOPI experiment, where, additionally, data for different collision systems is available. In this chapter, flow calculations from the SMASH model are compared to the FOPI data. In this energy range (the energy range $0.2\,\mathrm{GeV} \leq E_{\mathrm{kin}}/A \leq 1.5\,\mathrm{GeV}$ is considered here), the baryon density increases with increasing energy as matter becomes more compressed. Therefore, the collisions at larger incident energy probe the EoS at higher densities. The variation of the incident energies helps to disentangle the density dependence of the EoS. This chapter is based on [3].

5.1 Setup and Analysis

Before comparing the model to the experimental data, we first clarify the technical setup of the calculation. We begin by outlining the key aspects of the numerical setup, followed by an introduction to the scaled variables commonly used in the FOPI experiment. Finally, we define and verify the centrality selection criteria before presenting the results.

5.1.1 Calculation Setup

For the calculations presented in this work, the Skyrme and symmetry potential are applied including the momentum-dependent term. The Coulomb potential is not applied in this study because it was at the time the calculations were performed not sufficiently tested. Additionally the inclusion of the electromagnetic potentials in the current implementation is numerically very expensive.

In this work, the formation of light nuclei is in most cases taken into account with the final version of the coalescence model as described in Section 2.3. In some cases a comparison to the dynamic formation of deuterons and $A = 3$ nuclei via the stochastic collision criterion is presented.

On the technical side, the two approaches require different settings. For the application of the coalescence model, the oversampling with test particles makes it more difficult to define light nuclei in the final state. In this setup it is more straight-forward to obtain a stable density calculation applying the parallel ensemble technique with a single test particle per real particle in each ensemble. For this calculation 300 parallel ensembles are used.

The stochastic collision criterion does rely on a sufficient number of test particles per cell and for this reason, the setup established in [183] is used. It contains 25 test particles per real particle with no parallel ensembles. For both calculation setups, the time step size is $\Delta t = 0.1\,\mathrm{fm}$. The system is evolved at least until no more interactions take place. To achieve this, the evolution os performed until $t = 100\,\mathrm{fm}$ after the initial nuclei touch. A study of the time evolution of the system is shown in the beginning of Section 5.2. One can see there that the dynamics of the system change mostly in the first 30 fm but a flattening can be observed afterwards. Ending the evolution at 100 fm is therefore safe.

5.1.2 Observables and kinematic variables

Flow coefficients are the main observable studied here. They are calculated using the reaction plane method in this study (see Section 1.2.2) for the definition of flow coefficients). This method is very reliable if the reference plane can be estimated experimentally.

Following published data, the directed and elliptic flow coefficients are presented as a function of transverse momentum per nucleon and rapidity, both normalized to the projectile values. These are defined as $p_{\mathrm{T}}^{(0)} = (p_{\mathrm{T}}/A)/(p_{\mathrm{P}}/A_{\mathrm{P}})$ and $y^{(0)} = (y/y_{\mathrm{P}})$, respectively. The subscript P denotes characteristics of the projectile. In this chapter, this quantities are called for simplicity transverse momentum and rapidity, although they are normalized quantities.

The impact of the detector acceptance loss for very forward angles ($\theta_{\mathrm{lab}} < 1.2°$) was tested and found negligible. Thus, this geometrical cut is not applied in the

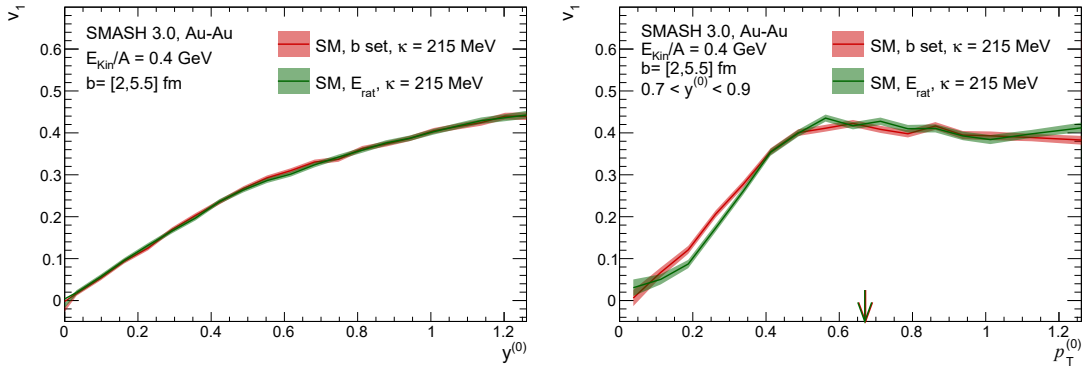

Abbildung 5.1: Directed flow coefficient v_1 as a function of rapidity (left) and transverse momentum for $y^{(0)} = 0.7 - 0.9$ (right) for Au–Au collisions at $0.4A\,\mathrm{GeV}$. Two centrality selection methods are compared, based on b and, as in data, employing E_{rat}. The arrows in the right panel indicate the mean $p_{\mathrm{T}}^{(0)}$. Taken from [3].

simulations.

5.1.3 Centrality selection

The default way for the collision centrality selection in the SMASH simulations is a direct setting of the impact parameter b. Since b can not be experimentally measured directly, the collisions in the experimental data are divided based on the charged-particle multiplicity and the E_{rat} variable defined as

$$E_{\mathrm{rat}} = \frac{\sum_i E_{\perp,i}}{\sum_i E_{\parallel,i}}\,, \tag{5.1}$$

where the sums run over the transverse and longitudinal kinetic energy components of all the particles detected in an event. First, the multiplicity distribution is divided into classes, based on percentiles of the inelastic (geometric) cross section. Then, based on the correlation between E_{rat} and the multiplicity, the collisions with the highest multiplicities and highest E_{rat} are selected as the most central collisions. For the analysis performed here, the actual ranges of b used for different centrality classes are taken from the assignments performed in Ref [196], [197].

In order to check that centrality selections based on the impact parameter lead to the same centrality ranges as in the experimental selection, the E_{rat} method is used in simulations and compared with the selection based on the impact parameter. The result of this check is shown in Figure 5.1 for semi-central Au–Au collisions at $E_{\mathrm{kin}}/A = 0.4\,\mathrm{GeV}$. As can be seen, the two methods give practically identical results for v_1, both as a function of rapidity and transverse momentum. In the appendix, similar figures are provided also for the other two studied collision systems, Xe–CsI

and Ni–Ni, showing consistency of the two methods in these cases, too. Based on this, the selection on the impact parameter is used in the following analysis.

5.1.4 Particle selection

Particle selection in the model is performed as for the data, namely $Z = 1$ particles. In SMASH, deuterons and tritons are produced with an afterburner based on the coalescence model as described in Sec. 2.3. In the case of the study of v_2 at midrapidity, the stochastic collision criterion is used as well, as described in Sec. 2.3. In this case, the simulations are marked in the legends of the figures with an additional ß", e.g. HMs stands for Hard EoS with momentum-dependent potentials and the stochastic collision criterion. The impact of spectator nuclei, which can significantly influence directed flow at forward rapidities, is suppressed by selecting only particles which interacted at least once during the evolution of the system. This is not possible in case of the stochastic collision criterion, where also the particles in the spectator part of the colliding nuclei interact. As a consequence, the stochastic collision criterion is used only for the studies of v_2 at midrapidity, where the impact of the spectators is negligible.

5.2 Results

5.2.1 Evolution of the System

The time evolution of the average density in the central cell of the participant zone at $E_{\mathrm{kin}}/A = 0.4\,\mathrm{GeV}$ is shown in Figure 5.2 (left) for two impact parameter ranges of Au-Au collisions. The impact parameter range shown for Ni–Ni collisions corresponds to the more central Au–Au class. For both systems, soft and hard EoS parametrizations are compared. As expected, a soft EoS leads to larger average densities than the hard EoS. While differences between the two EoS parametrizations are significant, the dependence on the system size is rather weak. The duration of the dense phase is shorter in Ni–Ni compared to Au–Au following the expectation. In Figure 5.2 (right), the evolution of the directed flow coefficient v_1 with time for two centralities in Au–Au collisions is shown. The directed flow is larger for the stiffer EoS. It mainly builds up between 10 and 30 fm and continues to rise at later times when the density is already significantly smaller in the central cell. One can observe that the directed flow builds up earlier and more rapidly with a stiff EoS, which can be associated to a stronger bounce off compared with the case of soft EoS.

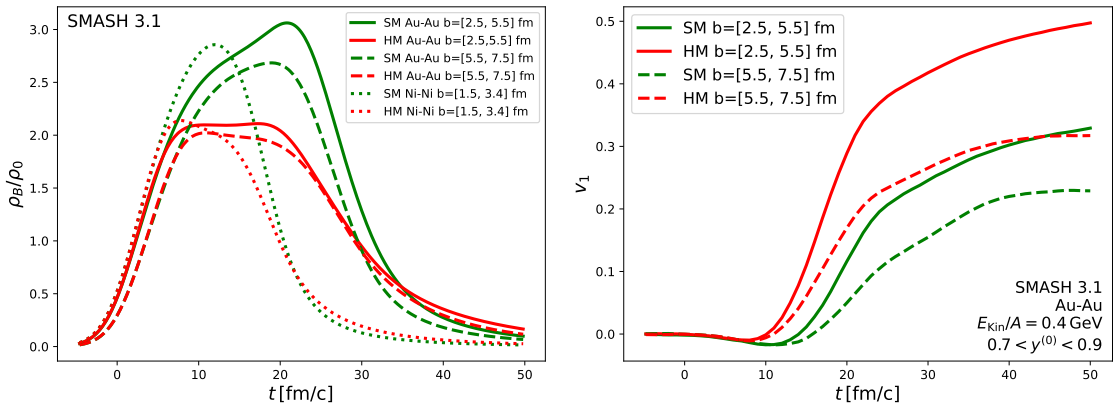

Abbildung 5.2: Left: normalized baryon density for two centrality classes in Au–Au collisions and one centrality for Ni–Ni collisions at $0.4A$ GeV as a function of time. Right: the directed flow v_1 of protons at forward rapidity for Au–Au collisions in two centrality classes as a function of time. Taken from [3].

5.2.2 Comparison of Directed Flow

To study the EoS and the impact of different potentials, a beginning is made by investigating the directed flow v_1 of charged particles as a function of rapidity and transverse momentum. Figure 5.3 compares v_1 for Au–Au collisions at $E_{\text{kin}}/A = 0.4\,\text{GeV}$ with a broad set of model settings. It is found that the momentum dependent potentials lead to a higher directed flow for $p_{\text{T}}^{(0)}$-integrated values (l.h.s.). When studying v_1 as a function of $p_{\text{T}}^{(0)}$ in a selected bin of rapidity (r.h.s) it is observed that the larger v_1 values originate from high transverse momenta, while at low $p_{\text{T}}^{(0)}$ there is very little, if any, sensitivity to the momentum-dependent potentials. The mean $p_{\text{T}}^{(0)}$, $\langle p_{\text{T}}^{(0)} \rangle$, also increases in case of momentum dependent potentials, as visible in the right panel of Figure 5.3. The sensitivity on the EoS (κ) is larger at lower $p_{\text{T}}^{(0)}$ values. For other collision systems and energies discussed below, only Hard EoS and Soft EoS, both with momentum dependent potentials, are studied as bracketing cases.

Figures 5.4 and 5.5 present the results of the directed flow coefficient for Ni–Ni and Xe–CsI collisions, respectively. Like in Au-Au collisions, the soft EoS with momentum dependence (SM) reproduces the overall data better than the hard EoS with momentum dependence (HM) within the SMASH model. However, for all studied collision systems, one can notice a poor description of the directed flow v_1 at low $p_{\text{T}}^{(0)}$, which for the SM EoS is significantly weaker than in experimental data.

The description of directed flow as function of rapidity is in good agreement with the measurements for the soft momentum-dependent EoS. This is due to the fact, that the directed flow close to the mean transverse momentum is in good agreement

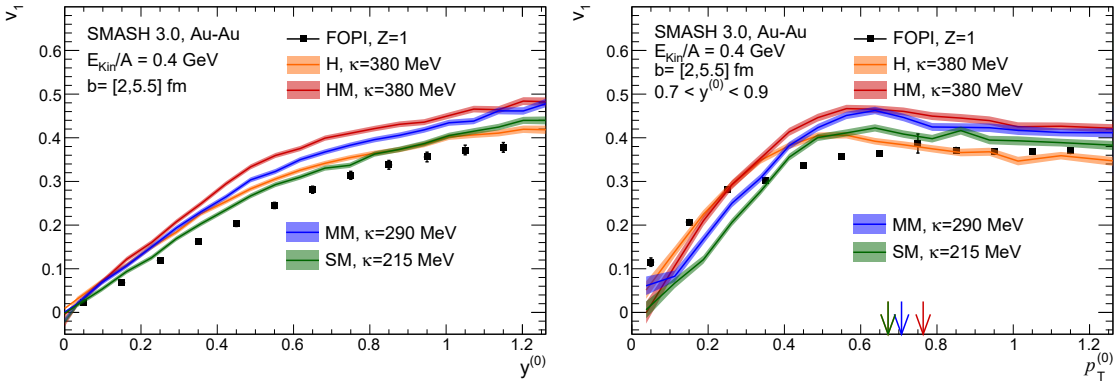

Abbildung 5.3: Directed flow coefficient v_1 for different EoS parametrizations and potentials as a function of rapidity (left) and transverse momentum (right), compared with the FOPI data [197] in Au–Au collisions at $E_{\mathrm{kin}}/A = 0.4\,\mathrm{GeV}$. The arrows in the right panel indicate $\langle p_{\mathrm{T}}^{(0)} \rangle$ values (note that the orange and dark green arrows overlap). Taken from [3].

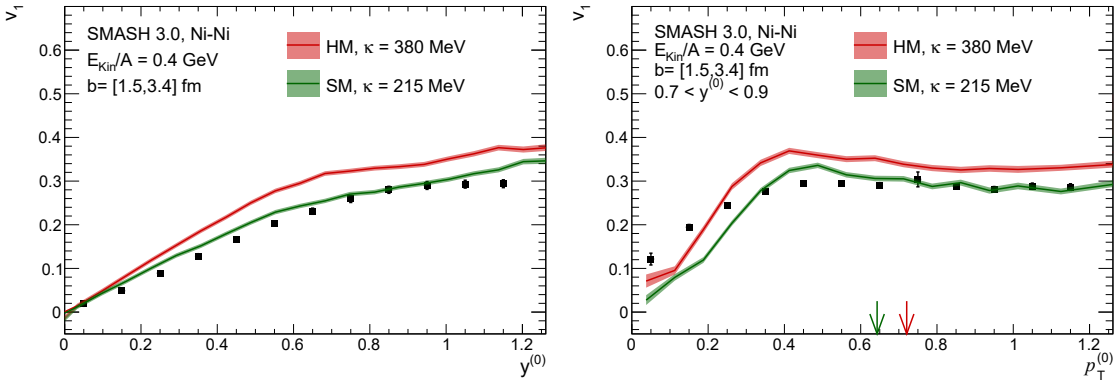

Abbildung 5.4: Directed flow coefficient v_1 for Hard and Soft EoS with momentum dependent potential as a function of rapidity (left) and transverse momentum (right) compared with the FOPI data [197] in Ni–Ni collisions at $E_{\mathrm{kin}}/A = 0.4\,\mathrm{GeV}$. The arrows in the right panel indicate $\langle p_{\mathrm{T}}^{(0)} \rangle$ values. Taken from [3].

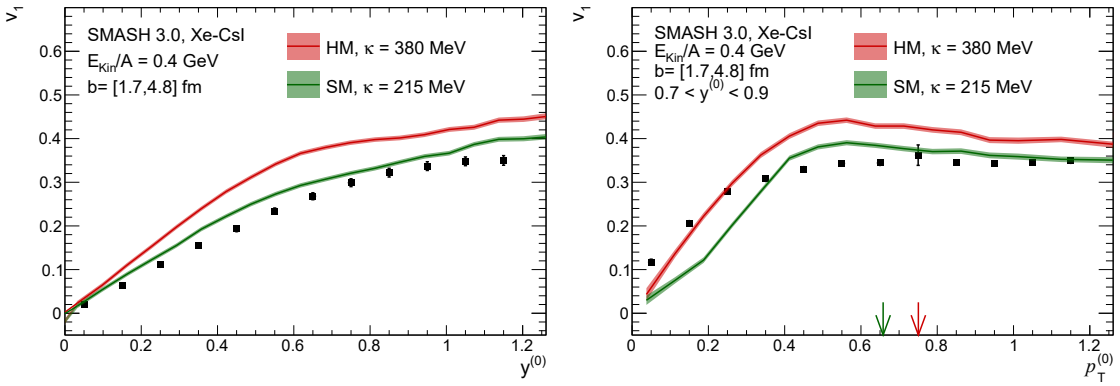

Abbildung 5.5: As Figure 5.4 but for Xe–CsI collisions. Taken from [3].

with the data. At smaller momenta there might be ambiguities in the spectator selection that affect the results.

5.2.3 Comparison of Elliptic Flow

The elliptic flow coefficient as a function of p_T in Au–Au collisions at midrapidity is shown in Figure 5.6. Model calculations at $E_{\text{kin}} = 0.4$ and $1.0\,\text{GeV}$ are compared to FOPI data [196]. For the collision energy $0.4A\,\text{GeV}$ (left panel of Figure 5.6), the complete set of different EoS versions is shown, including, for some cases, calculations with the stochastic collision criterion. The impact of the momentum-dependent potentials is illustrated and appears significant both for the medium and hard EoS. Using a constant potential overshoots the measured elliptic flow coefficients very strongly in both cases. When switching on the momentum dependence of the potentials, the direction of v_2 is reversed and brings the coefficients much closer to the data. This effect is similar for both the hard and medium EoS. The soft EoS (with momentum dependence) seems to describe the data on average the best, but the trends seen in the data are not fully reproduced by the model. A milder dependence on $p_{\text{T}}^{(0)}$ is exhibited by the model starting around $p_{\text{T}}^{(0)} = 0.7$, which roughly coincides with the mean $p_{\text{T}}^{(0)}$ value. At a collision energy of $E_{\text{kin}}/A = 1\,\text{GeV}$, shown in the right panel of Figure 5.6, the hard EoS fits the data better, but we notice again that the $p_{\text{T}}^{(0)}$ dependence of the data is not reproduced well. Data-model comparisons for other collision energies between 0.4 and $1.5A\,\text{GeV}$ can be found in Appendix C.

The elliptic flow coefficient of protons as a function of rapidity in Au–Au collisions at two energies is calculated as well and compared with FOPI data published in [112]. For this data set an integration on $p_{\text{T}}^{(0)}$ is performed for $p_{\text{T}}^{(0)} > 0.8$; note also that the centrality ranges are slightly different compared to the other data sets. The results for mid-peripheral collisions at $E_{\text{kin}}/A = 0.4\,\text{GeV}$ and $E_{\text{kin}}/A = 1.5\,\text{GeV}$ are shown

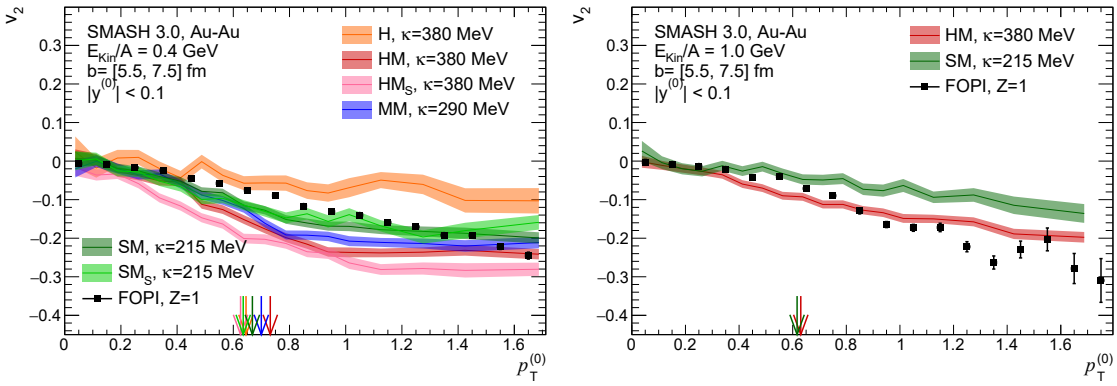

Abbildung 5.6: Elliptic flow coefficient v_2 for different EoS parametrizations as a function of transverse momentum at $E_{\mathrm{kin}}/A = 0.4\,\mathrm{GeV}$ (left) and $E_{\mathrm{kin}}/A = 1.0\,\mathrm{GeV}$ (right) compared to FOPI data [196]. HMs stands for Hard EoS with momentum dependent potentials and the stochastic collision criterion. The arrows indicate $\langle p_{\mathrm{T}}^{(0)} \rangle$ values. Taken from [3].

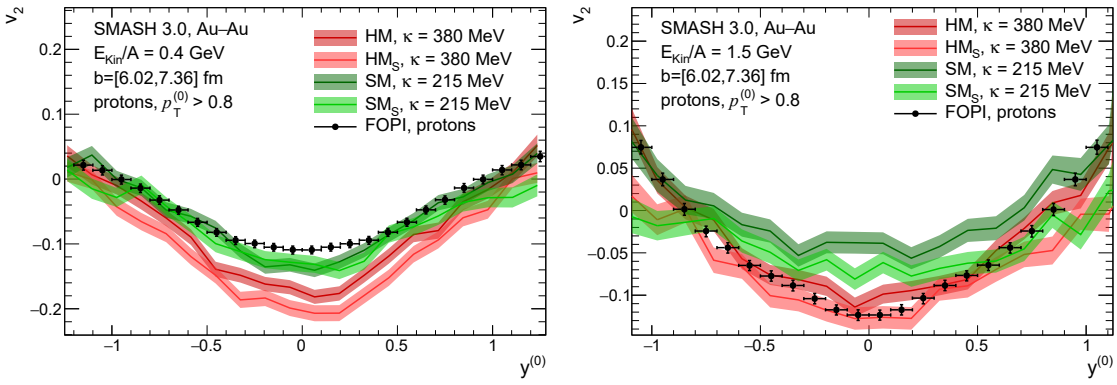

Abbildung 5.7: Elliptic flow coefficient v_2 of protons, integrated for $p_{\mathrm{T}}^{(0)} > 0.8$, as a function of rapidity for mid-peripheral Au–Au collisions at $E_{\mathrm{kin}}/A = 0.4\,\mathrm{GeV}$ (left) and $E_{\mathrm{kin}}/A = 1.5\,\mathrm{GeV}$ (right), compared with FOPI data [112]. Taken from [3].

in Figure 5.7. The SMASH predictions with and without the stochastic criterion agree with each other in the rapidity range $|y^{(0)}| < 1$. It can be observed that at the low collision energy ($E_{\mathrm{kin}}/A = 0.4\,\mathrm{GeV}$), the soft EoS describes the data clearly better than the hard EoS, while the opposite is true for $E_{\mathrm{kin}}/A = 1.5\,\mathrm{GeV}$. The comparisons for mid-central collisions and for $p_{\mathrm{T}}^{(0)} > 0.4$ can be found in Appendix C.

The $p_{\mathrm{T}}^{(0)}$-integrated elliptic flow at mid-rapidity in Au–Au collisions as a function of beam energy is presented in Figure 5.8 for two centrality classes. As this measurement represents $Z = 1$ particles at mid-rapidity, it is not affected by spectators. Thus, the predictions with and without the stochastic criterion, which are shown as well, largely overlap with one another for both centrality classes and different EoS in agreement with expectations. At the lowest collision energy considered here, $E_{\mathrm{kin}}/A = 0.25\,\mathrm{GeV}$, the model strongly overestimates the elliptic flow magnitude for both EoS parametrizations, suggesting that the model reaches its limits below $E_{\mathrm{kin}}/A \simeq 0.4\,\mathrm{GeV}$. At those low beam energies, it is important to correct the cross-sections for the part already treated in potentials by employing medium modified cross-sections, which was not done for the present work. Generally, both EoS parametrizations, with and without stochastic criterion, predict an energy dependence of the elliptic flow parameter v_2 that is significantly stronger than what is found in data. Moreover, the hard EoS overestimates the elliptic flow magnitude at all energies and approaches the data only above $E_{\mathrm{kin}}/A \simeq 1.2\,\mathrm{GeV}$. The soft EoS, on the other hand, describes the data fairly well for collision energies between 0.4 and 0.8 $A\,\mathrm{GeV}$, and slightly underestimates the data at higher energies. Due to limitations of the model, the data points at $E_{\mathrm{kin}}/A = 0.25\,\mathrm{GeV}$ in the $\chi^2/n.d.f.$ calculations presented below are disregarded and one should keep in mind that conclusions about the EoS are in general based on the model including its shortcomings.

5.2.4 Mean Transverse Momentum

The only studied observable for which the calculation with stochastic collision criterion significantly differ from the geometric one, is the mean transverse momentum for $Z = 1$ particles at midrapidity. As seen in Figure 5.9, this difference is significant only for low collision energies while for $E_{\mathrm{kin}}/A > 0.6\,\mathrm{GeV}$ all four sets of simulations lead to rather comparable values for the mean $p_{\mathrm{T}}^{(0)}$. In this energy range, however, the model overestimates the measured value for both centrality classes.

5.2.5 Quantification of Agreement with Data

In order to better quantify which version of EoS (potentials) best describes the experimental data within the model, the χ^2 per number of degrees of freedom (*n.d.f.*)

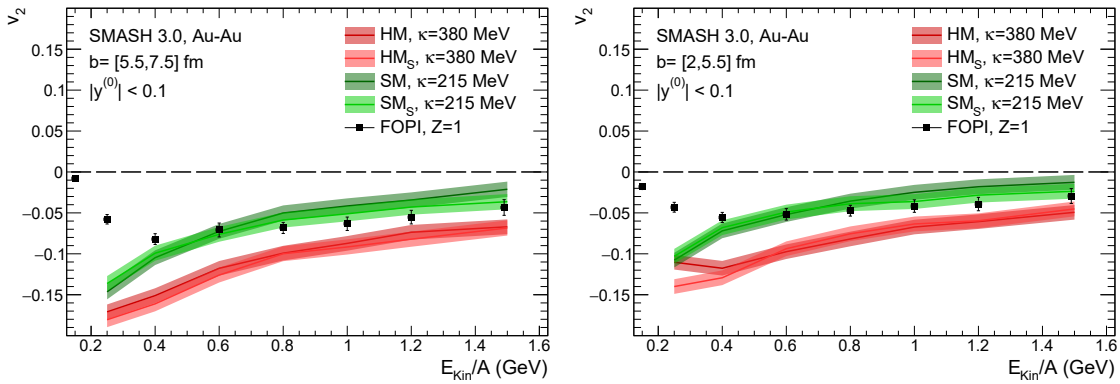

Abbildung 5.8: Elliptic flow coefficient of $Z = 1$ particles as a function of the beam kinetic energy for two centrality classes, mid-peripheral (left) and mid-central (right), compared with FOPI data [196]. Taken from [3].

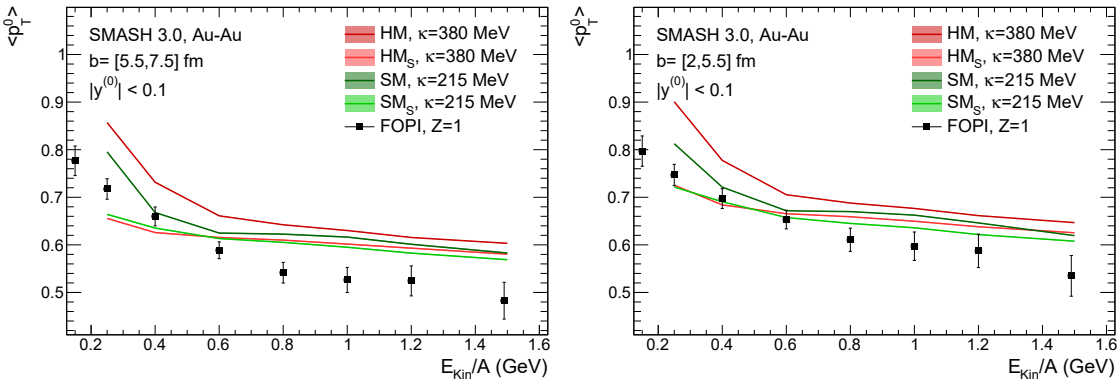

Abbildung 5.9: Mean normalized transverse momentum of $Z = 1$ particles at midrapidity as a function of the beam kinetic energy for two centrality classes, mid-peripheral (left) and mid-central (right), compared with FOPI data [196]. Taken from [3].

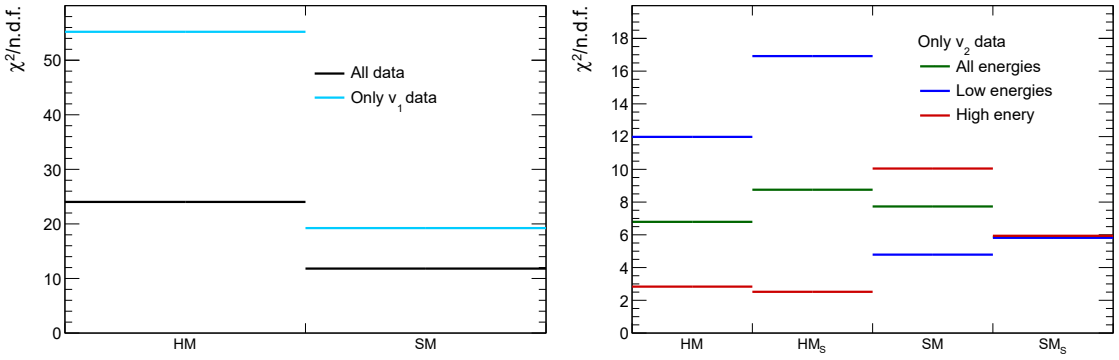

Abbildung 5.10: χ^2 per number of degrees of freedom between the SMASH predictions for different EoS parametrizations and FOPI data [196], [197]. Left: $\chi^2/n.d.f$ using all available data points and only the directed flow data. Right: $\chi^2/n.d.f$ using elliptic flow data, complete and divided in two subsets, for low ($0.4A$, $0.6A$, $0.8A$ GeV) and high ($1.0A$, $1.2A$, $1.5A$ GeV) collision energies. Taken from [3].

is calculated, where the uncertainties are those of the data (statistical and systematic) and the model (statistical) added in quadrature. The results are summarised in Figure 5.10. In the left panel, $\chi^2/n.d.f.$ is shown for all 435 available data points for the standard geometric collision criterion and is compared with $\chi^2/n.d.f.$ for a sub-sample of 155 data points containing only the v_1 results in all collision systems at $E_{\mathrm{kin}}/A = 0.4\,\mathrm{GeV}$, where the v_1 data points are available. In both cases, the soft EoS is characterized by a lower $\chi^2/n.d.f.$. By taking into account only the v_1 data, the $\chi^2/n.d.f.$ for the hard EoS increases by a factor of 2.3 while the one for the soft EoS only by a factor of 1.64, reflecting the large deviations of the HM-EoS from data, seen in Figure 5.3. This can be seen also in the right panel of Figure 5.10, where $\chi^2/n.d.f.$ is calculated separately for all the v_2 data (279 data points), v_2 at low collision energies (E_{kin}/A =0.4, 0.6, and 0.8 GeV, representing a total of 121 data points, including the $p_{\mathrm{T}}^{(0)}$ dependent points in Figure 5.6 and C.3, and rapidity dependent points from Figure 5.7,C.4, and C.5), and high collision energies ($1.0A$, $1.2A$, and $1.5A$ GeV; 158 data points, including the $p_{\mathrm{T}}^{(0)}$ dependent points in Fig 5.6 and C.3, and rapidity dependent points from Fig 5.7,C.4, and C.5). The $\chi^2/n.d.f.$ for the soft EoS and stochastic criterion is the same for all three cases, but there is an ordering for the geometric criterion showing the lowest $\chi^2/n.d.f.$ for lower collision energies. This ordering is reversed for the hard EoS for both criteria with larger difference between low and high collision energy. The comparison of our model to experimental data favors a transition from soft to hard EoS as a function of energy. The BUU transport model of Danielewicz [111], [198] predicted a similar trend [196], while a study within the IQMD model [113] found a preference for a

soft EOS throughout this energy range. An onset of a softening of the EoS is implied by elliptic flow data for $E_{\mathrm{kin}}/A \simeq 2\,\mathrm{GeV}$ [198], [199]. The conclusions about the stiffness of the EoS in the energy regime from $E_{\mathrm{kin}}/A = 1\,\mathrm{GeV}$ and higher also depend on the amount of resonances employed in the transport approach (see e.g. [110]).

5.3 Conclusions

An exploratory study of the description of directed and elliptic flow in the SMASH transport model at collision energies spanning $E_{\mathrm{kin}}/A = 0.25 - 1.5\,\mathrm{GeV}$ is performed in this chapter. While the model clearly shows its limitations at $E_{\mathrm{kin}}/A = 0.25\,\mathrm{GeV}$, it describes the data well for $E_{\mathrm{kin}}/A \geq 0.4\,\mathrm{GeV}$. Clearly, the momentum-dependent potentials are important and the sensitivity to the EoS is significant. While overall a soft EoS is preferred by the data, the elliptic flow data are better described by a hard EoS for the higher collision energies explored here ($E_{\mathrm{kin}}/A = 1.0 - 1.5\,\mathrm{GeV}$). The results presented in Chapter 4 agree with this finding as a relatively stiff equation of state was preferred in a comparison to HADES data taken at $1.23A\,\mathrm{GeV}$.

Further quantitative studies are needed in order to understand systematic uncertainties in transport approaches in general, and in SMASH in particular. The relevance of better constraints on the EoS from heavy-ion collisions (together with further constraints on the symmetry energy) for neutron stars and their collisions will certainly motivate such studies.

Kapitel 6

Light Nuclei Formation at RHIC Beam Energy Scan

Until now, this thesis has focused on the equation of state of nuclear matter. To understand how nuclear potentials affect the dynamics of baryons, the formation of light nuclei is crucial, particularly for comparing theoretical models to experimental data. This chapter shifts focus to the formation and dynamics of light nuclei themselves. As composite objects made up of baryons, light nuclei provide insights into event-by-event fluctuations of the baryon number. These fluctuations are expected to be enhanced near the critical point in the nuclear matter phase diagram.

The Beam Energy Scan program at RHIC aims to explore the QCD matter phase diagram by varying both the beam energy and system size. This exploration focuses on a region where a critical point of QCD matter may lie, and the production of light nuclei could serve as a key observable for identifying the critical point in experimental data. This chapter is based on [4], where the formation of light nuclei is modeled in the afterburner phase of heavy-ion collisions at three different energies from the BES program.

The deuteron yield has been measured in heavy-ion collisions by the ALICE collaboration [200]. The interest in the light nuclei formation increased due to the striking observation that the yield can be described using the statistical hadronization model [41], [42] (see Section 1.2.3). This finding suggests that light nuclei are formed and survive at a temperature of ~ 150 MeV. Studies within afterburner calculations have shown that this does not necessarily correspond to the chemical freeze-out of deuterons but their yield stays constant as formation and disintegration processes are balanced [201]. A similar result was obtained by solving the coupled reaction rate equations for the light nuclei yields in an expanding system [202].

A possible critical point is one of the most interesting features of the QCD phase diagram. The production of light nuclei was suggested to serve as a probe for critical fluctuations [26]. Calculations within a coalescence model allow to relate fluctuations

and correlations to the light nuclei ratios [203], [204]. The STAR collaboration hence published the measured particle number ratios N_d/N_p, N_t/N_p and N_tN_p/N_d^2 [205]. Further microscopic calculations allow to relate light nuclei ratios to the interaction between nucleons near the critical point [206], [207].

The production of deuterons and other light nuclei can be studied from a theory perspective in various approaches. Many works successfully apply a transport description for the evolution of a heavy-ion collision. One possibility to produce light nuclei based on a transport model is to apply coalescence based on the distribution of nucleons in phase-space in the final state of the transport calculation. Coalescence is the most extreme scenario of late stage formation of light nuclei. Deuteron formation with a coalescence approach applied to UrQMD [115] calculations has been studied for a wide range of energies in [187]. A further study within the UrQMD model takes more light nuclei into account [208] and the aforementioned particle ratios are presented as a function of collision energy. A nontrivial structure in the excitation function is observed but is not related to critical fluctuations as they are not incorporated in the model. Light nuclei production via coalescence has also been studied in the JAM model [209] and the particle ratios are shown as a function of the collision energy as well [210]. In this calculation, hardly any energy dependence of the N_tN_p/N_d^2 ratios is found.

Another possibility to realize light nuclei production in a transport model is via scatterings. This approach was applied in the aforementioned work [201] to describe the production of deuterons at the LHC within the SMASH transport model [128]. This work was continued for lower collision energies to compare to data from the RHIC BES [211]. The flow of deuterons within this model has been studied at SIS18 energies [1]. While in these works the deuterons are formed in binary reactions, including an artificial intermediate state for the pion and nucleon catalysis reactions, the stochastic collision criterion was applied in a further step to perform multi-particle reactions [184]. Light nuclei production via multi-particle reactions has been studied first in [180]. The relativistic kinetic equations from this work have been recently applied to study the production of deuterons, tritons and ^{3}He nuclei as well as yield ratios at RHIC and LHC energies [212]. In [213] multi-particle reactions are implemented to investigate deuteron formation within the PHQMD model [119]. In the PHQMD framework clusters can be identified by using the minimum spanning tree procedure [155] or the Simulated Annealing Clusterization Algorithm[214], [215].

6.1 Calculation Setup

This work aims to shed further light on the formation of light nuclei in heavy-ion collisions. For this purpose, a dynamic model is essential as it allows to access the

time evolution of the system. Hybrid approaches have proven to be well suited for the description of heavy-ion collisions in the considered energy region (see Chapter 1). A hybrid model is applied that was previously developed in [211] for a study of deuteron production and further applied in [184].

The evolution of the hot and dense phase of a heavy-ion collision is formulated with the (3+1)D relativistic viscous hydrodynamic equations. A solution of the hydrodynamic equations is obtained using the MUSIC code [53], [59], [135], [136] where the equation of state from [216] is used. The evolution starts after an initial state from a collision-geometry-based 3D model [217]. As the fireball expands, the system becomes more dilute and is more realistically described within a transport model. As in the previous work, an energy density of $\epsilon = 0.26\text{GeV/fm}^3$ is used to define the hypersurface where the switch between models takes place. The hypersurface is found using CORNELIUS [62] and the switch from a macroscopic to a microscopic description is performed using Cooper-Frye sampling [63]. For the final stage, the SMASH transport model [128] is incorporated for hadronic rescattering.

6.2 Validation

Before showing results in the next section, the multi-particle reactions as described in Section 2.3 to the test. For validation, a comparison to an analytical solution is well suited. An analytical solution for the evolution of particle multiplicities in a box with a limited number of processes can be obtained by solving the rate equations [218]. Note that the description of a realistic heavy-ion collision requires the full transport calculation as it incorporates all non-equilibrium dynamics and numerous cross sections. The rate equations used in [184] are for this purpose extended to further include the reactions for triton, helium and hypertriton. The equations are given in Appendix D.

The rate equations can be solved numerically and the results are compared with the multiplicities from the SMASH calculation in Figure 6.1. The multiplicities for different particle species, such as nucleons, pions, Λ-baryons and light nuclei are calculated in a box of $(10\text{ fm})^3$ at $T = 150$ MeV for 4000 events. The box is initially filled with each 60 nucleons and pions.

One can observe in Figure 6.1 the formation of light nuclei over time and find that the analytical equilibrium multiplicities are correctly reproduced by the transport approach. We observe however a slightly slower equilibration. Hence, we investigate technical parameters such as test particles and time step size. Finer time steps did not change our results. The same goes for the number of test particles for which a calculation with double the number of test particles is shown, denoted by the full line in Figure 6.1. Since no difference can be observed, calculations for the following sections are performed with 10 test particles.

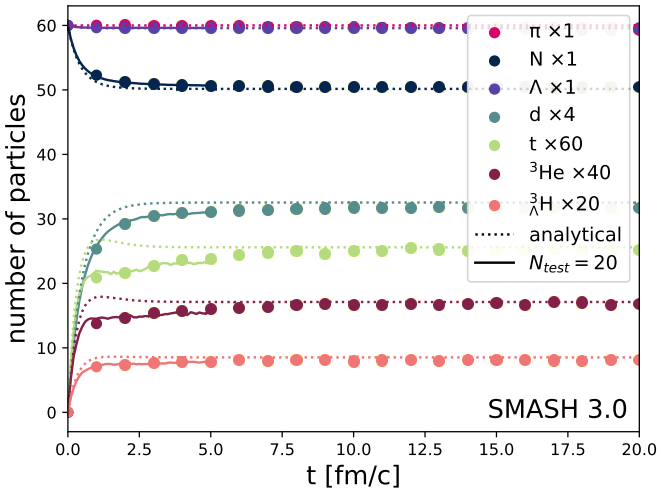

Abbildung 6.1: Particle multiplicities over time in a box of $(10\text{fm})^3$ and $T = 150$ MeV. The circles represent calculations with 10 test particles, and the full lines represent calculations performed with 20 test particles. The solutions from the rate equations are shown as dotted curves. Taken from [4].

6.3 Light nuclei production

In this section, results for the light nuclei production in gold-gold collisions at RHIC-BES-energies are presented. More precisely, the production of deuterons, ^{3}He nuclei, tritons and hypertritons at 7.7 GeV, 14.5 Gev and 19.6 GeV in the 10% most central events is investigated.

In the follwoing, results for the transverse momentum spectra for each nucleus at the three different energies are shown. Next, particle ratios including light nuclei are evaluated because they may give some insight on the presence of a critical point. Further, the time evolution of the light nuclei multiplicities is studied with the aim to understand when and under which circumstances they are formed. To understand which processes are essential for the production of light nuclei, the production mechanisms and their frequencies are studied separately.

6.3.1 Transverse momentum spectra

The light nuclei transverse momentum spectra are calculated at mid-rapidity for the three different energies. Here the dynamic light nuclei formation via stochastic rates is compared to the production via coalescence. In both scenarios the evolution within the transport model starts based on particles sampled on the Cooper-Frye

hypersurface of a hydrodynamic evolution. For the dynamic production the sampled particles include light nuclei. They undergo interactions and can be destroyed or newly formed in this stage.

However in the coalescence scenario no light nuclei are sampled on the Cooper-Frye hypersurface. In the afterburner stage within this setup, rescattering also takes place but the nuclei are not present. Instead they are formed in the final sate of the afterburner out of nucleons based on their distance in phase-space (see Section 2.3).

For comparison, the spectra of nuclei sampled on the hydrodynamic hypersurface without hadronic rescattering in the afterburner stage are additionally calculated. The impact of the afterburner stage is illustrated this way.

The transverse momentum spectra for the three different energies are compared to data from the STAR collaboration in figure 6.2. One can find, that both, coalescence and dynamic production describe the data points well for all energies and each particle species with a slight undershoot for higher p_T at lower collision energy. The slopes of the nuclei spectra without any rescattering (dashed curves) are too steep and the data clearly favors the calculations including the hadronic afterburner stage. We conclude that this stage is important to obtain realistic light nuclei spectra as it is the case for proton spectra (see [219] and references therein).

6.3.2 Particle ratios

The STAR collaboration has published ratios of protons and light nuclei multiplicities such as N_d/N_p, N_t/N_p and N_tN_p/N_d^2 [205]. Calculations with the coalescence model show that the ratios are sensitive to fluctuations of the baryon density, which in turn appear close to the critical end point or a first order phase transition [203], [204]. The ratios can further be used to extract information on the interaction of nucleons [206], [207].

In Figure 6.3 one can find three different particle ratios. These ratios are calculated at the end of the afterburner at mid-rapidity for different energies. The two upper plots show the single ratios for the number of deuterons and tritons divided by the number of protons respectively. In the lower plot the double ratio N_tN_p/N_d^2 is presented.

Comparing our calculations to STAR data [205] one can see, that the single ratios are well described by both the dynamic production and the coalescence model. The motivation to investigate the double ratio is that it can be related to critical fluctuations. For both calculations an energy independent double ratio is observed. The coalescence model performs better for the double ratio but one should emphasize, that critical fluctuations are not implemented in the model.

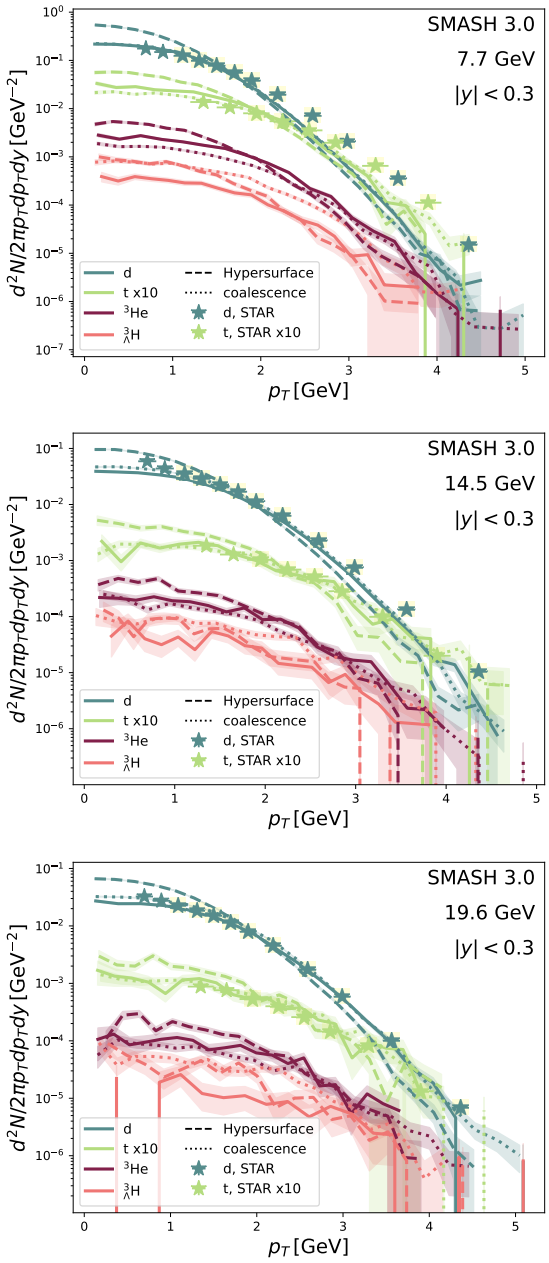

Abbildung 6.2: Transverse momentum spectra for different light nuclei species at mid-rapidity for different energies in central Au-Au collisions. Data points are taken from [220] and [205]. Taken from [4].

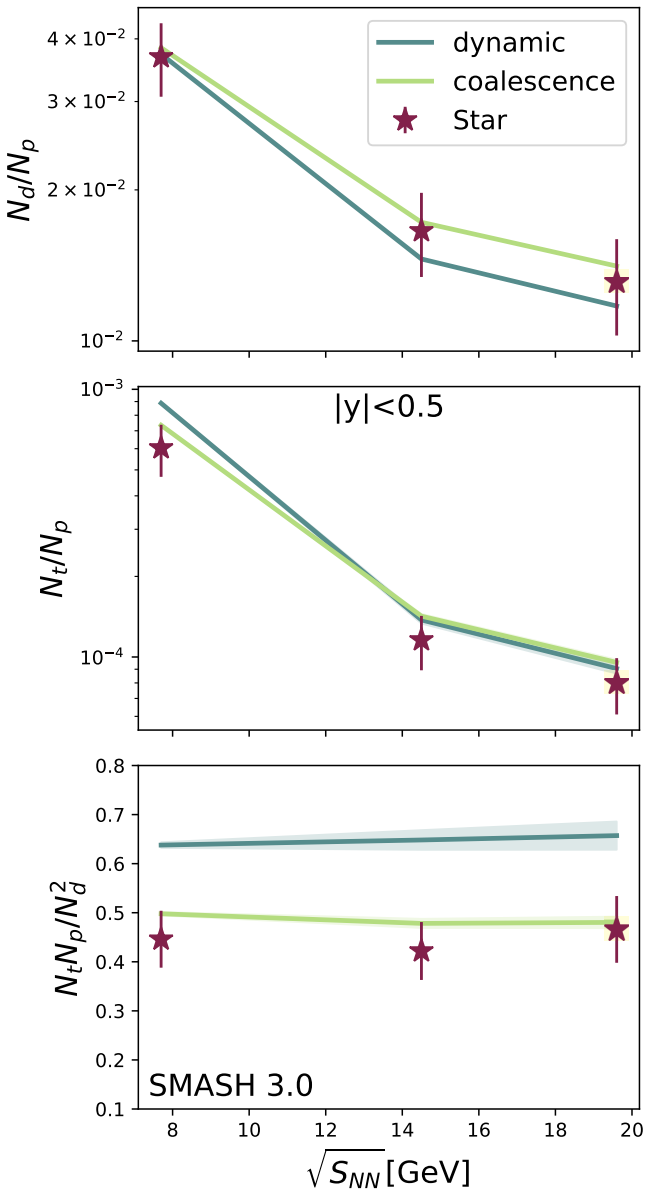

Abbildung 6.3: Collision energy dependence of particle ratios at mid-rapidity in central Au-Au collisions. Data points are taken from [205]. Taken from [4].

6.3.3 Time dependence of light nuclei multiplicities

In this section the light nuclei multiplicities as a function of time are presented at 7.7, 14.5 and 19.6 GeV. Multiplicities for deuterons, tritons and hypertritons are shown for mid-rapidity and the full phase space. Calculations for ^{3}He nuclei yield very similar results as tritons and are not presented here (they are given in the appendix of [4]). For each particle species and each energy two curves are compared: the solid curve represents the nuclei produced in multi-particle reactions in the afterburner stage. The dashed curve denotes the nuclei, sampled on the hydrodynamic Cooper-Frye hypersurface without performing the afterburner stage.

Figure 6.4 shows the deuteron yield as a function of time together with the experimentally observed yield in the final state [220]. At mid-rapidity one can observe for all energies that the dynamic production of deuterons leads to a higher number of nuclei compared to the number of sampled deuterons on the hydrodynamic hypersurface. This means, that at mid-rapidity, more nuclei are produced than destroyed in the afterburner stage. This could be caused by a large number of protons and neutrons at mid-rapidity so that the deuteron production can take place frequently. The agreement with experimental data is improved by reactions in the afterburner stage. In the 4π scenario the situation changes. The afterburner multiplicity stays slightly below the number of particles from the hypersurface in the beginning of the evolution and the amount of light nuclei is reduced at later times. This can be understood by taking into account that the density decreases, as the system expands. The destruction processes outweigh the formation processes as a consequence. Section 6.3.4 contains a detailed analysis of the corresponding production rates. In summary, the total number of deuterons is reduced as the system expands but more deuterons are formed at mid-rapidity.

We continue with the triton multiplicities as a function of time as presented in Figure 6.5. At mid-rapidity, we can observe a similar behavior as for the deuteron. The increase at early times is in this case slightly more pronounced and the reduction of the mid-rapidity multiplicity towards later times is larger. The data points are well reproduced for the higher energies but the afterburner calculation overshoots the measurement at 7.7 GeV as the afterburner increases the mid-rapidity yield at this energy, where the net-baryon density is the largest. At 4π the afterburner reduces the yields drastically, even stronger for lower energies. It is interesting to see that for this energy at 4π the deviation from the hydro curve is immense compared to the mid-rapidity region. The behavior for the ^{3}He nuclei is very similar to the triton so that the results are not presented here. They can however be found in [4].

In figure 6.6 one can find the multiplicities for the hypertritons. At mid-rapidity the afterburner curves exceed the hydrodynamic curves at earlier times like it is the case for the other nuclei. Within statistical uncertainties, the afterburner calculations reach the multiplicities from the hypersurface at later times. Overall, once can

observe at mid-rapidity the same behavior as for d, t and ^{3}He except the reduction of the hypertriton yield brings the multiplicity down to the number of particles from the hydrodynamic hypersurface whereas the yield of other nuclei increases due to the afterburner stage. Hypertritons at 4π show a unique feature at 7.7 GeV: For other light nuclei, the multiplicity is reduced during the afterburner stage. However, for the ${}^3_\Lambda H$ more nuclei are produced in the beginning and then the multiplicity converges to the number of particles on the hydrodynamic hypersurface at later times.

To summarize these results, at 4π the afterburner reduces the amount of nuclei at later times for all energies and all nuclei species, except the 7.7 GeV hypertriton curve. This reduction is eminently pronounced for the triton and for the ^{3}He nuclei. At mid-rapidity the dynamical production leads to a higher amount of nuclei in the final state except for the hypertriton. In this case the multiplicities equilibrate to the hydrodynamic curves.

A possible interpretation of the unique behaviour of the hypertriton may be the following. In general, $4 \rightarrow 2$ reactions become less likely as the system expands compared to $2 \rightarrow 4$ reactions. This naturally leads to a reduction of the $A = 3$ nuclei yield. The hypertriton is mainly formed in the reaction $\Lambda pn\pi \rightarrow {}^3_\Lambda \mathrm{H}\pi$, so that a Λ is required for the production. Compared to nucleons, the Λ has only small hadronic cross sections, so that the probability to participate in a process to form a hypertriton is increased. This may lead to the observed enhancement of the hypertriton yield. A further aspect to consider is how many nucleons and Λ baryons are present in an excited state. Resonances do not participate in reactions to form or destroy light nuclei in the current state of the model.

Based on the results presented in this section, we can calculate the time dependence of the particle ratios discussed in Section 6.3.2. In Figure 6.7 the time evolution of the double ratio $N_t N_p / N_d^2$ is shown. At all energies the ratios behave in a similar way: the curves rise in the beginning and saturate towards later times. The similarity between the curves is not surprising, considering the energy independence observed in the lower panel of Figure 6.3. The non-trivial time dependence of deuteron and triton yields observed in Figures 6.4 and 6.5 cancel out in the double ratio, as the curves rise monotonically. Figure 6.7 also includes the experimentally measured ratios[205] and the ones obtained from final state coalescence. Like in Figure 6.3 the coalescence and the experimental data points coincide while the dynamic production overshoots slightly.

6.3.4 Production mechanisms

To get a better understanding about the formation process during the afterburner one can have a look on the light nuclei production mechanisms. This is motivated by the fact, that one cannot retrace the reactions in the afterburner properly by

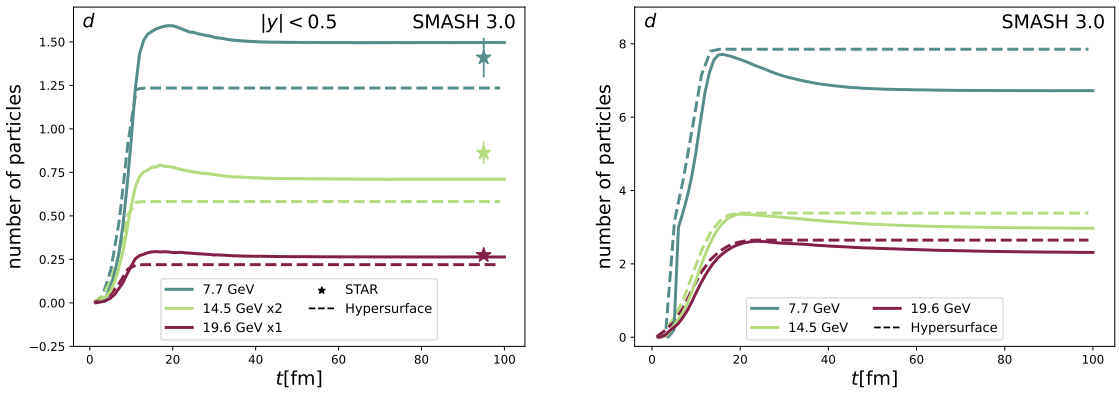

(a) Yield at mid-rapidity.

(b) Total yield.

Abbildung 6.4: Multiplicities of deuterons at different energies in central Au-Au collisions as a function of time. The full lines represent the full afterburner calculations and the dashed lines are the multiplicities, sampled on the Cooper-Frye hypersurface of the hydrodynamic calculation. Data points are taken from [220]. Taken from [4].

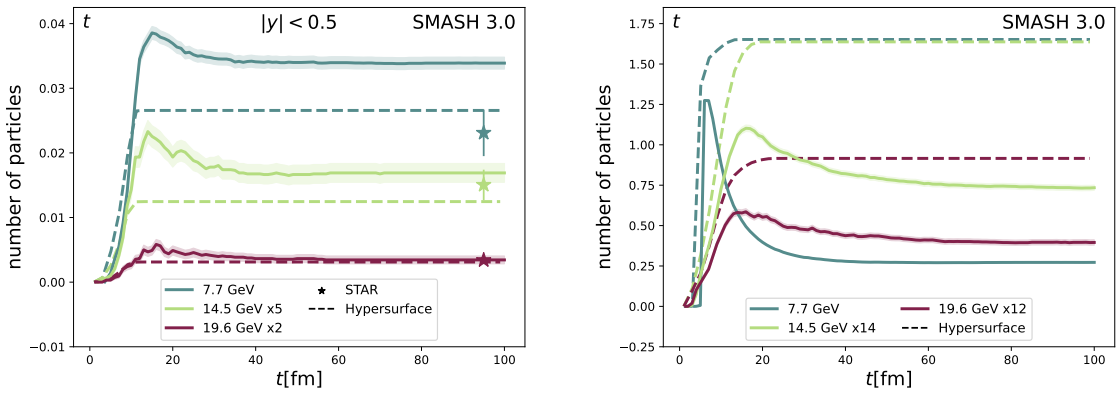

(a) Yield at mid-rapidity.

(b) Total yield.

Abbildung 6.5: Multiplicities of tritons at different energies in central Au-Au collisions as a function of time. The full lines represent the full afterburner calculations and the dashed lines are the multiplicities, sampled on the Cooper-Frye hypersurface of the hydrodynamic calculation. Data points are taken from [205]. Taken from [4].

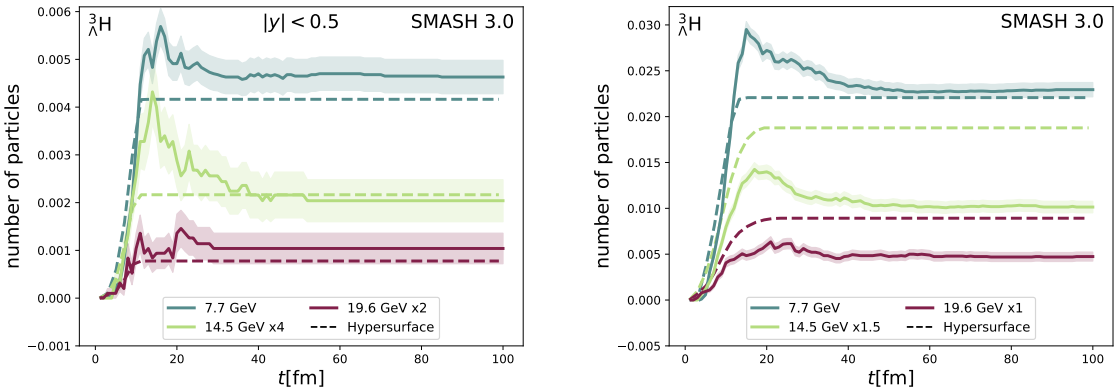

(a) Yield at mid-rapidity.

(b) Total yield.

Abbildung 6.6: Multiplicities of hypertritons at different energies in central Au-Au collisions as a function of time. The full lines represent the full afterburner calculations and the dashed lines are the multiplicities, sampled on the Cooper-Frye hypersurface of the hydrodynamic calculation. Taken from [4].

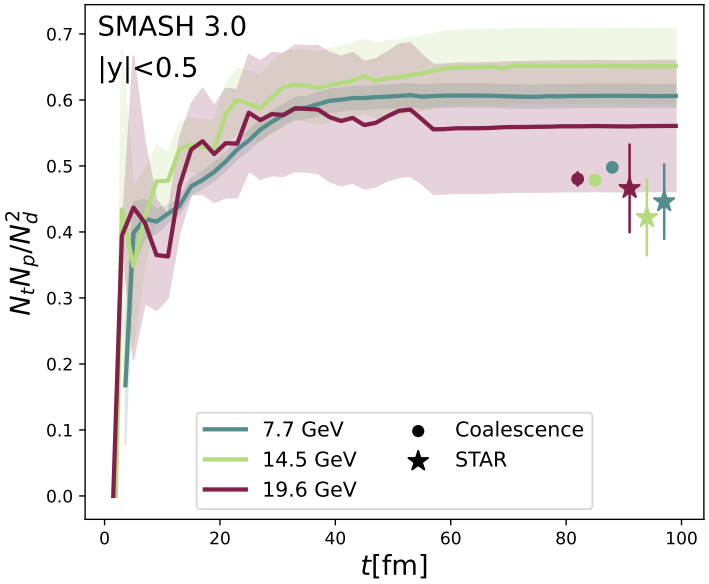

Abbildung 6.7: The double ratio $N_t N_p / N_d^2$ in Au-Au collisions at mid-rapidity is calculated as a function of time. Three different energies are shown. The curves are compared to the the ratios obtained by coalescence at the end of the afterburner (circles) and to data from the STAR collaboration [205] (stars). Taken from [4].

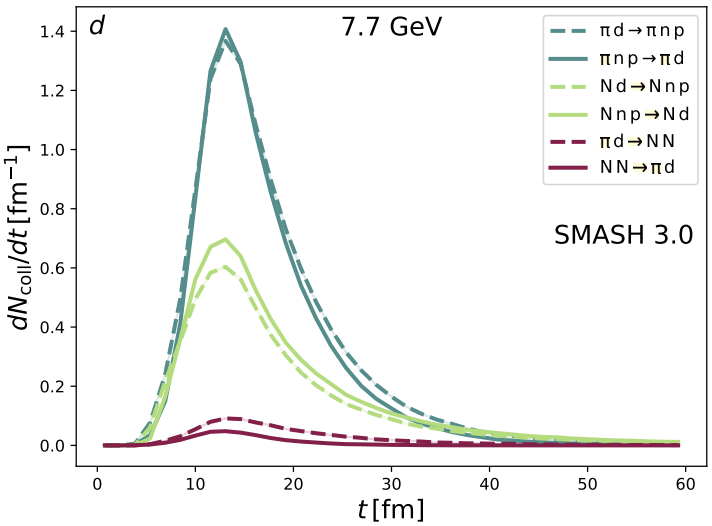

Abbildung 6.8: Scattering rates for deuterons at 7.7 GeV in central Au-Au-collisions. The solid curves represent formation mechanisms while the dashed curves represent disintegration mechanisms. Taken from [4].

only knowing the yields. For example a constant number of particles can either be achieved by no reactions or by as many forward as backward reactions. Also a small reduction of the nuclei yield during the afterburner, as the case for the deuterons in 4π (see figure 6.4), does not imply that there are only few reactions. To illustrate the production mechanisms we calculate the collision rates of the different reactions for the formation and disintegration of deuterons, tritons and hypertritons. The rates are shown in Figures 6.8, 6.9 and 6.10 for the energy 7.7 GeV. Here most of the hadronic rescattering takes place in the first 30 to 40 fm and the maximum is located around 10 to 15 fm for each particle species.

For deuterons (see Figure 6.8) one can observe that in the first 20 fm the formation and disintegration processes are roughly balanced. At later times the disintegration outweighs slightly. This is consistent with the 7.7 GeV curve in Figure 6.4, where the yield of dynamically produced nuclei in the final state at 4π is smaller than the yield on the Cooper-Frye hypersurface. The small rates of the $NN \leftrightarrow \pi d$ reactions verify that the multiparticle reactions are the most important contribution for the light nuclei production. For the production of deuterons, the pion catalysis reactions are most frequent. In Appendix E the rates for higher collision energies are shown. One can observe that with increasing energy the pion catalysis reactions become more dominant. This can be attributed to the fact that the population of pions is larger at higher energies.

The reaction for the formation and disintegration of tritons is presented in Figure

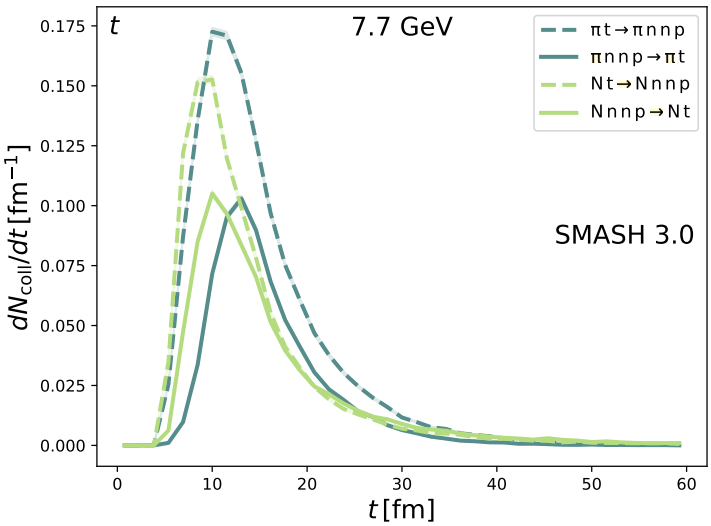

Abbildung 6.9: Scattering rates for tritons at 7.7 GeV in central Au-Au-collisions. The solid curves represent formation mechanisms, while the dashed curves represent disintegration mechanisms. Taken from [4].

6.9. The disintegration of tritons clearly dominates and therefore the rescattering reduces the yields drastically. This is in accord with the final yield at 7.7 GeV in Figure 6.5. For the tritons we observe that the nucleon catalysis reactions are as important as the pion catalysis reactions at this energy. For higher energies we observe, again, that pion catalysis becomes more important (see Appendix E).

The reaction rates relevant for the hypertriton production are shown in Figure 6.10. We observe slightly more formation than disintegration in the first 20 fm which is why the afterburner stage increases the 4π yield of hypertritons (Figure 6.6) in this time frame. Between 20 and 40 fm the disintegration outweighs slightly. This leads to the same multiplicity on the Cooper-Frye hypersurface as in the final state of the afterburner. For the hypertriton, the pion catalysis outweighs the nucleon catalysis reactions already at 7.7 GeV. Collision rates at higher energies can, also here, be found in Appendix E.

In Figures 6.11, 6.12 and 6.13 one can find the cumulative collision numbers for the formation processes compared to the disintegration processes to point out the change in the final particle yield. The difference between the cumulative production number and destruction number corresponds to the change in the yield of the considered nucleus compared to the particle number sampled on the hypersurface. We observe that the difference, and hence the impact of the afterburner on the multiplicity, is relatively small for deuterons and hypertritons. This does not mean that the afterburner stage can be disregarded as we see that the number of reactions

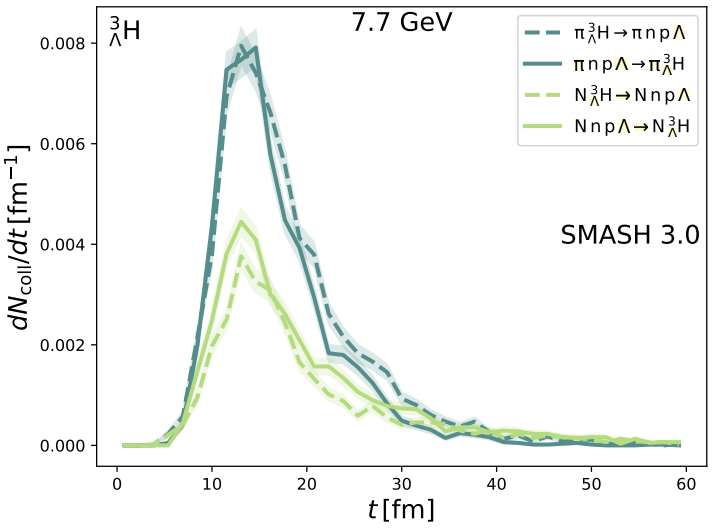

Abbildung 6.10: Scattering rates for hypertritons at 7.7 GeV in central Au-Au-collisions. The solid curves represent formation mechanisms, while the dashed curves represent disintegration mechanisms. Taken from [4].

that involve light nuclei is large and significantly contributes to the dynamics of the system. The importance of the afterburner stage has been demonstrated already in Section 6.3.1. For the triton, a reasonable number of formation reactions takes place, but the disintegration processes dominate, leading to the reduced triton yield in the final state of the afterburner stage.

6.4 Summary and Conclusions

In this study, the dynamic production of deuterons, tritons, ^{3}He nuclei and hypertritons in the afterburner stage of a hybrid approach is investigated. The afterburner calculation is performed using the transport model SMASH, where nuclei are formed via multi-particle reactions realized with the stochastic collision criterion or via coalescence.

For validation, the multiplicities obtained using multi-particle reactions in a box calculation were compared to results from rate equations. The equilibrium multiplicities are found to be correctly reproduced and a slightly slower equilibration as compared to the rate equation is observed.

In the next step, transverse momentum spectra of light nuclei are confronted with experimental data. A good agreement with the measurement is found for the dynamic production of light nuclei and for the coalescence approach, as long as the afterburner stage is performed.

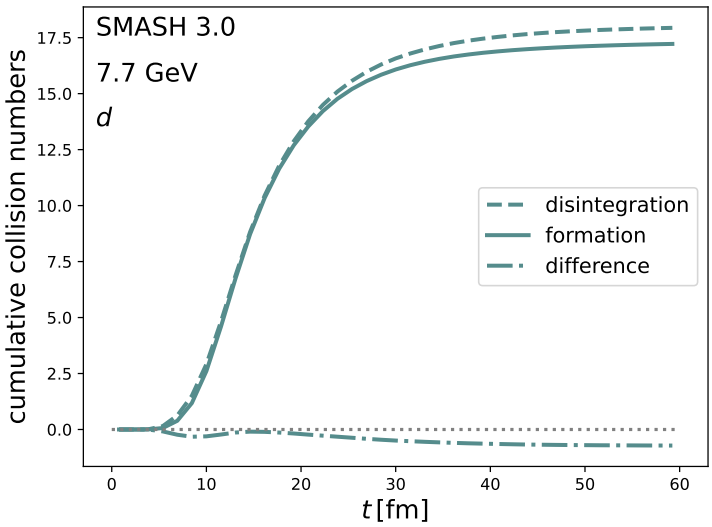

Abbildung 6.11: Cumulative collision numbers for disintegration and formation reactions of deuterons at 7.7 GeV are shown. They are compared to the difference between these two curves to illustrate the change in the final particle yield. Taken from [4].

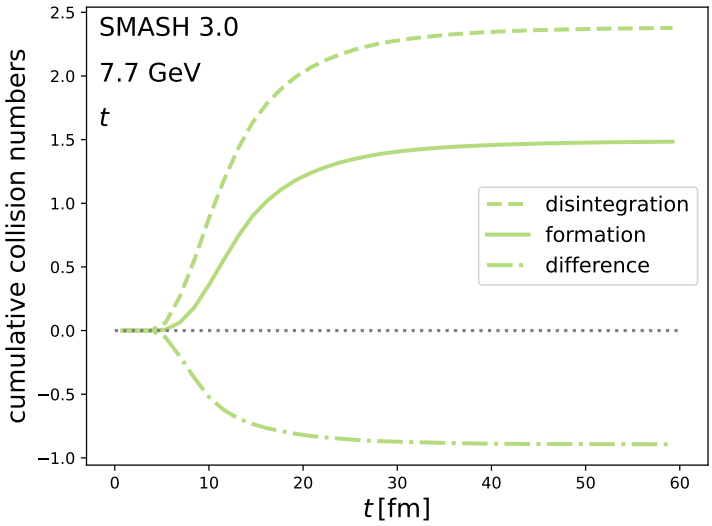

Abbildung 6.12: Cumulative collision numbers for disintegration and formation reactions of tritons at 7.7 GeV are shown. They are compared to the difference between these two curves to illustrate the change in the final particle yield. Taken from [4].

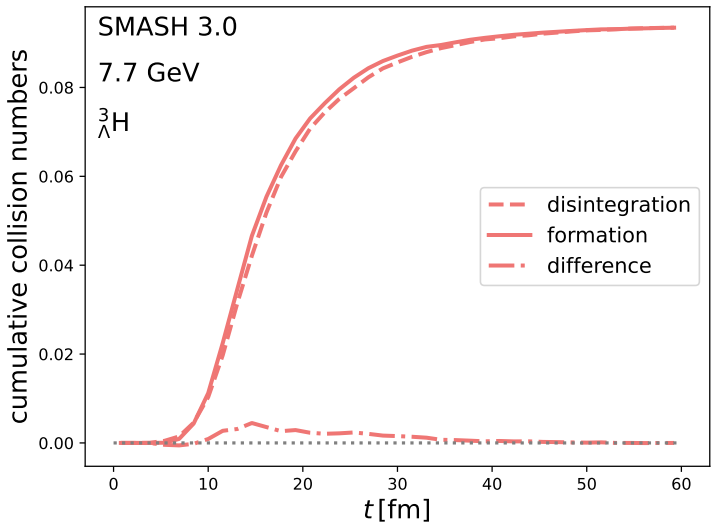

Abbildung 6.13: Cumulative collision numbers for disintegration and formation reactions of hypertritons at 7.7 GeV are shown. They are compared to the difference between these two curves to illustrate the change in the final particle yield. Taken from [4].

Results for the particle ratios N_d/N_p, N_t/N_p and $N_t N_p/N_d^2$ are further presented. For the single ratios, a good agreement with the experimental data is found with both the dynamic production of nuclei and the coalescence approach. The double ratio is better described by the coalescence approach but the double ratio was proposed to be sensitive to the critical point which is not included in the model.

To get a better understanding of the time evolution of the light nuclei production, the multiplicity of light nuclei as a function of time at mid-rapidity and for the full phase-space are presented. Considering the full phase-space, the yield of light nuclei is observed to decrease in general as the system expands, except for the hypertriton which experiences a slight increase in multiplicity at $\sqrt{s_{NN}} = 7.7\,\text{GeV}$. The yield relaxes back to the one on the hydrodynamic Cooper-Frye hypersurface towards later times. In contrast to the 4π multiplicities, light nuclei multiplicities tend to increase at mid-rapidity during the afterburner stage and a good agreement with the experimentally measured yields at mid-rapidity is found.

Finally, the scattering rates for the formation and disintegration of light nuclei are studied. As in the considered systems the number of pions is large, one can observe that the pion catalysis reactions are most important for the formation of light nuclei in many cases. For deuterons and hypertritons the relatively small change in the multiplicities does not imply a small interaction number. Instead, forward and backward reactions are frequent and the rates are roughly balanced. For the tritons

a larger number of disintegration compared to the formation processes are observed. This is consistent with the observed decrease in triton multiplicity in the afterburner stage. Multi-particle reactions in the afterburner stage are successful at capturing the dynamics and production of light nuclei.

Kapitel 7

Summary and Conclusions

The main focus of this work lies on the equation of state of nuclear matter. Constraints on the EoS come from multiple sources, including studies of atomic nuclei, astrophysical observations, heavy-ion collisions, and purely theoretical considerations. Given that the EoS can be probed from various perspectives, significant progress has been made in this area.

This thesis presents work on the EoS based on heavy-ion collisions. Like astrophysical observations, these collisions probe nuclear matter at densities well above saturation. Heavy-ion collisions, provide the only possibility to study the EoS at high densities in terrestrial experiments. The ability to repeat experiments indefinitely in the laboratory, coupled with specifically developed detectors around the collision, allows for the collection of highly accurate data, capturing the final state of the collision. Therefore, heavy-ion collisions offer invaluable insights into the EoS.

Many studies have been performed, aiming to constrain the equation of state using heavy-ion collisions. The difficulty in this endeavor arises, however, from the theoretical description of a collision. Heavy-ion collisions are extremely rapid processes, making them extremely difficult to model. Theoretical modeling of the collisions is absolutely essential to draw conclusions about the hot and dense phase of the system, based solely on the final state particles measured in the detector. In fact, much effort is ongoing to understand differences in theoretical models with the ultimate goal to converge to a unique constraint on the EoS based on heavy-ion collision data.

The matter created in a heavy-ion collision is far from thermal equilibrium, making transport theory the natural framework for modeling such processes. The calculations presented in this thesis are performed using the transport model SMASH, which is described in detail. To study the equation of state, the most crucial components of the transport calculation are the mean-field potentials. Therefore, a thorough explanation of these potentials is provided, beginning with the Skyrme potential, to which a momentum-dependent term has been added for this work. The symmetry potential is also discussed along with the calculation of electric and ma-

gnetic fields. For each potential, the corresponding equations of motion derived from the test particle ansatz are explained. Since the accurate evaluation of mean-field potentials requires a detailed density calculation, it is described thoroughly, including an analysis of the influence of various technical parameters.

The nuclear potentials are a key focus of this work, but the collision term in the Boltzmann equation is equally essential for accurately describing heavy-ion collisions. Therefore, a detailed description of each interaction type and its modeling is provided. The interactions considered include elastic scattering, resonance formation and decay, inelastic binary scattering, and string excitation. For each interaction, the corresponding partial cross section is given, along with an explanation of how the final state is determined. The section on the collision term concludes with a description of the collision criteria used to identify collisions in a dynamical simulation.

The last main topic considered in the model description is the formation of light nuclei. Light nuclei formation is essential throughout this thesis. At low collision energies, a large fraction of nucleons is bound in nuclei, making them a necessity in theoretical modeling. At higher energies, the formation of light nuclei is extremely interesting, because it may provide valuable insights into the structure of the QCD phase diagram. In the context of this work, the SMASH transport model is coupled to a coalescence afterburner, which creates light nuclei based on the particle distribution in the final state. Alternatively, a dynamic model for the formation of light nuclei can be applied, where light nuclei are formed and destroyed through pion-catalysis or nucleon-catalysis reactions, either in multiparticle processes or in binary reactions with an intermediate step.

The results section starts with an analysis of how flow observables are sensitive to both the equation of state and light nuclei formation. For gold–gold collisions at $E_{\mathrm{kin}} = 1.23A\,\mathrm{GeV}$, as measured at the HADES experiment, flow coefficients of protons and deuterons are computed. During this analysis, the stiffness of the EoS is varied to confirm the well-known sensitivity of flow observables to the EoS, as reported in the literature. Additionally, light nuclei formation is modeled using both coalescence and dynamic formation, and the results are compared. The treatment of light nuclei has a significant effect on the flow coefficients, especially in certain regions of phase space. By comparing the different models, regions where light nuclei formation strongly influences the flow observables can be identified. At the same time, regions in phase space can be identified, where the stiffness of the EoS strongly affects the results, but the treatment of light nuclei plays a subleading role. Exactly these regions are desirable, because they allow for a clean extraction of the EoS.

Generally, few light nuclei are formed from protons at high transverse momentum. The main finding of the first study is that the flow coefficients of protons in the transverse momentum range $1.0\,\mathrm{GeV} < p_T < 1.5\,\mathrm{GeV}$ are particularly well-suited for extracting the EoS. However, this study was conducted without the inclusion of

momentum-dependent potentials, which resulted in an inability to adequately describe the experimental data. As a result, the conclusions drawn from this study do not allow for direct inferences about the EoS."

To allow for conclusions on the EoS, the momentum-dependent term was added to the Skyrme potential. Based on this and the identification of the best suited observables from the previous study, systematic constraints on the EoS are extracted in a subsequent investigation. After quantifying the effects of the momentum dependence, the Coulomb potential, and an improved centrality selection, Bayesian inference was used to draw conclusions about the EoS. By analyzing the directed and elliptic flow of protons and deuterons in the specified transverse momentum range, the posterior distributions for the incompressibility of nuclear matter and the symmetry potential were extracted. The results indicate a relatively stiff EoS with very small statistical uncertainty, demonstrating that the experimental data provides valuable information for constraining the EoS. However, the constraints obtained here do not align with those from previous studies, primarily because no uncertainty on model choices was included in this estimate. Further work is certainly needed to understand differences in transport models to progress in the endeavor to find the EoS of nuclear matter.

Additional information about the density dependence of the EOS can be drawn from the measurements taken at the FOPI experiment, because heavy-ion collisions have been performed at various collision energies. With increasing collision energy, the nuclear matter becomes more compressed. Therefore, the energy-dependence of the flow observables may be studied. This provides an opportunity to investigate whether the EoS softens or stiffens as the density increases. For this purpose, calculations from the SMASH model are compared with the FOPI measurement in the energy range from $E_{\mathrm{kin}} = 250\,\mathrm{MeV}$ to $E_{\mathrm{kin}} = 1.5\,\mathrm{GeV}$. The experimental data is confronted with a soft and a hard EoS, with and without momentum-dependence. For each of the settings, the agreement with the experiment is quantified using a χ^2 estimate. Splitting the data into lower and higher energies, one can observe that a soft EoS is clearly favored at lower collision energies, but a stiffer EoS describes the elliptic flow better at higher collision energies. This may be a hint that the density dependence assumed with the Skyrme potential is too simple, and there could be an interesting structure in the EoS.

For the final results presented in this thesis, the main focus is put on the formation of light nuclei, which are studied in the energy range $7.7\,\mathrm{GeV} < \sqrt{s_{NN}} < 19.6\,\mathrm{GeV}$, as measured by the STAR experiment within the Beam Energy Scan program. The formation of light nuclei is sensitive to fluctuations of the baryon number. Fluctuations increase in the vicinity of a critical point, so that the production of light nuclei may shed light on the phase diagram of QCD matter.

The chosen collision energies are selected to probe key phase structures, such as

a first-order phase transition or a critical point. Therefore, a model that goes beyond hadronic degrees of freedom is required. In this study, a hybrid approach is employed, where light nuclei formation is considered in the afterburner stage. Light nuclei can be formed dynamically in multiparticle reactions during this stage or through coalescence in the final state. By comparing the transverse momentum spectra of deuterons and tritons with experimental data, it is shown that the afterburner stage is essential for a realistic description of the system. The light nuclei sampled on the Cooper-Frye hypersurface do not yield a reasonable description of the measurement.

Ratios of light nuclei are presented for both the coalescence model and the dynamic formation. The calculated single ratios N_d/N_p and N_t/N_p agree well with experimental observations in both cases. However, the double ratio $N_t N_p/N_d^2$ is particularly sensitive to baryon number fluctuations. Since critical fluctuations are not included in the model, it is not surprising that the dynamic formation of light nuclei results in an overestimation of this ratio.

Finally, a closer look into the dynamical evolution of the system is taken. The production mechanisms of different nuclei are investigated, together with the time evolution of the light nuclei yields. Insights on the importance of the various channels can be gained from this comparison. Most importantly, it becomes evident, that an unchanged number of light nuclei in the afterburner does not imply that the system is frozen out. Instead, the scattering rate is large, but the production and disintegration processes are balanced, so that the number of light nuclei is unchanged. This underlines the importance of the afterburner phase.

Anhang A

Natural Units

For the description of a physical system, it is instructive to choose units best suited to the situation. This can be to obtain a relatable scale, for example by denoting the masses of astrophysical objects in solar masses as compared to kilograms that would be unhandy for the description of very heavy objects.

In this thesis the main focus lies on the microscopic description of heavy-ion collisions for which the natural units of high energy physics (see for example [28]) are applied. For this problem, the length and time scales are extremely small. The typical length scale is on the order of femtometers abbreviated by fm where $1\,\mathrm{fm} = 10^{-15}\,\mathrm{m}$. A typical energy scale for such problems is a gigaelectronvolt which is roughly the rest energy of a proton. It is abbreviated as $1\,\mathrm{GeV} = 10^{9}\,\mathrm{eV}$ where an electronvolt (eV) is the energy a particle with a single elementary charge $q = e = 1.602 \cdot 10^{-19}\,\mathrm{C}$ obtains traversing a voltage of one Volt.

Different units are connected through natural constants. Units can be chosen such that some constants are 1. In this work the speed of light c, the reduced Planck constant $\hbar = h/2\pi$ and the Boltzmann constant k_B are set to $c = \hbar = k_B = 1$. This way, various quantities are expressed in terms of the same units. All quantities appearing in this thesis can be expressed either in powers of GeV of in powers of fm.

The time is usually given in terms of fm, which really stands for $\mathrm{fm}/c = \frac{10^{-15}\mathrm{m}}{2.998 \cdot 10^{8}\mathrm{m/s}} \approx 3.3 \cdot 10^{-24}\,\mathrm{s}$.

The mass can be related to the energy in Einsteins theory of relativity. This is reflected in the units as masses are given in terms of GeV or GeV/c^2

$$1\,\frac{\mathrm{GeV}}{c^2} = \frac{10^{9} \cdot 1.602 \cdot 10^{-19}\,\mathrm{J}}{(2.998 \cdot 10^{8}\,\mathrm{m/s})^2} \approx 1.78 \cdot 10^{-27}\,\mathrm{kg}\,, \tag{A.1}$$

where we used that a Joule is $\mathrm{J} = \mathrm{kg}\frac{\mathrm{m}^2}{\mathrm{s}^2}$.

The temperature in a heavy-ion collision is quoted in terms of MeV/k_B, which

corresponds to an unimaginably large temperature in Kelvin

$$1\frac{\mathrm{MeV}}{k_B} = \frac{10^6 \cdot 1.602 \cdot 10^{-19}\,\mathrm{J}}{1.381 \cdot 10^{-23}\,\mathrm{J/K}} \approx 1.16 \cdot 10^{10}\,\mathrm{K}\,. \tag{A.2}$$

This is over a million times higher than the surface of the sun.

The baryon density is often given in terms of the nuclear ground-state density for which we take the value of $\rho_0 = 0.168\,\mathrm{fm}^{-3} = 1.68 \cdot 10^{44}\,\mathrm{m}^{-3}$. The mass density can be roughly estimated by multiplying with the average mass of a nucleon ($m \approx 1.67 \cdot 10^{-27}\,\mathrm{kg}$) leading to the immense mass density of $\rho \approx 2.81 \cdot 10^{17}\,\mathrm{kg/m}^3$. The density in a heavy-ion collision as well as the density in the center of neutron stars can exceed multiples of the nuclear ground-state density.

For the conversion between fm to GeV^{-1}, the relation $1 = \hbar c = 197.3\,\mathrm{MeV\,fm}$ is useful. Following this, a megaelectronvolt can be expressed as $1\,\mathrm{MeV} = 1/197.3\,\mathrm{fm}^{-1}$ and vice versa $1\,\mathrm{fm} = 1/197.3\,\mathrm{MeV}^{-1}$.

Anhang B

Relativistic Kinematics

Heavy-ion collisions are used as a tool to study the properties of strongly-interacting matter. This rapid process requires a relativistic description as the colliding nuclei are accelerated to velocities near the speed of light.

The most prominent result of special relativity is the equivalence of mass m and energy E often quoted as $E = mc^2$, which is only true for a free particle at rest. Taking into account the momentum $\mathbf{p}$ of the particle, the energy-momentum relation for a free particle reads

$$E = \sqrt{m^2c^4 + p^2c^2}\,, \tag{B.1}$$

where the speed of light is included explicitly. Using natural units, we will set the speed of light to one in the following (see Appendix A).

Relativistic kinematics are formulated in terms of four-vectors with indices running from 0 to 3. Most importantly the position in space-time

$$x^\mu = \begin{pmatrix} t \\ x \\ y \\ z \end{pmatrix} \tag{B.2}$$

includes the information about the time and the position in space and treats them on equal footing, which is a key concept of relativity[1].

Equally important to x^μ is the four-momentum p^μ that includes the energy in the 0-component

$$p^\mu = \begin{pmatrix} E \\ p_x \\ p_y \\ p_z \end{pmatrix}\,. \tag{B.3}$$

[1]The notation x^μ really only refers to a single component of the vector, namely the μ-th one. When writing out full vectors, we often keep the index on the left hand side free and provide all possibilities as a tuple on the right hand side.

The vectors are given in the contravariant form, meaning that the Lorentz-index is upstairs. One can obtain the covariant vector using the metric $g_{\mu\nu}$ given any Lorentz-vector y^μ

$$y_\mu = g_{\mu\nu} y^\nu \,. \tag{B.4}$$

The metric is flat in special relativity where its components are given by[2]

$$g_{\mu\nu} = \eta_{\mu\nu} = \begin{pmatrix} 1 & 0 & 0 & 0 \\ 0 & -1 & 0 & 0 \\ 0 & 0 & -1 & 0 \\ 0 & 0 & 0 & -1 \end{pmatrix} \tag{B.5}$$

In general relativity, the Einstein equations relate the metric to the energy-momentum tensor so that the space-time is curved due to matter and energy in general.

The word tensor means that the object behaves according under a Lorentz transformation $\Lambda^\mu{}_\nu$. A Lorentz vector is a rank one tensor. The transformation behavior is such that the vector observed in a different frame is given by

$$y'^\mu = \Lambda^\mu{}_\nu y^\nu \,. \tag{B.6}$$

For a rank two tensor it is

$$y'^{\mu\nu} = \Lambda^\mu{}_\alpha \Lambda^\nu{}_\beta y^{\alpha\beta} \tag{B.7}$$

and for a tensor of rank n

$$y'^{\mu_1\mu_2\ldots\mu_n} = \Lambda^{\mu_1}{}_{\nu_1} \Lambda^{\mu_2}{}_{\nu_2} \ldots \Lambda^{\mu_n}{}_{\nu_n} y^{\nu_1\nu_2\ldots\nu_n} \,. \tag{B.8}$$

This transformation behavior is only for contravariant indices but it works in a similar way for covariant indices. The Lorentz-transformation can incorporate a translation, rotation and a boost to a system with a constant relative velocity.

There are also Lorentz-scalars, which do not have a Lorentz-index and are frame independent. A possibility to obtain a Lorentz-scalar is by summing over a covariant and a contravariant Lorentz index, for example $y_\mu y^\mu = y^\mu g_{\mu\nu} y^\nu = y'_\mu y'^\mu$.

In the case for the momentum four-vector, one obtains

$$p_\mu p^\mu = E^2 - \mathbf{p}^2 = m^2 \,, \tag{B.9}$$

where we used the energy-momentum relation given in Equation B.1.

Another invariant quantity can be obtained from the position four-vector

$$x_\mu x^\mu = t^2 - \mathbf{x} \cdot \mathbf{x} = \tau^2 \,, \tag{B.10}$$

[2]There are two different commonly used conventions for the metric tensor. Besides the one quoted here the metric $\eta_{\mu\nu} = \mathrm{diag}(-1, 1, 1, 1)$ is often applied especially in literature related to general relativity.

where $\mathbf{x}$ denotes the position three-vector $(x, y, z)^T$. As this quantity is invariant and there is a rest-frame of the particle where it is located at $\mathbf{x} = \mathbf{0}$ at all times[3], one can identify τ as the eigentime. This invariant quantity is used to define the four-velocity as a rank one tensor

$$u^\mu = \frac{dx^\mu}{d\tau} = \frac{dx^\mu}{dt}\frac{dt}{d\tau} = \gamma \begin{pmatrix} 1 \\ \beta \end{pmatrix} , \tag{B.11}$$

with the velocity $\beta = d\mathbf{x}/dt$ and the gamma factor $\gamma = (1 - \beta^2)^{-0.5}$. For the propagation of free particles the velocity is required, which can be obtained from the energy and momentum because the $mu^\mu = p^\mu$

$$\beta = \frac{\mathbf{p}}{E} . \tag{B.12}$$

The propagation of test-particles in the vicinity of mean-field potentials is described in Section 2.1.

[3]Only if the particle moves at constant speed, which is the case for free particles.

Anhang C

Additional Comparison to FOPI Data

In this appendix, additional figures for the study presented in Chapter 5 are provided. The plots given here are taken from [3]. A wealth of experimental data of flow coefficients, measured by the FOPI experiment, are available. Only the most important comparisons to the measurement are covered directly in Chapter 5. Still, the χ^2 calculation, on which the conclusions are based, includes a larger set of experimental data points. More of this data is given in this appendix. Before additional comparisons to the measurement are provided, a comparison of the different methods for the centrality selection is given in Figure C.1. The directed flow in Au–Au collisions at $E_{\mathrm{kin}} = 0.4A\,\mathrm{GeV}$ in Figure C.2, as a function of both rapidity and transverse momentum. Further, the elliptic flow at mid-rapidity in Au–Au collisions is shown for different collision energies in Figure C.3 as a function of transverse momentum. Finally, Figures C.4 and C.5 illustrate the elliptic flow as a function of rapidity. Here, Figure C.4 focuses on mid-central collisions for different energies. Figure C.5 shows different centralities for the highest collision energy $E_{\mathrm{kin}} = 1.5A\,\mathrm{GeV}$.

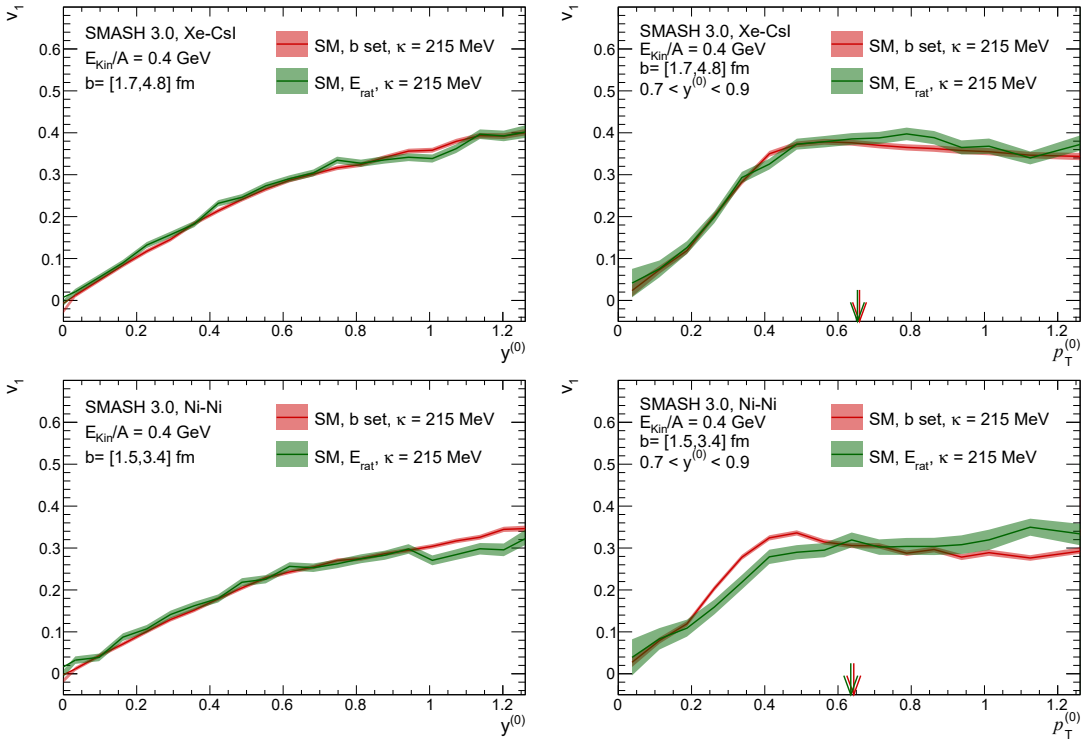

Abbildung C.1: Directed flow coefficient for Xe–CsI (upper panel) and Ni–Ni (lower panel) collisions for centrality selection based on b and E_{rat}. Taken from [3].

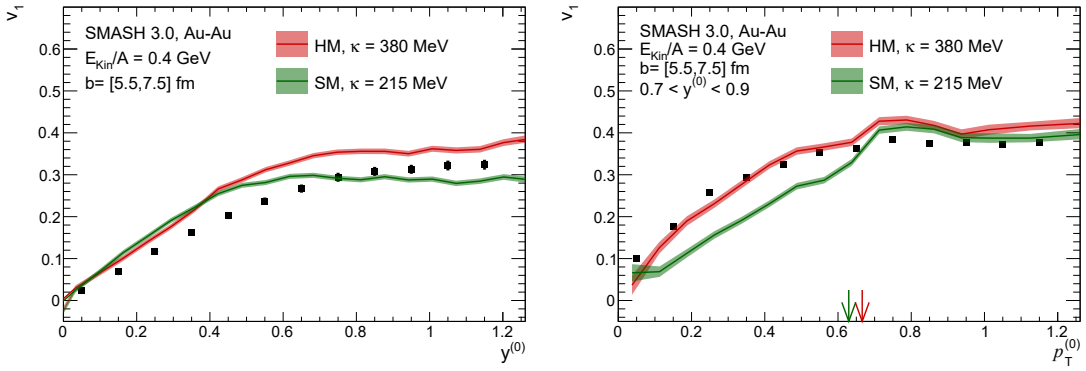

Abbildung C.2: Directed flow coefficient for Au–Au collisions in the centrality class corresponding to $5.5\,\mathrm{fm} \leq b \leq 7.5\,\mathrm{fm}$. Taken from [3].

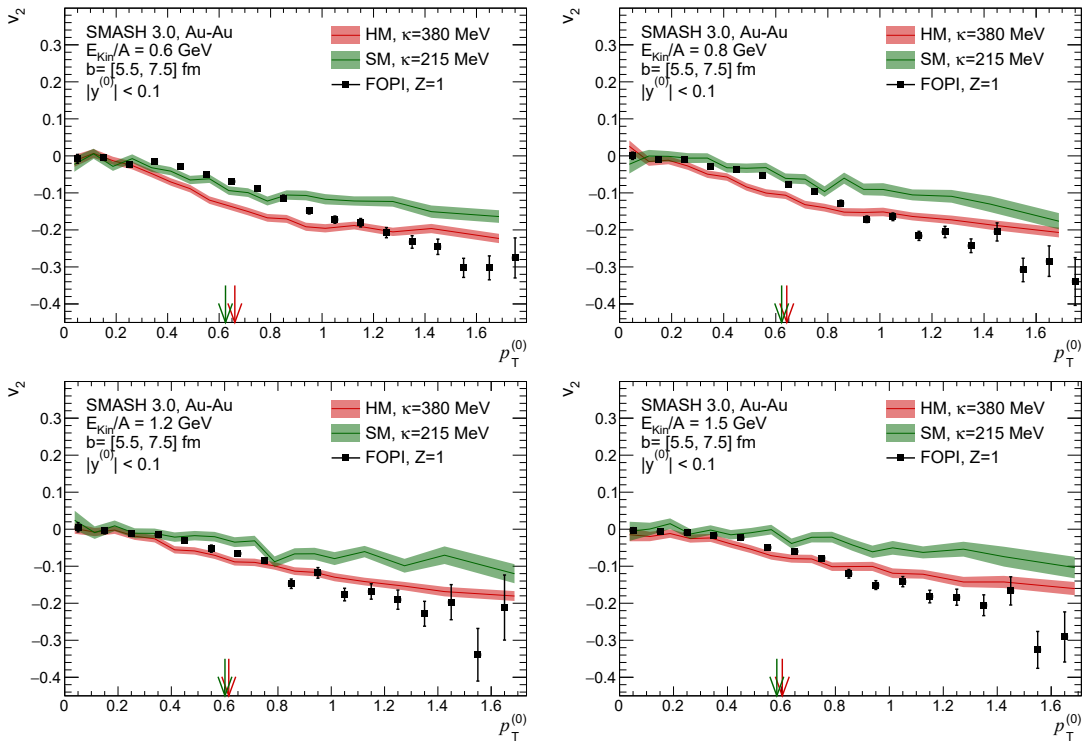

Abbildung C.3: Elliptic flow coefficient as a function of $p_{\mathrm{T}}^{(0)}$ for Au–Au at four collision energies. Taken from [3].

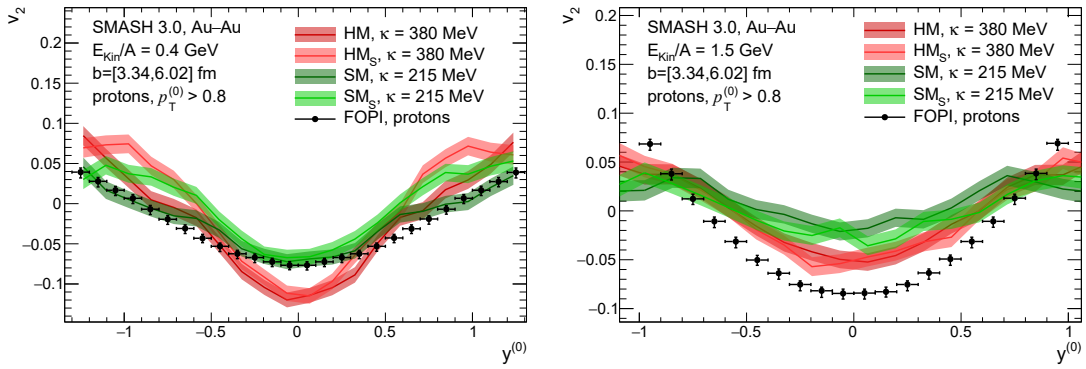

Abbildung C.4: Elliptic flow coefficient v_2 for protons with $p_{\mathrm{T}}^{(0)} > 0.8$ as a function of rapidity for mid-central Au–Au collisions at $E_{\mathrm{kin}}/A = 0.4\,\mathrm{GeV}$ (left) and $E_{\mathrm{kin}}/A = 1.5\,\mathrm{GeV}$ (right), SMASH calculations compared with FOPI data [112]. Taken from [3].

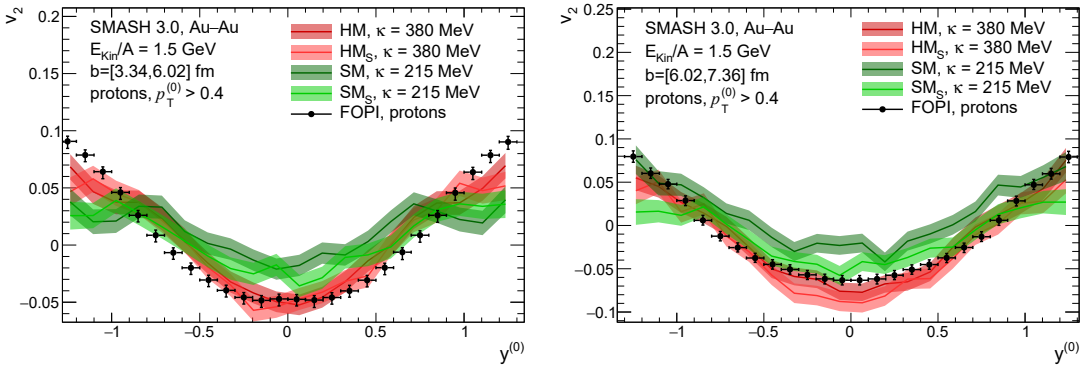

Abbildung C.5: Elliptic flow coefficient v_2 for protons with $p_{\mathrm{T}}^{(0)} > 0.4$ as a function of rapidity for mid-central (left) and mid-peripheral (right) Au–Au collisions at $E_{\mathrm{kin}}/A = 1.5\,\mathrm{GeV}$, SMASH calculations compared with FOPI data [112]. Taken from [3].

Anhang D

Rate equations

This appendix contains additional information on the study presented in Chapter 6. It is based on [4]. We validated the newly introduced multi-particle reactions to create $A = 2$ and $A = 3$ nuclei in Section 6.2. For this purpose we calculated the multiplicities of different particle species as a function of time in a periodic box (see Figure 6.1). To verify these calculations we compared them to the analytical solutions, which are obtained by solving the corresponding rate equations. In Equation D.1 the implemented reactions are shown.

$$\begin{aligned} \pi pn &\leftrightarrow \pi d & \pi ppn &\leftrightarrow \pi \mathrm{He}^3 \\ Npn &\leftrightarrow Nd & Nppn &\leftrightarrow N\mathrm{He}^3 \\ \pi pnn &\leftrightarrow \pi t & \pi pn\Lambda &\leftrightarrow \pi^3_\Lambda\mathrm{H} \\ Npnn &\leftrightarrow Nt & Npn\Lambda &\leftrightarrow N^3_\Lambda\mathrm{H} \end{aligned} \tag{D.1}$$

The equation $NN \leftrightarrow \pi d$ is also implemented in the model but for the calculations in Figure 6.1 it is switched off, as it is not included in the rate equations. The rate equations read as follows

$$\begin{aligned} R_d &= n_d^{th}\left[\langle\sigma v_{\mathrm{rel}}\rangle_{\pi d} n_\pi^{th}\lambda_\pi + \langle\sigma v_{\mathrm{rel}}\rangle_{pd} n_p^{th}\lambda_p + \langle\sigma v_{\mathrm{rel}}\rangle_{nd} n_n^{th}\lambda_n\right] \\ R_t &= n_t^{th}\left[\langle\sigma v_{\mathrm{rel}}\rangle_{\pi t} n_\pi^{th}\lambda_\pi + \langle\sigma v_{\mathrm{rel}}\rangle_{pt} n_p^{th}\lambda_p + \langle\sigma v_{\mathrm{rel}}\rangle_{nt} n_n^{th}\lambda_n\right] \\ R_{^3\mathrm{He}} &= n_{^3\mathrm{He}}^{th}\left[\langle\sigma v_{\mathrm{rel}}\rangle_{\pi^3\mathrm{He}} n_\pi^{th}\lambda_\pi + \langle\sigma v_{\mathrm{rel}}\rangle_{p^3\mathrm{He}} n_p^{th}\lambda_p + \langle\sigma v_{\mathrm{rel}}\rangle_{n^3\mathrm{He}} n_n^{th}\lambda_n\right] \\ R_{^3_\Lambda\mathrm{H}} &= n_{^3_\Lambda\mathrm{H}}^{th}\left[\langle\sigma v_{\mathrm{rel}}\rangle_{\pi^3_\Lambda\mathrm{H}} n_\pi^{th}\lambda_\pi + \langle\sigma v_{\mathrm{rel}}\rangle_{p^3_\Lambda\mathrm{H}} n_p^{th}\lambda_p + \langle\sigma v_{\mathrm{rel}}\rangle_{n^3_\Lambda\mathrm{H}} n_n^{th}\lambda_n\right] \end{aligned} \tag{D.2}$$

$$
\begin{aligned}
n_d^{th}\dot{\lambda_d} &= R_d(\lambda_p\lambda_n - \lambda_d) \\
n_t^{th}\dot{\lambda_t} &= R_t(\lambda_p\lambda_n\lambda_n - \lambda_t) \\
n_{^3\mathrm{He}}^{th}\dot{\lambda_{^3\mathrm{He}}} &= R_{^3\mathrm{He}}(\lambda_p\lambda_p\lambda_n - \lambda_{^3\mathrm{He}}) \\
n_{^3_\Lambda\mathrm{H}}^{th}\dot{\lambda_{^3_\Lambda\mathrm{H}}} &= R_{^3_\Lambda\mathrm{H}}(\lambda_p\lambda_n\lambda_\Lambda - \lambda_{^3_\Lambda\mathrm{H}}) \\
n_p^{th}\dot{\lambda_p} &= -n_d^{th}\dot{\lambda_d} - n_t^{th}\dot{\lambda_t} - 2n_{^3\mathrm{He}}^{th}\dot{\lambda_{^3\mathrm{He}}} - n_{^3_\Lambda\mathrm{H}}^{th}\dot{\lambda_{^3_\Lambda\mathrm{H}}} \\
n_n^{th}\dot{\lambda_n} &= -n_d^{th}\dot{\lambda_d} - 2n_t^{th}\dot{\lambda_t} - n_{^3\mathrm{He}}^{th}\dot{\lambda_{^3\mathrm{He}}} - n_{^3_\Lambda\mathrm{H}}^{th}\dot{\lambda_{^3_\Lambda\mathrm{H}}} \\
n_\Lambda^{th}\dot{\lambda_\Lambda} &= -n_{^3_\Lambda\mathrm{H}}^{th}\dot{\lambda_{^3_\Lambda\mathrm{H}}} \\
\dot{\lambda_\pi} &= 0\,.
\end{aligned}
\tag{D.3}
$$

Anhang E

Scattering Rates at Higher Energies

This appendix contains additional information on the study presented in Chapter 6. It is based on [4].

In Section 6.3.4 we only showed the results for the lowest energy 7.7 GeV. Additionally we present here the results for 14.5 GeV and 19.6 GeV as well. Figures E.1, E.2 and E.3 show the scattering rates for deuterons, tritons, ^{3}He nuclei and hypertritons. Nuclei formation via pion (blue curve) or nucleon (green curve) catalysis reactions is compared to disintegration. As already discussed in Section 6.3.4, deuterons can also be formed and disintegrated via inelastic $2 \rightarrow 2$ scattering as depicted by the red curves in Figure E.1.

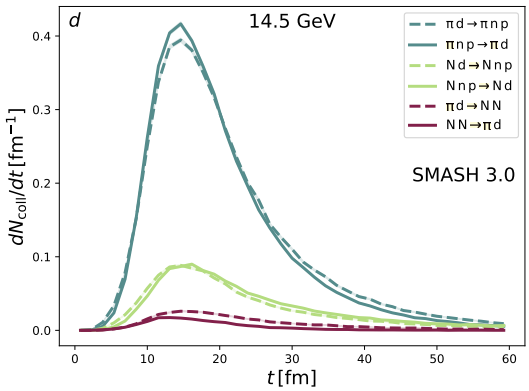

(a) Scattering rates at $\sqrt{s_{NN}} = 14.5\,\text{GeV}$

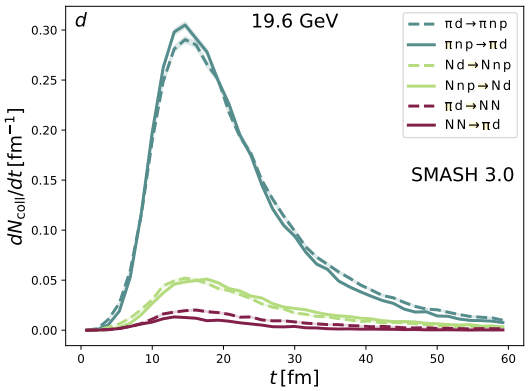

(b) Scattering rates at $\sqrt{s_{NN}} = 19.6\,\text{GeV}$. Taken from [4].

Abbildung E.1: Scattering rates for deuterons in central Au-Au-collisions. The solid curves represent formation mechanisms, while the dashed curves represent disintegration mechanisms.

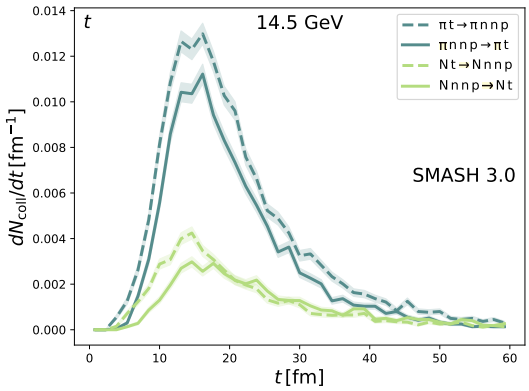

(a) Scattering rates at $\sqrt{s_{NN}} = 14.5\,\text{GeV}$

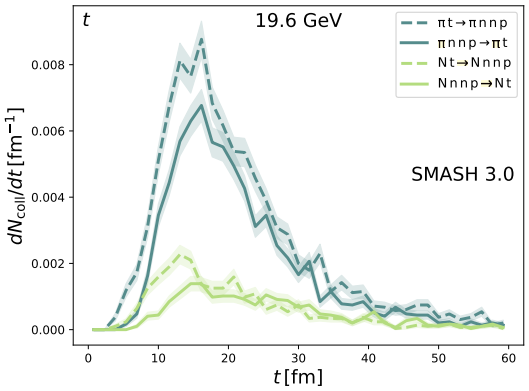

(b) Scattering rates at $\sqrt{s_{NN}} = 19.6\,\text{GeV}$

Abbildung E.2: Scattering rates for tritons in central Au-Au-collisions. The solid curves represent formation mechanisms, while the dashed curves represent disintegration mechanisms. Taken from [4].

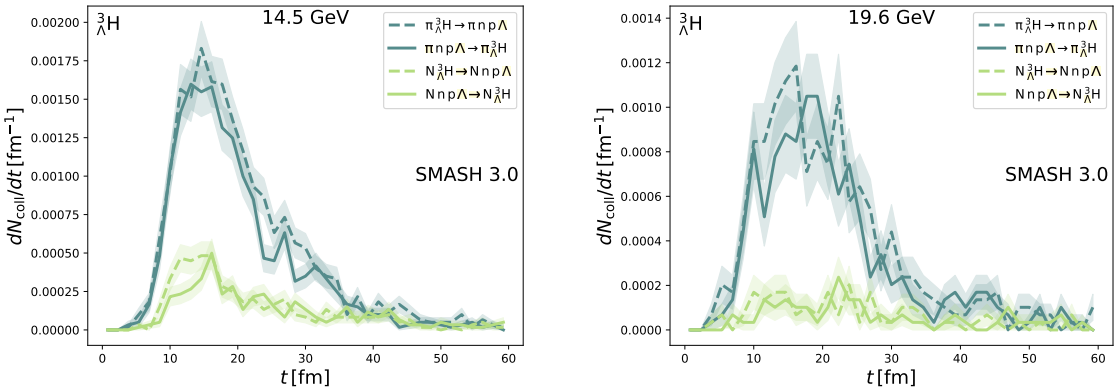

(a) Scattering rates at $\sqrt{s_{NN}} = 14.5\,\text{GeV}$ (b) Scattering rates at $\sqrt{s_{NN}} = 19.6\,\text{GeV}$

Abbildung E.3: Scattering rates for hypertritons in central Au-Au-collisions. The solid curves represent formation mechanisms, while the dashed curves represent disintegration mechanisms. Taken from [4].

Literatur

[1] J. Mohs, M. Ege, H. Elfner und M. Mayer, "Collective flow at SIS energies within a hadronic transport approach: Influence of light nuclei formation and equation of state," *Phys. Rev. C*, Jg. 105, Nr. 3, S. 034 906, 2022. DOI: 10.1103/PhysRevC.105.034906. arXiv: 2012.11454 [nucl-th].

[2] J. Mohs, S. Spies und H. Elfner, "Constraints on the Equation of State of Nuclear Matter from Systematically Comparing SMASH Calculations to HADES Data," Sep. 2024. arXiv: 2409.16927 [nucl-th].

[3] L. A. Tarasovičová, J. Mohs, A. Andronic, H. Elfner und K.-H. Kampert, "Flow and Equation of State of nuclear matter at $\mathbf{E}_{\mathrm{kin}}$/A=0.25-1.5 GeV with the SMASH transport approach," Mai 2024. arXiv: 2405.09889 [nucl-th].

[4] M. Ege, J. Mohs, J. Staudenmaier und H. Elfner, "Deuteron, triton, helium-3 and hypertriton production in relativistic heavy-ion collisions via stochastic multi-particle reactions," Sep. 2024. arXiv: 2409.04209 [nucl-th].

[5] A. Einstein, "The foundation of the general theory of relativity.," *Annalen Phys.*, Jg. 49, Nr. 7, J.-P. Hsu und D. Fine, Hrsg., S. 769–822, 1916. DOI: 10.1002/andp.19163540702.

[6] M. E. Peskin und D. V. Schroeder, *An Introduction to quantum field theory*. Reading, USA: Addison-Wesley, 1995, ISBN: 978-0-201-50397-5, 978-0-429-50355-9, 978-0-429-49417-8. DOI: 10.1201/9780429503559.

[7] C. MissMJ, *Elementary particles included in the Standard Model*, https://en.wikipedia.org/wiki/Elementary_particle, [Online; accessed 16-September-2024].

[8] F. Karsch, "Lattice QCD at high temperature and density," *Lect. Notes Phys.*, Jg. 583, W. Plessas und L. Mathelitsch, Hrsg., S. 209–249, 2002. DOI: 10.1007/3-540-45792-5_6. arXiv: hep-lat/0106019.

[9] Y. Koma, M. Koma und H. Wittig, "Nonperturbative determination of the QCD potential at O(1/m)," *Phys. Rev. Lett.*, Jg. 97, S. 122 003, 2006. DOI: 10.1103/PhysRevLett.97.122003. arXiv: hep-lat/0607009.

[10] B. Andersson, G. Gustafson, G. Ingelman und T. Sjostrand, "Parton Fragmentation and String Dynamics," *Phys. Rept.*, Jg. 97, S. 31–145, 1983. DOI: 10.1016/0370-1573(83)90080-7.

[11] V. Khachatryan u. a., "Constraints on parton distribution functions and extraction of the strong coupling constant from the inclusive jet cross section in pp collisions at $\sqrt{s} = 7$ TeV," *Eur. Phys. J. C*, Jg. 75, Nr. 6, S. 288, 2015. DOI: 10.1140/epjc/s10052-015-3499-1. arXiv: 1410.6765 [hep-ex].

[12] F. J. Dyson, "The S matrix in quantum electrodynamics," *Phys. Rev.*, Jg. 75, S. 1736–1755, 1949. DOI: 10.1103/PhysRev.75.1736.

[13] J. S. Schwinger, "On the Green's functions of quantized fields. 1.," *Proc. Nat. Acad. Sci.*, Jg. 37, S. 452–455, 1951. DOI: 10.1073/pnas.37.7.452.

[14] C. Wetterich, "Exact evolution equation for the effective potential," *Phys. Lett. B*, Jg. 301, S. 90–94, 1993. DOI: 10.1016/0370-2693(93)90726-X. arXiv: 1710.05815 [hep-th].

[15] H. Gies, "Introduction to the functional RG and applications to gauge theories," *Lect. Notes Phys.*, Jg. 852, S. 287–348, 2012. DOI: 10.1007/978-3-642-27320-9_6. arXiv: hep-ph/0611146.

[16] A. Bazavov u. a., "Equation of state in (2+1)-flavor QCD," *Phys. Rev. D*, Jg. 90, S. 094 503, 2014. DOI: 10.1103/PhysRevD.90.094503. arXiv: 1407.6387 [hep-lat].

[17] S. Borsanyi, Z. Fodor, C. Hoelbling u. a., "Is there still any T_c mystery in lattice QCD? Results with physical masses in the continuum limit III," *JHEP*, Jg. 09, S. 073, 2010. DOI: 10.1007/JHEP09(2010)073. arXiv: 1005.3508 [hep-lat].

[18] S. Borsanyi, Z. Fodor, C. Hoelbling, S. D. Katz, S. Krieg und K. K. Szabo, "Full result for the QCD equation of state with 2+1 flavors," *Phys. Lett. B*, Jg. 730, S. 99–104, 2014. DOI: 10.1016/j.physletb.2014.01.007. arXiv: 1309.5258 [hep-lat].

[19] https://home.cern, Accessed: 2024-09-24.

[20] "New State of Matter created at CERN. Un nouvel état de la matière," 2000, Issued on 10 Feb 2000. Adresse: https://cds.cern.ch/record/716634.

[21] https://www.bnl.gov/rhic/, Accessed: 2024-09-24.

[22] "RHIC Scientists Serve Up 'Perfect' Liquid - New state of matter more remarkable than predicted — raising many new questions," 2005, Issued on 18 April 2005. Adresse: https://www.bnl.gov/newsroom/news.php?a=110303.

[23] M. Gyulassy und L. McLerran, "New forms of QCD matter discovered at RHIC," *Nucl. Phys. A*, Jg. 750, D. Rischke und G. Levin, Hrsg., S. 30–63, 2005. DOI: 10.1016/j.nuclphysa.2004.10.034. arXiv: nucl-th/0405013.

[24] N. Cabibbo und G. Parisi, "Exponential Hadronic Spectrum and Quark Liberation," *Phys. Lett. B*, Jg. 59, S. 67–69, 1975. DOI: 10.1016/0370-2693(75)90158-6.

[25] Y. Aoki, G. Endrodi, Z. Fodor, S. D. Katz und K. K. Szabo, "The Order of the quantum chromodynamics transition predicted by the standard model of particle physics," *Nature*, Jg. 443, S. 675–678, 2006. DOI: 10.1038/nature05120. arXiv: hep-lat/0611014.

[26] A. Bzdak, S. Esumi, V. Koch, J. Liao, M. Stephanov und N. Xu, "Mapping the Phases of Quantum Chromodynamics with Beam Energy Scan," *Phys. Rept.*, Jg. 853, S. 1–87, 2020. DOI: 10.1016/j.physrep.2020.01.005. arXiv: 1906.00936 [nucl-th].

[27] E. Rutherford, "The scattering of alpha and beta particles by matter and the structure of the atom," *Phil. Mag. Ser. 6*, Jg. 21, S. 669–688, 1911. DOI: 10.1080/14786440508637080.

[28] B. Povh, K. Rith, C. Scholz, F. Zetsche und W. Rodejohann, *Particles and Nuclei. An Introduction to the Physical Concepts* (Graduate Texts in Physics). 2015, ISBN: 978-3-662-46320-8, 978-3-662-49583-4, 978-3-662-46321-5. DOI: 10.1007/978-3-662-46321-5.

[29] "Report of the workshop on GeV/nucleon collisions of heavy ions: how and why, November 29–December 1, 1974, Bear Mountain, New York," Jan. 1974. Adresse: https://www.osti.gov/biblio/4061527.

[30] G. Baym, "Ultrarelativistic heavy ion collisions: the first billion seconds," *Nucl. Phys. A*, Jg. 956, Y. Akiba, S. Esumi, K. Fukushima u. a., Hrsg., S. 1–10, 2016. DOI: 10.1016/j.nuclphysa.2016.03.007. arXiv: 1701.03972 [nucl-ex].

[31] "LHC Machine," *JINST*, Jg. 3, L. Evans und P. Bryant, Hrsg., S08001, 2008. DOI: 10.1088/1748-0221/3/08/S08001.

[32] J. Mohs, S. Ryu und H. Elfner, "Particle Production via Strings and Baryon Stopping within a Hadronic Transport Approach," *J. Phys. G*, Jg. 47, Nr. 6, S. 065 101, 2020. DOI: 10.1088/1361-6471/ab7bd1. arXiv: 1909.05586 [nucl-th].

[33] J. Adamczewski-Musch u. a., "Probing dense baryon-rich matter with virtual photons," *Nature Phys.*, Jg. 15, Nr. 10, S. 1040–1045, 2019. DOI: 10.1038/s41567-019-0583-8.

[34] B. Friman, C. Hohne, J. Knoll u. a., Hrsg., *The CBM physics book: Compressed baryonic matter in laboratory experiments*. 2011, Bd. 814. DOI: 10.1007/978-3-642-13293-3.

[35] G. Agakishiev u. a., "The High-Acceptance Dielectron Spectrometer HADES," *Eur. Phys. J. A*, Jg. 41, S. 243–277, 2009. DOI: 10.1140/epja/i2009-10807-5. arXiv: 0902.3478 [nucl-ex].

[36] A. Gobbi u. a., "A Highly segmented Delta E time-of-flight wall as forward detector of the 4 pi system for charged particles at the SIS / ESR accelerator," *Nucl. Instrum. Meth. A*, Jg. 324, S. 156–176, 1993. DOI: 10.1016/0168-9002(93)90974-M.

[37] K. H. Ackermann u. a., "STAR detector overview," *Nucl. Instrum. Meth. A*, Jg. 499, S. 624–632, 2003. DOI: 10.1016/S0168-9002(02)01960-5.

[38] P. Braun-Munzinger und J. Stachel, "(Non)thermal aspects of charmonium production and a new look at J / psi suppression," *Phys. Lett. B*, Jg. 490, S. 196–202, 2000. DOI: 10.1016/S0370-2693(00)00991-6. arXiv: nucl-th/0007059.

[39] A. Andronic, P. Braun-Munzinger, K. Redlich und J. Stachel, "Statistical hadronization of charm in heavy ion collisions at SPS, RHIC and LHC," *Phys. Lett. B*, Jg. 571, S. 36–44, 2003. DOI: 10.1016/j.physletb.2003.07.066. arXiv: nucl-th/0303036.

[40] A. Andronic, P. Braun-Munzinger, K. Redlich und J. Stachel, "Statistical hadronization of heavy quarks in ultra-relativistic nucleus-nucleus collisions," *Nucl. Phys. A*, Jg. 789, S. 334–356, 2007. DOI: 10.1016/j.nuclphysa.2007.02.013. arXiv: nucl-th/0611023.

[41] A. Andronic, P. Braun-Munzinger, J. Stachel und H. Stocker, "Production of light nuclei, hypernuclei and their antiparticles in relativistic nuclear collisions," *Phys. Lett. B*, Jg. 697, S. 203–207, 2011. DOI: 10.1016/j.physletb.2011.01.053. arXiv: 1010.2995 [nucl-th].

[42] A. Andronic, P. Braun-Munzinger, K. Redlich und J. Stachel, "Decoding the phase structure of QCD via particle production at high energy," *Nature*, Jg. 561, Nr. 7723, S. 321–330, 2018. DOI: 10.1038/s41586-018-0491-6. arXiv: 1710.09425 [nucl-th].

[43] P. Braun-Munzinger, B. Dönigus und N. Löher, "ALICE investigates 'snowballs in hell'," *CERN Courier*, Jg. 55, Nr. 7, S. 26–30, 2015. Adresse: https://cds.cern.ch/record/2232490.

[44] M. L. Miller, K. Reygers, S. J. Sanders und P. Steinberg, "Glauber modeling in high energy nuclear collisions," *Ann. Rev. Nucl. Part. Sci.*, Jg. 57, S. 205–243, 2007. DOI: 10.1146/annurev.nucl.57.090506.123020. arXiv: nucl-ex/0701025.

[45] F. Gelis und R. Venugopalan, "Particle production in field theories coupled to strong external sources," *Nucl. Phys. A*, Jg. 776, S. 135–171, 2006. DOI: 10.1016/j.nuclphysa.2006.07.020. arXiv: hep-ph/0601209.

[46] B. Schenke, P. Tribedy und R. Venugopalan, "Fluctuating Glasma initial conditions and flow in heavy ion collisions," *Phys. Rev. Lett.*, Jg. 108, S. 252 301, 2012. DOI: 10.1103/PhysRevLett.108.252301. arXiv: 1202.6646 [nucl-th].

[47] C. Gale, S. Jeon, B. Schenke, P. Tribedy und R. Venugopalan, "Event-by-event anisotropic flow in heavy-ion collisions from combined Yang-Mills and viscous fluid dynamics," *Phys. Rev. Lett.*, Jg. 110, Nr. 1, S. 012 302, 2013. DOI: 10.1103/PhysRevLett.110.012302. arXiv: 1209.6330 [nucl-th].

[48] J. S. Moreland, J. E. Bernhard und S. A. Bass, "Alternative ansatz to wounded nucleon and binary collision scaling in high-energy nuclear collisions," *Phys. Rev. C*, Jg. 92, Nr. 1, S. 011 901, 2015. DOI: 10.1103/PhysRevC.92.011901. arXiv: 1412.4708 [nucl-th].

[49] D. Everett u. a., "Multisystem Bayesian constraints on the transport coefficients of QCD matter," *Phys. Rev. C*, Jg. 103, Nr. 5, S. 054 904, 2021. DOI: 10.1103/PhysRevC.103.054904. arXiv: 2011.01430 [hep-ph].

[50] I. A. Karpenko, P. Huovinen, H. Petersen und M. Bleicher, "Estimation of the shear viscosity at finite net-baryon density from $A + A$ collision data at $\sqrt{s_{\mathrm{NN}}} = 7.7 - 200$ GeV," *Phys. Rev. C*, Jg. 91, Nr. 6, S. 064 901, 2015. DOI: 10.1103/PhysRevC.91.064901. arXiv: 1502.01978 [nucl-th].

[51] A. Schäfer, I. Karpenko, X.-Y. Wu, J. Hammelmann und H. Elfner, "Particle production in a hybrid approach for a beam energy scan of Au+Au/Pb+Pb collisions between $\sqrt{s_{\mathrm{NN}}} = 4.3$ GeV and $\sqrt{s_{\mathrm{NN}}} = 200.0$ GeV," *Eur. Phys. J. A*, Jg. 58, Nr. 11, S. 230, 2022. DOI: 10.1140/epja/s10050-022-00872-x. arXiv: 2112.08724 [hep-ph].

[52] Z.-W. Lin, C. M. Ko, B.-A. Li, B. Zhang und S. Pal, "A Multi-phase transport model for relativistic heavy ion collisions," *Phys. Rev. C*, Jg. 72, S. 064 901, 2005. DOI: 10.1103/PhysRevC.72.064901. arXiv: nucl-th/0411110.

[53] B. Schenke, S. Jeon und C. Gale, "(3+1)D hydrodynamic simulation of relativistic heavy-ion collisions," *Phys. Rev. C*, Jg. 82, S. 014 903, 2010. DOI: 10.1103/PhysRevC.82.014903. arXiv: 1004.1408 [hep-ph].

[54] J. .-. Rose, J. M. Torres-Rincon, A. Schäfer, D. R. Oliinychenko und H. Petersen, "Shear viscosity of a hadron gas and influence of resonance lifetimes on relaxation time," *Phys. Rev. C*, Jg. 97, Nr. 5, S. 055 204, 2018. DOI: 10.1103/PhysRevC.97.055204. arXiv: 1709.03826 [nucl-th].

[55] J.-B. Rose, M. Greif, J. Hammelmann u. a., "Cross-conductivity: novel transport coefficients to constrain the hadronic degrees of freedom of nuclear matter," *Phys. Rev. D*, Jg. 101, Nr. 11, S. 114 028, 2020. DOI: 10.1103/PhysRevD.101.114028. arXiv: 2001.10606 [nucl-th].

[56] J. Hammelmann, J. Staudenmaier und H. Elfner, "Collision term dependence of the hadronic shear viscosity and diffusion coefficients," Juli 2023. arXiv: 2307.15606 [nucl-th].

[57] P. Kovtun, D. T. Son und A. O. Starinets, "Viscosity in strongly interacting quantum field theories from black hole physics," *Phys. Rev. Lett.*, Jg. 94, S. 111 601, 2005. DOI: 10.1103/PhysRevLett.94.111601. arXiv: hep-th/0405231.

[58] J. E. Bernhard, J. S. Moreland, S. A. Bass, J. Liu und U. Heinz, "Applying Bayesian parameter estimation to relativistic heavy-ion collisions: simultaneous characterization of the initial state and quark-gluon plasma medium," *Phys. Rev. C*, Jg. 94, Nr. 2, S. 024 907, 2016. DOI: 10.1103/PhysRevC.94.024907. arXiv: 1605.03954 [nucl-th].

[59] G. S. Denicol, C. Gale, S. Jeon, A. Monnai, B. Schenke und C. Shen, "Net baryon diffusion in fluid dynamic simulations of relativistic heavy-ion collisions," *Phys. Rev. C*, Jg. 98, Nr. 3, S. 034 916, 2018. DOI: 10.1103/PhysRevC.98.034916. arXiv: 1804.10557 [nucl-th].

[60] M. Greif, J. A. Fotakis, G. S. Denicol und C. Greiner, "Diffusion of conserved charges in relativistic heavy ion collisions," *Phys. Rev. Lett.*, Jg. 120, Nr. 24, S. 242 301, 2018. DOI: 10.1103/PhysRevLett.120.242301. arXiv: 1711.08680 [hep-ph].

[61] J. A. Fotakis, M. Greif, C. Greiner, G. S. Denicol und H. Niemi, "Diffusion processes involving multiple conserved charges: A study from kinetic theory and implications to the fluid-dynamical modeling of heavy ion collisions," *Phys. Rev. D*, Jg. 101, Nr. 7, S. 076 007, 2020. DOI: 10.1103/PhysRevD.101.076007. arXiv: 1912.09103 [hep-ph].

[62] P. Huovinen und H. Petersen, "Particlization in hybrid models," *Eur. Phys. J. A*, Jg. 48, S. 171, 2012. DOI: 10.1140/epja/i2012-12171-9. arXiv: 1206.3371 [nucl-th].

[63] F. Cooper und G. Frye, "Comment on the Single Particle Distribution in the Hydrodynamic and Statistical Thermodynamic Models of Multiparticle Production," *Phys. Rev. D*, Jg. 10, S. 186, 1974. DOI: 10.1103/PhysRevD.10.186.

[64] M. Oertel, M. Hempel, T. Klähn und S. Typel, "Equations of state for supernovae and compact stars," *Rev. Mod. Phys.*, Jg. 89, Nr. 1, S. 015 007, 2017. DOI: 10.1103/RevModPhys.89.015007. arXiv: 1610.03361 [astro-ph.HE].

[65] M. Wang, G. Audi, A. H. Wapstra u. a., "The Ame2012 atomic mass evaluation," *Chin. Phys. C*, Jg. 36, Nr. 12, S. 1603–2014, 2012. DOI: 10.1088/1674-1137/36/12/003.

[66] R. Hofstadter, H. R. Fechter und J. A. McIntyre, "High-Energy Electron Scattering and Nuclear Structure Determinations," *Phys. Rev.*, Jg. 92, Nr. 4, S. 978, 1953. DOI: 10.1103/PhysRev.92.978.

[67] H. De Vries, C. W. De Jager und C. De Vries, "Nuclear charge and magnetization density distribution parameters from elastic electron scattering," *Atom. Data Nucl. Data Tabl.*, Jg. 36, S. 495–536, 1987. DOI: 10.1016/0092-640X(87)90013-1.

[68] I. Angeli und K. P. Marinova, "Table of experimental nuclear ground state charge radii: An update," *Atom. Data Nucl. Data Tabl.*, Jg. 99, Nr. 1, S. 69–95, 2013. DOI: 10.1016/j.adt.2011.12.006.

[69] J. P. Blaizot, "Nuclear Compressibilities," *Phys. Rept.*, Jg. 64, S. 171–248, 1980. DOI: 10.1016/0370-1573(80)90001-0.

[70] J. Piekarewicz, "Unmasking the nuclear matter equation of state," *Phys. Rev. C*, Jg. 69, S. 041 301, 2004. DOI: 10.1103/PhysRevC.69.041301. arXiv: nucl-th/0312020.

[71] E. Khan und J. Margueron, "Towards a better knowledge of the nuclear equation of state from the isoscalar breathing mode," Apr. 2013. arXiv: 1304.4721 [nucl-th].

[72] J. M. Lattimer und Y. Lim, "Constraining the Symmetry Parameters of the Nuclear Interaction," *Astrophys. J.*, Jg. 771, S. 51, 2013. DOI: 10.1088/0004-637X/771/1/51. arXiv: 1203.4286 [nucl-th].

[73] E. Lipparini und S. Stringari, "Sum rules and giant resonances in nuclei," *Physics Reports*, Jg. 175, Nr. 3, S. 103–261, 1989, ISSN: 0370-1573. DOI: https://doi.org/10.1016/0370-1573(89)90029-X. Adresse: https://www.sciencedirect.com/science/article/pii/037015738990029X.

[74] L. Trippa, G. Colo und E. Vigezzi, "The Giant Dipole Resonance as a quantitative constraint on the symmetry energy," *Phys. Rev. C*, Jg. 77, S. 061 304, 2008. DOI: 10.1103/PhysRevC.77.061304. arXiv: 0802.3658 [nucl-th].

[75] A. Tamii u. a., "Complete electric dipole response and the neutron skin in 208Pb," *Phys. Rev. Lett.*, Jg. 107, S. 062 502, 2011. DOI: 10.1103/PhysRevLett.107.062502. arXiv: 1104.5431 [nucl-ex].

[76] P. .-. Reinhard und W. Nazarewicz, "Information content of a new observable: The case of the nuclear neutron skin," *Phys. Rev. C*, Jg. 81, S. 051 303, 2010. DOI: 10.1103/PhysRevC.81.051303. arXiv: 1002.4140 [nucl-th].

[77] X. Roca-Maza, M. Centelles, X. Viñas u. a., "Electric dipole polarizability in ^{208}Pb: Insights from the droplet model," *Phys. Rev. C*, Jg. 88, Nr. 2, S. 024 316, 2013. DOI: 10.1103/PhysRevC.88.024316. arXiv: 1307.4806 [nucl-th].

[78] Z. Zhang und L.-W. Chen, "Electric dipole polarizability in ^{208}Pb as a probe of the symmetry energy and neutron matter around $\rho_0/3$," *Phys. Rev. C*, Jg. 92, Nr. 3, S. 031 301, 2015. DOI: 10.1103/PhysRevC.92.031301. arXiv: 1504.01077 [nucl-th].

[79] J. M. Lattimer und A. W. Steiner, "Constraints on the symmetry energy using the mass-radius relation of neutron stars," *Eur. Phys. J. A*, Jg. 50, S. 40, 2014. DOI: 10.1140/epja/i2014-14040-y. arXiv: 1403.1186 [nucl-th].

[80] A. Kurkela, P. Romatschke und A. Vuorinen, "Cold Quark Matter," *Phys. Rev. D*, Jg. 81, S. 105 021, 2010. DOI: 10.1103/PhysRevD.81.105021. arXiv: 0912.1856 [hep-ph].

[81] T. Gorda, A. Kurkela, P. Romatschke, S. Säppi und A. Vuorinen, "Next-to-Next-to-Next-to-Leading Order Pressure of Cold Quark Matter: Leading Logarithm," *Phys. Rev. Lett.*, Jg. 121, Nr. 20, S. 202 701, 2018. DOI: 10.1103/PhysRevLett.121.202701. arXiv: 1807.04120 [hep-ph].

[82] S. Gandolfi, A. Y. Illarionov, K. E. Schmidt, F. Pederiva und S. Fantoni, "Quantum Monte Carlo calculation of the equation of state of neutron matter," *Phys. Rev. C*, Jg. 79, S. 054 005, 2009. DOI: 10.1103/PhysRevC.79.054005. arXiv: 0903.2610 [nucl-th].

[83] I. Tews, T. Krüger, K. Hebeler und A. Schwenk, "Neutron matter at next-to-next-to-next-to-leading order in chiral effective field theory," *Phys. Rev. Lett.*, Jg. 110, Nr. 3, S. 032 504, 2013. DOI: 10.1103/PhysRevLett.110.032504. arXiv: 1206.0025 [nucl-th].

[84] E. Annala, T. Gorda, A. Kurkela, J. Nättilä und A. Vuorinen, "Evidence for quark-matter cores in massive neutron stars," *Nature Phys.*, Jg. 16, Nr. 9, S. 907–910, 2020. DOI: 10.1038/s41567-020-0914-9. arXiv: 1903.09121 [astro-ph.HE].

[85] S. Altiparmak, C. Ecker und L. Rezzolla, "On the Sound Speed in Neutron Stars," *Astrophys. J. Lett.*, Jg. 939, Nr. 2, S. L34, 2022. DOI: 10.3847/2041-8213/ac9b2a. arXiv: 2203.14974 [astro-ph.HE].

[86] A. C. Semposki, C. Drischler, R. J. Furnstahl, J. A. Melendez und D. R. Phillips, "From chiral EFT to perturbative QCD: a Bayesian model mixing approach to symmetric nuclear matter," Apr. 2024. arXiv: 2404.06323 [nucl-th].

[87] J. Schaffner-Bielich, *Compact Star Physics*. Cambridge University Press, Aug. 2020, ISBN: 978-1-316-84835-7, 978-1-107-18089-5. DOI: 10.1017/9781316848357.

[88] J. R. Oppenheimer und G. M. Volkoff, "On massive neutron cores," *Phys. Rev.*, Jg. 55, S. 374–381, 1939. DOI: 10.1103/PhysRev.55.374.

[89] P. Demorest, T. Pennucci, S. Ransom, M. Roberts und J. Hessels, "Shapiro Delay Measurement of A Two Solar Mass Neutron Star," *Nature*, Jg. 467, S. 1081–1083, 2010. DOI: 10.1038/nature09466. arXiv: 1010.5788 [astro-ph.HE].

[90] J. Antoniadis u. a., "A Massive Pulsar in a Compact Relativistic Binary," *Science*, Jg. 340, S. 6131, 2013. DOI: 10.1126/science.1233232. arXiv: 1304.6875 [astro-ph.HE].

[91] E. Fonseca u. a., "Refined Mass and Geometric Measurements of the High-mass PSR J0740+6620," *Astrophys. J. Lett.*, Jg. 915, Nr. 1, S. L12, 2021. DOI: 10.3847/2041-8213/ac03b8. arXiv: 2104.00880 [astro-ph.HE].

[92] T. E. Riley u. a., "A NICER View of the Massive Pulsar PSR J0740+6620 Informed by Radio Timing and XMM-Newton Spectroscopy," *Astrophys. J. Lett.*, Jg. 918, Nr. 2, S. L27, 2021. DOI: 10.3847/2041-8213/ac0a81. arXiv: 2105.06980 [astro-ph.HE].

[93] T. Salmi u. a., "The Radius of the High-mass Pulsar PSR J0740+6620 with 3.6 yr of NICER Data," *Astrophys. J.*, Jg. 974, Nr. 2, S. 294, 2024. DOI: 10.3847/1538-4357/ad5f1f. arXiv: 2406.14466 [astro-ph.HE].

[94] D. Choudhury u. a., "A NICER View of the Nearest and Brightest Millisecond Pulsar: PSR J0437–4715," *Astrophys. J. Lett.*, Jg. 971, Nr. 1, S. L20, 2024. DOI: 10.3847/2041-8213/ad5a6f. arXiv: 2407.06789 [astro-ph.HE].

[95] B. P. Abbott u. a., "GW170817: Observation of Gravitational Waves from a Binary Neutron Star Inspiral," *Phys. Rev. Lett.*, Jg. 119, Nr. 16, S. 161 101, 2017. DOI: 10.1103/PhysRevLett.119.161101. arXiv: 1710.05832 [gr-qc].

[96] B. P. Abbott u. a., "Multi-messenger Observations of a Binary Neutron Star Merger," *Astrophys. J. Lett.*, Jg. 848, Nr. 2, S. L12, 2017. DOI: 10.3847/2041-8213/aa91c9. arXiv: 1710.05833 [astro-ph.HE].

[97] B. P. Abbott u. a., "GW170817: Measurements of neutron star radii and equation of state," *Phys. Rev. Lett.*, Jg. 121, Nr. 16, S. 161 101, 2018. DOI: 10.1103/PhysRevLett.121.161101. arXiv: 1805.11581 [gr-qc].

[98] P. Russotto, M. D. Cozma, E. De Filippo, A. L. Fèvre, Y. Leifels und J. Łukasik, "Studies of the equation-of-state of nuclear matter by heavy-ion collisions at intermediate energy in the multi-messenger era: A review focused on GSI results," *Riv. Nuovo Cim.*, Jg. 46, Nr. 1, S. 1–70, 2023. DOI: 10.1007/s40766-023-00039-4. arXiv: 2302.01453 [nucl-ex].

[99] J. Xu u. a., "Understanding transport simulations of heavy-ion collisions at 100A and 400A MeV: Comparison of heavy-ion transport codes under controlled conditions," *Phys. Rev. C*, Jg. 93, Nr. 4, S. 044 609, 2016. DOI: 10.1103/PhysRevC.93.044609. arXiv: 1603.08149 [nucl-th].

[100] J. Aichelin und C. M. Ko, "Subthreshold Kaon Production as a Probe of the Nuclear Equation of State," *Phys. Rev. Lett.*, Jg. 55, S. 2661–2663, 1985. DOI: 10.1103/PhysRevLett.55.2661.

[101] C. Fuchs, "Kaon production in heavy ion reactions at intermediate energies," *Prog. Part. Nucl. Phys.*, Jg. 56, S. 1–103, 2006. DOI: 10.1016/j.ppnp.2005.07.004. arXiv: nucl-th/0507017.

[102] C. Hartnack, H. Oeschler und J. Aichelin, "Hadronic matter is soft," *Phys. Rev. Lett.*, Jg. 96, S. 012 302, 2006. DOI: 10.1103/PhysRevLett.96.012302. arXiv: nucl-th/0506087.

[103] C. Fuchs, A. Faessler, E. Zabrodin und Y.-M. Zheng, "Probing the nuclear equation of state by K+ production in heavy ion collisions," *Phys. Rev. Lett.*, Jg. 86, S. 1974–1977, 2001. DOI: 10.1103/PhysRevLett.86.1974. arXiv: nucl-th/0011102.

[104] A. Le Fèvre, Y. Leifels, C. Hartnack und J. Aichelin, "Origin of elliptic flow and its dependence on the equation of state in heavy ion reactions at intermediate energies," *Phys. Rev. C*, Jg. 98, Nr. 3, S. 034 901, 2018. DOI: 10.1103/PhysRevC.98.034901. arXiv: 1611.07500 [nucl-th].

[105] W. Reisdorf und H. G. Ritter, "Collective flow in heavy-ion collisions," *Ann. Rev. Nucl. Part. Sci.*, Jg. 47, S. 663–709, 1997. DOI: 10.1146/annurev.nucl.47.1.663.

[106] J. J. Molitoris und H. Stoecker, "FURTHER EVIDENCE FOR A STIFF NUCLEAR EQUATION OF STATE FROM A TRANSVERSE MOMENTUM ANALYSIS OF Ar (1800-MEV/NUCLEON) + KCl," *Phys. Rev. C*, Jg. 32, S. 346–348, 1985. DOI: 10.1103/PhysRevC.32.346.

[107] J. Aichelin, A. Rosenhauer, G. Peilert, H. Stoecker und W. Greiner, "Importance of Momentum Dependent Interactions for the Extraction of the Nuclear Equation of State From High-energy Heavy Ion Collisions," *Phys. Rev. Lett.*, Jg. 58, S. 1926–1929, 1987. DOI: 10.1103/PhysRevLett.58.1926.

[108] Q.-b. Pan und P. Danielewicz, "From sideward flow to nuclear compressibility," *Phys. Rev. Lett.*, Jg. 70, S. 2062–2065, 1993, [Erratum: Phys.Rev.Lett. 70, 3523 (1993)]. DOI: 10.1103/PhysRevLett.70.2062.

[109] J.-m. Zhang, S. Das Gupta und C. Gale, "Momentum dependent nuclear mean fields and collective flow in heavy ion collisions," *Phys. Rev. C*, Jg. 50, S. 1617–1625, 1994. DOI: 10.1103/PhysRevC.50.1617. arXiv: nucl-th/9405006.

[110] A. Hombach, W. Cassing, S. Teis und U. Mosel, "Analysis of flow effects in relativistic heavy ion collisions within the CBUU approach," *Eur. Phys. J. A*, Jg. 5, S. 157–172, 1999. DOI: 10.1007/s100500050272. arXiv: nucl-th/9812050.

[111] P. Danielewicz, R. Lacey und W. G. Lynch, "Determination of the equation of state of dense matter," *Science*, Jg. 298, S. 1592–1596, 2002. DOI: 10.1126/science.1078070. arXiv: nucl-th/0208016.

[112] W. Reisdorf u. a., "Systematics of azimuthal asymmetries in heavy ion collisions in the 1 A GeV regime," *Nucl. Phys. A*, Jg. 876, S. 1–60, 2012. DOI: 10.1016/j.nuclphysa.2011.12.006. arXiv: 1112.3180 [nucl-ex].

[113] A. Le Fèvre, Y. Leifels, W. Reisdorf, J. Aichelin und C. Hartnack, "Constraining the nuclear matter equation of state around twice saturation density," *Nucl. Phys. A*, Jg. 945, S. 112–133, 2016. DOI: 10.1016/j.nuclphysa.2015.09.015. arXiv: 1501.05246 [nucl-ex].

[114] J. Adamczewski-Musch u. a., "Directed, Elliptic, and Higher Order Flow Harmonics of Protons, Deuterons, and Tritons in Au + Au Collisions at $\sqrt{s_{NN}} = 2.4$ GeV," *Phys. Rev. Lett.*, Jg. 125, S. 262 301, 2020. DOI: 10.1103/PhysRevLett.125.262301. arXiv: 2005.12217 [nucl-ex].

[115] S. A. Bass u. a., "Microscopic models for ultrarelativistic heavy ion collisions," *Prog. Part. Nucl. Phys.*, Jg. 41, S. 255–369, 1998. DOI: 10.1016/S0146-6410(98)00058-1. arXiv: nucl-th/9803035.

[116] M. Bleicher u. a., "Relativistic hadron hadron collisions in the ultrarelativistic quantum molecular dynamics model," *J. Phys. G*, Jg. 25, S. 1859–1896, 1999. DOI: 10.1088/0954-3899/25/9/308. arXiv: hep-ph/9909407.

[117] P. Hillmann, J. Steinheimer und M. Bleicher, "Directed, elliptic and triangular flow of protons in Au+Au reactions at 1.23 A GeV: a theoretical analysis of the recent HADES data," *J. Phys. G*, Jg. 45, Nr. 8, S. 085 101, 2018. DOI: 10.1088/1361-6471/aac96f. arXiv: 1802.01951 [nucl-th].

[118] P. Hillmann, J. Steinheimer, T. Reichert u. a., "First, second, third and fourth flow harmonics of deuterons and protons in Au+Au reactions at 1.23 AGeV," *J. Phys. G*, Jg. 47, Nr. 5, S. 055 101, 2020. DOI: 10.1088/1361-6471/ab6fcf. arXiv: 1907.04571 [nucl-th].

[119] J. Aichelin, E. Bratkovskaya, A. Le Fèvre u. a., "Parton-hadron-quantum-molecular dynamics: A novel microscopic n -body transport approach for heavy-ion collisions, dynamical cluster formation, and hypernuclei production," *Phys. Rev. C*, Jg. 101, Nr. 4, S. 044 905, 2020. DOI: 10.1103/PhysRevC.101.044905. arXiv: 1907.03860 [nucl-th].

[120] V. Kireyeu, V. Voronyuk, M. Winn u. a., "Constraints on the equation-of-state from low energy heavy-ion collisions within the PHQMD microscopic approach with momentum-dependent potential," Nov. 2024. arXiv: 2411.04969 [nucl-th].

[121] C. Y. Tsang, M. B. Tsang, W. G. Lynch, R. Kumar und C. J. Horowitz, "Determination of the equation of state from nuclear experiments and neutron star observations," *Nature Astron.*, Jg. 8, Nr. 3, S. 328–336, 2024. DOI: 10.1038/s41550-023-02161-z. arXiv: 2310.11588 [nucl-th].

[122] S. Huth u. a., "Constraining Neutron-Star Matter with Microscopic and Macroscopic Collisions," *Nature*, Jg. 606, S. 276–280, 2022. DOI: 10.1038/s41586-022-04750-w. arXiv: 2107.06229 [nucl-th].

[123] M. Dutra, O. Lourenco, J. S. Sa Martins, A. Delfino, J. R. Stone und P. D. Stevenson, "Skyrme Interaction and Nuclear Matter Constraints," *Phys. Rev. C*, Jg. 85, S. 035 201, 2012. DOI: 10.1103/PhysRevC.85.035201. arXiv: 1202.3902 [nucl-th].

[124] M. Dutra, O. Lourenço, S. S. Avancini u. a., "Relativistic Mean-Field Hadronic Models under Nuclear Matter Constraints," *Phys. Rev. C*, Jg. 90, Nr. 5, S. 055 203, 2014. DOI: 10.1103/PhysRevC.90.055203. arXiv: 1405.3633 [nucl-th].

[125] M. Omana Kuttan, J. Steinheimer, K. Zhou und H. Stoecker, "QCD Equation of State of Dense Nuclear Matter from a Bayesian Analysis of Heavy-Ion Collision Data," *Phys. Rev. Lett.*, Jg. 131, Nr. 20, S. 202 303, 2023. DOI: 10.1103/PhysRevLett.131.202303. arXiv: 2211.11670 [hep-ph].

[126] D. Oliinychenko, A. Sorensen, V. Koch und L. McLerran, "Sensitivity of Au+Au collisions to the symmetric nuclear matter equation of state at 2–5 nuclear saturation densities," *Phys. Rev. C*, Jg. 108, Nr. 3, S. 034 908, 2023. DOI: 10.1103/PhysRevC.108.034908. arXiv: 2208.11996 [nucl-th].

[127] M. Tanabashi u. a., "Review of Particle Physics," *Phys. Rev. D*, Jg. 98, Nr. 3, S. 030 001, 2018. DOI: 10.1103/PhysRevD.98.030001.

[128] J. Weil u. a., "Particle production and equilibrium properties within a new hadron transport approach for heavy-ion collisions," *Phys. Rev. C*, Jg. 94, Nr. 5, S. 054 905, 2016. DOI: 10.1103/PhysRevC.94.054905. arXiv: 1606.06642 [nucl-th].

[129] A. Wergieluk, J. Weil, J. Tindall u. a., *smash-transport/smash: SMASH-3.1*, Version SMASH-3.1, Feb. 2024. DOI: 10.5281/zenodo.10707746. Adresse: https://doi.org/10.5281/zenodo.10707746.

[130] C. Rosenkvist und H. Elfner, in preparation.

[131] R. D. Woods und D. S. Saxon, "Diffuse Surface Optical Model for Nucleon-Nuclei Scattering," *Phys. Rev.*, Jg. 95, S. 577–578, 1954. DOI: 10.1103/PhysRev.95.577.

[132] I. Karpenko, P. Huovinen und M. Bleicher, "A 3+1 dimensional viscous hydrodynamic code for relativistic heavy ion collisions," *Comput. Phys. Commun.*, Jg. 185, S. 3016–3027, 2014. DOI: 10.1016/j.cpc.2014.07.010. arXiv: 1312.4160 [nucl-th].

[133] J. H. Putschke u. a., "The JETSCAPE framework," März 2019. arXiv: 1903.07706 [nucl-th].

[134] R. Sattler (sometimes referred to as *Robse the magician*), private communication, 25. Okt. 2024.

[135] B. Schenke, S. Jeon und C. Gale, "Elliptic and triangular flow in event-by-event (3+1)D viscous hydrodynamics," *Phys. Rev. Lett.*, Jg. 106, S. 042 301, 2011. DOI: 10.1103/PhysRevLett.106.042301. arXiv: 1009.3244 [hep-ph].

[136] J.-F. Paquet, C. Shen, G. S. Denicol u. a., "Production of photons in relativistic heavy-ion collisions," *Phys. Rev. C*, Jg. 93, Nr. 4, S. 044 906, 2016. DOI: 10.1103/PhysRevC.93.044906. arXiv: 1509.06738 [hep-ph].

[137] T. H. R. Skyrme, "CVII. The nuclear surface," *Phil. Mag.*, Jg. 1, S. 1043–1054, 1956. DOI: 10.1080/14786435608238186.

[138] B. D. Serot und J. D. Walecka, "Recent progress in quantum hadrodynamics," *Int. J. Mod. Phys. E*, Jg. 6, S. 515–631, 1997. DOI: 10.1142/S0218301397000299. arXiv: nucl-th/9701058.

[139] B. Blaettel, V. Koch und U. Mosel, "Transport theoretical analysis of relativistic heavy ion collisions," *Rept. Prog. Phys.*, Jg. 56, S. 1–62, 1993. DOI: 10.1088/0034-4885/56/1/001.

[140] A. B. Larionov, O. Buss, K. Gallmeister und U. Mosel, "Three-body collisions in Boltzmann-Uehling-Uhlenbeck theory," *Phys. Rev. C*, Jg. 76, S. 044 909, 2007. DOI: 10.1103/PhysRevC.76.044909. arXiv: 0704.1785 [nucl-th].

[141] O. Buss, T. Gaitanos, K. Gallmeister u. a., "Transport-theoretical Description of Nuclear Reactions," *Phys. Rept.*, Jg. 512, S. 1–124, 2012. DOI: 10.1016/j.physrep.2011.12.001. arXiv: 1106.1344 [hep-ph].

[142] C.-Y. Wong, "Dynamics of nuclear fluid. VIII. Time-dependent Hartree-Fock approximation from a classical point of view," *Phys. Rev. C*, Jg. 25, S. 1460–1475, 1982. DOI: 10.1103/PhysRevC.25.1460.

[143] G. F. Bertsch und S. Das Gupta, "A Guide to microscopic models for intermediate-energy heavy ion collisions," *Phys. Rept.*, Jg. 160, S. 189–233, 1988. DOI: 10.1016/0370-1573(88)90170-6.

[144] S. Hama, B. C. Clark, E. D. Cooper, H. S. Sherif und R. L. Mercer, "Global Dirac optical potentials for elastic proton scattering from heavy nuclei," *Phys. Rev. C*, Jg. 41, S. 2737–2755, 1990. DOI: 10.1103/PhysRevC.41.2737.

[145] E. D. Cooper, S. Hama, B. C. Clark und R. L. Mercer, "Global Dirac phenomenology for proton nucleus elastic scattering," *Phys. Rev. C*, Jg. 47, S. 297–311, 1993. DOI: 10.1103/PhysRevC.47.297.

[146] C. Gale, G. Bertsch und S. Das Gupta, "Heavy-ion collision theory with momentum-dependent interactions," *Phys. Rev. C*, Jg. 35, S. 1666–1671, 1987. DOI: 10.1103/PhysRevC.35.1666.

[147] K. Weber, B. Blaettel, W. Cassing u. a., "A Relativistic effective interaction for heavy ion collisions," *Nucl. Phys. A*, Jg. 539, S. 713–751, 1992. DOI: 10.1016/0375-9474(92)90134-6.

[148] G. M. Welke, M. Prakash, T. T. S. Kuo, S. Das Gupta und C. Gale, "Azimuthal distributions in heavy ion collisions and the nuclear equation of state," *Phys. Rev. C*, Jg. 38, S. 2101–2107, 1988. DOI: 10.1103/PhysRevC.38.2101.

[149] C. F. V. Weizsacker, "Zur Theorie der Kernmassen," *Z. Phys.*, Jg. 96, S. 431–458, 1935. DOI: 10.1007/BF01337700.

[150] H. A. Bethe und R. F. Bacher, "Nuclear Physics A. Stationary States of Nuclei," *Rev. Mod. Phys.*, Jg. 8, S. 82–229, 1936. DOI: 10.1103/RevModPhys.8.82.

[151] G. Royer und G. Gautier, "Coefficients and terms of the liquid drop model and mass formula," *Phys. Rev. C*, Jg. 73, S. 067 302, 2006. DOI: 10.1103/PhysRevC.73.067302. arXiv: nucl-th/0608064.

[152] G. Jhang u. a., "Symmetry energy investigation with pion production from Sn+Sn systems," *Phys. Lett. B*, Jg. 813, S. 136 016, 2021. DOI: 10.1016/j.physletb.2020.136016. arXiv: 2012.06976 [nucl-ex].

[153] C. B. Das, S. D. Gupta, C. Gale und B.-A. Li, "Momentum dependence of symmetry potential in asymmetric nuclear matter for transport model calculations," *Phys. Rev. C*, Jg. 67, S. 034 611, 2003. DOI: 10.1103/PhysRevC.67.034611. arXiv: nucl-th/0212090.

[154] D. Oliinychenko und H. Petersen, "Deviations of the Energy-Momentum Tensor from Equilibrium in the Initial State for Hydrodynamics from Transport Approaches," *Phys. Rev. C*, Jg. 93, Nr. 3, S. 034 905, 2016. DOI: 10.1103/PhysRevC.93.034905. arXiv: 1508.04378 [nucl-th].

[155] J. Aichelin, "'Quantum' molecular dynamics: A Dynamical microscopic n body approach to investigate fragment formation and the nuclear equation of state in heavy ion collisions," *Phys. Rept.*, Jg. 202, S. 233–360, 1991. DOI: 10.1016/0370-1573(91)90094-3.

[156] H. Wolter u. a., "Transport model comparison studies of intermediate-energy heavy-ion collisions," *Prog. Part. Nucl. Phys.*, Jg. 125, S. 103 962, 2022. DOI: 10.1016/j.ppnp.2022.103962. arXiv: 2202.06672 [nucl-th].

[157] N. Sass, M. Müller, O. Garcia-Montero und H. Elfner, "Global angular momentum generation in heavy-ion reactions within a hadronic transport approach," *Phys. Rev. C*, Jg. 108, Nr. 4, S. 044 903, 2023. DOI: 10.1103/PhysRevC.108.044903. arXiv: 2212.14385 [nucl-th].

[158] J. Cugnon, J. Vandermeulen und D. L'Hote, "Simple parametrization of cross-sections for nuclear transport studies up to the GeV range," *Nucl. Instrum. Meth. B*, Jg. 111, S. 215–220, 1996. DOI: 10.1016/0168-583X(95)01384-9.

[159] J. Adam u. a., "Results on total and elastic cross sections in proton–proton collisions at $\sqrt{s} = 200$ GeV," *Phys. Lett. B*, Jg. 808, S. 135 663, 2020. DOI: 10.1016/j.physletb.2020.135663. arXiv: 2003.12136 [hep-ex].

[160] D. M. Manley und E. M. Saleski, "Multichannel resonance parametrization of pi N scattering amplitudes," *Phys. Rev. D*, Jg. 45, S. 4002–4033, 1992. DOI: 10.1103/PhysRevD.45.4002.

[161] J. M. Blatt und V. F. Weisskopf, *Theoretical nuclear physics*. New York: Springer, 1952, ISBN: 978-0-471-08019-0. DOI: 10.1007/978-1-4612-9959-2.

[162] V. Dmitriev, O. Sushkov und C. Gaarde, "Δ Formation in the ^{1}H (^{3}He, ^{3}H) Δ^{++} Reaction at Intermediate-energies," *Nucl. Phys. A*, Jg. 459, S. 503–524, 1986. DOI: 10.1016/0375-9474(86)90158-2.

[163] G. Agakishiev u. a., "Baryon resonance production and dielectron decays in proton-proton collisions at 3.5 GeV," *Eur. Phys. J. A*, Jg. 50, S. 82, 2014. DOI: 10.1140/epja/i2014-14082-1. arXiv: 1403.3054 [nucl-ex].

[164] V. Steinberg, J. Steinheimer, H. Elfner und M. Bleicher, "Constraining resonance properties through kaon production in pion–nucleus collisions at low energies," *J. Phys. G*, Jg. 48, Nr. 2, S. 025 109, 2021. DOI: 10.1088/1361-6471/abd232. arXiv: 1912.09895 [nucl-th].

[165] V. K. Steinberg, "Particle production via resonances in heavy-ion collisions," Diss., Goethe U., Frankfurt (main), 2023.

[166] T. Sjöstrand, S. Ask, J. R. Christiansen u. a., "An introduction to PYTHIA 8.2," *Comput. Phys. Commun.*, Jg. 191, S. 159–177, 2015. DOI: 10.1016/j.cpc.2015.01.024. arXiv: 1410.3012 [hep-ph].

[167] R. Corke und T. Sjostrand, "Multiparton Interactions and Rescattering," *JHEP*, Jg. 01, S. 035, 2010. DOI: 10.1007/JHEP01(2010)035. arXiv: 0911.1909 [hep-ph].

[168] J. Weil, "Vector Mesons in Medium in a Transport Approach," Diss., Giessen U., 2013.

[169] G. A. Schuler und T. Sjostrand, "Hadronic diffractive cross-sections and the rise of the total cross-section," *Phys. Rev. D*, Jg. 49, S. 2257–2267, 1994. DOI: 10.1103/PhysRevD.49.2257.

[170] R. D. Ball, V. Bertone, S. Carrazza u. a., "Parton distributions with QED corrections," *Nucl. Phys. B*, Jg. 877, S. 290–320, 2013. DOI: 10.1016/j.nuclphysb.2013.10.010. arXiv: 1308.0598 [hep-ph].

[171] T. Sjostrand und M. van Zijl, "A Multiple Interaction Model for the Event Structure in Hadron Collisions," *Phys. Rev. D*, Jg. 36, S. 2019, 1987. DOI: 10.1103/PhysRevD.36.2019.

[172] G. Ingelman und P. E. Schlein, "Jet Structure in High Mass Diffractive Scattering," *Phys. Lett. B*, Jg. 152, S. 256–260, 1985. DOI: 10.1016/0370-2693(85)91181-5.

[173] C. Bierlich u. a., "A comprehensive guide to the physics and usage of PYTHIA 8.3," *SciPost Phys. Codeb.*, Jg. 2022, S. 8, 2022. DOI: 10.21468/SciPostPhysCodeb.8. arXiv: 2203.11601 [hep-ph].

[174] A. Aduszkiewicz u. a., "Measurements of $\pi^{\pm}$, $K^{\pm}$, p and $\bar{p}$ spectra in proton-proton interactions at 20, 31, 40, 80 and 158 GeV/c with the NA61/SHINE spectrometer at the CERN SPS," *Eur. Phys. J. C*, Jg. 77, Nr. 10, S. 671, 2017. DOI: 10.1140/epjc/s10052-017-5260-4. arXiv: 1705.02467 [nucl-ex].

[175] K. Gallmeister und U. Mosel, "Time Dependent Hadronization via HERMES and EMC Data Consistency," *Nucl. Phys. A*, Jg. 801, S. 68–79, 2008. DOI: 10.1016/j.nuclphysa.2007.12.009. arXiv: nucl-th/0701064.

[176] A. Ono u. a., "Comparison of heavy-ion transport simulations: Collision integral with pions and Δ resonances in a box," *Phys. Rev. C*, Jg. 100, Nr. 4, S. 044 617, 2019. DOI: 10.1103/PhysRevC.100.044617. arXiv: 1904.02888 [nucl-th].

[177] J. Hammelmann, J. M. Torres-Rincon, J.-B. Rose, M. Greif und H. Elfner, "Electrical conductivity and relaxation via colored noise in a hadronic gas," *Phys. Rev. D*, Jg. 99, Nr. 7, S. 076 015, 2019. DOI: 10.1103/PhysRevD.99.076015. arXiv: 1810.12527 [hep-ph].

[178] T. Kodama, S. B. Duarte, K. C. Chung, R. Donangelo und R. A. M. S. Nazareth, "Causality and relativistic effects in intranuclear cascade calculations," *Phys. Rev. C*, Jg. 29, S. 2146–2152, 1984. DOI: 10.1103/PhysRevC.29.2146.

[179] T. Hirano und Y. Nara, "Dynamical modeling of high energy heavy ion collisions," *PTEP*, Jg. 2012, 01A203, 2012. DOI: 10.1093/ptep/pts007. arXiv: 1203.4418 [nucl-th].

[180] P. Danielewicz und G. F. Bertsch, "Production of deuterons and pions in a transport model of energetic heavy ion reactions," *Nucl. Phys. A*, Jg. 533, S. 712–748, 1991. DOI: 10.1016/0375-9474(91)90541-D.

[181] W. Cassing, "Anti-baryon production in hot and dense nuclear matter," *Nucl. Phys. A*, Jg. 700, S. 618–646, 2002. DOI: 10.1016/S0375-9474(01)01322-7. arXiv: nucl-th/0105069.

[182] Z. Xu und C. Greiner, "Thermalization of gluons in ultrarelativistic heavy ion collisions by including three-body interactions in a parton cascade," *Phys. Rev. C*, Jg. 71, S. 064 901, 2005. DOI: 10.1103/PhysRevC.71.064901. arXiv: hep-ph/0406278.

[183] J. Staudenmaier, "Multi-particle interactions in hadronic transport approaches," Diss., Goethe U., Frankfurt (main), Goethe U., Frankfurt (main), 2021. DOI: 10.21248/gups.63506.

[184] J. Staudenmaier, D. Oliinychenko, J. M. Torres-Rincon und H. Elfner, "Deuteron production in relativistic heavy ion collisions via stochastic multiparticle reactions," *Phys. Rev. C*, Jg. 104, Nr. 3, S. 034 908, 2021. DOI: 10.1103/PhysRevC.104.034908. arXiv: 2106.14287 [hep-ph].

[185] O. Garcia-Montero, J. Staudenmaier, A. Schäfer, J. M. Torres-Rincon und H. Elfner, "Role of proton-antiproton regeneration in the late stages of heavy-ion collisions," *Phys. Rev. C*, Jg. 105, Nr. 6, S. 064 906, 2022. DOI: 10.1103/PhysRevC.105.064906. arXiv: 2107.08812 [hep-ph].

[186] W. Reisdorf u. a., "Systematics of central heavy ion collisions in the 1A GeV regime," *Nucl. Phys. A*, Jg. 848, S. 366–427, 2010. DOI: 10.1016/j.nuclphysa.2010.09.008. arXiv: 1005.3418 [nucl-ex].

[187] S. Sombun, K. Tomuang, A. Limphirat u. a., "Deuteron production from phase-space coalescence in the UrQMD approach," *Phys. Rev. C*, Jg. 99, Nr. 1, S. 014 901, 2019. DOI: 10.1103/PhysRevC.99.014901. arXiv: 1805.11509 [nucl-th].

[188] D. Oliinychenko, L.-G. Pang, H. Elfner und V. Koch, "Light Nuclei Production in Ultra-Relativistic Heavy Ion Collisions," *Springer Proc. Phys.*, Jg. 250, D. Elia, G. E. Bruno, P. Colangelo und L. Cosmai, Hrsg., S. 307–313, 2020. DOI: 10.1007/978-3-030-53448-6_48.

[189] B. Kardan, "Collective flow and correlations measurements with HADES in Au+Au collisions at 1.23 AGeV," *Nucl. Phys. A*, Jg. 982, F. Antinori, A. Dainese, P. Giubellino, V. Greco, M. P. Lombardo und E. Scomparin, Hrsg., S. 431–434, 2019. DOI: 10.1016/j.nuclphysa.2018.09.061. arXiv: 1809.07821 [nucl-ex].

[190] J. Adamczewski-Musch u. a., "Centrality determination of Au + Au collisions at 1.23A GeV with HADES," *Eur. Phys. J. A*, Jg. 54, Nr. 5, S. 85, 2018. DOI: 10.1140/epja/i2018-12513-7. arXiv: 1712.07993 [nucl-ex].

[191] H. H. Gutbrod, B. W. Kolb, H. R. Schmidt, A. M. Poskanzer, H. G. Ritter und K. H. Kampert, "A New Component of the Collective Flow in Relativistic Heavy Ion Collisions," *Phys. Lett. B*, Jg. 216, S. 267–271, 1989. DOI: 10.1016/0370-2693(89)91113-1.

[192] E. D. Cooper, S. Hama und B. C. Clark, "Global Dirac optical potential from helium to lead," *Phys. Rev. C*, Jg. 80, S. 034 605, 2009. DOI: 10.1103/PhysRevC.80.034605.

[193] J. Adamczewski-Musch u. a., "Charged-pion production in **Au + Au** collisions at $\sqrt{s_{NN}} = 2.4$ **GeV**: HADES Collaboration," *Eur. Phys. J. A*, Jg. 56, Nr. 10, S. 259, 2020. DOI: 10.1140/epja/s10050-020-00237-2. arXiv: 2005.08774 [nucl-ex].

[194] C. Hartnack, L. Sehn, J. Jaenicke, H. Stoecker und J. Aichelin, "Kaon production at subthreshold energies," *Nucl. Phys. A*, Jg. 580, S. 643–678, 1994. DOI: 10.1016/0375-9474(94)90786-2.

[195] J. Adamczewski-Musch u. a., "Deep sub-threshold ϕ production in Au+Au collisions," *Phys. Lett. B*, Jg. 778, S. 403–407, 2018. DOI: 10.1016/j.physletb.2018.01.048. arXiv: 1703.08418 [nucl-ex].

[196] A. Andronic u. a., "Excitation function of elliptic flow in Au+Au collisions and the nuclear matter equation of state," *Phys. Lett. B*, Jg. 612, S. 173–180, 2005. DOI: 10.1016/j.physletb.2005.02.060. arXiv: nucl-ex/0411024.

[197] A. Andronic u. a., "Directed flow in Au + Au, Xe + CsI and Ni + Ni collisions and the nuclear equation of state," *Phys. Rev. C*, Jg. 67, S. 034 907, 2003. DOI: 10.1103/PhysRevC.67.034907. arXiv: nucl-ex/0301009.

[198] P. Danielewicz, R. A. Lacey, P. B. Gossiaux u. a., "Disappearance of elliptic flow: a new probe for the nuclear equation of state," *Phys. Rev. Lett.*, Jg. 81, S. 2438–2441, 1998. DOI: 10.1103/PhysRevLett.81.2438. arXiv: nucl-th/9803047.

[199] C. Pinkenburg u. a., "Elliptic flow: Transition from out-of-plane to in-plane emission in Au + Au collisions," *Phys. Rev. Lett.*, Jg. 83, S. 1295–1298, 1999. DOI: 10.1103/PhysRevLett.83.1295. arXiv: nucl-ex/9903010.

[200] J. Adam u. a., "Production of light nuclei and anti-nuclei in pp and Pb-Pb collisions at energies available at the CERN Large Hadron Collider," *Phys. Rev. C*, Jg. 93, Nr. 2, S. 024 917, 2016. DOI: 10.1103/PhysRevC.93.024917. arXiv: 1506.08951 [nucl-ex].

[201] D. Oliinychenko, L.-G. Pang, H. Elfner und V. Koch, "Microscopic study of deuteron production in PbPb collisions at $\sqrt{s} = 2.76TeV$ via hydrodynamics and a hadronic afterburner," *Phys. Rev. C*, Jg. 99, Nr. 4, S. 044 907, 2019. DOI: 10.1103/PhysRevC.99.044907. arXiv: 1809.03071 [hep-ph].

[202] T. Neidig, K. Gallmeister, C. Greiner, M. Bleicher und V. Vovchenko, "Towards solving the puzzle of high temperature light (anti)-nuclei production in ultra-relativistic heavy ion collisions," *Phys. Lett. B*, Jg. 827, S. 136 891, 2022. DOI: 10.1016/j.physletb.2022.136891. arXiv: 2108.13151 [hep-ph].

[203] K.-J. Sun, L.-W. Chen, C. M. Ko und Z. Xu, "Probing QCD critical fluctuations from light nuclei production in relativistic heavy-ion collisions," *Phys. Lett. B*, Jg. 774, S. 103–107, 2017. DOI: 10.1016/j.physletb.2017.09.056. arXiv: 1702.07620 [nucl-th].

[204] K.-J. Sun, L.-W. Chen, C. M. Ko, J. Pu und Z. Xu, "Light nuclei production as a probe of the QCD phase diagram," *Phys. Lett. B*, Jg. 781, S. 499–504, 2018. DOI: 10.1016/j.physletb.2018.04.035. arXiv: 1801.09382 [nucl-th].

[205] M. Abdulhamid u. a., "Beam Energy Dependence of Triton Production and Yield Ratio ($N_t \times N_p/N_d^2$) in Au+Au Collisions at RHIC," *Phys. Rev. Lett.*, Jg. 130, S. 202 301, 2023. DOI: 10.1103/PhysRevLett.130.202301. arXiv: 2209.08058 [nucl-ex].

[206] E. Shuryak und J. M. Torres-Rincon, "Baryon clustering at the critical line and near the hypothetical critical point in heavy-ion collisions," *Phys. Rev. C*, Jg. 100, Nr. 2, S. 024 903, 2019. DOI: 10.1103/PhysRevC.100.024903. arXiv: 1805.04444 [hep-ph].

[207] E. Shuryak und J. M. Torres-Rincon, "Baryon preclustering at the freeze-out of heavy-ion collisions and light-nuclei production," *Phys. Rev. C*, Jg. 101, Nr. 3, S. 034 914, 2020. DOI: 10.1103/PhysRevC.101.034914. arXiv: 1910.08119 [nucl-th].

[208] X. G. Deng und Y. G. Ma, "Light nuclei production in Au + Au collisions at $\sqrt{s_{NN}}$ = 7.7-80 GeV from UrQMD model," *Phys. Lett. B*, Jg. 808, S. 135 668, 2020. DOI: 10.1016/j.physletb.2020.135668. arXiv: 2006.12337 [nucl-th].

[209] Y. Nara, N. Otuka, A. Ohnishi, K. Niita und S. Chiba, "Study of relativistic nuclear collisions at AGS energies from p + Be to Au + Au with hadronic cascade model," *Phys. Rev. C*, Jg. 61, S. 024 901, 2000. DOI: 10.1103/PhysRevC.61.024901. arXiv: nucl-th/9904059.

[210] H. Liu, D. Zhang, S. He, K.-j. Sun, N. Yu und X. Luo, "Light nuclei production in Au+Au collisions at sNN = 5–200 GeV from JAM model," *Phys. Lett. B*, Jg. 805, S. 135 452, 2020, [Erratum: Phys.Lett.B 829, 137132 (2022)]. DOI: 10.1016/j.physletb.2020.135452. arXiv: 1909.09304 [nucl-th].

[211] D. Oliinychenko, C. Shen und V. Koch, "Deuteron production in AuAu collisions at $\sqrt{s_{NN}}$ =7–200 GeV via pion catalysis," *Phys. Rev. C*, Jg. 103, Nr. 3, S. 034 913, 2021. DOI: 10.1103/PhysRevC.103.034913. arXiv: 2009.01915 [hep-ph].

[212] K.-J. Sun, R. Wang, C. M. Ko, Y.-G. Ma und C. Shen, "Unveiling the dynamics of little-bang nucleosynthesis," *Nature Commun.*, Jg. 15, Nr. 1, S. 1074, 2024. DOI: 10.1038/s41467-024-45474-x. arXiv: 2207.12532 [nucl-th].

[213] G. Coci, S. Gläßel, V. Kireyeu u. a., "Dynamical mechanisms for deuteron production at mid-rapidity in relativistic heavy-ion collisions from energies available at the GSI Schwerionensynchrotron to those at the BNL Relativistic Heavy Ion Collider," *Phys. Rev. C*, Jg. 108, Nr. 1, S. 014 902, 2023. DOI: 10.1103/PhysRevC.108.014902. arXiv: 2303.02279 [nucl-th].

[214] R. K. Puri, C. Hartnack und J. Aichelin, "Early fragment formation in heavy ion collisions," *Phys. Rev. C*, Jg. 54, R28–R31, 1996. DOI: 10.1103/PhysRevC.54.R28.

[215] R. K. Puri und J. Aichelin, "Simulated annealing clusterization algorithm for studying the multifragmentation," *J. Comput. Phys.*, Jg. 162, S. 245–266, 2000. DOI: 10.1006/jcph.2000.6534. arXiv: nucl-th/9811018.

[216] A. Monnai, B. Schenke und C. Shen, "Equation of state at finite densities for QCD matter in nuclear collisions," *Phys. Rev. C*, Jg. 100, Nr. 2, S. 024 907, 2019. DOI: 10.1103/PhysRevC.100.024907. arXiv: 1902.05095 [nucl-th].

[217] C. Shen und S. Alzhrani, "Collision-geometry-based 3D initial condition for relativistic heavy-ion collisions," *Phys. Rev. C*, Jg. 102, Nr. 1, S. 014 909, 2020. DOI: 10.1103/PhysRevC.102.014909. arXiv: 2003.05852 [nucl-th].

[218] Y. Pan und S. Pratt, "Baryon annihilation and regeneration in heavy ion collisions," *Phys. Rev. C*, Jg. 89, Nr. 4, S. 044 911, 2014. DOI: 10.1103/PhysRevC.89.044911.

[219] H. Petersen, "Anisotropic flow in transport + hydrodynamics hybrid approaches," *J. Phys. G*, Jg. 41, Nr. 12, S. 124 005, 2014. DOI: 10.1088/0954-3899/41/12/124005. arXiv: 1404.1763 [nucl-th].

[220] J. Adam u. a., "Beam energy dependence of (anti-)deuteron production in Au + Au collisions at the BNL Relativistic Heavy Ion Collider," *Phys. Rev. C*, Jg. 99, Nr. 6, S. 064 905, 2019. DOI: 10.1103/PhysRevC.99.064905. arXiv: 1903.11778 [nucl-ex].